Development of explicit and constitutive lattice-Boltzmann models for food product rheology

Kallum Jack William Wyatt Burgin

A thesis submitted in partial fulfilment of the requirements of
Sheffield Hallam University
for the degree of Doctor of Philosophy

Materials and Engineering Research Institute
Sheffield Hallam University
United Kingdom
September 2018

Abstract

Emulsions are found throughout various industries including oil extraction, biological materials, and food products such as milk, condiments, and spreads. The study of their rheology is therefore important due to its impact on manufacturing efficiency and end product desirability. A key rheological measure is the emulsion viscosity, the fluid's resistance to flow, which affects the power required in production as well as the taste and texture. An emulsion's viscosity displays complex behaviour due to the droplet interfaces and interactions. Similarly, the sheared self-diffusion coefficient measures the amount of movement the droplets exhibit, due to the interactions between droplets.

The presented mesoscopic lattice-Boltzmann models allow for these macroscopic properties to emerge from the simulations due to the explicit modelling of the droplets. A continuous surface force is applied to the lattice fluids to model droplet interfaces. The model is implemented in such a way as to allow the simulation of hundreds of droplets with limited computing power.

The model is initially applied to a pipe flow, with the development of a pressure boundary condition. Boundary effects from the solid walls require their removal, using Lees-Edwards boundary conditions to represent bulk flow in a sheared system. The boundary conditions are extended to the multi-component flow, which allowed simulations to provide results for various emulsion systems with varying droplet concentrations, surface tensions, viscosity ratios, and shear rates. Trends and results from experimental and theoretical literature are recovered and constitutive models of emulsion viscosity have been evaluated. The agreement of these two dimensional lattice-Boltzmann models with three dimensional experimental results shows the usefulness of the method. The structure of the droplets and clustering behaviour they exhibit are examined and compared to solid particle suspension literature. Finally, the model is used in exploratory simulations to examine the effect of droplet bidispersity on the macroscopic properties; the witnessed effect agrees well with solid suspension literature.

This mesoscopic model will allow for phenomenon on this scale to be more easily studied and may provide more accurate information for multi-scale analysis.

Acknowledgements

I would like to thank my supervisors Dr. T. J. Spencer, Dr. I. Halliday, and Dr. T. Schenkel for their help and unwavering support during these past years. I would also like to thank the Pro Vice-Chancellor for Research, Professor Paul Harrison, for starting the scholarship scheme that allowed many of us to undertake our projects. I will be forever grateful to my parents for their guidance, support, and love throughout my life; they are truly an inspiration to me, providing me with the motivation to see this thesis complete. Finally, I would like to thank my wife, for her unending patience and for being there for me during the troubling times of this process.

Advanced Studies

Below is a list of scientific and academic activities that were undertaken during the PhD programme, in chronological order:

- MERI Research Seminars have been attended fortnightly (during university semesters) since October 2014.
- Sheffield Hallam University Doctoral School events have been attended on topics such as: Research Ethics and Integrity, Effective Writing, and Open Data.
- Message Passing Programming with MPI, attended the three day course 28-30th January 2015 at University of Sheffield.
- Advanced School in Soft Condensed Matter 'Solutions in the Spring' 2015, attended the four day workshop 13-16th April 2015 at Loughborough University.
- MERI Symposium 2015 poster with the title "Evaluation of a new pressure boundary condition for lattice-Boltzmann simulations" presented on 19/05/2015 at Sheffield Hallam University.
- Presentation about my research to undergraduate students to encourage research as a pathway, with the title "Modelling Complex Fluids" presented on 26/02/2016 at Sheffield Hallam University.
- MERI Symposium 2016 presentation with the title "Development of computer simulations of the emergent non-Newtonian viscosity behaviour of emulsions: Can we model mayonnaise?" presented on 17/05/2016 at Sheffield Hallam University.
- International Conference for Mesoscopic Methods in Engineering and Science (ICMMES) 2016 poster with the title "Development of computer simulations of the emergent non-Newtonian viscosity behaviour of emulsions" presented on 19/07/2016 at Hamburg, Germany.
- Hermes summer school 2016 presented the poster developed for ICMMES 2016 on 27/07/2016 at Windsor, UK.
- MERI/BMRC Winter Poster Event 2016 presented the poster developed for ICMMES 2016 on 15/12/2016 at Sheffield Hallam University.
- Topical Research Meeting on Physics in Food Manufacturing 2017 presentation with the title "Modelling the emergent flow behaviour of emulsions" presented on 09/01/2017 at Sheffield Hallam University.

- Colloid Young Researchers Meeting 2017 presentation with the title "Computer simulations of the emergent behaviour of emulsions" presented on 10/04/2017 at Sheffield, UK.

- International Conference for Discrete Simulation of Fluid Dynamics (DSFD) 2017 presentation with the title "Lattice-Boltzmann Method for Many Component Simulations of Emulsion Flow: Measuring Viscosity and Self-Diffusion" presented on 10/07/2017 at Erlangen, Germany.

Below is a list of scientific outputs relating to the research undertaken in for this thesis:

- I. Halliday, S. V. Lishchuk, T. J. Spencer, K. Burgin, T. Schenkel (2017). Interfacial micro-currents in continuum-scale multi-component lattice Boltzmann equation hydrodynamics. Computer Physics Communications. `https://doi.org/10.1016/j.cpc.2017.06.005` [1]

- I. Halliday, X. Xu, K. Burgin (2017). Shear viscosity of a two-dimensional emulsion of drops using a multiple-relaxation-time-step lattice Boltzmann method. Physical Review E, 95(1), 023301. `https://doi.org/10.1103/PhysRevE.95.023301` [2]

- X. Xu, K. Burgin, M. A. Ellis, I. Halliday (2017). Benchmarking of three-dimensional multicomponent lattice Boltzmann equation. Physical Review E, 96(5), 053308. `https://doi.org/10.1103/PhysRevE.96.053308` [3]

- I. Halliday, K. Burgin, X. Xu (2018). Analysis of the Phase Field Segregation Scheme Kinematics for Multi-Component Lattice Boltzmann Simulation with a Large Density Contrast. Computers and Fluids. In review.

Contents

List of Figures

List of Tables

Chapter 1

Introduction

The flow of fluids has been studied for many hundreds of years. Even without studying such a topic, it would impact our lives constantly: from drawing air into our lungs, to pumping blood around our bodies. *Rheology* is then a critical area to understand.

A key component of rheology is the viscosity of fluids; how much a fluid resists flowing under stress [5]. Newtonian fluids, such as liquids and gases, behave consistently independent of the applied stress.

However, we are frequently interacting with *complex fluids*; neither wholly liquid nor gas, but may be a combination of these, as well as solids. Emulsions are a class of complex fluids which are made up of liquid droplets dispersed through another liquid component. The viscosity of such a fluid becomes dependent on many variables: the concentration and size of the dispersed droplets, the density and viscosity ratios between the suspended and suspending fluids, as well as interfacial tension between the fluids, to name a few variables. Fig. 1.1 shows the predicted effect of increasing the droplet concentration from a range of theoretical and empirical models; as a greater concentration of droplets are introduced into the system, the fluid becomes much more resistant to flow.

The interfaces and interactions between emulsion droplets result in complex behaviour described as non-Newtonian. The non-Newtonian behaviour of an emulsion can present itself in various forms, but in essence it is the variability of viscosity under stress. One of the most significant aspects of non-Newtonian viscosity—particularly for emulsions—is a shear-thinning behaviour, which means the fluid's viscosity decreases when it is sheared more. Notably, in food condiments, an emulsion may remain stationary (on your plate or food) until forced to flow or spread.

Conversely, shear-thickening can also be present in emulsions; shear-thickening means a fluid gets more resistive the more it is sheared. This can be due to the agglomeration or clustering of its constituents, making it harder for the surrounding fluid to flow.

The change in the microstructure of a suspension (solid particles dispersed in a

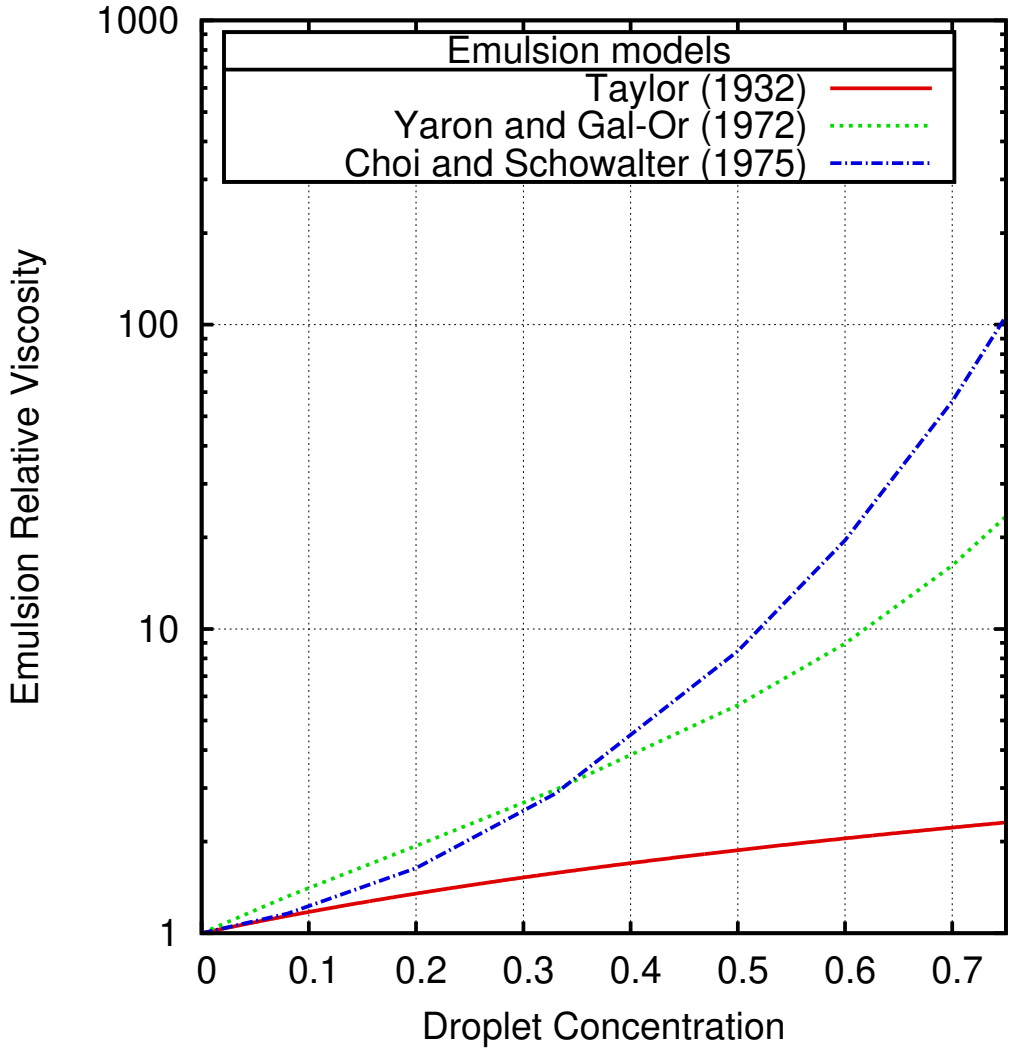

Figure 1.1: The viscosity of an emulsion, predicted by models [6, 7, 8] for a range of droplet concentrations.

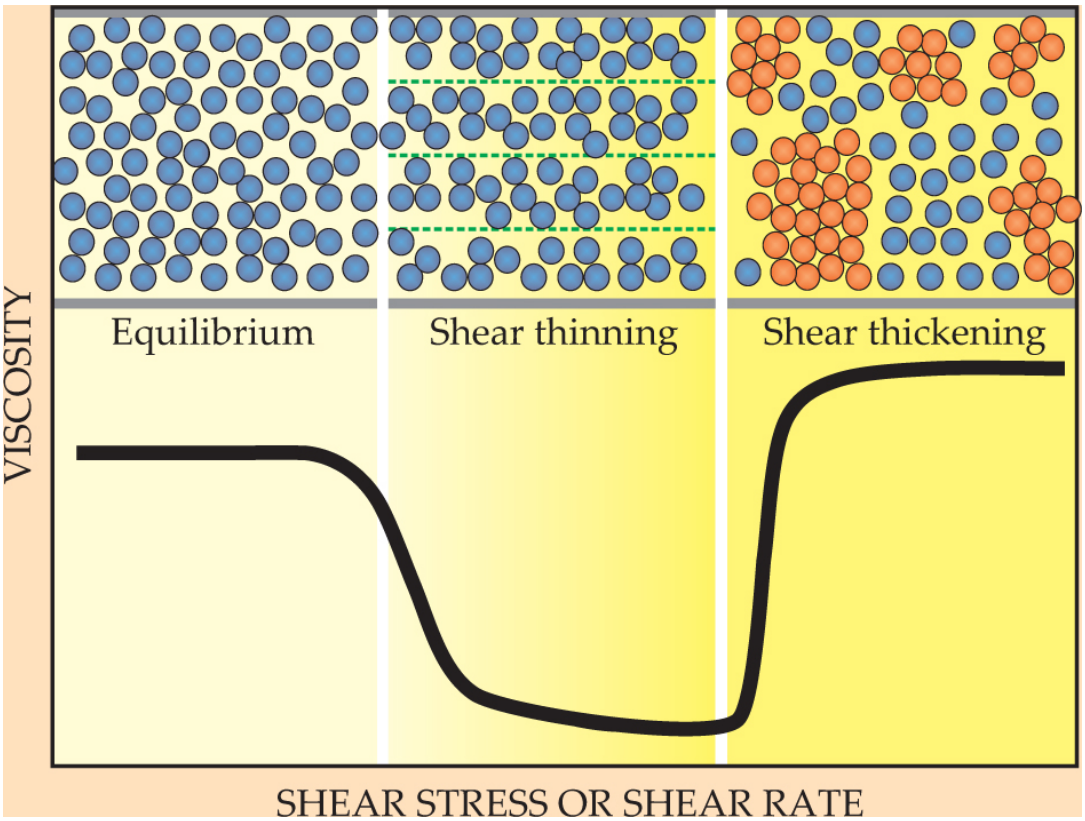

Figure 1.2: Reproduced from Wagner and Brady (2009) [9], with the permission of the American Institute of Physics. The viscosity of a complex fluid varying with the shear rate. At the top are overviews showing the microstructure of the fluid, and below is the effect on the fluid viscosity. An increase in the shear rate results in the fluid leaving the Newtonian regime and exhibiting shear thinning due to the alignment of particles. A further increase can then make suspended particles start to cluster, restricting the fluid flow and increasing the viscosity.

liquid) is visible in Fig. 1.2, showing changes due to the shear rate and the resulting effect on the viscosity. Both shear thinning and shear thickening can be seen for the same fluid in different ranges of the shear rate.

These behaviours, and even Newtonian viscosity, are important to various industries. Many food products such as mayonnaise and milk are emulsions, or may be modelled as such. Key characteristics like the taste and texture may be determined and controlled by the emulsion viscosity. The end product is therefore highly dependant on the structure of the fluid. The concentration of the dispersed phase, the viscosity ratio between the phases, the size of the dispersed particles or droplets, are all factors that will determine the quality of the end product and customer experience.

In other industries such as manufacturing or oil extraction, the viscosity of a fluid being pumped through pipes is a vital measurement to get right. The viscosity controls how much power is required to transport the fluid, with a more viscous fluid requiring more powerful pumps. With non-Newtonian behaviours also present, predicting the transport requirements can be a complex procedure.

Numerical models of fluid viscosity have been under development for a century [10, 6], with computer simulations entering the area more recently. Models of complex, non-Newtonian behaviour have also been presented, but mostly from a macroscopic perspective [11, 12]. These models must, by definition, make assumptions about the underlying structure of the fluid; they will be outlined and discussed in Chapter 2.1.

Such macroscopic models fit themselves within the overarching equation of fluid motion, the Navier-Stokes equation: [13]

$$\frac{\partial \mathbf{u}}{\partial t} + (\mathbf{u} \cdot \nabla)\,\mathbf{u} \;=\; -\frac{1}{\rho}\nabla p + \eta \nabla^2 \mathbf{u} + \mathbf{g}\,, \tag{1.1}$$

where $\mathbf{u}$ is the fluid velocity, ρ is the fluid density, p is the fluid pressure, η is the fluid viscosity, and $\mathbf{g}$ is an external force on the fluid (i.e. gravity). This equation governs the flow of all fluid, from blood flow within veins to interstellar gases flowing around the galaxy. The viscosity, η, can be constant, for a Newtonian fluid, or a macroscopic model can be used to describe any effects by the shear rate or droplet concentration. Numerical methods can, in some cases, solve this system of non-linear partial differential equations to find the velocity field for a given system. Such methods can be highly complex and computationally expensive, fortunately dimensionless numbers and the law of similarities allow for the solution to a non-dimensional system to be applicable to any scale of system. For example, the simulations contained in Chapter 5 have droplets with radius 21 grid spaces. If each grid space is decided to represent 1µm then the droplets have radius 21um (with all other simulation parameters then being calculable from this ratio), however the choice is free to be made.

As well as viscosity, the measurement of the sheared self-diffusion provides insight into the droplet behaviour. The sheared self-diffusion coefficient measures the movement of droplets due to the interaction with other droplets, i.e. the movement perpendicular to the flow direction. Studying this behaviour on the scale of droplets can provide an understanding of transport processes associated with the fluid. For example, the dispersion of medicinal drugs in flowing blood will be impacted by the diffusion happening within the fluid. Additionally, the diffusion and migration of droplets may provide insight into how inclusions such as emulsion droplets can be passively filtered (smaller droplets may be pushed to the boundaries, allowing them to be filtered by the geometry of the system, for example).

In Chapter 2 of this thesis, models of viscosity will be described and models using the lattice-Boltzmann method (LBM) relevant to emulsion rheology will be discussed. Chapter 3 details and validates a lattice-Boltzmann model of emulsion flow. This model is then firstly applied to a pipe flow with an analytic solution in Chapter 4. To escape boundary issues from the solid walls, the method is then applied to the bulk flow of emulsions in Chapter 5, which forms the majority of

the reported rheological data. The results, including measures of relative viscosity, sheared self-diffusion coefficient, and average droplet deformation, will be discussed and compared to macroscopic models. Chapter 6 displays the structure of the fluid droplets and the clustering behaviours witnessed. Having been applied to monodisperse emulsions throughout the previous sections, a subset of results are gathered for bidisperse emulsions in Chapter 7. The conclusions of the thesis are in Chapter 8, as well as an outline of possible future work. Appendix A provides a Chapman Enskog analysis of the method in Chapter 3. Finally, Appendix B provides a table of videos from the simulations carried out in this thesis.

1.1 Aims and Objectives

The intention of this thesis is to present a model of emulsion flow at the mesoscopic scale, that explicitly models the droplets in the fluid structure. The aims and objectives of this thesis break down as follows:

- Develop computer simulations to model the bulk flow of concentrated, explicit emulsion droplets.
  - Develop a model capable of simulating emulsion droplet flow. The droplet and interface should be resolved appropriately. The model should be able to drive the fluid at a wide range of shear rates.
  - Extend the model to allow for concentrated emulsions. This is likely to require multiple droplets to be modelled, so the model must support this. The droplets should not coalesce and the model must allow for the simulation of monodisperse emulsions to simplify the parameter space, also allowing enabling comparisons to macroscopic models.
  - The flow should be free from boundary effects, in order to take measurements of the bulk fluid.
  - The possibility of modelling emulsions that aren't monodisperse should be considered.
- Obtain rheological data from said models that can be compared to and enhance experimental results.
  - The viscosity of the emulsion should be measurable and comparable to existing experimental results as well as macroscopic models.
  - The applicability of existing macroscopic models should be explored—how well can they represent such a fluid?
  - Consider the possibility of using macroscopic models to conduct multi-scale analysis of the fluid.

- Droplet behaviour, such as the sheared self-diffusion and deformation should be measured.
- The microstructure of the fluid should be examined.

Chapter 2

Background

2.1 Emulsion Rheology

The aim of this chapter is to provide context for the models developed in Chapter 3. Existing macroscopic equations are detailed—some theoretical and some empirical—which may allow us to better describe the fluids or trends. Some of these models are exact results, so they may supply validations for new techniques. Additionally, current meso-scale methods are described which may compare or contrast with Chapter 3.

Firstly, however, experimental measurements are an important part of validating simulation results. A brief description of these methods is provided so these measurements can be confidently used later. Various types of viscometers or rheometers can determine a fluid's viscosity; a proper description of non-Newtonian fluids will require the flexibility of rheometers. There are just a few types of rheometers, and some are more relevant here than others. Concentric cylinder rheometers, for example, place the fluid between a cylinder forced to rotate and a cylinder that has its rotation measured; the force that the fluid exerts on the free cylinder can then be measured. The fluid sample undergoes a simple shear in a geometry that can be closely approximated by computer simulation. Changing the speed of the rotating cylinder allows the user to control the shear rate within the system; several measurements can then be taken which describe the non-Newtonian fluid.

Some macroscopic models aim to convey this change in viscosity with the shear rate [14, 15], whilst others focus on the material properties [6, 16]. Descriptions of various models are provided below.

2.1.1 Suspension Models

Einstein [10] laid the foundation for viscosity modelling in 1906 when he determined that the effective viscosity of a dilute suspension is:

$$\eta_{\text{eff}} \;=\; \eta_0 \left(1 + 2.5\phi\right), \tag{2.1}$$

where η_0 is the viscosity of the suspending fluid and ϕ is the volume fraction (concentration) of the suspended particles. Specifically, this models a suspension with solid, non-deforming, spherical particles. Whilst emulsion "particles" are liquid droplets that may deform, this model remains relevant due to the impact it had as a starting point for other models. Additionally, solid particle models may be able to describe similar trends to emulsion data, but they should be used cautiously [17]. However, the major limitation in this model is the very dilute concentration requirement, i.e. the suspension is so dilute ($< 2\%$ concentration) that the particles have negligible effect on each other.

Mooney [18] extends the model to finite concentrations, positing a crowding factor that affects the emulsion viscosity. The theory is limited to first order interactions only, taking into account just the geometric crowding.

Considering the approach of adding particles in two stages and using Einstein's equation as the limit of zero concentration, Mooney determines the relative viscosity of a monodisperse suspension to be:

$$\eta_\mathrm{r} \;=\; \frac{\eta_\mathrm{eff}}{\eta_0} \;=\; \exp\left(\frac{2.5\phi}{1-k\phi}\right), \tag{2.2}$$

where k is a crowding factor, more recently described as a maximum packing fraction $\phi_\mathrm{m} = \frac{1}{k}$. This maximum packing fraction imposes the upper limit whereby $\eta_\mathrm{r} \to \infty$ as $\phi \to \phi_\mathrm{m}$. The value of ϕ_m depends on the particles, but is in the region of 0.63–0.74 for spherical particles. For practical purposes, both ϕ_m and the 2.5 may be used to fit the model; the value 2.5 often chosen to follow Einstein in the spherical limit. This model fits a variety of experimental data on suspensions and emulsions [4] with modest concentrations. Fig. 2.1 shows a comparison of different methods, with (2.2) being the most accurate, on average, for a range of emulsions.

The Krieger-Dougherty (KD) [16] model uses the same max packing fraction concept:

$$\eta_\mathrm{r} \;=\; \left(1-\frac{\phi}{\phi_\mathrm{m}}\right)^{-2.5\phi_\mathrm{m}}, \tag{2.3}$$

however, using a power rather than exponential function. Through this choice, the mathematical limits are more physically consistent [19] and a widely used viscosity model was created.

Bian [20] uses smooth particle hydrodynamics—discussed in Section 2.1.4—to simulate particulate flow and shows that the KD model fits well. This is especially true as the channel gap is widened, i.e. the suspension is less confined. Whilst describing a new theoretical model, Brady [21] shows KD in excellent agreement with experimental results of van der Werff and de Kruif [22].

Similarly, Eilers [23] developed an empirical model including a max packing

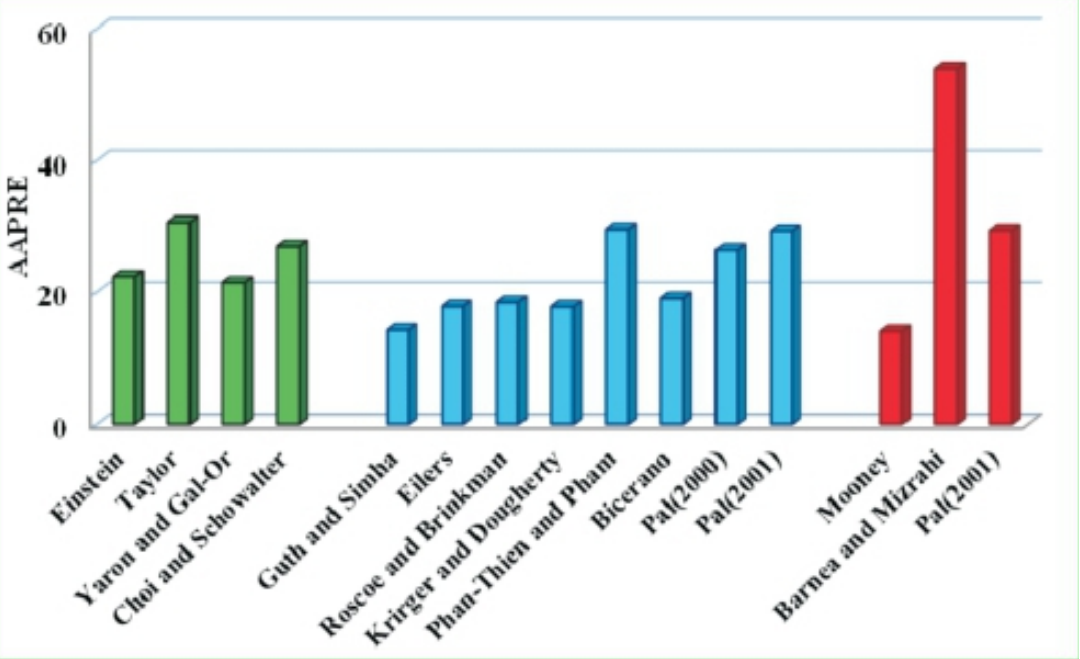

Figure 2.1: Reproduced from Pajouhandeh et al. [4] The average absolute percentage relative error between the various models for a variety of emulsions.

fraction:

$$\eta_{\mathrm{r}} \;=\; \left(1+\frac{1.25\phi}{1-\frac{\phi}{\phi_{\mathrm{m}}}}\right)^{2}\,, \tag{2.4}$$

which captures Einstein's limit at low concentrations and increases to a singularity when $\phi \;=\; \phi_{\mathrm{m}}$.

Bicerano et al. [24] develop another hard-sphere model of a different form:

$$\eta_{\mathrm{r}} \;=\; \left(1-\frac{\phi}{\phi_{\mathrm{m}}}\right)^{-2}\left[1-0.4\left(\frac{\phi}{\phi_{\mathrm{m}}}\right)+0.34\left(\frac{\phi}{\phi_{\mathrm{m}}}\right)^{2}\right]\,. \tag{2.5}$$

This model again uses the max-packing concept to impose an upper limit that may be dependant upon particle shape, size, and distribution. By allowing ϕ_{m} to vary with the Peclet Number, the model can become applicable to non-zero-shear regimes [25]. These models compare well with experimental results, with (2.3) and (2.5) showing wide applicability [26, 27].

2.1.2 Emulsion Models

The aforementioned models have all assumed the suspended material is solid, whereas Taylor [6] extended Einstein's model to include a viscosity ratio; enabling a flow inside the droplet. By assuming: the droplets are small enough that surface tension will keep them spherical, there is no slipping on the surface, and the stress tangential to the surface is continuous, Taylor estimates that the effective emulsion viscosity

is:

$$\eta_{\mathrm{r}} \;=\; 1 + 2.5\phi \left(\frac{\eta_1 + \frac{2}{5}\eta_0}{\eta_1 + \eta_0} \right), \tag{2.6}$$

where η_0 and η_1 are the viscosities of the suspending and suspended fluids respectively and ϕ is the concentration of the suspended fluid in the emulsion. This model also inherits the assumption from Einstein's work that there is a very low concentration of particles/droplets.

Taylor's model, like Einstein's, is exact when the assumptions are met and is shown to be accurate in its target regime (low Reynolds and Capillary numbers) [3], however this is of limited applicability in real emulsion systems; droplets are likely to get deformed and/or concentrated emulsions may be required.

Yaron and Gal-Or [7] use a cell model, whereby the random placement and movement of concentrated droplets means that a statistical average velocity profile around the average drop can be calculated. The velocity profile is then used to calculate energy dissipation and thus the viscosity:

$$\eta_{\mathrm{r}} \;=\; 1 + \phi \left\{ \frac{5.5\left[4\phi^{\frac{7}{3}} + 10 - \frac{84}{11}\phi^{\frac{2}{3}} + \frac{4}{K}\left(1 - \phi^{\frac{7}{3}}\right)\right]}{10\left(1 - \phi^{\frac{10}{3}}\right) - 25\phi\left(1 - \phi^{\frac{4}{3}}\right) + \frac{10}{K}\left(1 - \phi\right)\left(1 - \phi^{\frac{7}{3}}\right)} \right\}, \tag{2.7}$$

Where $K = \frac{\eta_1}{\eta_0}$ is the viscosity ratio between the suspended and suspending fluid. This model is valid only for a low capillary number.

Choi and Schowalter [8] also use a cell model, however the model incorporates droplet deformability. Their viscosity model:

$$\eta_{\mathrm{r}} \;=\; 1 + \phi \left\{ \frac{2\left[(5K + 2) - 5\left(K - 1\right)\phi^{\frac{7}{3}}\right]}{4\left(K + 1\right) - 5\left(5K + 2\right)\phi + 42K\phi^{\frac{5}{3}} - 5\left(5K - 2\right)\phi^{\frac{7}{3}} + 4\left(K - 1\right)\phi^{\frac{10}{3}}} \right\} \tag{2.8}$$

is said to be one of the most precise at representing a water-in-oil emulsion by Pajouhandeh et al. [4]; confusingly the average error is reported to be one of the highest. At the zero concentration limit, this model reduces to the Taylor equation, which is an improvement for physical realism over (2.7). Nonetheless, this model is shown to over-predict viscosity and (2.7) is shown to be more accurate in [28, 29], where various oil-in-water and water-in-oil emulsions are considered.

2.1.3 Non-Newtonian Models (Shear-Dependence)

Another class of viscosity models aim to describe the shear-dependant behaviour of non-Newtonian fluids. Models in the previous sections have been focussed on the material properties and how this affects viscosity, ignoring inertial effects by using low Capillary and Reynolds number assumptions. It is almost the opposite for models in this section. The material under flow is modelled, incorporating the effect that shearing has on the material.

Ostwald [30] and de Waele [31] independently described this relationship using the power law:

$$\eta_{\text{eff}} = k\dot{\gamma}^{(n-1)}, \tag{2.9}$$

where k is a consistency index, $\dot{\gamma}$ is the shear rate, and n is the flow index. k and n are frequently used as fitting parameters, however they do have physical links: the consistency index is the viscosity of the fluid at zero shear, whilst the flow index describes the shear-dependant behaviour that is seen. A flow index of 1 indicates Newtonian behaviour and no dependence on the shear rate. A flow index greater than 1 indicates a dilatant fluid where the fluid becomes more viscous with increasing shear. Finally, a flow index below 1 describes a pseudoplastic fluid that exhibits shear-thinning behaviour.

Clearly, this model can be applied across various non-Newtonian behaviour, however the shear thinning regime ($n < 1$) is most applicable to emulsions.

Herschel and Bulkley [14] proposed their successful viscosity model that introduced a yield stress into the power law model:

$$\eta_{\text{eff}} = k\dot{\gamma}^{n-1} + \frac{\tau_0}{\dot{\gamma}}, \tag{2.10}$$

$$\eta_{\text{eff}} = \begin{cases} \eta_0, & \dot{\gamma} \leq \dot{\gamma}_0 \\ k\dot{\gamma}^{n-1} + \tau_0\dot{\gamma}^{-1}, & \dot{\gamma} \geq \dot{\gamma}_0 \end{cases}, \tag{2.11}$$

$$\eta_{\text{r}} = \begin{cases} 1, & \dot{\gamma} \leq \dot{\gamma}_0 \\ \frac{k\dot{\gamma}^{n-1}}{\eta_0} + \frac{\tau_0\dot{\gamma}^{-1}}{\eta_0}, & \dot{\gamma} \geq \dot{\gamma}_0 \end{cases}, \tag{2.12}$$

where τ_0 is yield stress.

Casson [15] also developed a model with yield stress, initially for printer inks, which has been widely adopted for modelling chocolate:

$$\eta_{\text{eff}} = \eta_0 + \frac{2\sqrt{\eta_0\tau_0}}{\sqrt{\dot{\gamma}}} + \frac{\tau_0}{\dot{\gamma}} \tag{2.13}$$

$$\eta_{\text{r}} = 1 + \frac{2\sqrt{\tau_0}}{\sqrt{\eta_0\dot{\gamma}}} + \frac{\tau_0}{\eta_0\dot{\gamma}} \tag{2.14}$$

Both equations (2.12) and (2.14) are shown to represent shear thinning behaviour of food products very well [32]. A plot of the above non-Newtonian models is visible in Fig. 2.2. Whilst the power-law model produces a straight line on a log-log plot, indicating the shear thinning behaviour is consistent, the other two models produce a curve, proposing that the shear-thinning lessens at higher shear rates. The Casson model in particular converges on a viscosity at higher shear, once the yield stress of the fluid has been overcome.

Four-parameter models have been developed which aim to represent the viscosity

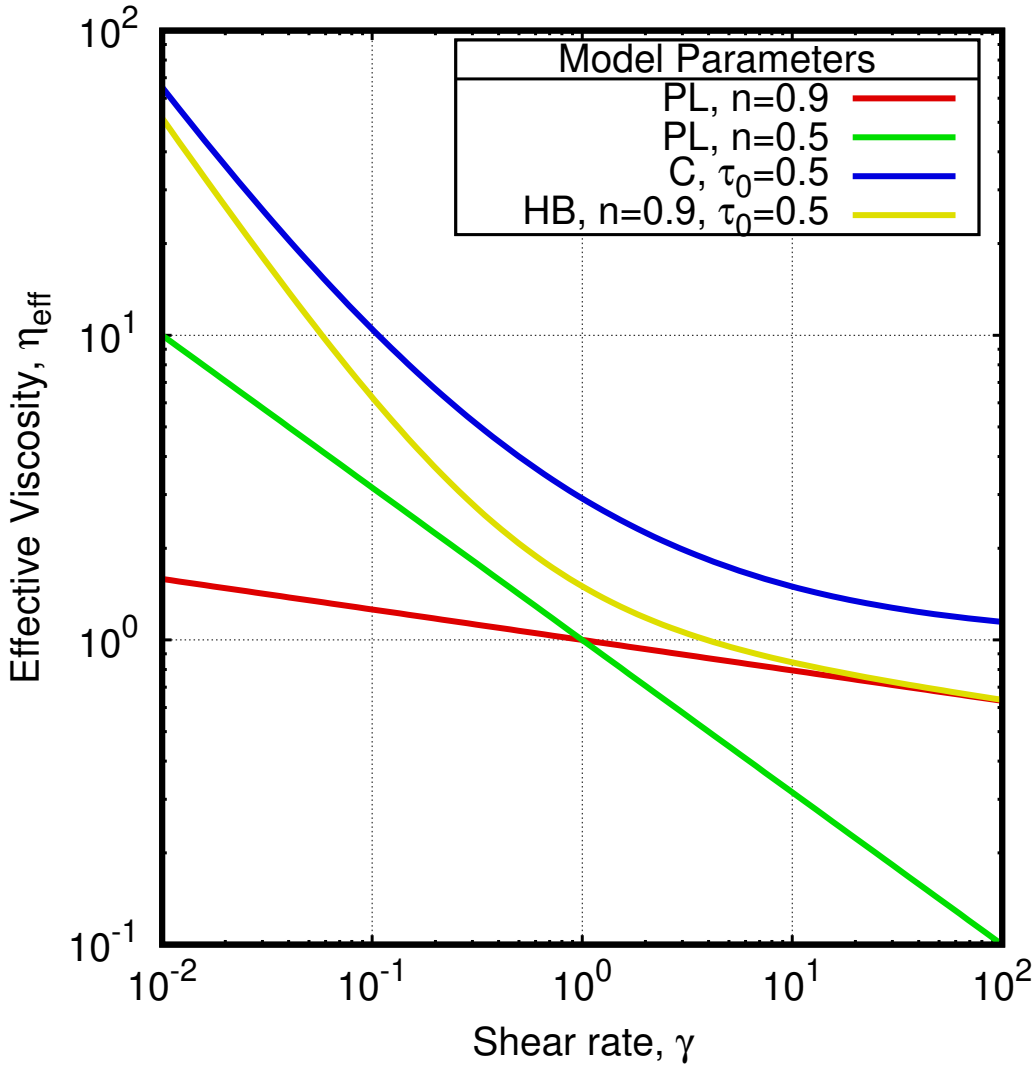

Figure 2.2: The effective viscosity of a fluid, predicted by non-Newtonian models for a range of shear rates. The red and green lines are the power-law model of (2.9), the blue line is the Casson model of (2.14), and the yellow line is the Herschel-Bulkley model of (2.12). All the lines are showing shear thinning behaviour, with varying model parameters. The consistency index, k, is set to 1 for all the models and lines.

over a full range of shear rates, capturing both zero-shear and infinite-shear limits of viscosity. One such model is the Cross model [11]:

$$\frac{\eta_{\text{eff}} - \eta_\infty}{\eta_z - \eta_\infty} = \frac{1}{1 + (\lambda\dot{\gamma})^m}, \tag{2.15}$$

where η_z is the zero-shear viscosity limit, η_∞ is the infinite-shear viscosity limit, λ is related to the shear rate at which the viscosity leaves the Newtonian zero-shear regime, and m is power-index similar—but not identical to—the power-law flow index. The power index is limited to $0 \leq m \leq 1$, whereby a value of 0 indicates Newtonian behaviour and values closer to 1 show a viscosity that is increasingly dependent on the shear rate.

A similar four-parameter model is the Carreau-Yasuda model [12, 33]:

$$\frac{\eta_{\text{eff}} - \eta_\infty}{\eta_z - \eta_\infty} = \frac{1}{[1 + (\lambda\dot{\gamma})^a]^{\frac{1-n}{a}}}, \tag{2.16}$$

whereby a is often taken as 2 (making it a four-parameter model), and n is another power index. Both of these models split the viscosity-shear equation into three stages: a Newtonian zero-shear regime, a shear-thinning regime, and a Newtonian infinite-shear regime [34]. Álvarez et al. [35] conducted a study of the viscosity of various jams. Each of the presented non-Newtonian models were used (except the Casson model) to understand the relationship between the temperature and the viscosity of the jams. The authors find that all of the models provide an excellent fit, with the parameters to shift as expected as the temperature changes.

These non-Newtonian models are all mathematically constructed equations, unlike some of the theoretical models of previous sections. Whilst clearly allowing the characterisation of flows, the dimensionality of the equations is sometimes complex; often the shear rate is raised to a power, making the units of viscosity less clear.

With material properties such as concentration and viscosity contrast absent from these models, they work well to characterise fluid flow data but not necessarily predict how a given fluid will flow, i.e. tests and fits must first be done to provide a curve for a fluid.

2.1.4 Meso-scale models

Detailed above are constitutive models that can describe the effect of changes in material properties on the viscosity of a fluid at near-zero shear, as well as models that can characterise fluid flow where viscosity varies with the shear rate. These are macroscopic models since they focus on the time and length scales relevant to industry and abstract away much of the microscopic physics. By looking at the meso-scale, where the fluid structure can be modelled along with the flow, it's possible to get a more accurate picture of how different parameters interact and study more

phenomena.

At this scale, above molecular dynamics but below traditional computational fluid dynamics, there are a few methods capable of modelling droplet flow. Lattice-Boltzmann methods, utilising several multi-phase models, are popular and developing rapidly. This method and the models built upon will be detailed in Section 2.2.

Loewenberg and Hinch [36] use the boundary-integral method to study the deformation of droplets in a sheared flow. Whilst limited to a droplet concentration of less than 30%, this work is one of the first attempts to simulate a non-dilute emulsion in order to understand the effect of the microstructure on the macroscopic properties. Their method's computational costs scale heavily with the number of droplets and the number of elements used to make up the droplet surface. The model does not allow for the breakup and coalescence of droplets. They limit the number of droplets per unit-cell to 12, which is said to have been sufficient in convergence tests. Their simulations then show increasing deformation with increasing capillary number. As noted, the high deformation and alignment to the flow decreases the collision cross-section, hence allowing the droplets to slip past each other more easily. This behaviour results in a decreased viscosity with increased shear, i.e. shear thinning, which is expected due to theory [14, 15] and experiments [28]. However, whilst in qualitative agreement, no quantitative comparisons are made.

Dissipative particle dynamics (DPD) [37] is another method that has been employed to model complex fluid flows [38]. Single-phase models of complex flow have been developed [39], with multi-phase models more recently [40]. The multi-phase models focus on true *multi-phase*, i.e. liquid-gas, rather than liquid-liquid emulsions. The particle-based nature of the method is less efficient than grid-based techniques like lattice-Boltzmann and level-set, which may limit the physical scale that an emulsion model could realistically reach.

Similarly, smooth particle hydrodynamics (SPH) is an established particle-based method, whereby the particles are replaced with smooth, curved functions, and a continuous field is made up of the superposition of all discrete functions [41]. SPH models are capable of multi-phase simulations by labelling particles and adjusting the interaction force accordingly [42]. As with DPD, the scale of SPH simulations may be limited by the particle-based fundamentals. These models are most appropriate for studying open flows as the introduction of boundaries is complex.

Finally, continuous surface stress models using the level-set method are able to describe liquid droplet behaviour [43]. This method has been developed to model multiple droplets, describing their deformation and viscosity in a shear flow. This author is unaware of any thorough evaluation of this method against theoretical and empirical models. Kim and Hwang [44] show the method is able to reproduce a variety of droplet systems, with varying viscosity ratios and capillary numbers. The accuracy of the results is only explored so-far as to say that the trends in viscosity

agree with the models of Taylor [6] and Pal [45].

Coupling this with the volume-of-fluid method, Kagawa et al. [46] were able to study the permeation of an emulsion through a pore. By adjusting the wettability and size of the pore, they showed differing amounts of droplet coalescence during and after traversing the pore. This method was again restricted to just a few droplets, though it seems possible this could be used to study concentrated sheared flow.

2.1.5 Sheared Self-Diffusion

Whilst the above models focus on viscosity, another key rheological property to complete a macroscopic model [47] is the diffusion in the fluid. This can be in various forms, for example small particles will diffuse due to Brownian motion in all directions. However, since this movement will be overwhelmed by the shearing of the fluid the focus here is on the *sheared self-diffusion*—the movement of the particles perpendicular to the shear direction as a result of the hydrodynamics (rather than thermal fluctuations, for example). Note that the size of emulsion droplets means that the effect of Brownian motion is expected to be minimal [48].

In the lab, it has recently become possible to measure the movement of particles in a suspension [49, 50]. The fluid is doped with tracer particles, which may be visible due to refractive index mismatching. Optical tweezers and lasers can be used to trap the tracer particle and to keep track of its location. The diffusion and microviscosity can then be extracted from the movement of the tracer particle. As Wilson et al. show [49], this method is capable of obtaining data in line with literature and other methods. Note, however, the application to solid suspended particles; the technique has not yet been used to get measurements of emulsions. The introduction of solid tracer particles into an emulsion may impact the rheology too significantly. Though as optical tweezers can be used on emulsion droplets, solid tracer particles may not be required and image analysis of emulsion diffusion may be possible in the future.

Simulations tend to have easier access to this data because they usually know the position of the suspended particles. This removes the need for a tracer particle and allows system-wide averages to increase precision. Sierou and Brady [51] do exactly this with accelerated Stokesian dynamics simulations. With 1000 particles being tracked in the simulation, the sheared self-diffusion with respect to the suspension concentration recovers results close to other simulated and experimental measurements. There has yet to be development of macroscopic models for the self-diffusion of emulsions.

2.2 Lattice-Boltzmann

The lattice-Boltzmann method (LBM) uses a probability distribution on a grid of nodes, each connected to their neighbours using discrete velocities, where each of the connecting links carries a probability of finding a fluid particle travelling along the link [52]. $f_i(\mathbf{x}, t)$ represents this probability, where $\mathbf{x}$ is the node, t is the timestep, and i is the direction of travel. The discrete velocities, $\mathbf{c}_i$, are such that a probability travels between neighbours in exactly one timestep; see Fig. 2.3 for a diagram and table of the velocities. The standard lattice-Boltzmann algorithm repeats two distinct stages: propagation and collision. A properly specified LBM can provide a solution to the Navier-Stokes equation of fluid flow [53, 52]

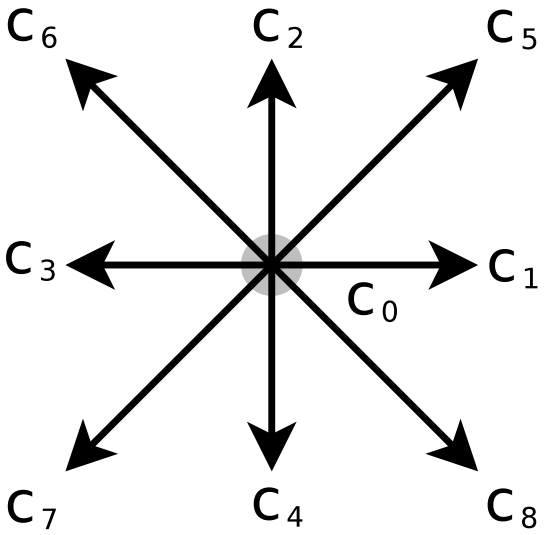

i	x	y	Length
0	0	0	0
1	1	0	1
2	0	1	1
3	-1	0	1
4	0	-1	1
5	1	1	$\sqrt{2}$
6	-1	1	$\sqrt{2}$
7	-1	-1	$\sqrt{2}$
8	1	-1	$\sqrt{2}$

Figure 2.3: An example of velocities for a two dimensional, nine link lattice (D2Q9). Other layouts may be chosen, but these are the velocities used throughout this work. Links 1-4 are short links whilst 5-8 are long links.

During propagation the probabilities are moved along to their neighbours:

$$f_i(\mathbf{x} + \mathbf{c}_i \Delta t, t + \Delta t) \;=\; f_i^{\dagger}(\mathbf{x}, t), \tag{2.17}$$

where $f_i^{\dagger}$ is the post-collision distribution, Δt is the time interval and hence $\mathbf{c}_i \Delta t$ is the vector to the neighbour node in the i^{th} direction.

The collision is then calculated as:

$$f_i^{\dagger}(\mathbf{x}, t) \;=\; f_i(\mathbf{x}, t) - \frac{1}{\tau}\left[f_i(\mathbf{x}, t) - f_i^{\mathrm{eq}}(\mathbf{x}, \mathbf{u}, \rho, t)\right], \tag{2.18}$$

where τ is the relaxation to equilibrium time and f_i^{eq} is the equilibrium distribution value defined as:

$$f_i^{(\mathrm{eq})}(\mathbf{x}, \mathbf{u}, \rho, t) \;=\; t_i \rho \left[1 + \frac{\mathbf{u} \cdot \mathbf{c}_i}{c_s^2} + \frac{(\mathbf{u} \cdot \mathbf{c}_i)^2}{2c_s^4} - \frac{\mathbf{u}^2}{2c_s^2}\right], \tag{2.19}$$

where t_i are the link weights (detailed shortly), ρ is the fluid density at $\mathbf{x}$, $\mathbf{u}$ is the fluid velocity at $\mathbf{x}$, and c_s is the speed of sound in the fluid. The link weights, t_i, and sound speed, c_s, are specific to the lattice used (D2Q9 in this case); the weights are selected such that its moments satisfy several symmetry and isotropy conditions and are as follows:

$$t_i = \begin{cases} \frac{4}{9} & i = 0, \\ \frac{1}{9} & i = 1, 2, 3, 4 \text{ (short links)}, \\ \frac{1}{36} & i = 5, 6, 7, 8 \text{ (long links)}, \end{cases} \tag{2.20}$$

whilst the sound speed is $c_s = \frac{1}{\sqrt{3}}$.

Now, by taking moments of the distribution, several macroscopic properties are recovered:

$$\rho = \sum_i f_i, \tag{2.21}$$

$$\rho u_\alpha = \sum_i c_{i_\alpha} f_i, \tag{2.22}$$

$$\Pi_{\alpha\beta} = \sum_i c_{i_\alpha} c_{i_\beta} f_i. \tag{2.23}$$

The 0^{th} moment provides the total fluid density at the node by summing all the distribution values. The 1^{st} moment returns the local fluid momentum and the 2^{nd} moment recovers the momentum flux.

Combining the propagation and collision provides a lattice-Boltzmann evolution equation that describes the algorithm carried out at each timestep:

$$f_i(\mathbf{x} + \mathbf{c}_i \Delta t, t + \Delta t) - f_i(\mathbf{x}, t) = \frac{1}{\tau} \left[f_i^{(\mathrm{eq})}(\mathbf{x}, \mathbf{u}, \rho, t) - f_i(\mathbf{x}, t) \right]. \tag{2.24}$$

The above algorithm is frequently referred to as the lattice-Bhatnagar-Gross-Krook (LBGK) method and may be seen as the starting point for current lattice-Boltzmann development. This method was introduced in the early 1990s by Qian et al. [54] and Chen et al. [55]. Qian et al. proposed the method as a way of removing the disadvantages—poor isotropy and lack of Galilean invariance—of the previous discrete lattice-gas models by using a relaxation method as the collision term:

$$N_i(t + 1, \mathbf{x} + \mathbf{c}_i) = (1 - \omega) N_i(t, \mathbf{x}) + \omega N_{ie}(t, \mathbf{x}), \tag{2.25}$$

which can be seen as equivalent to (2.24), whilst equilibrium equation (2.19) is also proposed by Qian [56]. The authors also suggest link weights, t_i, that ensure lattice isotropy and Galilean invariance for various lattices, including D2Q9.

One of the major changes that LBGK models introduced was the single relaxation time, ω or $\frac{1}{\tau}$, as opposed to the collision matrices of previous methods. This

results in a much simpler algorithm and greater computing efficiency, but also imposes restrictions like the fixed ratio of kinematic and bulk viscosity. Whilst the collision matrix was previously responsible for ensuring the conservation of physical quantities, the single relaxation time cannot achieve this, thus the local distribution equilibrium is used to impose conservation:

$$\sum_i f_i^{\mathrm{eq}} \;=\; \sum_i f_i \;=\; \rho. \tag{2.26}$$

This means much less tolerance of fluctuations from equilibrium so we are restricted to smaller force terms. Whilst this is manageable and suitable for some applications, it is possible to loosen this requirement by splitting the relaxation into two.

Ginzburg [57] introduced this by performing the collision on symmetric, s, and anti-symmetric, a, parts of the distribution. These parts are described by:

$$\begin{aligned} f_{is}^{(\mathrm{eq})} &= f_i^{(\mathrm{eq})} + f_{-i}^{(\mathrm{eq})}, \\ f_{is} &= f_i + f_{-i}, \\ f_{ia}^{(\mathrm{eq})} &= f_i^{(\mathrm{eq})} - f_{-i}^{(\mathrm{eq})}, \\ f_{ia} &= f_i - f_{-i}, \end{aligned} \tag{2.27}$$

where $-i$ represents the link pointing in the opposite direction to i, i.e. $\mathbf{c}_{-i} = -\mathbf{c}_i$. The collision step in (2.18) then becomes:

$$\begin{aligned} f_i^{\dagger}(\mathbf{x},t) \;=\; f_i(\mathbf{x},t) &- \frac{1}{\tau_s}\left(f_{is}\left(\mathbf{x},t\right) - f_{is}^{(\mathrm{eq})}\left(\mathbf{x},t\right)\right) \\ &- \frac{1}{\tau_a}\left(f_{ia}\left(\mathbf{x},t\right) - f_{ia}^{(\mathrm{eq})}\left(\mathbf{x},t\right)\right), \end{aligned} \tag{2.28}$$

where τ_s and τ_a are the symmetric and anti-symmetric parts of the relaxation parameter. τ_s is now linked to viscosity as $\nu = \frac{c_s^2}{2}(2\tau_s - 1)$ and τ_a is calculated from τ_s as $\tau_a = 0.5 + \frac{\Lambda}{\tau_s - 0.5}$ where $\Lambda = \frac{3}{16}$.

This two-relaxation-times (TRT) method has other advantages over LBGK too, such as improving the accuracy and stability of the method at small or large viscosities. It is shown that LBGK introduces errors when $\tau \neq 1$, and that moving to the TRT scheme rectifies this through the use of the *magic parameter*, Λ [58, 57]. The TRT scheme is a simplified, special case of a multiple-relaxation-times (MRT) scheme, in which more than two relaxation times may be used and tweaked. TRT, however, provides much of the benefit of MRT whilst remaining as computationally efficient as LBGK and making the algorithm only slightly more complex.

The algorithm described above will only produce incompressible Navier-Stokes results when several assumptions are satisfied. One of these assumptions is that the density fluctuation is negligible. This may become a problem when also implementing multi-phase elements or certain boundary conditions. Pressure and density are

linked through the ideal gas equation $p = \rho c_s^2$, so driving the fluid with a pressure gradient or introducing a droplet with a Laplace pressure step will also create a density gradient.

He and Luo [58] developed an incompressible algorithm to allow density to become constant throughout the system. They used an adjusted equilibrium as follows:

$$f_i^{\mathrm{eq}}(\mathbf{x}, \mathbf{u}, \rho, t) \;=\; t_i \left\{ \rho + \rho_0 \left[\frac{\mathbf{u} \cdot \mathbf{c}_i}{c_s^2} + \frac{(\mathbf{u} \cdot \mathbf{c}_i)^2}{2c_s^4} - \frac{\mathbf{u}^2}{2c_s^2} \right] \right\}, \tag{2.29}$$

where ρ_0 is now the fluid density, whilst ρ is still the sum of the local distribution values. The moments of the distribution (2.21, 2.22, 2.23) now become:

$$\frac{p}{c_s^2} \equiv \rho \;=\; \sum_i f_i, \tag{2.30}$$

$$\rho_0 u_\alpha \;=\; \sum_i c_{i_\alpha} f_i, \tag{2.31}$$

$$\Pi_{\alpha\beta} \;=\; \sum_i c_{i_\alpha} c_{i_\beta} f_i. \tag{2.32}$$

This now allows the local distribution density to vary whilst keeping the physical fluid density constant.

Note that this incompressible method is relevant only when there are significant pressure gradients in the system, otherwise the standard equilibrium may be more appropriate [59].

2.2.1 Boundary Conditions

Boundary conditions are required to fully describe any system, which in the LBM can be very simple. Firstly, one of the most commonly used conditions is that of a periodic flow. This is simply achieved by wrapping the last layer of nodes round to the first [52]:

$$\begin{aligned} f_{\mathrm{inlet}}^{\mathrm{in}} \;&=\; f_{\mathrm{outlet}}^{\mathrm{out}}, \\ f_{\mathrm{outlet}}^{\mathrm{in}} \;&=\; f_{\mathrm{inlet}}^{\mathrm{out}}, \end{aligned} \tag{2.33}$$

where f^{out} represents the distribution values leaving the domain and f^{in} represents the respective values entering the domain (which would otherwise be unknown). This basic boundary is frequently used to represent the open ends of a pipe flow, where fluid continuously flows round the system.

Periodic boundaries can also be adjusted to enforce a pressure gradient through the system that will drive the fluid flow. Zhang and Kwok [60] describe a periodic pressure boundary condition in the weakly-compressible LBGK form of LBM. As pressure is tied to the density, $p = c_s^2 \rho$ where ρ is the fluid density in this method, the pressure gradient can be applied using a density gradient. Aiming to apply a

pressure gradient of $\hat{\beta}$, a density step of $\frac{\hat{\beta}L}{c_s^2}$ between one system and its image should be introduced:

$$p(x=0,y) \;=\; p(x=L,y) + \hat{\beta}L\,, \tag{2.34}$$

where L is the length of the system. The average density of the fluid arriving at the inlet is set to be $\rho_{\mathrm{S}} + \frac{\hat{\beta}}{c_s^2}$, where ρ_{S} here represents the initialised LBGK density value of the fluid:

$$f_i \;=\; t_i \rho_{\mathrm{S}}\,, \tag{2.35}$$

assuming the system is initialised uniformly. The unknown distribution values can then be defined as:

$$\begin{aligned} f_{\mathrm{inlet}}^{\mathrm{in}} &= f_{\mathrm{outlet}}^{\mathrm{out}} \frac{\rho_{\mathrm{S}} + \frac{\hat{\beta}}{c_s^2}}{\bar{\rho}_{\mathrm{outlet}}}\,, \\ f_{\mathrm{outlet}}^{\mathrm{in}} &= f_{\mathrm{inlet}}^{\mathrm{out}} \frac{\rho_{\mathrm{S}} - \frac{\hat{\beta}L}{c_s^2}}{\bar{\rho}_{\mathrm{inlet}}}\,, \end{aligned} \tag{2.36}$$

where $\bar{\rho}_{\mathrm{inlet}}$ and $\bar{\rho}_{\mathrm{outlet}}$ are the average densities among the nodes defined as inlet or outlet respectively.

This method is shown to be inaccurate (producing an incorrect density profile and gradient) by Kim and Pitsch [61], who propose their own widely used boundary condition. In this newer method, the unknown distributions arriving on the inlet and outlet nodes are defined as:

$$\begin{aligned} f_{\mathrm{inlet}}^{\mathrm{in}} &= f^{(\mathrm{eq})}(\rho_I, \mathbf{u}_I) + f_{\mathrm{outlet}} - f_{\mathrm{outlet}}^{(\mathrm{eq})}, \\ f_{\mathrm{outlet}}^{\mathrm{in}} &= f^{(\mathrm{eq})}(\rho_O, \mathbf{u}_O) + f_{\mathrm{inlet}} - f_{\mathrm{inlet}}^{(\mathrm{eq})}, \end{aligned} \tag{2.37}$$

and the values used in the new equilibriums are calculated:

$$\rho_I \;=\; \rho_{\mathrm{outlet}} + (\hat{\rho}_{\mathrm{inlet}} - \bar{\rho}_{\mathrm{outlet}})\,, \tag{2.38}$$

$$\rho_O \;=\; \rho_{\mathrm{inlet}} + (\hat{\rho}_{\mathrm{outlet}} - \bar{\rho}_{\mathrm{inlet}})\,, \tag{2.39}$$

$$\mathbf{u}_I \;=\; \frac{\rho_{\mathrm{outlet}} \cdot \mathbf{u}_{\mathrm{outlet}}}{\rho_I}\,, \tag{2.40}$$

$$\mathbf{u}_O \;=\; \frac{\rho_{\mathrm{inlet}} \cdot \mathbf{u}_{\mathrm{inlet}}}{\rho_O}\,. \tag{2.41}$$

$\hat{\rho}_{\mathrm{inlet}}$ and $\hat{\rho}_{\mathrm{outlet}}$ are the target densities—note pressure $p \;=\; \rho c_s^2$. $\bar{\rho}_{\mathrm{inlet}}$ and $\bar{\rho}_{\mathrm{outlet}}$ are the average densities among the nodes defined as inlet or outlet respectively. The inlet and outlet nodes are the first and last real computational nodes respectively. This boundary pulls the average density among a set of nodes towards the target, whilst allowing for spatial fluctuations. The target densities in LBGK can

be calculated from a pressure gradient, $\hat{\beta}$, as:

$$\begin{aligned} \hat{\rho}_{\text{inlet}} &= \rho_0 + \frac{\hat{\beta}}{c_s^2}\,, \\ \hat{\rho}_{\text{outlet}} &= \rho_0 - \frac{\hat{\beta} L}{c_s^2}\,, \end{aligned} \tag{2.42}$$

where ρ_0 is the initial density of the fluid and L is the length of the system (the number of nodes between the inlet and outlet).

Implemented with the incompressible method mentioned in Section 2.2 there will be no density gradient as ρ is just the sum of the distribution values, proportional to the pressure. These methods will be applied in the initial results chapter (Chapter 4), when a pipe flow is modelled.

A periodic boundary condition, be it driven by a pressure gradient or body force [62], is a widely appropriate method. Tarksalooyeh et al. [63] use a small periodic area to feed particles into the main simulation in a consistently randomised manner. The small pre-inlet area simulates particles in a simple geometry, which are then copied over into an inlet region of a coupled simulation. The fluid distributions are similarly copied. This kind of treatment allows the inflowing particles to be unaffected by the complex geometry in the main simulation, i.e. the pre-inlet system will deliver a consistent mix of particle sizes even if certain sizes might traverse the main simulation differently to other sizes. Without such treatment it's possible that, for example, large particles could get trapped within the main system geometry and the inflow of such particles would diminish. This boundary condition [63] is applied to an aneurysm in blood, where a normal periodic boundary might result in all the platelets getting trapped and the blood not being of the correct hematocrit.

Another common boundary condition is the bounce-back condition, used to represent a solid no-slip wall. This is another testament to the possible simplicity of boundaries in the LBM; the distribution values propagating to the wall nodes are reversed on the node they are propagating from. See Fig. 2.4 for a graphical representation. This technique places the wall half-way between the real fluid node and the *ghost* wall node—no calculation is carried out on such a node, it exists purely to simplify the bounce back algorithm—to second order accuracy. Note that using TRT or MRT allows the wall position to be exactly half-way between nodes, which may not be the case when using LBGK.

The solid wall can also be given momentum [64, 65] in order to drive the fluid flow. Whilst this may provide a way of shearing a fluid—possibly modelling a rheometer mentioned at the start of Section 2.1—it will also confine the fluid and introduce boundary effects [66]. In order to model and study the bulk material away from the boundary, a large system or a high resolution may be required.

A Lees-Edwards (LE) boundary provides a way around this; shearing the fluid

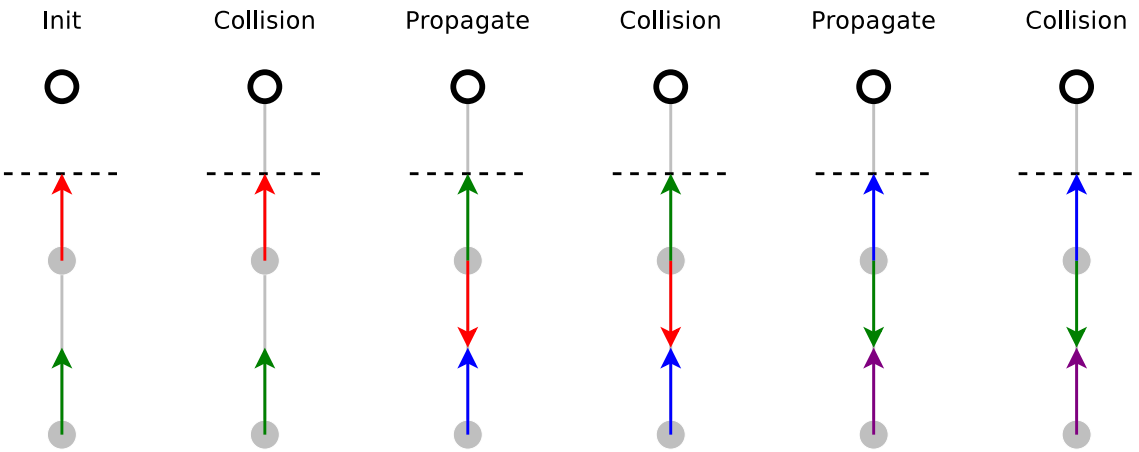

Figure 2.4: A selection of distribution values during the mid-link bounce-back algorithm, focused on a top wall. Progressing left to right through repeated LBM timesteps. Colours represent the same distribution value over time. Hollow nodes are boundary, or ghost, nodes.

without introducing a solid wall. Lees and Edwards developed such a boundary for Molecular Dynamics [67] and the method has since been applied to the LBM by Wagner and Pagonabarraga [68]. This boundary condition imposes periodic behaviour in all directions, except in one direction it is assumed that the periodic images are moving. There are two key stages of the condition, firstly transforming the velocity of the distributions crossing to a periodic image, and secondly shifting the position of the distribution values so they propagate into the moving periodic image in the correct place.

Assuming that a periodic image in the y-direction is moving with velocity $\mathbf{U}$ in the x-direction (and the periodic image in the negative y-direction is moving with velocity $-\mathbf{U}$), a distribution value that will cross the boundary must have it's momentum ($\rho\mathbf{u}$) transformed to $\rho(\mathbf{u}-\mathbf{U})$ or $\rho(\mathbf{u}+\mathbf{U})$ depending on whether it's travelling up the velocity gradient or down it. The transformation is applied as:

$$f_i' = \begin{cases} f_i + f_i^{(\mathrm{eq})}(\mathbf{u}-\mathbf{U}) - f_i^{(\mathrm{eq})}(\mathbf{u}) & \text{if } c_{iy} > 0 \\ f_i + f_i^{(\mathrm{eq})}(\mathbf{u}+\mathbf{U}) - f_i^{(\mathrm{eq})}(\mathbf{u}) & \text{if } c_{iy} < 0, \end{cases} \tag{2.43}$$

assuming, as above, that the velocity is increasing in the positive y-direction and that f_i' is the new distribution value.

The second part of the algorithm is required due to the moving periodic image; if a value propagates from the top of the system back round to the bottom it will not be in the correct position unless the displacement of the system is tracked and accounted for. Given a constant system velocity of $\mathbf{U}$, the displacement of the system over time is $d_x = tU_x$. This will rarely be an integer, therefore it is split into integer and real number parts: d_x^I and d_x^R. Wagner and Pagonabarraga [68] then apply a linear interpolation in order to shift the distributions onto the two nodes

closest to where the actual displacement puts the distribution:

$$f_i'(\mathbf{x},t) \;=\; \left(1-d_x^R\right) f_i\left(\mathbf{x}+d_x^I,t\right) + d_x^R f_i\left(\mathbf{x}+d_x^I+1,t\right), \tag{2.44}$$

for the distributions in the top row travelling upwards out of the domain, and

$$f_i'(\mathbf{x},t) \;=\; \left(1-d_x^R\right) f_i\left(\mathbf{x}-d_x^I,t\right) + d_x^R f_i\left(\mathbf{x}-d_x^I-1,t\right), \tag{2.45}$$

for the distributions in the bottom row travelling downwards out of the domain.

Both stages of the LE algorithm should be carried out just before propagating distributions. In this case, a usual propagation step set up to handle periodic boundaries will put the distributions in their correct places. Note that the system displacement must be kept in mind for other parts of the LBM which aren't node-local, gradient calculations for example.

A final key element to the LE boundary is the use of multiple planes within one domain. Whilst a naive implementation may align a single LE boundary with the edge of the system domain (or put the LE boundary in the centre), this limits the reachable shear rate due to the limit of the LBM velocity [53, 52]. This can be overcome by placing multiple shear planes evenly spread through the system, allowing for much greater overall system shear rates. The same algorithm (transform then shift) just has to be applied along multiple rows to achieve this.

Wagner and Pagonabarraga [68] note that linear interpolation may have introduced errors into the results and that it may be possible to improve upon it. A reported error in velocity of 3% may be fine for many applications, however, Javaran et al. [69] use the LE boundary with particles in the flow and note a disturbance to a particle's angular momentum as it crosses an LE boundary. This unintended effect on the particle is overcome by moving to a third-order interpolation, rather than the linear one, when applying the positional shift.

Javaran et al. [66] then apply this method to study the bulk rheological properties of suspensions. They find excellent agreement with several models outlined in Section 2.1.1. Highlighted within is the importance of using LE boundary conditions to impose a shear rather than standard moving bounce-back when measuring bulk properties. When using solid walls, the authors show an increase in the effective viscosity of the suspension over that measured when using LE. This is due to a *depletion zone* near the walls, forcing the particles closer to the centre of the channel and increasing the frequency of particle interactions, effectively increasing the particle concentration. Using a LE boundary condition then lessens the need for larger system averages if the entire domain is navigable by the particles.

2.2.2 Multi-component

Similar to boundary conditions, multi-component methods aim to model the interface between several fluids and the effect of such an interface on the fluid flow. Several of these methods have been developed for the LBM, each best applied to certain applications. For instance, to study phase separation the free-energy method [70] may be most appropriate. If approaching from a molecular dynamics background then the Shan-Chen pseudopotential [71] method may be most familiar. This work proceeds with the colour-gradient method [72, 73, 74] for a variety of reasons: the relatively low micro-current activity (spurious fluid velocities that arise in most multi-component methods); the ability to prescribe a surface tension value; and the demonstrated [75, 76] scalability to many fluid droplets without exponential computing power increases.

The method imposes a force on what is essentially a single fluid, targeted at the fluid interface, creating a pressure step in the fluid [72]. To start, the single fluid distribution function, f_i is split into functions for the two fluids: $f_i^{(0)}$ and $f_i^{(1)}$. The majority of the algorithm still uses the single fluid distribution which is now: $f_i = f_i^{(0)} + f_i^{(1)}$. Both of the fluids then have local density:

$$\rho^{(k)} = \sum_i f_i^{(k)}, \tag{2.46}$$

and the total nodal fluid density is:

$$\rho = \sum_k \rho^{(k)}. \tag{2.47}$$

The fluid velocity remains as:

$$u_\alpha = \frac{1}{\rho} \sum_i c_{i\alpha} f_i. \tag{2.48}$$

The interface between the two fluids is then determined by a phase field:

$$\rho^N = \frac{\rho^{(0)} - \rho^{(1)}}{\rho^{(0)} + \rho^{(1)}}, \tag{2.49}$$

which is in the range of $-1 \leq \rho^N \leq 1$. In the bulk of each fluid this will tend to the limits, so only over a finite amount of nodes will the phase field vary.

Now, knowing the location of the interface, a Laplacian pressure step must be created. The LBM evolution equation can have a source term, ϕ_i, through which a force can be applied:

$$f_i(\mathbf{x} + \mathbf{c}_i \Delta t, t + \Delta t) - f_i(\mathbf{x}, t) = \frac{1}{\tau} \left[f_i^{(\mathrm{eq})}(\mathbf{x}, \mathbf{u}, \rho, t) - f_i(\mathbf{x}, t) \right] + \phi_i(\mathbf{x}). \tag{2.50}$$

It has been shown [62] that the source term can apply a spatially variant macroscopic

force, $\mathbf{F}$, via the following relationship:

$$\phi_i(\mathbf{x}) = t_i\left(1-\frac{1}{2\tau}\right)\left[\frac{(\mathbf{c}_i-\mathbf{u}^*)}{c_s^2}+\frac{(\mathbf{c}_i\cdot\mathbf{u}^*)}{c_s^4}\mathbf{c}_i\right]\cdot\mathbf{F}(\mathbf{x}), \tag{2.51}$$

where $\mathbf{u}^*$ is a modified fluid velocity:

$$\mathbf{u}^* = \frac{1}{\rho}\left(\sum_i f_i\mathbf{c}_i+\frac{\mathbf{F}(\mathbf{x})}{2}\right). \tag{2.52}$$

Note this modified velocity must be used in the relaxation and equilibrium, as well as (2.51) above.

Halliday et al. [73] propose the force term:

$$\mathbf{F}(\mathbf{x}) = -\frac{1}{2}\sigma\kappa\boldsymbol{\nabla}\rho^N. \tag{2.53}$$

Inspecting this force term: σ is the assignable surface tension between the two fluids; κ is the local curvature of the interface; the force is positioned on the fluid interface by using the gradient of the phase field—as the phase field tends to a constant value in the bulk, its gradient will tend to zero.

The above force term is proportional to the local curvature of the interface, which can be calculated as:

$$\kappa = n_x n_y\left(\frac{\partial}{\partial y}n_x+\frac{\partial}{\partial x}n_y\right)-n_x^2\frac{\partial}{\partial y}n_y-n_y^2\frac{\partial}{\partial x}n_x, \tag{2.54}$$

where $\hat{\boldsymbol{n}}$ is the interface unit normal:

$$\hat{\boldsymbol{n}} = -\frac{\boldsymbol{\nabla}\rho^N}{|\boldsymbol{\nabla}\rho^N|}. \tag{2.55}$$

Note the gradient of the phase field will be perpendicular to the interface, hence using it to calculate the interface normal.

To complete the description of this method, the segregation algorithm—which defines the two fluid distribution functions and enforces the interface between them—must be presented. Once the collision step is complete, performed on the single fluid (colour-blind) distribution function, the fluid distributions are determined by:

$$f_i^{(k)} = \frac{\rho^{(k)}}{\rho^{(0)}+\rho^{(1)}}f_i^\dagger+\beta t_i\frac{\rho^{(0)}\cdot\rho^{(1)}}{\rho^{(0)}+\rho^{(1)}}\hat{\boldsymbol{n}}\cdot\boldsymbol{c}_i, \tag{2.56}$$

where $f_i^\dagger$ is the post-collision distribution, and β is a segregation parameter that controls the width of the interface. The first term in (2.56) assigns fluid to each colour distribution, proportional to the fluid density at the node. The second term forces each fluid away from the interface into the respective fluid bulk by pushing the fluid density onto the links facing away from the interface. Here, β must be

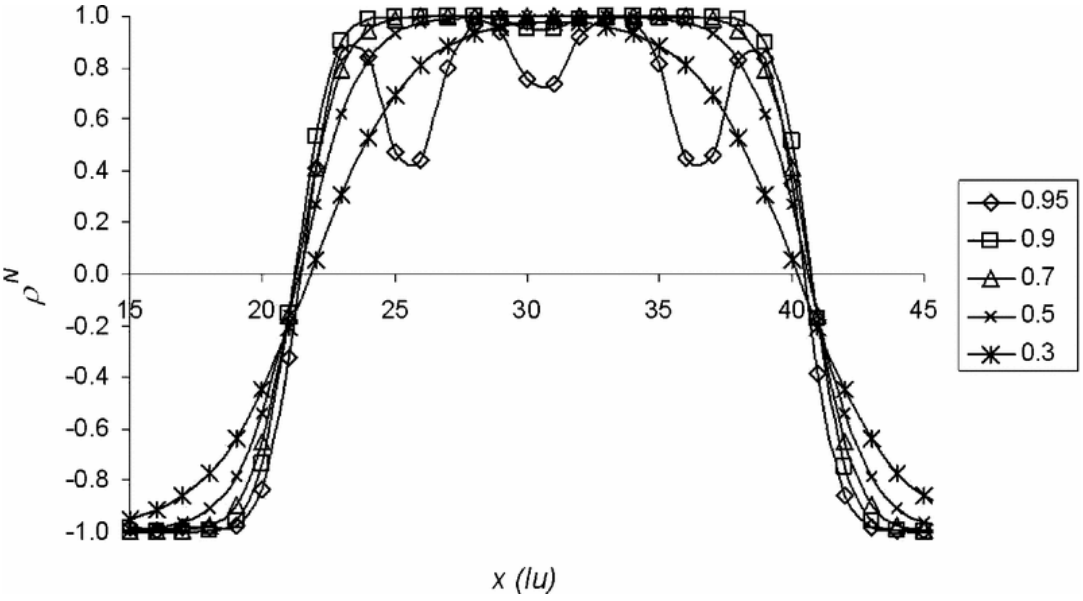

Figure 2.5: Reproduced with permission from Halliday et al. [73]. This shows the variation of the phase-field parameter, ρ^N, across a droplet of approximate initial radius 10 lattice units for a range of segregation parameters, β. The parameter must be carefully chosen: too high and the droplet is unstable, whilst too low and the interface is spread over many nodes.

chosen to provide a balance between stability and interface width. A full analysis of this, and other aspects of the segregation rule, is carried out by Halliday et al. [73] Fig 2.5 shows the effect of β on the interface; too low and the interface is spread over many nodes, too high and instabilities appear. Ideally the interface should be as thin as possible, as physical fluids have discontinuous interfaces so a finite interface brings resolution issues.

A three-dimensional equivalent to this model has been compared [3] with the Taylor-Einstein equation shown in (2.6). The agreement with the exact theoretical equation is excellent over a moderate range of viscosity ratio.

The above choice of force term in (2.53) applied via the source term is only one option; Spencer et al. [74] propose another:

$$\phi_i(\mathbf{x}) = \frac{t_i \beta \sigma}{\tau c_s^4} \frac{\rho^{(0)} \rho^{(1)}}{\left(\rho^{(0)} + \rho^{(1)}\right)^2} \left(\hat{n}_\alpha \hat{n}_\beta - \delta_{\alpha\beta}\right) \left(c_{i\alpha} c_{i\beta} - c_s^2 \delta_{\alpha\beta}\right). \tag{2.57}$$

This imposes an equivalent spatially-variant Guo [62] body force as the explicit force in (2.53). However, this is applied in the second moment of the source term, (2.51), as a pressure perturbation, rather than in the zero-th moment as an explicit force, which has several consequences. Firstly, it requires no adjustment to the velocity definition—see (2.52)—simplifying the implementation and analysis of the algorithm. Secondly, the terms are localised, i.e. the gradient of the interface normal is no longer present, increasing the efficiency of the algorithm. Lastly the microcurrents are slightly increased. The result is a simpler, more efficient way of imposing

an equivalent interfacial force.

Both forcing algorithms are able to be extended beyond two fluids [75, 74]. The same process is used, however the improved efficiency of (2.57) makes it highly suitable for this purpose. The extra non-local terms needed for (2.53) become an even bigger overhead for many-component fluids.

The extension can be carried out naively by creating N fluid lattices, then performing the forcing and segregation on each pair of fluids. This, however, means an exponential growth in required computing resources as the number of components increases. To avoid this, only non-negligible fluids, those with a concentration above a certain threshold, need to be processed and stored on each particular lattice node. The number of non-negligible fluids per node is stated to be around 5 or 6 [75, 74]. Storing only these few fluids per node has a drastic effect on the computational efficiency, but requires careful implementation to ensure fluid mass doesn't get misplaced—the 6 fluids on node x may be different from the 6 fluids stored on neighbouring node y. Dupin et al. [75] introduce an extra *tracker* lattice to keep an index of which fluid is on which node/link, which does mean a slight hit to efficiency but keeps the computational scaling detached from the number of fluid components. Without this detachment it's possible that many-component flows become too computationally expensive to all but the most costly computer cluster systems. Note that the LBM algorithm is very memory intensive; storing as few fluids as possible benefits in two ways: the method becomes more accessible to lesser computer hardware and the computer can spend more time calculating rather than moving data between memory areas. The key point is that rather than exponential growth in resources, these models can be restricted to using the amount required for approximately 5 or 6 fluid components. Some mass loss will be inevitable, but, with an appropriately chosen concentration threshold, it should be negligible.

A key area in which both forcing methods need improvement is the ability to implement a density ratio between the droplets. In fact, this is an area in which all multi-component lattice-Boltzmann methods struggle [52]. Some emulsions contain fluids with similar densities, for which these methods would be ideal. However, many emulsions will contain fluids with differing densities and this may or may not be relevant to the modelling. In cases where a density difference is present, modifications to the above algorithm may be possible.

Similar colour-gradient models have already seen such modifications. Grunau et al. [77] propose adjustments to the multi-component model of Gunstensen [78], using a hexagonal lattice. More recently, Reis and Phillips [79] develop similar adjustments to a more popular square lattice model. Most notable is the introduction of an extra parameter in the fluid equilibrium that provides freedom to the rest link and controls the speed of sound in each fluid. Tuning these parameters helps stabilise the interface between fluids with a density difference. Reis and Phillips [79] show not only correct

reproduction of Laplacian surface tension, but also good agreement with analytic results for velocity profiles with a viscosity ratio. Foremost, is a droplet coalescence test with a density ratio of 18.5 between the droplets and the surrounding fluid. The test shows the adjacent droplets coalesce whilst preserving the mass of each fluid.

Further models have been proposed; Lishchuk et al. [80] achieve a stable static droplet with a density ratio of 1000, however a more rigorous bubble rising test proves stable only to a density ratio of 10. Liu et al. [81] propose a model capable of the same bubble rising test stable to a density ratio of nearly 100.

Most recently, however, Ba et al. [82] have developed a model resembling that of Grunau et al. [77] and Reis and Phillips [79]. Ba et al. [82] implement a multiple-relaxation-time model to complement the multi-component algorithm and see a valuable increase in the simulation stability. No bubble rising test is conducted, however, a layered two-phase flow performs well up to a density ratio of 1000. Whilst this test includes flow, it will not involve interfacial forces due to the interface being flat. Simulations by Ba et al. show a droplet splashing on a surface, which becomes unstable above a density ratio of 100.

Progress is being made towards stable simulations with a large density ratio. A stable droplet, under flow, with a density ratio of 1000 would be a major milestone as 1000 would closely represent the difference between water and air, making such simulation truly multi-phase.

2.2.3 Application to Emulsions

Whilst extending their multi-component method to accommodate multiple immiscible droplets, Spencer et al. [74] showcase the ability of the algorithm to explicitly simulate the deformable droplets of an emulsion. They are able to see droplet behaviours, such as migration to the lower shear rate channel centre (minimising deformation), as well as recover trends from macroscopic models—increasing the droplet concentration increases the fluid viscosity. Comparisons to a power-law solution for the velocity profile are made, however it would be useful to be able to compare this against other macroscopic emulsion models.

Using the Shan-Chen pseudopotential multi-component method, Benzi et al. [83, 84] develop a model of a flowing emulsion-like system. This model results in various mesoscopic structures occurring, which includes emulsion droplets but also includes caging structures that can surround and trap droplets. The fluid-fluid interface profile shows numerical artefacts, resembling a Gibbs-like phenomenon. In further work, Benzi et al. [85] show their simulations produce reasonable agreement with the Herschel-Bulkley yield stress model. This form of multi-component LBM has an interfacial tension that emerges as a result of the potential function applied, which may make it more challenging to study emulsion rheology when exploring the effect of the droplet material properties.

These appear to be the only works looking at emulsions on such a large scale using the LBM. Other work in the LBM has focused on individual droplet behaviour, i.e. deformability [86, 87], breakup [86, 88, 87], and wetting [89, 90, 91].

Pickering emulsions, in which the emulsion is stabilised by small solid particles, have also been simulated within LBM, for example by Jansen and Harting [92]. The authors used the Shan-Chen multi-component LBM coupled with solid particle techniques developed by Ladd [64, 65] to investigate the effect of particle concentration and the fluid ratio on the formation of Pickering emulsions. The fluid ratio (the ratio of the amount of each fluid in the multiphase system) is found to have the most impact, however, the contact angle (determined by making the particle favour a certain fluid phase) is also important. The model agrees with previous simulations and experimental data, and could prove useful if Pickering emulsions become more widely used.

Whilst stabilisation with small solid particles is possible, most emulsions are stabilised by surfactants. Their wide industrial use has encouraged their inclusion in numerical models. While most of the immiscible models described in Section 2.2.2 assume surfactants are equally distributed and 100% effective at keeping droplets coalescing, Farhat et al. [93] developed a hybrid lattice-Boltzmann scheme that pairs the colour-gradient multi-component LBM with a surfactant model solved using a finite-difference scheme. This hybrid model was used to study the effects in shear and extensional flow of the surfactant coverage of a droplet, among other variables. This kind of model may become useful to any work following this report due to the importance of surfactants in the food industry.

There has been much work developing LBM for modelling fluid filled vesicles or capsules. Much of this has been undertaken in immersed boundary methods, whereby the interface is characterised by tracking markers that flow along with the fluid [94]. Such markers are paired with the underlying LBM and may have additional physics acting upon them, such as elasticity.

Using these methods, Krüger [95] was able to study the margination of platelets in blood flow. An immersed boundary method was used to model both platelets and much larger red blood cells. By varying the tube diameters and Capillary numbers, it was possible to see that platelets would marginate to the tube wall as the Capillary number increased. Once at the tube wall, in the cell-free-layer, the platelets were unlikely to re-enter the bulk flow. The deformation of the red blood cells was also found to increase with both the tube diameter and the Capillary number.

Without using an immersed boundary method, it is still possible to introduce vesicle dynamics. Halliday et al. [96] propose an extension to their multi-component model described above, which allows the force term to maintain a constant interface length. This model provides a simpler alternative without the need for an interface mesh, however the finite width of the interface will require an increased resolution

of simulation in order to become negligible. Whilst an extension to multiple vesicles in flow is said to require minimal modifications, nothing on the scale of immersed boundary methods has been demonstrated.

2.3 Conclusion

To summarise, there is much interest in the modelling of emulsion behaviour, as described in Section 2.1. The study at the meso-scale, where the droplet behaviour and structure can be examined, however, still has many areas unexplored. Whilst individual (or a small selection of) droplets have been modelled, thorough exploration into the bulk flow—made up of many emulsion droplets—has yet to be undertaken. Works using the lattice-Boltzmann method have been taking steps in this direction, with some showing multi-droplet emulsions in a confined shear flow.

It is important that these numerical models are extended to bulk flow and that computational efficiency is good enough to allow for fully resolved simulations to be carried out. These simulations at the meso-scale would allow for the study of droplet behaviours in bulk flow, as well as the evaluation of theoretical and empirical macroscopic models discussed in Section 2.1. With explicitly simulated droplets, data on the sheared self-diffusion—equivalent to that available for suspensions—may be recoverable.

Chapter 3

Methods

This chapter aims to fully describe an exactly incompressible lattice-Boltzmann method (EILBM) that incorporates various techniques discussed in the previous chapter. The closing boundary conditions will be described in the coming chapters, when applicable, as there are several different variations (pipe-flow, bulk-flow).

3.1 EILBM for multiple immiscible fluids with a TRT collision step

Recall that the LBM uses a probability distribution across a lattice of discrete nodes. The set of velocities are designed to enable the distribution values to move from one node to the neighbour in a single timestep. Here, the D2Q9 lattice is used, as shown previously. The propagation of distribution values is followed by a collision step, where the fluid relaxes towards equilibrium. These two steps are continuously repeated to run the simulation.

The presented model uses a two-relaxation-time collision operator, which is a special case of the multi-relaxation-time algorithm, to provide increased performance. An exactly incompressible method is also adopted, which allows for the separation of density and pressure. Emulsion droplets will emerge in the flow due to an applied stress perturbation and accompanying segregation algorithm. The ability to simulate many liquid droplets simultaneously will be facilitated by an efficient memory-saving algorithm that caps the number of stored lattices. In the following chapters, this model is built upon with boundary conditions to simulate specific geometries and systems.

Now, a more thorough description of the developed model is provided. Firstly, the overall evolution equation of the model, which combines the propagation and

collision steps, is:

$$\begin{aligned} f_i(\mathbf{x}+\mathbf{c}_i\Delta t, t+\Delta t) &= f_i(\mathbf{x},t) - \frac{1}{\tau_s}\left(f_{is}(\mathbf{x},t) - f_{is}^{(\mathrm{eq})}(\mathbf{x},\mathbf{u},\rho,t)\right) \\ &\quad - \frac{1}{\tau_a}\left(f_{ia}(\mathbf{x},t) - f_{ia}^{(\mathrm{eq})}(\mathbf{x},\mathbf{u},\rho,t)\right) \\ &\quad + \frac{t_i\Delta t\beta^{mn}\sigma^{mn}}{\tau_s c_s^4}\frac{\rho^{(m)}\rho^{(n)}}{\rho^2}\left(\hat{n}_\alpha^{mn}\hat{n}_\beta^{mn} - \delta_{\alpha\beta}\right)\left(c_{i\alpha}c_{i\beta} - c_s^2\delta_{\alpha\beta}\right), \end{aligned} \tag{3.1}$$

where $\mathbf{x}$ is the node, t is the timestep, and i is the direction of travel. Note the final term shows this model uses the multicomponent forcing algorithm of Spencer et al [74], which imposes a continuous surface force as a stress perturbation in the second moment of the Guo [62] force term. The equilibrium is defined by [58]:

$$f_i^{(\mathrm{eq})}(\mathbf{x},\mathbf{u},\rho,t) = t_i\left\{\rho + \rho_0\left[\frac{\mathbf{u}\cdot\mathbf{c}_i}{c_s^2} + \frac{(\mathbf{u}\cdot\mathbf{c}_i)^2}{2c_s^4} - \frac{\mathbf{u}^2}{2c_s^2}\right]\right\}. \tag{3.2}$$

This and the associated f_is split into symmetric and anti-symmetric parts as follows [57]:

$$\begin{aligned} f_{is}^{(\mathrm{eq})} &= f_i^{(\mathrm{eq})} + f_{-i}^{(\mathrm{eq})}, \\ f_{is} &= f_i + f_{-i}, \\ f_{ia}^{(\mathrm{eq})} &= f_i^{(\mathrm{eq})} - f_{-i}^{(\mathrm{eq})}, \\ f_{ia} &= f_i - f_{-i}, \end{aligned} \tag{3.3}$$

where $-i$ represents the link pointing in the opposite direction to i, i.e. $\mathbf{c}_{-i} = -\mathbf{c}_i$. Hence, the method uses a TRT algorithm to provide a balance of simplicity and accuracy. The physical fluid density, ρ_0, is the same for each fluid. Also, ρ should be thought of as the nodal density fluctuation [58] and is recovered from the moments of the distribution function along with the momentum:

$$\frac{p}{c_s^2} \equiv \rho = \sum_i f_i, \tag{3.4}$$

$$\rho_0 u_\alpha = \sum_i c_{i_\alpha} f_i, \tag{3.5}$$

$$\Pi_{\alpha\beta} = \sum_i c_{i_\alpha} c_{i_\beta} f_i. \tag{3.6}$$

Similarly, the distribution function and the nodal fluid density fluctuation of each

fluid, k, is

$$f_i = \sum_k f_i^{(k)}, \tag{3.7}$$

$$\rho^{(k)} = \sum_i f_i^{(k)}. \tag{3.8}$$

The remaining variables in (3.1) are as follows:

- $\mathbf{c}_i$ are the discrete lattice velocities, which are chosen to be the D2Q9 structure seen in Fig. 2.3.
- Δt is the timestep, taken to be 1.0.
- τ_s and τ_a are the symmetric and anti-symmetric relaxation times. Note that these are linked to the fluid viscosity and may vary from one node to another in a multi-component system. See Section 3.3.
- t_i are the link weights given in (2.20).
- β^{mn} is the segregation parameter between fluids m and n.
- σ^{mn} is the interfacial tension parameter between fluids m and n.
- $\hat{\mathbf{n}}^{mn}$ is the normal vector pointing into fluid m perpendicular to the interface of fluids m and n, calculated from the gradient of the phase field.
- $\delta_{\alpha\beta}$ is the Kronecker delta, which equals 1 when $\alpha = \beta$ and 0 when $\alpha \neq \beta$.

The speed of sound in this particular lattice is $c_s = \frac{\Delta x}{\Delta t\sqrt{3}}$, where both the time and space steps here are 1.0. The viscosity of each fluid is linked to the symmetric relaxation parameter $\nu^{(k)} = \frac{c_s^2}{2}\left(2\tau_s^{(k)} - 1\right)$, whilst the overall τ_s and τ_a are some function of the fluid relaxation parameters $\tau_s^{(k)}$ and $\tau_a^{(k)}$ (see Section 3.3). The anti-symmetric relaxation parameter can be calculated from the symmetric part as $\tau_a = 0.5 + \frac{\Lambda}{\tau_s - 0.5}$ where $\Lambda = \frac{3}{16}$. The *magic parameter*, Λ, is chosen to provide an exact position for solid walls [97], though other choices are possible [98].

The last part of the algorithm is the post-collision fluid component segregation process, to obtain the individual fluid distributions. As per (2.56) above, an appropriate equation is: [73]

$$f_i^{(k)} = \frac{\rho^{(k)}}{\rho} f_i^{\dagger} + \sum_{m, m\neq k} \beta^{km} t_i \frac{\rho^{(k)} \cdot \rho^{(m)}}{\rho} c_{i\alpha} \hat{n}_\alpha^{km}. \tag{3.9}$$

The summation in the above is cycling through each unique pair of fluids (here k identifies one of the fluids). Note, $\hat{n}_\alpha^{km} = -\hat{n}_\alpha^{mk}$, hence (3.9) can be applied in a pairwise fashion. These segregated fluid distribution values are then propagated:

$$f_i^{(k)}(\mathbf{x} + \mathbf{c}_i \Delta t, t + \Delta t) = f_i^{(k)}(\mathbf{x}, t). \tag{3.10}$$

To summarise, the background fluid and each droplet will have fluid distributions, $f_i^{(k)}$, density fluctuations, $\rho^{(k)}$, and relaxation parameters (hence viscosities), $\tau_s^{(k)}$. Each pair of fluids is also able to have unique pairwise parameters to define interfacial tension and the interface width. Note that for the remainder of this thesis, every fluid pair has the same interface width, via the segregation parameter $\beta = 0.65$. Also, only two interfacial parameters are used; one for all of the droplet-background interfaces and one for all of the droplet-droplet interfaces. The droplet-droplet interfacial tension parameter, σ_1 , was always chosen to be a magnitude larger than the droplet-background parameter, σ_0 , to prevent droplet coalescence. This forms a complete algorithm for a multi-component LBM.

A Chapman-Enskog analysis of this model, outlined in Appendix A, shows that it reproduces the correct Navier-Stokes and Laplacian interfacial tension behaviour.

One key issue is the computational requirements of such a model, if trying to simulate several droplets. However, as discussed in Section 2.2.2, it is possible to restrict the resources required to that of just 5-6 fluids.

3.2 Memory Saving Technique

This section is brief, but is vital to the simulations in this thesis. Without these optimisations the simulations performed here would either be limited to the low concentration regime or require more computer power than currently feasible.

Using a similar concept to Dupin [75, 76] and Spencer [74], the number of stored distribution functions is formally detached from the number of fluid colours. Before the collision step, whilst the propagated distribution values are having their moments calculated (i.e. fluid density fluctuation and velocity) fluids with a relative node concentration, $\frac{\rho^{(k)}(\mathbf{x})}{\rho(\mathbf{x})}$, below a threshold are discarded. An appropriate threshold for this is found to be 10^{-9} as it limits the fluids per node to $L \in [4, 5]$, whilst introducing negligible mass loss over millions of timesteps. The total discarded mass at each node can be spread proportionally over the remaining fluids at the node, in order to retain overall mass conservation.

Most of the algorithm can now be converted to use a maximum of L stored lattices, where L can be far lower than the number of different fluids, N. Rather than $f_i^{(k)}$, define $la_i^{(k)}$ as a sparse lattice of fluid distributions. An extra *tracker* lattice is introduced to keep track of which fluid colour, k, resides on which node and link; the memory impact of this is minimal since $k \in \mathbb{Z}^+$, saving many fluid lattices from being required. With $la_i^{(k)}$ a sparse array/lattice, an additional *tracker-like* lattice may be required to track how many fluids are present on a particular node. As before, having saved numerous floating-point lattices, an extra integer lattice is a negligible overhead; not only saving storage, but being sparse, the algorithm is allowed to skip calculations for absent fluids.

Calculating and storing the pairwise phase gradients and interface normals is one of the most time and memory consuming parts of the algorithm. Moving from pairs of fluids to pairs of sparse lattices makes an enormous difference as the number of fluids increases, for example the number of unique pairs of 100 fluids is 4950, whilst the number of unique pairs of sparse lattices remains below 10 (unique pairs $= \frac{N(N-1)}{2}$).

The parts of data that are relatively small may remain as non-sparse arrays, since to do otherwise would involve complicating the algorithm for very diminishing returns. For example, the fluid density fluctuations, $\rho^{(k)}$, require relatively little storage/memory compared the fluid distributions that are per-node and per-link.

The distribution function and the fluid density fluctuations can be calculated from the sparse arrays as follows:

$$f_i = \sum_{l}^{L} la_i^{(l)}, \tag{3.11}$$

$$\rho^{(\text{fluid}(l))} = \sum_{i} la_i^{(l)}, \tag{3.12}$$

where fluid(l) uses the tracker lattices to identify the fluid, k, of this particular lattice on this particular node.

The sparse lattices are propagated, which may mean also propagating the tracker. Care should be taken to address the correct fluid or lattice, replacing β^{mn} with $\beta^{\text{fluid}(k)\text{fluid}(l)}$ when considering lattices rather than fluids for example.

The implementation of the algorithm can be carried out in various ways, but it is essential if one is to simulate many-component systems. For this thesis, the algorithm was implemented in the C programming language, parallelised using the Message Passing Interface (MPI) standard to run on computer clusters. Fig. 3.1 shows the computational memory (RAM) usage of the implemented algorithm, before and after these optimisations were made. Without the optimisations, when each fluid requires its own lattice, the memory cost continues to increase greatly as the number of fluids is increased. This is overcome by implementing the optimisations, as the number of lattices can be kept constant above a certain number of fluids, L. Processor usage follows a similar, but not identical trend to the RAM usage. Processor usage doesn't quite plateau, even with optimisations, for two reasons: i) there is a slight overhead involved with checking which fluids are negligible, and ii) depending on the implementation, as more fluids are involved in the system, more lattices will require more computation to be carried out. Expanding on the ii), when only the background fluid is present on a lattice node then much computation can be skipped as much of it is pairwise; as more droplets enter the flow then the number of nodes with only the background fluid present will decrease.

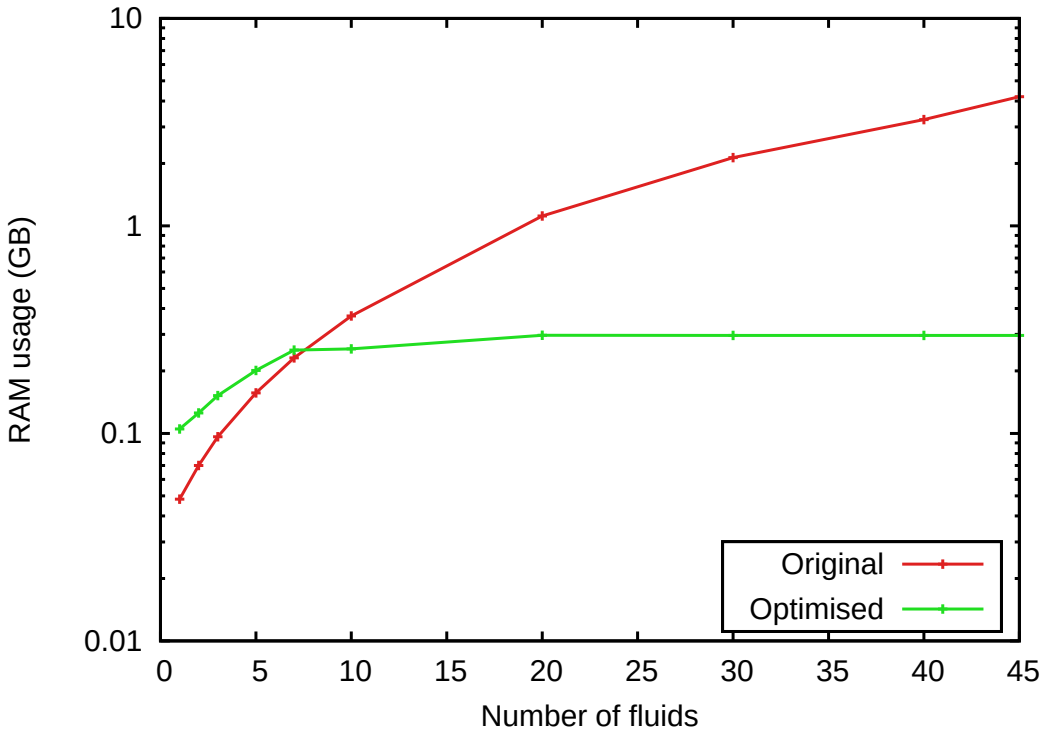

Figure 3.1: The computer memory (RAM) usage of the algorithm described in Section 3.1, with and without the optimisations outlined in Section 3.2. Without optimisation, the memory usage continues to grow, until the simulations are impossible for all but the most powerful machines. With the optimisation the memory usage is higher for a small number of fluids (the exact number will depend on the implementation), but quickly *plateaus*, as no extra lattices are required. The systems with optimisations used the same amount of lattices as fluids when lattices ≤ 7, and then stayed fixed at 7 when the number of fluids was greater than that.

3.3 Viscosity Interpolation

In the proximity of a fluid-fluid interface, where the fluids have differing viscosities (relaxation parameters), the τ_s parameter must be interpolated between the different values. Various methods have been applied to implement this interpolation. Linear interpolation [99, 100, 101] is the simplest choice:

$$\tau_s = \frac{\rho^{(k)}}{\sum_k \rho^{(k)}} \tau^{(k)} . \tag{3.13}$$

Quadratic [77, 79] and exponential [102] interpolations have also been used. Most recently, a harmonic mean [103, 104] of the viscosity:

$$\eta = \frac{\sum_k \rho^{(k)}}{\sum_k \frac{\rho^{(k)}}{\eta^{(k)}}} , \tag{3.14}$$

has been noted [104] to be physically correct at the sharp-interface limit [105].

Following [103, 104], it was decided to use (3.14), the physically correct harmonic mean of viscosity, to interpolate relaxation parameter, τ_s, over the interface. However, a misinterpretation resulted in this work using the harmonic mean of the relaxation time:

$$\tau_s = \frac{\sum_k \rho^{(k)}}{\sum_k \frac{\rho^{(k)}}{\tau^{(k)}}} . \tag{3.15}$$

While similar, the methods are not equivalent.

In essence, each method places the profile of the interpolation in line with some physical quantity, whether it be the velocity gradient through the interface [103, 104] or the phase field itself [99, 100, 101]. Investigations [3] into the implemented scheme have determined the interpolation is in line the with the multi-component force being applied to the fluid.

The viscosity ratio, K , is defined as: $K = \frac{\eta_1}{\eta_0}$, where η_0 and η_1 are the viscosities of two fluids. When modelling droplets, η_0 is the viscosity of the background fluid, and η_1 is the viscosity of all of the droplets.

Noting that this method deviates from what is said to be correct in the sharp-interface limit, validations and comparisons were carried out.

3.3.1 Bilayered flat-interface flow

The first possible validation case is that of a sheared two-component fluid with a flat interface. Applying Lees-Edwards boundary conditions (LEBC) [67, 68] (the multi-component implementation is described in Section 5.1.2) will provide a shear in a fully periodic system and the fluid-fluid interface is parallel to the velocity direction. This test is able to validate both the LBM and the viscosity interpolation scheme.

The analytic solution for a flat, sharp interface is:

$$U_x(y) \;=\; \frac{2\eta_0\eta_1 U_{\mathrm{LE}}}{w\,(\eta_0+\eta_1)\,\eta}y + \frac{U_{\mathrm{LE}}}{2}\frac{(\eta_1-\eta_0)}{(\eta_0+\eta_1)}\,, \tag{3.16}$$

where w is the system width, and η is the viscosity of the fluid at that location, i.e. η_0 when $y \leq \frac{w}{2}$ and η_1 when $y > \frac{w}{2}$.

Seeking to validate against (3.16), a system was set up as follows:

- 20 by 100 node lattice. Hence, $w = 100$.
- All fluid densities $\rho_0 \;=\; 1.0$.
- Viscosity of fluid 0, $\eta_0 \;=\; \frac{1}{6}$ lu, $\tau_0 \;=\; 1.0$.
- Interface segregation parameter, $\beta \;=\; 0.65$.
- Interfacial tension parameter between the fluids, $\sigma \;=\; 0.09$.
- Velocity on the Lees-Edwards boundary, $U_{\mathrm{LE}} \;=\; 0.01$ lu.
- Negligible fluid concentration threshold value, $\frac{\rho^{(k)}}{\rho} \leq 1 \;\times\; 10^{-9}$.

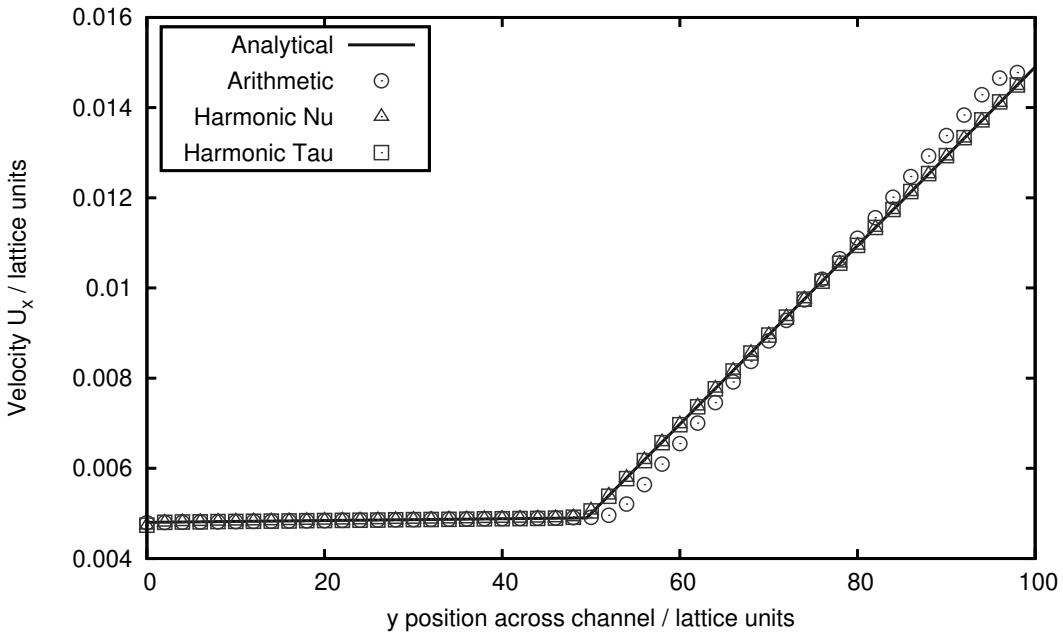

Figure 3.2: The velocity profile of a bilayered system (fluid-fluid interface at $y = 50$). This system had a viscosity ratio of 100. There are large discrepancies between the arithmetic (liner interpolation) method and the analytical solution. Both of the harmonic methods agree well with the analytical solution.

Fig. 3.2 shows the velocity profile of such a system when the viscosity ratio is 100. There is a clear difference between the interpolation methods, with the standard linear interpolation (via arithmetic mean of the viscosities) being far more rounded at the interfaces.

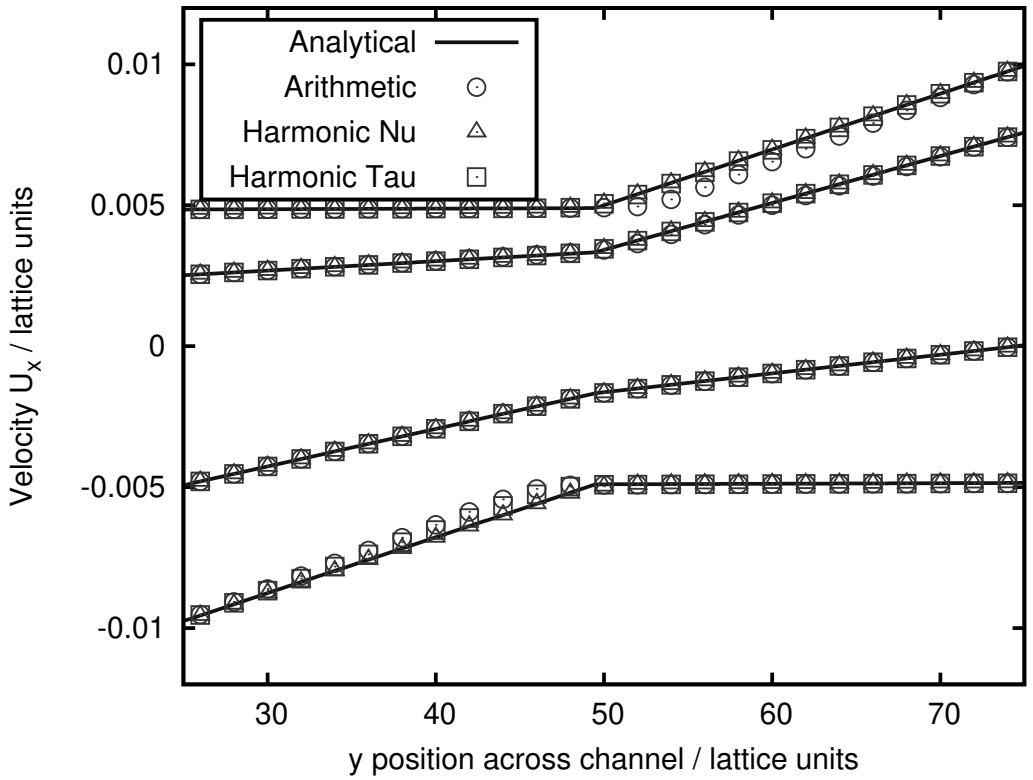

Figure 3.3: The velocity profile of several bilayered systems (fluid-fluid interface at $y = 50$). From top to bottom, the systems had viscosity ratios of 100, 5, 0.5, and 0.01. There are still large discrepancies between the arithmetic (liner interpolation) method and the analytical solutions. The harmonic mean of the relaxation time method appears to deviate towards the arithmetic method when the viscosity ratio $K < 1$. The horizontal axis was zoomed in, to resolve on the position of the interface.

Fig. 3.3 shows a zoomed in collection of these velocity profiles for different viscosity ratio systems. With a more modest viscosity ratio the difference between the schemes becomes less pronounced.

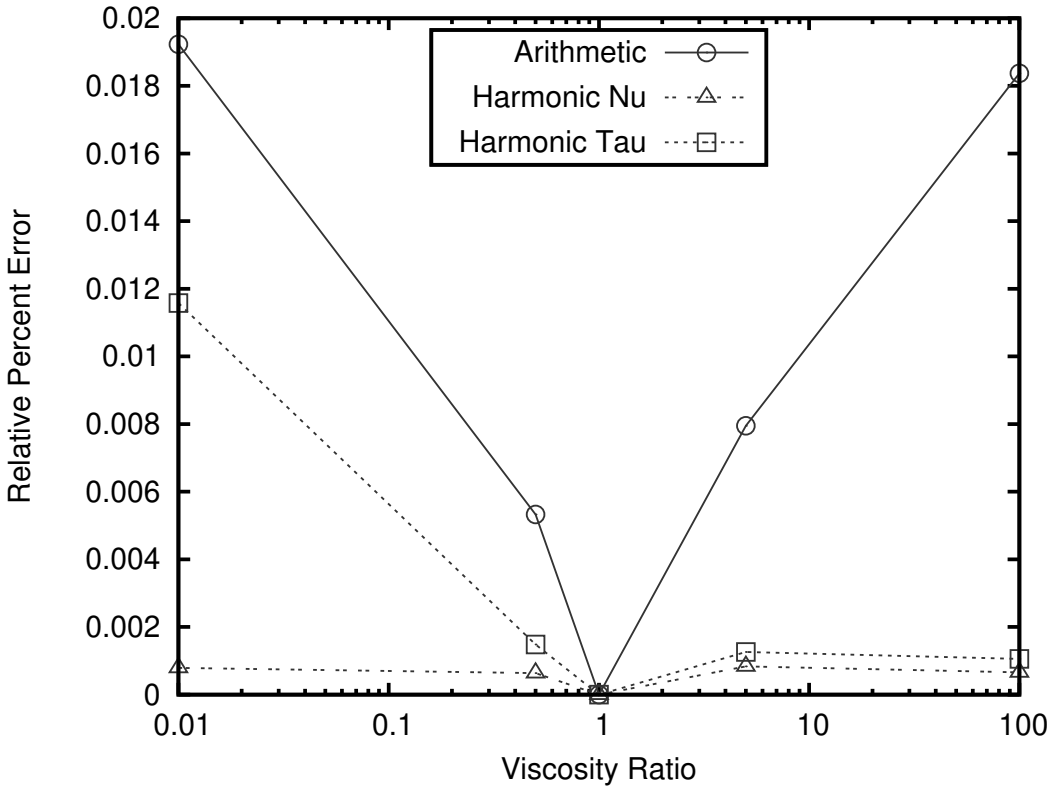

Figure 3.4: The average error (taken along the channel) between the interpolation method and the analytical solution for varying viscosity ratios. The harmonic mean of the relaxation time method appears to have comparable errors to that of the harmonic mean of viscosity when the viscosity ratio $K > 1$, however, it deviates towards the arithmetic method when the viscosity ratio $K < 1$. Note that lines are for reference only.

Fig. 3.4 displays the error between the measured velocity and the analytical solution. The linear interpolation clearly has the largest error, with an average of 1% in the systems tested. The method used through this thesis, the harmonic mean of the relaxation times has an average error of just 0.31% in these systems. This error is low and acceptable, however, using the harmonic mean of the viscosities reduces the average error further to just 0.06%.

This outcome is to be expected; this test assesses the influence of the interface on the velocity gradient. The harmonic mean of the viscosities enforces that the velocity gradient varies linearly with the phase-field, ρ^N, hence the change in velocity gradient here lines up most accurately with the interface $\rho^N = 0$. The harmonic mean of the relaxation times, however, is shown to place the viscosity interpolation in line with the multi-component force—this force is notably absent here due to curvature being zero—which may make it more appropriate when modelling droplets but makes it less suitable to a test such as this.

3.3.2 Taylor-Einstein

Secondly, the fully resolved flow fields were compared to the exact solution for a dilute emulsion droplet in the Re = 0 limit, the Taylor-Einstein [6] model ((2.6) of Section 2.1.2). A three dimensional (3D) model is, of course, necessary to carry out quantitative comparisons [3] (Such a model could not be used for further simulations due to the computational cost of 3D models). The main comparison of

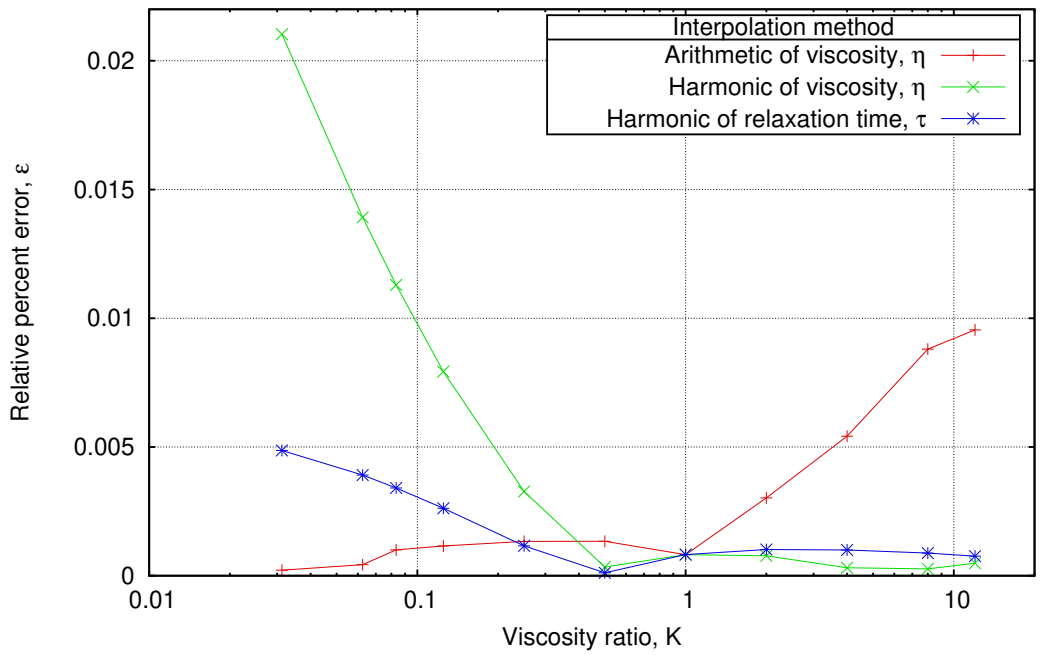

Figure 3.5: The relative error when comparing the measured emulsion viscosity, η, of each method and viscosity ratio, K, against the Taylor-Einstein result. Where $\epsilon = \frac{\eta^{(\mathrm{TE})} - \eta}{\eta^{(\mathrm{TE})}}$, and $\eta^{(\mathrm{TE})}$ is the predicted value of Taylor-Einstein. Lines are a guide to the eye only. Adapted from Xu et al. [3].

the data to the predictions of Taylor [6] is shown in Fig 3.5. The simplest method, the linear interpolation (arithmetic mean) of the fluid viscosity [99, 100, 101], saw greatly increasing error for a more viscous droplet. Whilst the harmonic mean of viscosity [103, 104] saw even worse errors for a more viscous background fluid. The viscosity interpolation of (3.15) provided the most accurate comparison over a wide range of viscosity ratios.

3.3.3 Emulsion data sensitivity analysis

Further validations involved a set of comparison simulations which were run to ascertain the effect that the interpolation method has on the physical outcomes, namely: relative viscosity, sheared self-diffusion coefficient, and average deformation parameter. The system design and simulation set up will be described in Chapter 5, but is essentially a sheared emulsion—the LBM algorithm is described above and the boundary conditions are Lees-Edwards boundaries (fully periodic with an imposed

shear rate) [67, 68]. The three measures above are taken from time averages, also described later. As mentioned, 3D simulations are currently too demanding on computer and time resources, hence 2D simulations were carried out. Note that these 2D simulations were able to provide comparisons for a wider range of viscosity ratio before numerical instabilities interrupted the simulations. The system for the data discussed in this section is as follows:

- 512 by 512 node lattice.
- Droplets of area 1369 lattice units (lu), radius 20.88 lu.
- All fluid densities $\rho_0 = 1.0$.
- Viscosity of the background fluid, $\eta_0 = \frac{1}{6}$ lu, $\tau_0 = 1.0$.
- Interface segregation parameter, $\beta = 0.65$.
- Interfacial tension parameter droplet to background, $\sigma_0 = 0.09$.
- Interfacial tension parameter droplet to droplet, $\sigma_1 = 10 \times \sigma_0 = 0.9$.
- Negligible fluid concentration threshold value, $\frac{\rho^{(k)}}{\rho} \leq 1 \times 10^{-9}$.

The effect of the interpolation method on the overall fluid viscosity is shown in Fig. 3.6. There is an average of 5.4% difference between the results (standard devi-

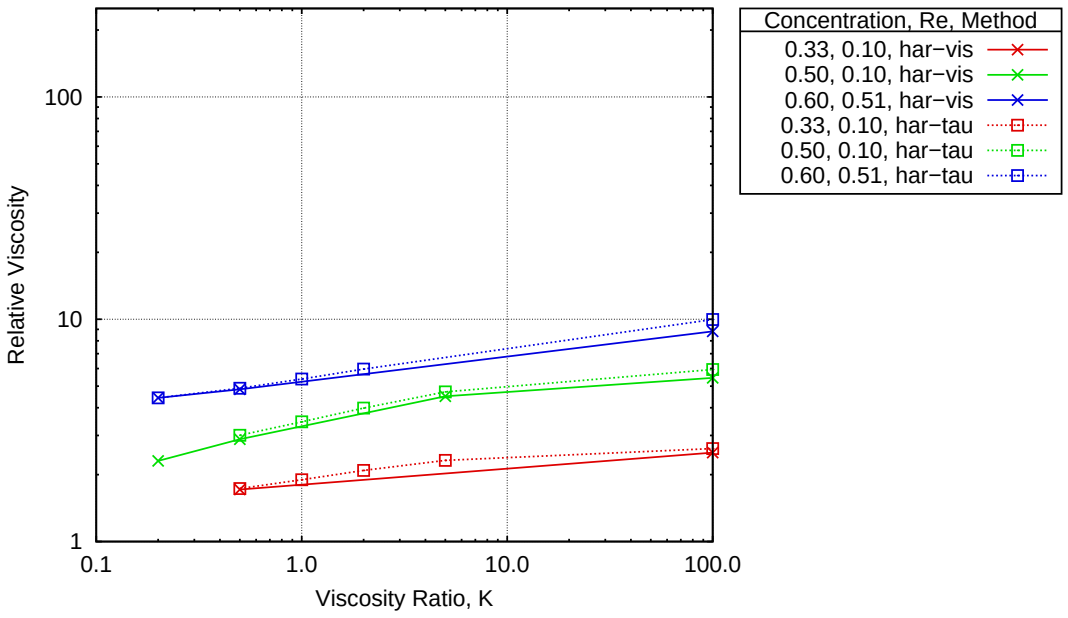

Figure 3.6: The relative viscosity results of a subset of emulsion simulations. Solid lines (crosses) show the results when using the interpolation method correct in the sharp-interface limit. Dotted lines (boxes) show the results when using the method described in (3.15), which is used throughout this thesis. Note that lines are a guide to the eye only and that not all configurations are replicated, due to time restrictions.

ation 4.4%), which is skewed by some relatively large differences when the viscosity ratio, K, is 100 (differences of up to 13.2%).

Similarly, Fig. 3.7 shows a comparison for the sheared self-diffusion results. Over-

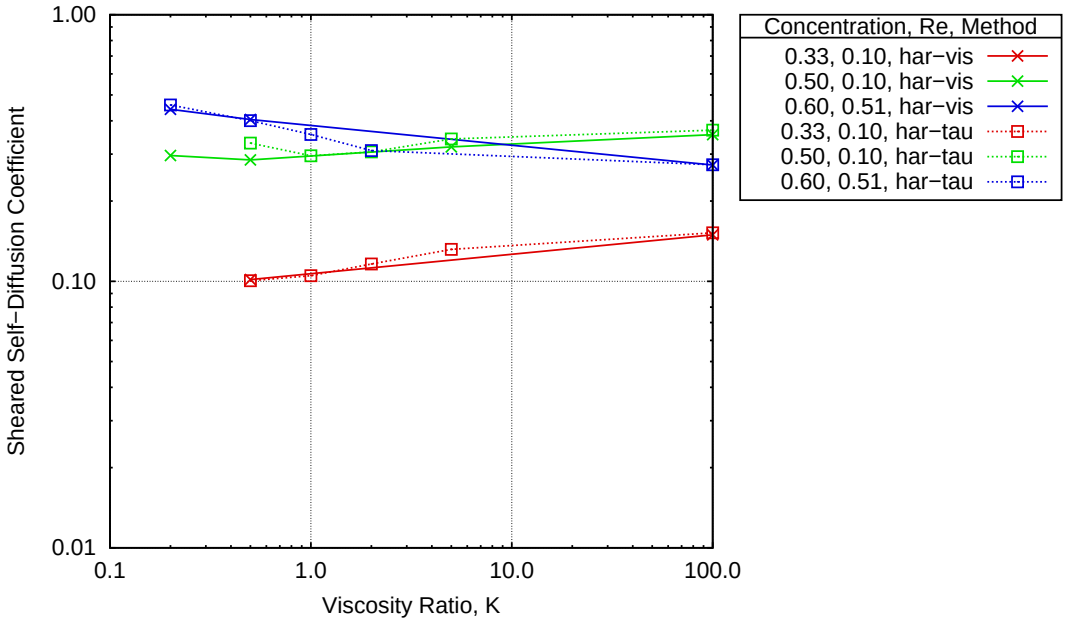

Figure 3.7: The sheared self-diffusion coefficient results of a subset of emulsion simulations. Solid lines (crosses) show the results when using (3.14), the harmonic mean of viscosity. Dotted lines (boxes) show the results when using the method described in (3.15), which is used throughout this thesis. Note that lines are a guide to the eye only and that not all configurations are replicated, due to time restrictions.

all, these match closer, with a difference of 4.4% (standard deviation of 5.5%) on average. There is one outlier that is significantly different, with a difference of 15.7%. This large difference isn't present for the other comparisons at $K = 0.5$, nor for the same concentration and shear rate configuration.

The same applies for a comparison of the average deformation parameter in Fig. 3.8. The average difference is just 5.2% (with a standard deviation of 5.4%). This value is skewed as previously, with a difference of 16.5% in this case.

Taken as a whole, these 2D comparisons show quite a different outcome from the validation against the 3D Taylor-Einstein model [3]. Whilst the first validation showed significant variation between the methods, with some results having errors of up to 30%, for emulsions as a whole it seems significantly less important. It is likely that the number of droplet interactions plays a part in making the exact interpolation method less significant.

It is important to bear in mind for the future results that there may be small quantitative errors arising from the viscosity interpolation method. Tests here show that such an error from (3.15) are at worst ~5% in the emulsion comparisons and are not expected to influence qualitative trends.

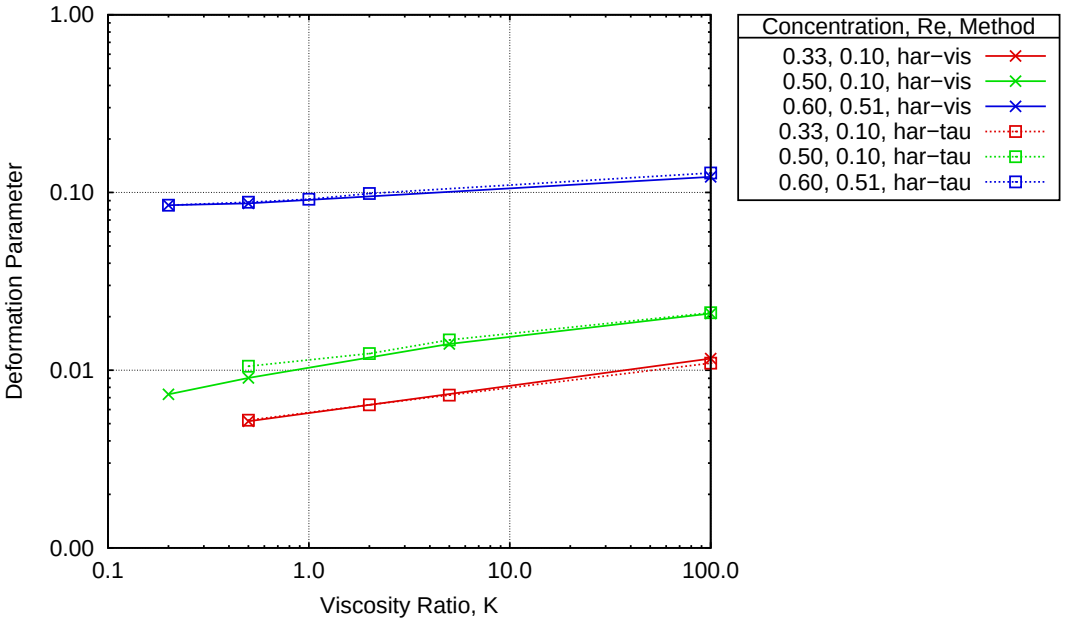

Figure 3.8: The average deformation parameter results of a subset of emulsion simulations. Solid lines (crosses) show the results when using the interpolation method correct in the sharp-interface limit. Dotted lines (boxes) show the results when using the method described in (3.15), which is used throughout this thesis. Note that lines are a guide to the eye only and that not all configurations are replicated, due to time restrictions.

3.4 Further Checks and Validations

3.4.1 Mass

The simulations below aim to explore the more basic requirements of the model. For example, the model shouldn't lose mass (neither as a whole fluid or the individual droplets), which is easily done when applying the memory saving technique described in Section 3.2. Losing or transferring mass may indicate inaccurate physics or result in the emulsion not being monodisperse. To test this, a system with multiple interacting droplets should be examined.

The system is set up as follows:

- 512 by 512 node lattice.
- 133 droplets, each of area 1369 lattice units (lu), radius 20.88 lu.
- Providing a droplet concentration of 69.5%.
- All fluid densities $\rho_0 = 1.0$.
- Viscosity of the background fluid, $\eta_0 = \frac{1}{6}$ lu, $\tau_{s_0} = 1.0$.
- Viscosity of the droplet fluids, $\eta_1 = \frac{100}{6}$, $\tau_{s_1} = \frac{101}{2}$.
- Viscosity ratio, $K = \frac{\eta_1}{\eta_0} = 100.0$.

- Interface segregation parameter, $\beta = 0.65$.
- Interfacial tension parameter droplet to background, $\sigma_0 = 0.09$.
- Interfacial tension parameter droplet to droplet, $\sigma_1 = 10 \times \sigma_0 = 0.9$.
- Negligible fluid concentration threshold value, $\frac{\rho^{(k)}}{\rho} \leq 1 \times 10^{-9}$.
- The number of unique fluids is 134, whilst the number of lattices was set to 10 (although only a maximum of 5 were ever populated at any given time).

An example snapshot from the simulation is shown in Fig. 3.9.

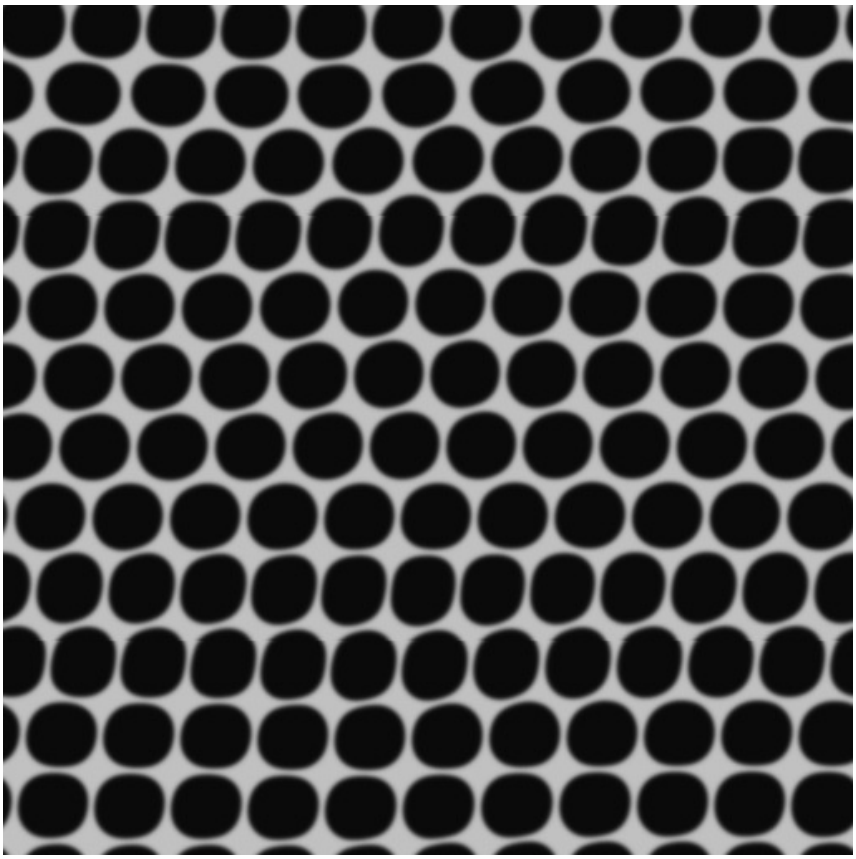

Figure 3.9: A snapshot of the simulation used to test the mass loss in the system. The colour is based on the concentration of the background fluid, light when only the background fluid is present and dark when only a droplet fluid is present (i.e. inside a droplet interface).

Shearing this system, in the same way as will be described in Chapter 5, ensures these highly concentrated droplets interact frequently. This check then also provides a backing for the implementation of the mentioned boundary condition. Running this for millions of timesteps provides the following performance values:

- The *lost mass* is calculated by taking the maximum mass of fluid through the duration of the simulation, subtracting the minimum mass of the same fluid. This can be divided by the initial fluid mass to find the percentage lost

through the entire simulation: $\rho_{\text{lost}}^{(k)} = \frac{\rho_{\max}^{(k)} - \rho_{\min}^{(k)}}{\rho_{\text{initial}}^{(k)}} \times 100\%$. To be more specific, this describes the largest change throughout the simulation, not just the loss, which will exaggerate the statistic slightly.

- The total overall fluid mass lost per million timesteps is 0.00018%.
- The average (maximum) amount of a specific fluid mass lost per million timesteps is 0.0012% (0.0023%) of its initial value.

This means that at the extreme end of the viscosity ratio, surface tension, and droplet concentration (maximising droplet interactions, likely sources of error, and number of overlapping fluids), each fluid will see a maximum of 0.0023% lost per million timesteps. Considering the longest simulations in this thesis run for 20 million timesteps, a droplet losing 0.046% of its mass can be considered negligible.

A final consideration is that, since the maximum mass lost from a specific droplet fluid exceeds that lost from the overall fluid, this may mean another droplet is gaining mass by approximately the same amount. This means two neighbouring droplets could be 0.092% different in their mass. This is still a negligible difference and the emulsion could still be considered as mono-disperse (i.e. made up of a single size and species of droplets).

3.4.2 Laplace law behaviour

Another key validation for a model containing emulsion droplets is the reproduction of Laplacian pressure difference across the fluid-fluid interface. The Young-Laplace equation links the interfacial tension, curvature, and pressure difference over the interface as [13]:

$$\Delta p = \sigma\kappa \,. \tag{3.17}$$

In 2D, the mean curvature of a drop is the inverse of the radius, hence:

$$\Delta p = \frac{\sigma}{R} \,. \tag{3.18}$$

This equation should be true for varying droplet sizes, viscosity differences, and interfacial tension parameters. Laplace law behaviour should be verified by measuring the pressure difference between the inside and outside of a static droplet under varying conditions.

Fig. 3.10 shows the model compared to the Young-Laplace equation for various interfacial tension parameters. The simulations used fully periodic systems of 100 by 100 lattices nodes, and a droplet of radius $\sqrt{\frac{1369}{\pi}} = 20.88$. The droplet was positioned in the centre of the system, hence it remains stationary relative to the lattice. To obtain the pressure difference, the pressure in the corner of the system (the farthest point from the droplet) was then subtracted from the pressure measured in the centre

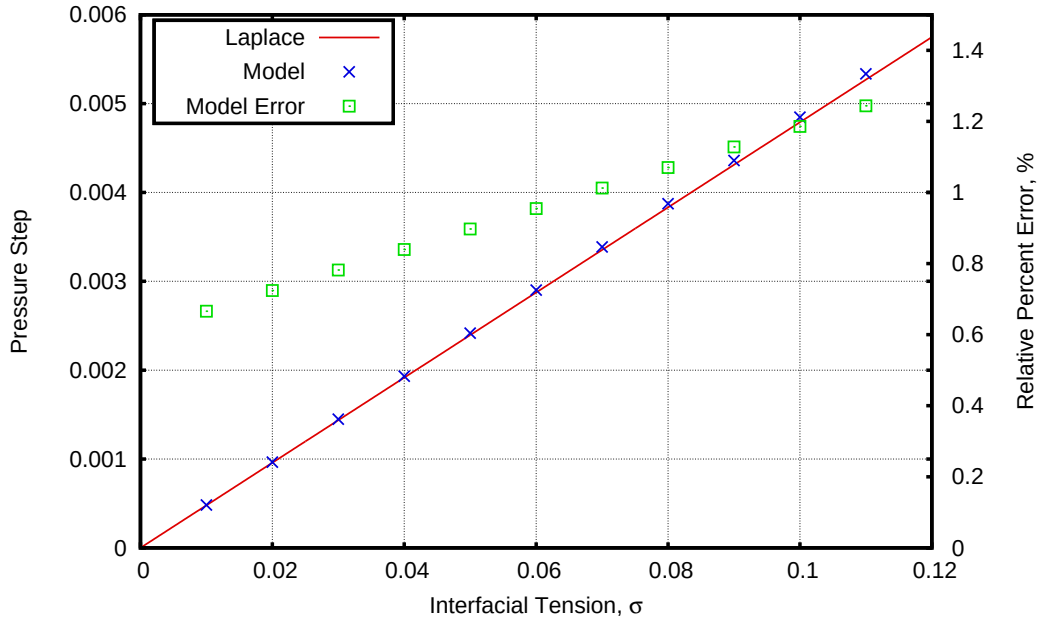

Figure 3.10: A comparison of the model (crosses) against the Young-Laplace equation (line). Also, the relative percent error (squares, second axis) between the pressure difference in this model and the Young-Laplace equation. The model reproduces an accurate pressure difference for a wide range of surface tension parameters, σ. The viscosity ratio, K, was set to 1.0.

of the droplet. It can be seen that the model produces an accurate—within 1.2%—pressure difference throughout the range of tested interfacial tension parameters. The relative error increases linearly with the interfacial tension parameter. However, the error remains acceptable even when the interfacial tension parameter is beyond what is used in this thesis.

Fig. 3.11 shows the low relative errors between the measured pressure difference and the Young-Laplace equation over a range of viscosity ratios. It can be seen that the model produces an accurate pressure difference throughout the range of tested viscosity ratios (using interpolation method (3.15)). The error is relatively constant with changing viscosity ratio (viscosity ratio is not a variable in the Young-Laplace equation) until the upper tested values. The largest error, 2.3%, is found in the test with the highest viscosity ratio and interfacial tension, but is still manageable.

Note that the error in the Laplace law pressure step displayed in Fig. 3.10 increases linearly with the interfacial tension parameter. This indicates that it may be possible to decrease the applied interfacial parameter to achieve a more accurate pressure step. Such a correction would be a very simple change to the initialisation step of a simulation. However, this corrective action will not be taken through this thesis as variable viscosity ratios will be explored and Fig. 3.11 shows the linearity in the error no longer holds.

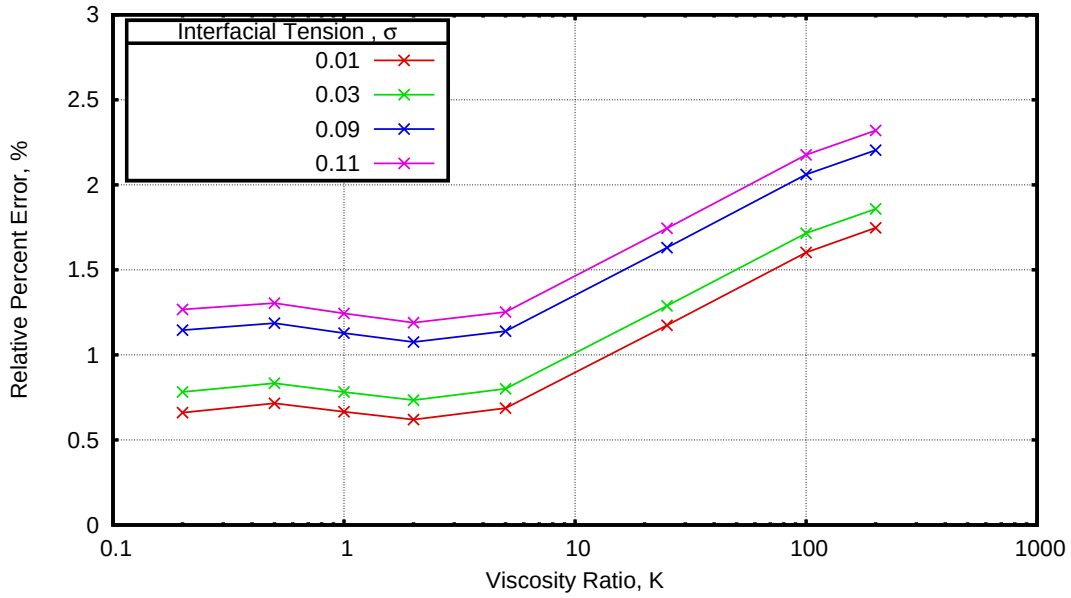

Figure 3.11: The relative percent error of the pressure difference between the model and the Young-Laplace equation. The model reproduces the correct pressure difference for a wide range of viscosity ratios, K. Lines are for guidance only.

3.4.3 Droplet Coalescence

The model has been shown to retain mass for each fluid and produce an accurate Laplacian pressure difference. Next, the droplets should not coalesce. It might be said that the model assumes surfactants on the interface are fully effective, keeping coalescence completely arrested. Any movements or gradients of the surfactants due to the flow are neglected.

A simple way to test the coalescence is to place two droplets next to each other. Fig. 3.12 shows the initial configuration of the droplets as well as the system after time has passed. The droplets immediately separate. A slight *bridge* between the droplets is noticeable until they separate more and the interface becomes smooth.

A more thorough test, albeit hypothetical, places the droplets together as two halves of a pseudo-Janus droplet. It would be hoped that the two different droplets would separate in the same way as before. Fig. 3.13 shows that behaviour for several systems. In the systems with a high interfacial tension (σ_1 becomes larger than 1.0), artefacts become noticeable along the interface—rather than flat, it becomes S-shaped. This doesn't prevent the droplets from separating, and is not present in the lower interfacial tension systems. The artefact is not visible in the lower viscosity ratio, either, most likely because the droplets separate much faster. Such a flat interface is unrealistic in a physically flowing emulsion.

Note that the interfacial tension parameter between the droplet fluids is ten times the parameter between the droplets and the background fluid. This means the parameter is extremely high in the cases with artefacts in Fig. 3.13(a and b). A flat interface between a droplet and the background fluid may be quite common,

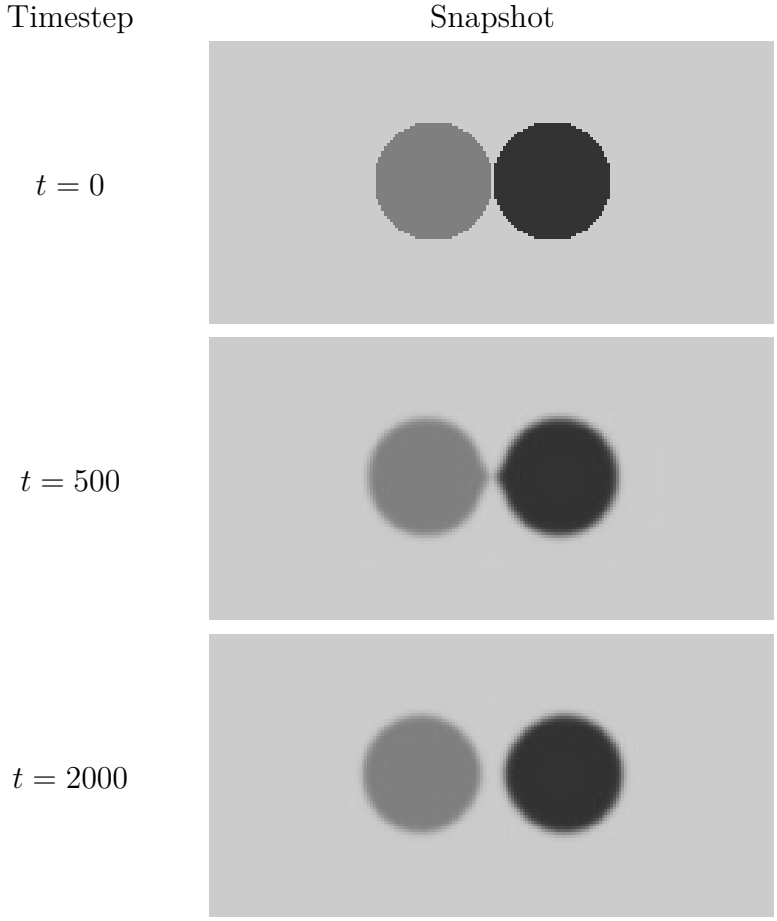

Figure 3.12: Snapshots of a system at different points in time where droplets are placed next to each other. The droplets do not coalesce, which is the correct behaviour when assuming surfactants are fully effective. This test was carried out with interfacial parameter $\sigma_0 = 0.11$ and viscosity ratio $K = 200$.

but there will be no artefacts present. As row d of Fig. 3.13 shows, a flat interface where the interfacial tension parameter is $10 \times 0.03 = 0.3$ shows no artefacts; the parameter between the droplets and the background fluid will be kept much lower than this.

Other than the artefact in the higher interfacial tension systems, the droplets behave as expected and all separate well.

3.5 Conclusion

The model has been validated at a low concentration [3] against the exact solution of the Taylor-Einstein equation, as well as in a bilayered flow. The model has also been shown to have mass conservation, an accurate Laplacian pressure step, and droplets that don't coalesce. The next step is to apply the method to more concentrated systems. This will happen in the next chapter, where the results of a Poiseuille flow will be analysed and compared to macroscopic models.

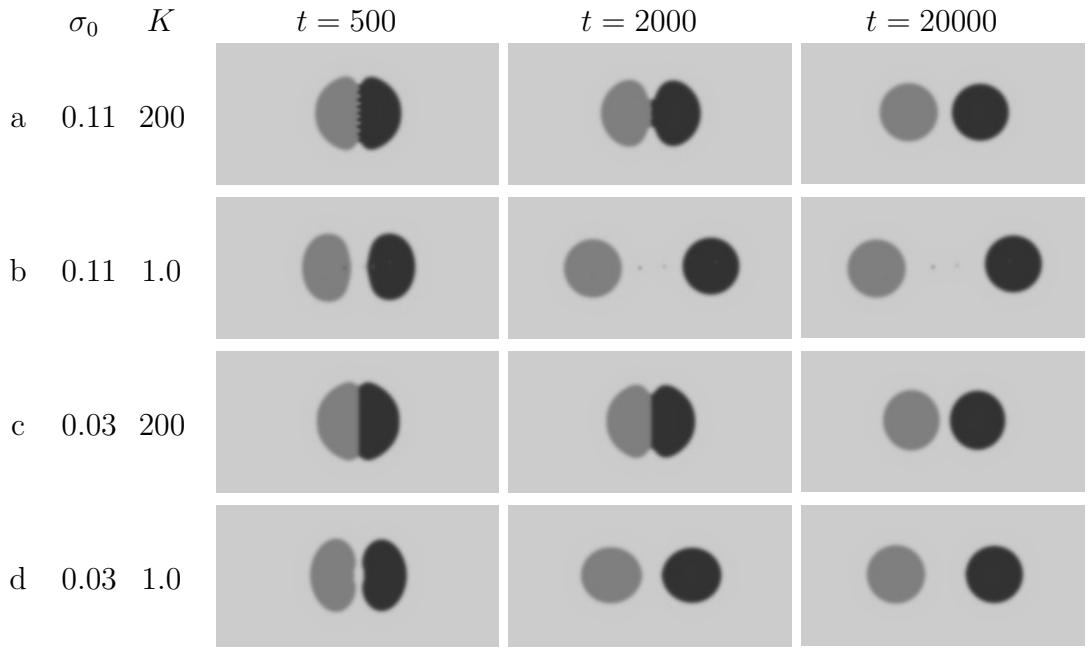

Figure 3.13: Snapshots of several systems at different points in time. High and low interfacial tension parameters and viscosity ratios were tested. The droplets start unrealistically close to each other, like a pseudo-Janus droplet, but still force themselves apart. The highest surface tension is above the maximum of the algorithm ($\sigma_1 = 10\sigma_0 > 1.0$), but is included to show successful separation in the extreme case. The higher viscosity ratio droplets are expected to move and separate much slower than their low viscosity ratio comparisons. The final position of the droplets is not expected to be the same from system to system due to the initialisation and the different amounts of dissipation associated with the varying material properties.

Chapter 4

Pipe Flow

This chapter will display some initial results, obtained by applying the method described in the previous chapter to an emulsion in a pipe flow. This appeared to be a relatively straight forward next step, with boundary conditions apparently documented, ready to implement [60, 61]. Once this chapter begins, however, this is found to be more complicated. A new boundary condition is developed that is able to drive a multi-component flow whilst maintaining mass conservation.

Driving the fluid through a pipe will validate the single-component code against an analytic solution. Once applied to an emulsion, the fluid is hypothesised to be a power-law fluid and this macroscopic model is fit to the data.

In addition, this chapter aims to show that simulations of up to O(100) of interacting, individually parametrisable droplets are readily achievable.

4.1 Boundaries and initial conditions

The system was set up with solid walls at the top and bottom, modelled with the bounce back method described in Section 2.2.1. Parameters such as the viscosity ratio and density ratio were kept at 1, to control the domain space. A single droplet was first tested to verify the model. To drive the flow, a pressure gradient is used. The boundary conditions described by Zhang and Kwok [60] as well as Kim and Pitsch [61] (see Section 2.2.1) were implemented and expected to work, but they both lost fluid mass and sent pressure fluctuations through the system when interacting with a droplet.

The first of these issues, the mass loss, is visible in Fig. 4.1. Each time the droplet interacts with the boundary condition, a not insignificant amount of mass is lost. On the timespan required to achieve pseudo-steady results, i.e. millions of timesteps, the significance of the lost mass becomes more apparent.

The second issue, the pressure fluctuation, is visible in Fig. 4.2. The pressure at a *monitoring station* was tracked as the droplet flowed past it and across the boundary condition (a schematic is visible in Fig. 4.3). Fluctuations labelled *a*

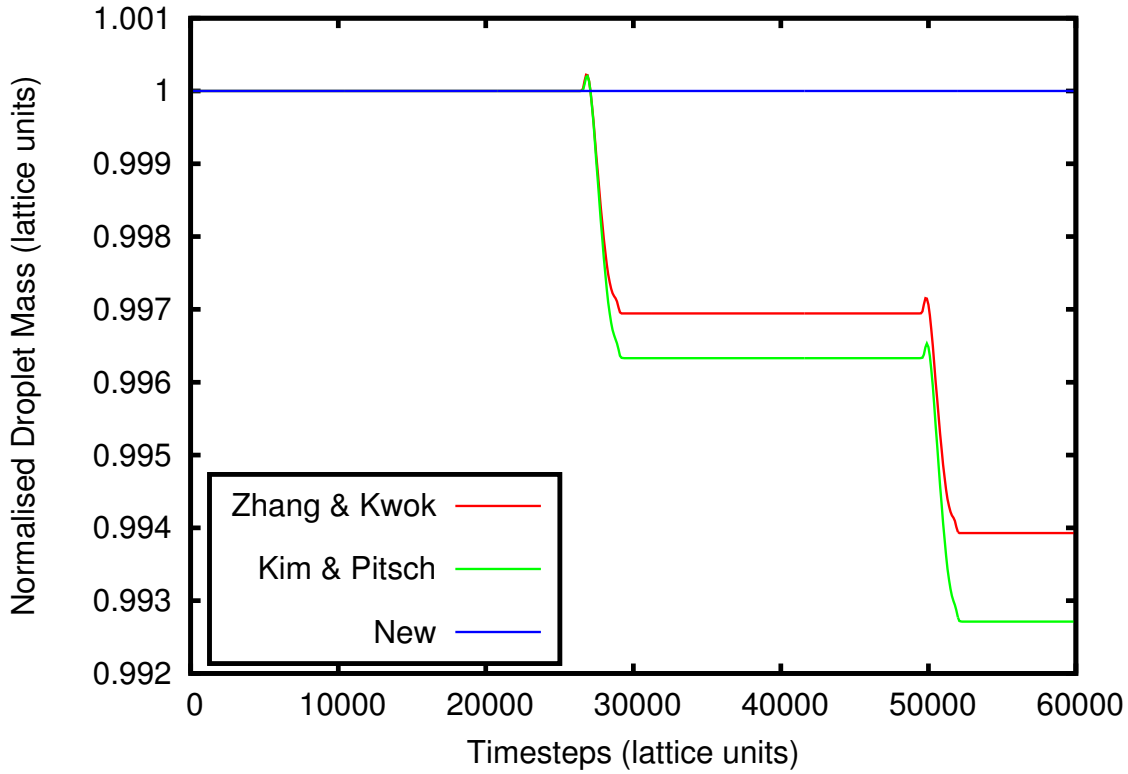

Figure 4.1: Normalised droplet mass over time, showing the droplet pass the boundary condition twice. The compared methods are of Zhang and Kwok [60], Kim and Pitsch [61], and the method described later in the section.

occur when the droplet crosses the boundary, whilst fluctuations labelled b occur as the droplet passes the monitoring location. The second type of fluctuation is natural, as the droplet creates a wake as it passes. This is, however, totally overwhelmed by the non-physical fluctuation that the boundary conditions exhibit. The small, physical fluctuations and subtle effects, may or may not be of interest, however the large fluctuation may result in undefined or undesirable flow. This issue is unlikely to improve if simulating multiple droplets, as in some systems it may be that a droplet is present on the interface more often than not. Another way to view this issue is via a video [106] showing the relative value of pressure throughout the system (white being high pressure, black being low pressure). This video shows the relative pressure over time when using the method of Kim and Pitsch. The physical variations are visible around the droplet, but the whole background goes black as the droplet interacts with the boundary condition. Note the flashing at the start of the video is a visible representation of the system settling down from initialisation, as seen at the start of Fig. 4.2.

As mentioned when discussing the boundary conditions in Section 2.2.1, the methods take an average of the pressure along the inlet and outlet of the channel. The introduction of droplets means that a pressure step within the interface is to be expected. It appears most likely that the averaging process is being disrupted by the pressure step, causing the droplet to lose mass and the imposed pressure

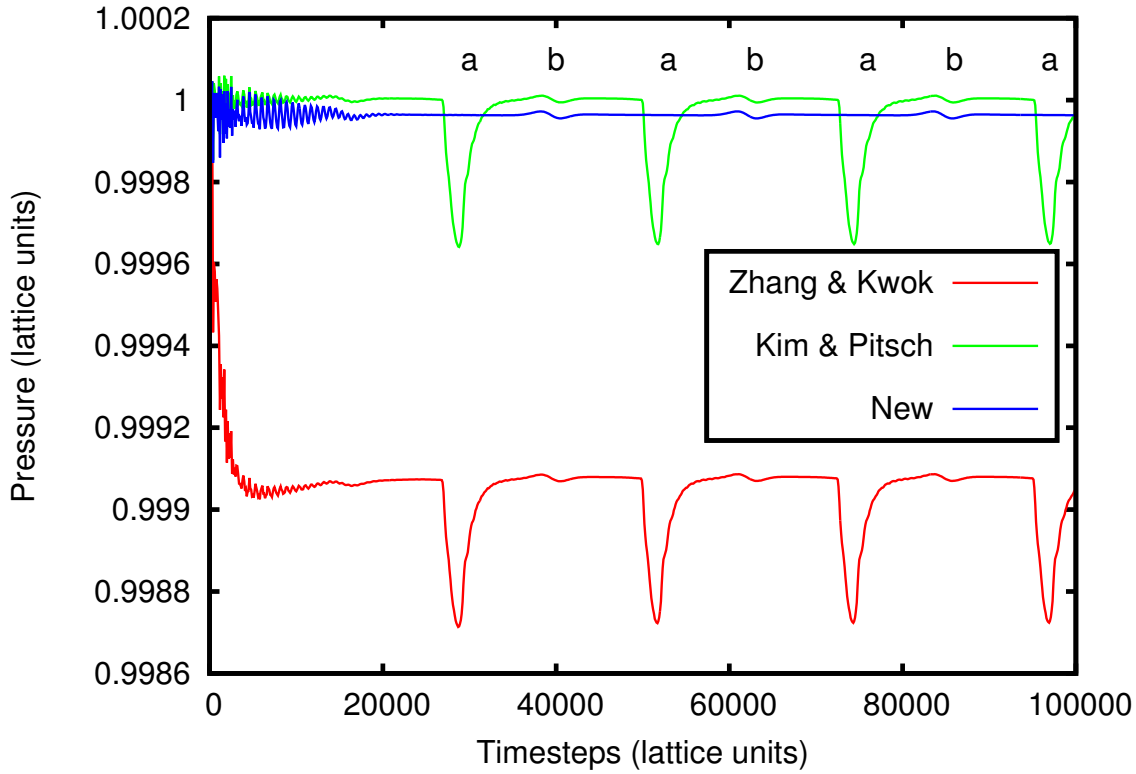

Figure 4.2: Pressure fluctuations over time, showing the droplet pass over the boundary condition three full times. Measured at a point half way along the channel—near the side—outside of the droplet (as shown in Fig. 4.3). The compared methods are of Zhang and Kwok [60], Kim and Pitsch [61], and the method described later in the section.

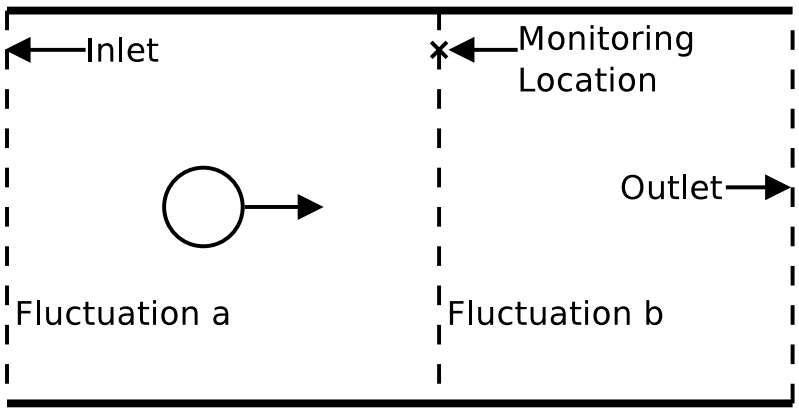

Figure 4.3: A diagram of where the monitoring station is location in the channel. The labelled dashed lines show the position of the droplet when the fluctuations visible in 4.2 occur.

gradient to be interrupted.

A final problem in current pressure boundary conditions is the production of incorrect pressure values through the boundary. As seen above, the boundary condition has an effect on the droplet when it is nearby, however, there is also an effect on the transmission of pressure. Kim and Pitsch [61] show in Fig. 4 that their method produces different pressure contours to that of an applied body force. They

do not show that these contours change depending on the location of the obstacle, i.e. the system is not properly periodic as the closeness to a boundary condition impacts upon the flow.

Following this, a new method was developed. Rather than an averaging process, a constant amount of fluid mass is transferred from the outlet to the inlet. For example, the unknown links entering the system will be:

$$\begin{aligned} f^{\text{in}}_{\text{inlet}} &= f^{\text{out}}_{\text{outlet}} + C\,, \\ f^{\text{in}}_{\text{outlet}} &= f^{\text{out}}_{\text{inlet}} - C\,. \end{aligned} \tag{4.1}$$

The amount added and subtracted will be determined by the desired pressure step:

$$C = \frac{\Delta p}{c_s^2}\,. \tag{4.2}$$

The unknown links are then:

$$f_i = f_i + t_i c_{ix} C\,, \tag{4.3}$$

where t_i distributes the added mass onto the short and long link accordingly, and c_{ix} will ensure the amount is added (subtracted) at the inlet (outlet). The pressure step of a droplet will have no impact on this method, preserving mass conservation. Removing the averaging process also has the benefit of improving computational efficiency.

Fig. 4.4 compares the new pressure boundary condition to the existing methods by reproducing and extending the figure by Kim and Pitsch [61] (Fig. 2). Note that to reproduce the figure, the method of Zhang and Kwok [60] was implemented in the compressible LBGK algorithm. This is the reason for the reference to *density*; technically each method on the figure is showing a density fluctuation rather than pressure. This shows the correct reproduction of the pressure gradient in a single-component system. Additionally, in the previous figures, Fig. 4.1 and Fig. 4.2, it can be seen that, for a multicomponent system, mass is indeed conserved and that the non-physical fluctuation is eliminated. A video using this boundary condition can also be viewed [107], this shows the pressure to be stable in the background fluid even when the droplet approaches the boundary condition.

Further study on this topic highlighted the work of Inamuro [108]. Whilst the paper describes the method as applied to a compressible algorithm of three dimensions, the method appears to be very similar with one subtle difference: the pressure step at any node along the channel is a constant, which means the exact amount added from node to node could vary.

With effective boundary conditions implemented, the method can be applied on more than just a single fluid. The emulsion will be mono-disperse and the droplets

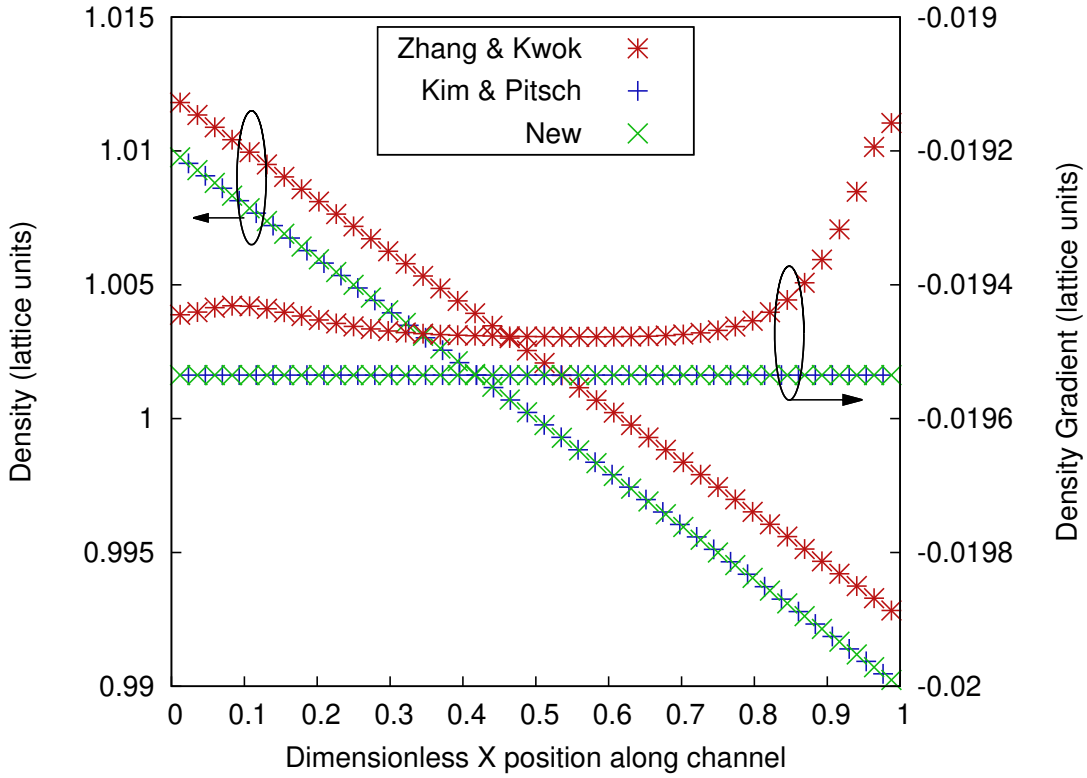

Figure 4.4: Reproduction, and extension, of Fig. 2 in Kim and Pitsch [61]. Streamwise comparison of the density/pressure profile and density/pressure gradient in a periodic pipe flow. The method of Zhang and Kwok uses a compressible LBGK algorithm, therefore is showing a density gradient ($p = \rho c_s^2$). The other two methods are implemented in an EILBGK algorithm, therefore they are showing a gradient in the density fluctuation (which is still $p = \rho c_s^2$,). Analytically, the gradient should be constant along the channel and was designed to provide a ρ of 1.01 and 0.99 at the inlet and outlet respectively (where $\rho = \sum_i f_i$ and refers to the LBGK density or EILBGK density fluctuation). Normalised from $x = 0$ to $x = 1$ along the channel length.

will have a relatively high interfacial tension (ensuring a near-circular droplet shape), keeping the experimental domain under control. The fluid density, ρ_0, and symmetric relaxation times were set to 1. Hence fluid viscosities are $\frac{1}{6}$. The fluid segregation parameters, β, were all set to 0.65. The interfacial tension parameter between the droplets and the background fluid, σ_0, was set to 4.72×10^{-2} and the interfacial tension parameter between the droplets, σ_1, was just over an order of magnitude higher, at 5×10^{-1}.

To apply the boundary condition to multiple fluids, the addition and subtraction is spread proportionally across the different fluid distributions once they have been segregated:

$$f_i^{(k)} = f_i^{(k)} + t_i c_{ix} C \frac{\rho^{(k)}(\mathbf{x}_{\text{inlet}})}{\rho(\mathbf{x}_{\text{inlet}})} . \tag{4.4}$$

Note that first attempts tried to use $\frac{\rho^{(k)}(\mathbf{x}_{\text{inlet}})}{\rho(\mathbf{x}_{\text{inlet}})}$ at the inlet and $\frac{\rho^{(k)}(\mathbf{x}_{\text{outlet}})}{\rho(\mathbf{x}_{\text{outlet}})}$ at the outlet. However, due to the mismatch between these values on the two different nodes, the conservation of mass couldn't be guaranteed. Therefore one must use a single column (inlet or outlet, preferably) to calculate the amount to be added to the fluid distributions.

A resolution test was carried out to determine satisfactory system dimensions. Allowing a single droplet to flow through the pipe, it will eventually migrate to a vertical resting position. Increasing the dimensions (both system and droplet, maintaining the ratio between them) showed the systems converging on a similar resting position, as visible in Fig. 4.5. With a radius $R = 20.9$, the resting position was 2.33% from the position using a radius of 23. Hence, sufficient resolution was achieved with a radius of 21 and this size was used for the further simulations. This set the channel length and width to 634 and 424 lattice units, respectively.

4.2 Results

Systems with varying numbers of droplets were then simulated, up to 120 droplets (a concentration of $\phi = 0.609$). An example system with 80 droplets ($\phi = 0.406$) is displayed in Fig. 4.6. Droplets were initialised at random positions in the channel (although it was ensured there were an equal number at the top and bottom of the pipe) and the flow starts from rest at $t = 0$.

The velocity profile across the channel for each simulation can be seen in Fig. 4.7 (pluses). An analytic solution to this flow is plotted as solid lines in Fig. 4.7. This analytic solution is possible by hypothesising that the fluid has a power-law viscosity. From Section 2.1.3:

$$\eta_{\text{eff}} = k\dot{\gamma}^{(n-1)} , \tag{4.5}$$

where the shear rate in this geometry becomes: $\dot{\gamma} = \partial_y U_x$. The general solution to

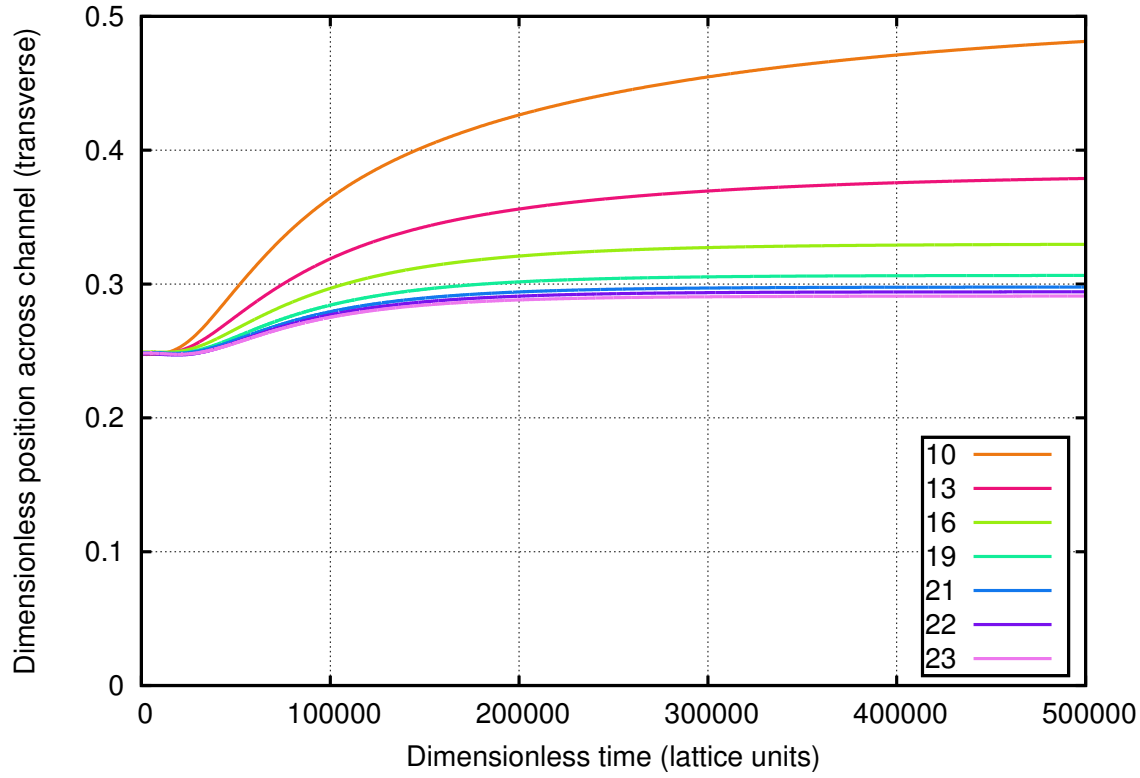

Figure 4.5: A plot of the droplet migration over time. Simulations were run for varying resolutions, indicated by the droplet radius (in lattice nodes) in the legend (more nodes is finer resolution). The viscosity of the fluid was $\eta = \frac{1}{6}$, the Reynolds number was $\mathrm{Re} = \frac{U_{\max} w}{\eta} = 1.1 \times 10^2$, and the Capillary number was $\mathrm{Ca} = \frac{U_{\max} \eta}{\sigma_0} = 1.5 \times 10^{-1}$. Colour available electronically.

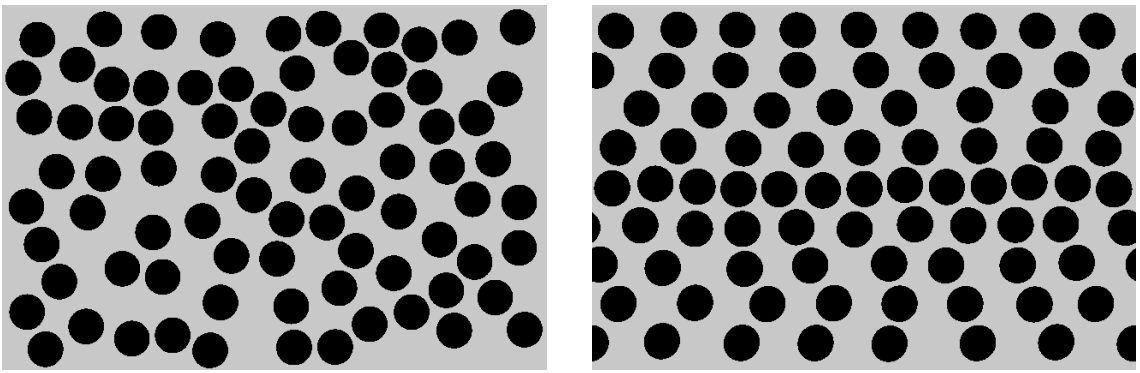

Figure 4.6: Overviews of an 80 droplet system ($\phi = 0.406$) at its initial (left) and final, pseudo-steady (right) states. The droplets are forced left to right, over periodic boundary conditions, by an applied pressure gradient. The top and bottom boundaries are solid walls. The right panel shows that the droplets have entered clear layers over the course of the simulation.

the velocity profile is:

$$U_x(y) = \left(\frac{G}{k}\right)^{\frac{1}{n}} \left(\frac{1}{\frac{1}{n}+1}\right) \left[\left(\frac{w}{2}\right)^{\frac{1}{n}+1} - y^{\frac{1}{n}+1}\right], \tag{4.6}$$

where G is the pressure gradient, k is the consistency index of the power law fluid

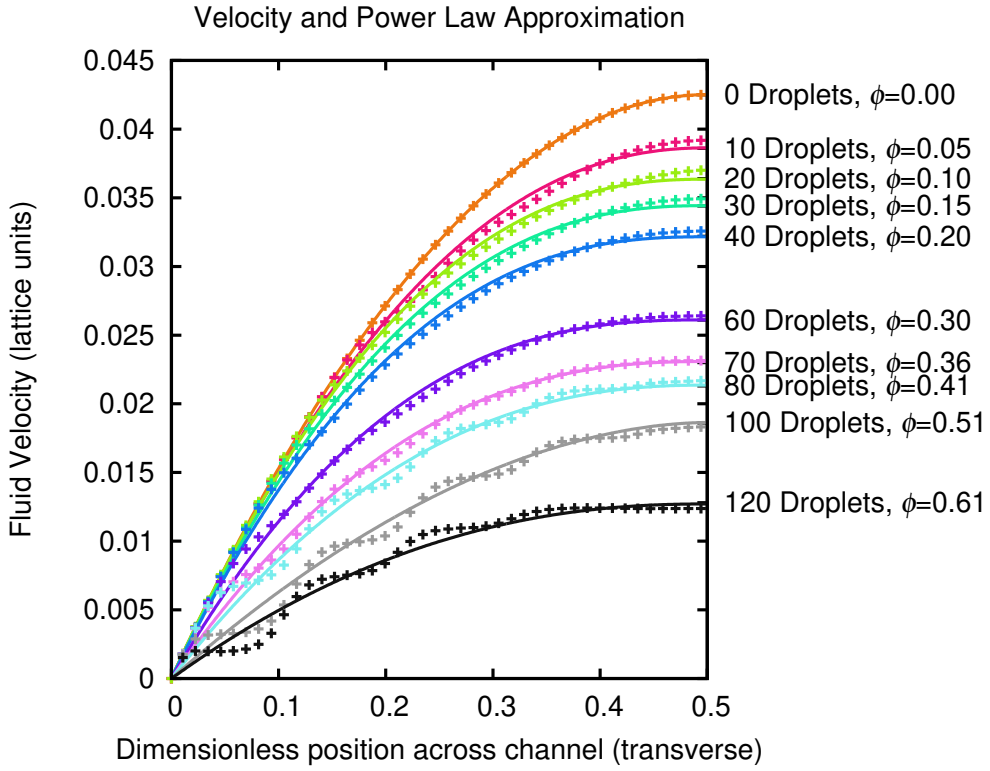

Figure 4.7: A plot of the simulated velocities (+), in lattice units, and the power-law approximations (solid lines) for varying numbers of droplets. The system was 634 nodes long and 424 nodes wide, with droplets of 21 node radius (hence the ratio of channel diameter to droplet diameter $\frac{w}{2R} = 10.1$).

(i.e. the fluid viscosity), w is the width of the system, and y is the position in the channel (upon which the velocity is dependant). When $n = 1$, the solution reduces to that of a Newtonian fluid in a pipe, which is an analytic solution. This can validate the simulation with no droplets in the flow. To measure the error between the analytic solution and the simulation, the measured flow rate is compared to the expected flow rate:

$$Q = \int_0^w U_x \, dy = -\frac{Gw^3}{12\eta}. \tag{4.7}$$

Using the above system dimensions and a pressure gradient of -3.15×10^{-7}, the analytic flow rate $Q_a = 12.015709$. Applying the same integral to the simulation velocity data, by summing up a column of velocity data, yields $Q_m = 12.015742$. This is an error of 0.0003%, providing confidence that the model accurately reproduces the correct velocity in such a geometry.

Continuing to multi-component results, the power-law solution is no longer analytic but it can be fit to the data. A time average of the measured velocity profile was taken, to smooth out the variation introduced by the droplets. The systems were left to flow for 8×10^6 timesteps, to allow them reach a pseudo-steady state. A time average was then taken every 5000 timesteps, 4000 times until 10^7 timesteps were complete. This length of time allows a droplet to flow from inlet to outlet at least 40

times when at the peak channel velocity. [1] The flow rate of the simulations was then calculated, and the power-law solution fitted against this (with the power-index, n, as the fitting parameter) using a non-linear least-squares Marquardt-Levenberg algorithm. Note the solution including the flow rate rather than the pressure gradient is:

$$U_x = \frac{Q}{w} \cdot \frac{2n+1}{n+1} \left[1 - \left(\frac{2|y|}{w} \right)^{1+\frac{1}{n}} \right], \tag{4.8}$$

where $y = 0$ is the centre of the channel.

As shown in Fig. 4.7, the fits represent the data well. For lower concentration fluids the model is highly representative (with errors $< 1\%$), however, at around 60 droplets ($\phi = 0.305$) there begins to be effects which are not captured by the model. Note that the largest fitting errors are just 3.5%. It's around this time that the droplets begin to form layers, or bands, particularly in proximity to the wall—see the right panel of Fig. 4.6 for an example of a layered system. Below this threshold, the droplets have an abundance of room in which to migrate transversely around the channel (away from the walls, generally), but in higher concentration systems the droplets are more packed together and the outer droplets are closer to the walls than before, resulting in a layer on the outside. As the number of droplets is increased further, the outer layer imposes layers further in, until around 80 droplets ($\phi \approx 0.35$) when the system becomes just a series of layers.

The *flow behaviour index*, n, can be seen plotted against the concentration in Fig. 4.8, which emphasises the range in which the power-law model appears valid. There is a clear trend towards a more shear-thinning fluid, until the system starts to form layers and n tends upwards. Note the outlying point at a concentration of 0.5 (100 droplets); there is nothing visibly different in the velocity profile nor the flow behaviour, yet fits to the profile consistently describe the system as shear thickening (exponent above 1.0). This highlights that the power-law model can not reliably represent systems with shear banding.

The power-law model doesn't attempt to capture the layering behaviour, so its use should be restricted to systems with more mobile drops. This is important due the large effect on the velocity profile that the layers have, and thus the velocity gradient (critical to non-Newtonian models like the power-law) which approaches zero within some of the layers. It should be noted that the banding behaviour may be encouraged by the relatively low channel diameter to droplet diameter ratio of 10.1, which may aid the walls to impose structure on the interior droplets. This highlights a limitation of previous work [109].

In the lower concentration systems, hence more mobile, the power-law model is highly accurate, providing a way for the reasonably costly mesoscopic simulations

[1] These figures were based on the simulation with 120 droplets, hence the slowest peak velocity. A droplet could pass through the domain twice or even thrice that amount in the less concentrated systems.

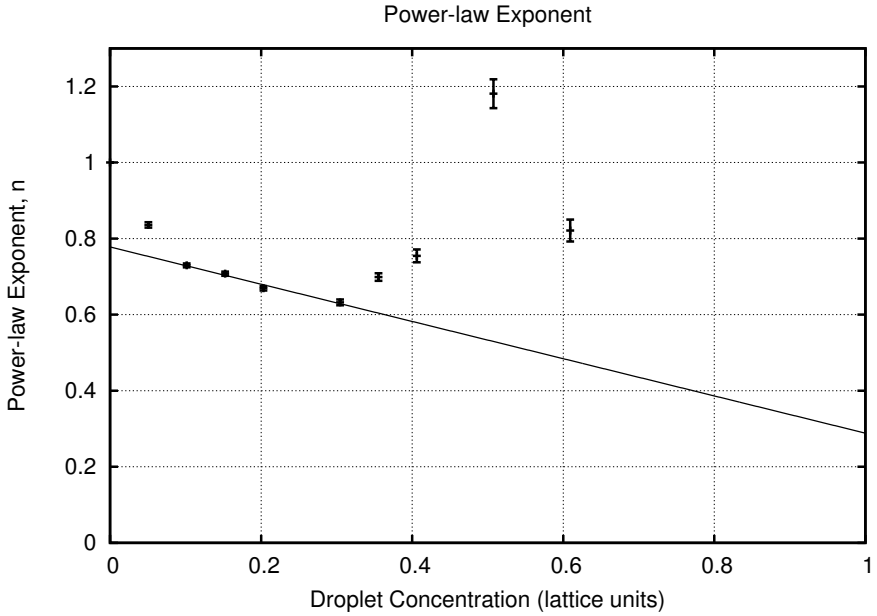

Figure 4.8: A chart to match the power-law exponent to the droplet concentration. The exponent is from the fitted data in Fig. 4.7. Error bars show the fitting uncertainty. A trendline is shown for points $0.1 < \phi < 0.35$ (20-60 droplets), where no layering occurs.

to be avoided in favour of approximated macroscopic methods.

The layering behaviour also effects the local concentration within the flow. Fig. 4.9 shows this effect, whereby in panel b the local concentration of droplets takes on extreme values. The concentration clearly spikes within a layer and is almost zero between layers. These are time averaged values, showing this is a prolonged effect. Macro-scale simulations may rely on the concentration being homogeneous, in which case mesoscopic models should be used to verify this assumption. In other cases, macroscopic simulations may benefit knowing the local droplet concentration as concentration gradients may form a part of the model.

Whilst these simulations have provided validations of the model and results that can connect to the macro-scale, there are issues. The flow within a pipe has varying shear rate through the system, hence exhibits droplet migration. The droplets drift away from the wall, leaving a *depletion zone*, effectively making the centre of the channel more concentrated. The depletion zone is visible in Fig. 4.9a, at both edges of the system the concentration tends toward zero. This is the same behaviour that Javaran et al. note in their simulation of hard particles [66]. Also visible is the alignment effect that the wall has, imposing a structure on the droplets.

Even with the depletion zones and alignment to the wall, the viscosity of a fluid has been measured using such a system as this. Zhou & Pozrikidis [110] and Spencer et al. [74] calculate the viscosity of the fluid using the flow rate, Q:

$$\eta_{\text{rel}} = \frac{\eta_{\text{eff}}}{\eta_0} = \frac{4}{6}\frac{wU_{\max}}{Q}, \tag{4.9}$$

a) $\phi = 0.15$

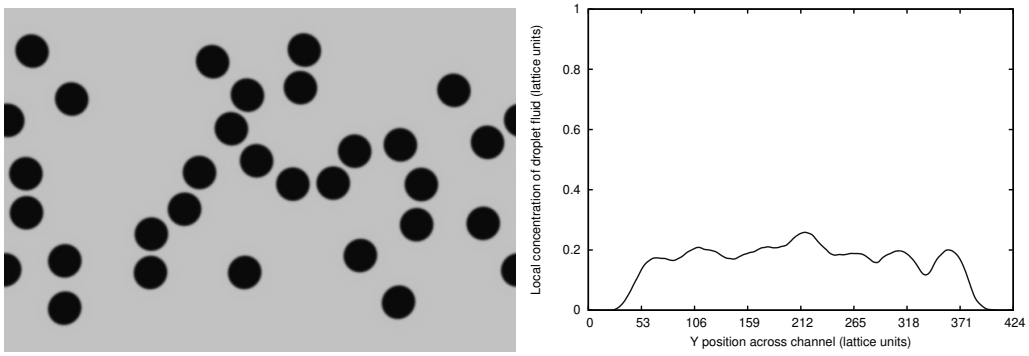

b) $\phi = 0.51$

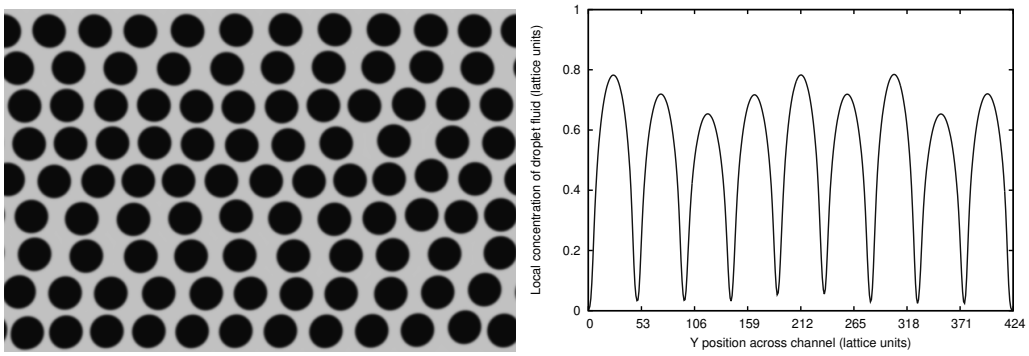

Figure 4.9: Comparisons of the local concentration across the pipe for systems of difference concentrations. Left panels give a snapshot of the system. Right panels show a time averaged local concentration of droplets at a slice across the channel (where a value of 1 indicates that a droplet is always present and a value of 0 indicates that a droplet is never present).

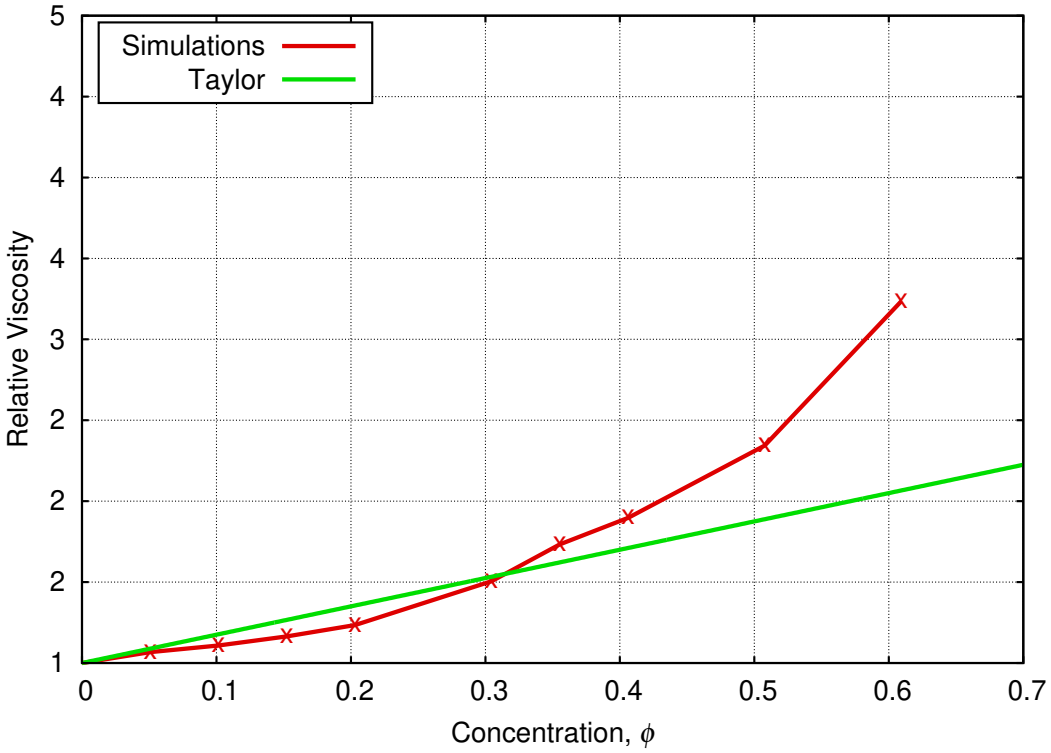

Figure 4.10: Relative viscosity of the emulsion systems, calculated using (4.9). This is compared to the model of Taylor [6].

where $U_{\max}$ is the maximum velocity of the system with no droplets. Applying this equation to the flow rates measured in the data here provides the relative viscosity plot in Fig. 4.10. The model of Taylor [6] (see (2.6) of Section 2.1.2) is plotted along side as a comparison, however this model is known to under-predict the viscosity of concentrated emulsions (in fact it is valid only up to a concentration of $\phi = 0.02$ due to neglecting the interactions between droplets) [29]. Measurements obtained this way are impacted by the conflicting boundary effects, namely: i) an increase in viscosity due to the depletion zones, and ii) a decrease in concentration as the droplets align into layers due to the solid walls.

The applicability of such models may also be limited by the physical scale, restricted due to the ratio of the droplets to the system width. For example, if the droplets are taken to be 2 µm fat globules in milk, the system width is then just over 20 µm, restricting the simulations to microfluidic geometries. Increasing the ratio between the droplet radius and the system width means either using unresolved droplet sizes or increasing the system width. Currently available computational power makes increasing the system size unworkable, but this will of course be possible in the future.

4.3 Conclusion

This chapter started by demonstrating that the LBM outlined in Chapter 3 could be applied to a pipe flow and reproduce the exact analytical solution. Emulsion droplets were introduced into the flow and simulations of hundreds of interacting droplets are shown. The power-law non-Newtonian viscosity model was fit to the resulting velocity profiles. The increasing concentration of the emulsions blunted the velocity profile and power-law fits showed the fluid becoming more shear-thinning until.

For this study a new periodic pressure boundary condition was developed that conserves fluid mass and is not effected by the presence of droplets (i.e. the interaction of the droplet does not send pressure shockwaves through the system, as seen in previous methods). This method also transmits pressure through it undisturbed, meaning that the system is properly periodic. The development and application of this boundary condition was vital to enabling the study of multi-component flow driven by a pressure gradient, as existing methods fail to extend satisfactorily to multi-component flows.

Chapter 5

Bulk flow

The previous chapter shows flow within a pipe, which exhibited severe wall effects, imposing a layered structure on the droplets and creating a depletion zone near the boundaries—increasing the concentration and viscosity closer to the centre of the channel. Having the solid boundaries also restricted the applicability due to the ratio of the droplet size to the channel size fixing the physical scale of the system.

This chapter aims to model the flow of an emulsion without imposing solid boundaries. Removing the solid boundaries remedies both of the aforementioned issues; there will be no walls to impose a layered structure and the physical scale of simulation is not restricted by the size of the simulation domain. Therefore simulations without solid boundaries should provide more meaningful bulk rheological measurements that can be compared to experimental work and measurements from, for example, rheometers. Lees-Edwards [67, 68] boundary conditions are used to impose a shear in a periodic system.

The bulk of the results within this thesis are contained in this chapter; measurements of relative viscosity, sheared self-diffusion coefficient, and average droplet deformation are studied in relation to the droplet concentration, shear rate, viscosity ratio, and interfacial tension. Macroscopic models outlined in Chapter 2 will be compared and fitted to these bulk measurements.

5.1 Boundaries, Initial Conditions, and Validations

To avoid imposing wall effects a bi-periodic system is used. This means droplets can cross the top and bottom boundaries as well as the right and left. Shearing the system can be achieved by using a Lees-Edwards boundary condition (LEBC) [67, 68]. Described in Section 2.2.1, the LEBC imposes a shear by sliding the periodic images above and below in opposite directions. The boundary condition applies a transformation to the distributions on the boundary, then shifts the values by the offset between the periodic images and the reference frame. An added benefit of using

these conditions is the ability to reach arbitrarily high shear rates by introducing more evenly spaced boundaries into the system.

Note, the interpolation used to shift the distribution values was adjusted from a linear interpolation to a third-order interpolation (additionally using the neighbours of the target nodes) for the next validation. This interpolation was then changed to use cubic splines in all future work (as well as previously in Section 3.3.1 and Section 3.3.3) to provide near-perfect mass conservation; this will be described in the following sections.

5.1.1 Transient single-component flow

A possible validation of the LEBC implementation in this LBM is to compare the analytical solution for a single-component flow velocity profile to that of the simulation data. The steady flow itself is very simple, a constant shear rate through the system. Hence, to test the dynamics of the algorithm, the transient solution is used as a validation:

$$U_x(y,t) \;=\; \frac{y}{h} + \sum_{n=1}^{100} \left[\frac{2}{\pi} \frac{(-1)^n}{n} \sin\left(n\pi \frac{y}{h}\right) \exp\left(\frac{-n^2\pi^2 t\eta}{\rho_0 h^2}\right)\right] \tag{5.1}$$

where h is the *height* of the system, y is the position in the system, and t is the timestep. A periodic domain technically has infinite height and width, hence here height refers to the distance between a point and its periodic image. This equation then describes the change from a zero-velocity system to one with a uniform flow profile over time.

Fig. 5.1 shows the velocity profiles from the simulation compared to the analytical solution for selected timesteps. The system was 10 nodes wide by 40 nodes tall. The fluid had a viscosity of $\frac{1}{6}$ lu, hence $\tau_s = 1.0$. The fluid density $\rho_0 = 1.0$ lu. The solution with the sum to 100 was found to have converged, with the errors showing negligible change when trying a sum to 1000. The measured data compares well, with relative percentage errors of $< 2\%$ in almost all cases, as shown in Fig. 5.2. At the very earliest of timesteps the error is much larger, sometimes up to 100%, which can be explained in two ways: firstly, after 9 timesteps, the numerical method will have only propagated the effect of the boundary velocity by 9 nodes, whereas the analytical solution shows miniscule velocities over a much wider reach. This means the measured velocities can be zero, where the analytical method has a finite velocity, hence 100% error. Secondly, the analytical velocities are very small (as low as 10^{-8}) at points with high relative error, which obviously inflates the relative error. The overall measured velocity profiles match the analytical profiles very well, even at the short timescales. This transient validation is important because the introduction of droplets will prevent a truly steady state solution; the droplets will disrupt the flow in the system, even near the boundary.

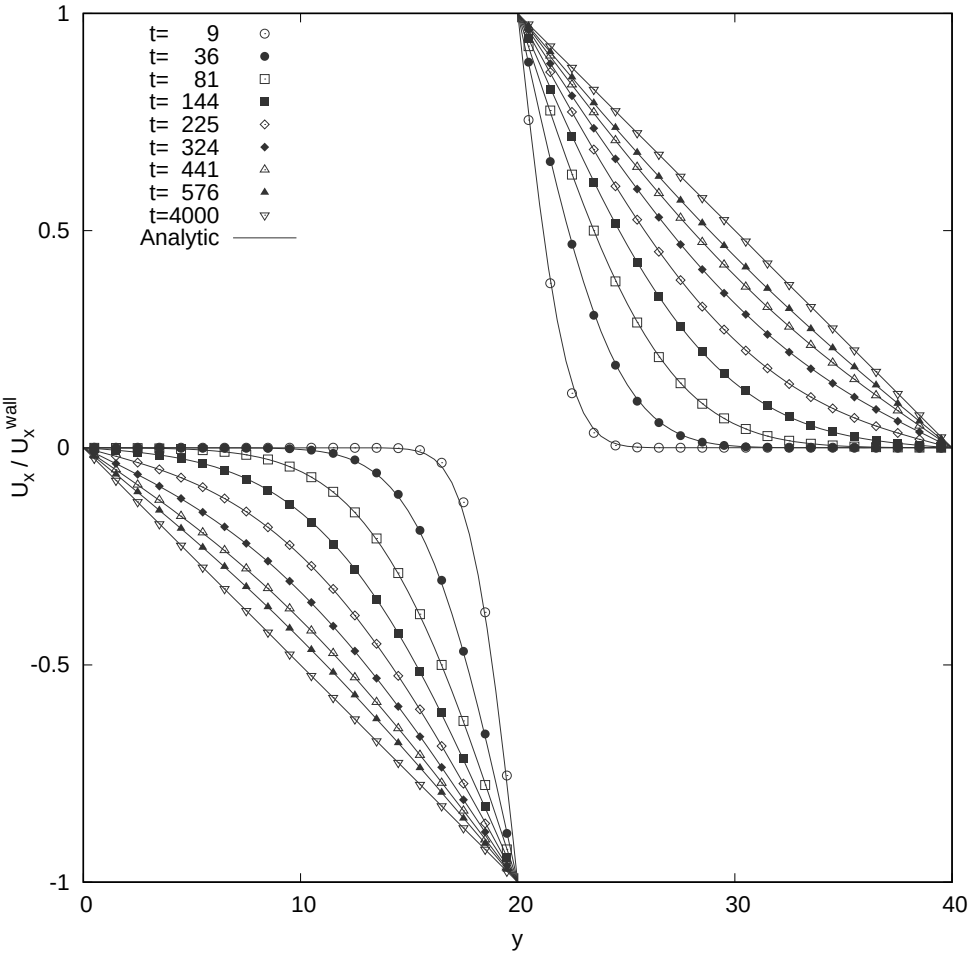

Figure 5.1: A validation of the LEBC comparing the analytical transient solution (solid lines) to the measured velocity profiles (points). The boundary is located at $y = 20$. The flow starts from rest at $t = 0$. See Fig. 5.2 for relative percentage error.

5.1.2 Multi-component Lees-Edwards boundary condition

The LEBC must now be adapted to interact with the multi-component flow. Both steps of the LE algorithm, the transformation and the shift, must be adjusted. Now, rather than the overall distribution function, f_i, the boundary interacts with the post-collision post-segregation fluid distributions $\mathrm{la}_i^{(l)}$. Note that this algorithm disconnects the lattices from the physical fluids (see Section 3.2). The Galilean transform is then applied to the lattices on the boundary, in the form:

$$\mathrm{la}_i'^{(l)} \;=\; \mathrm{la}_i^{(l)} + \frac{\rho^{(\mathrm{fluid}(l))}}{\rho}\left(f_i^{(\mathrm{eq})}(\mathbf{u} - \mathbf{U}c_{iy}) - f_i^{(\mathrm{eq})}(\mathbf{u})\right), \tag{5.2}$$

where c_{iy} acts to correct the sign based on the boundary direction, and $\frac{\rho^{(\mathrm{fluid}(l))}}{\rho}$ spreads the transformation across the lattices proportional to the local concentration. As $\sum_l \frac{\rho^{(\mathrm{fluid}(l))}}{\rho} \;=\; 1$, the full transformation will be applied across the present lattices.

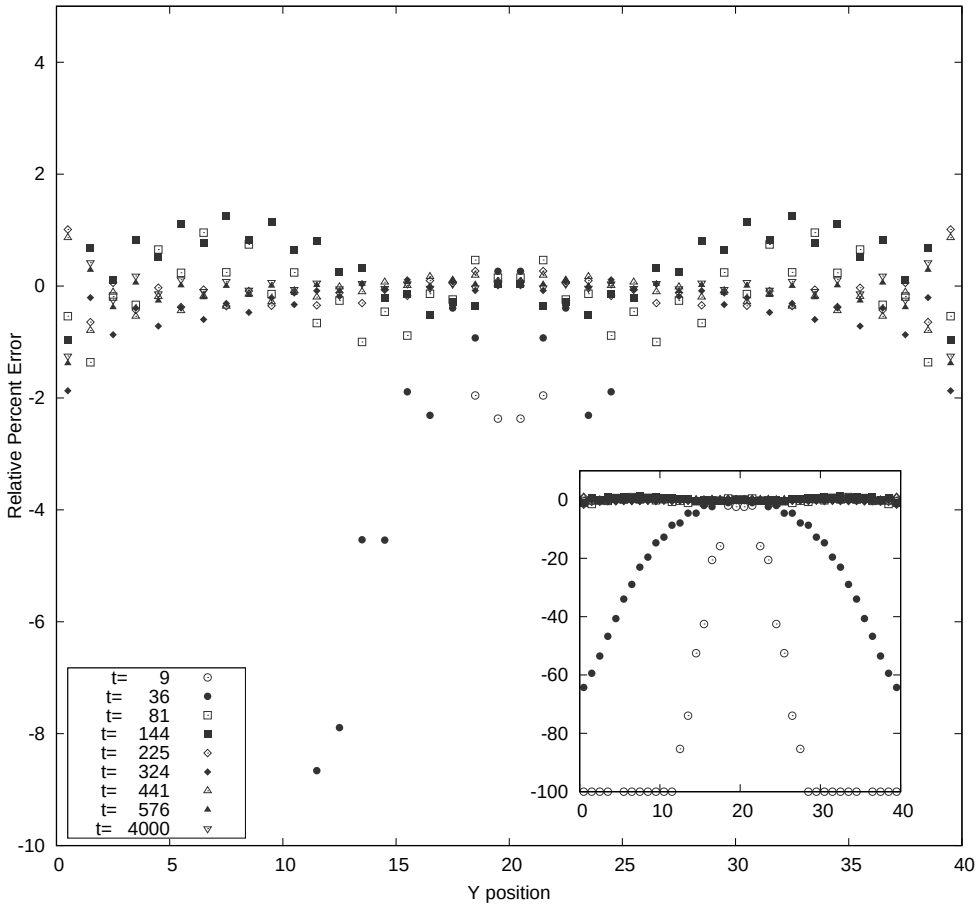

Figure 5.2: The relative percentage error of the validation against the analytical transient solution. Main figure shows a zoomed in y axis to be able to see the errors that occur later on in more detail. Inset shows the full picture of the errors, including at the very short timescale where the relative percentage error is higher.

The second step of the LE boundary condition, the shift, must also be applied to the fluid lattices. This is a straight forward extension, considering just the upwards travelling distributions in a linear interpolation:

$$\mathrm{la}_i'^{(l)}(\mathbf{x},t) \;=\; \left(1-d_x^R\right)\mathrm{la}_i'^{(l)}\left(\mathbf{x}+d_x^I,t\right)+d_x^R\mathrm{la}_i'^{(l)}\left(\mathbf{x}+d_x^I+1,t\right)\,. \tag{5.3}$$

Note that this equation assumes the same fluids are on the same lattices across different nodes, which is not always the case in this model, hence the applied method must ensure to identify matching fluids and use zero values for absent fluids. This simple extension will apply the shift to the multi-component lattices, however it will not conserve mass and will disturb the droplet interface shape. The following sections describe this problem, and the solution, in more detail.

5.1.3 Bisecting Drop

Similarly to the work of Javaran et al. [69], the linear interpolation when shifting the distribution values proved insufficient to handle a droplet interacting with the boundary. Fig. 5.3 shows the problem introduced by the linear interpolation in

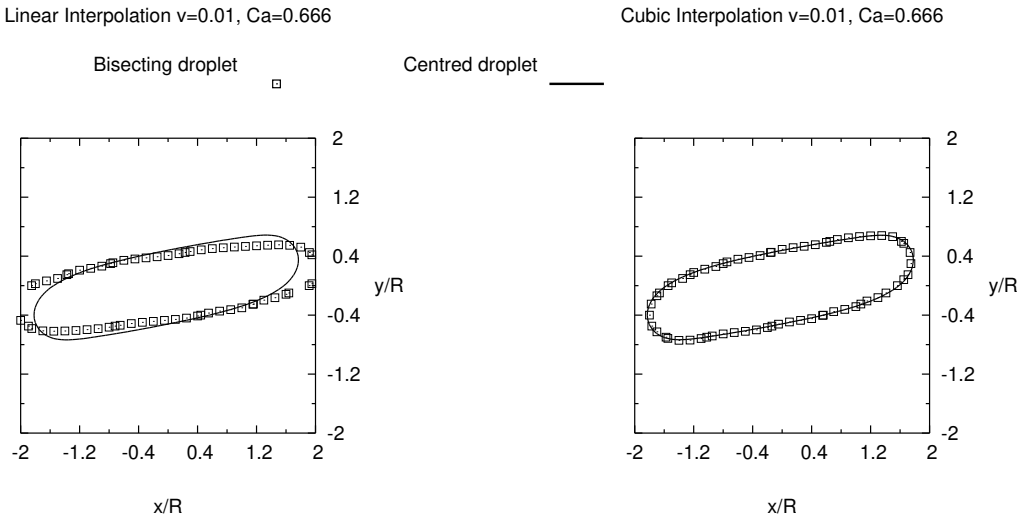

Figure 5.3: A comparison of the droplet interface (defined by $\rho^N = 0$) when the droplet is away from the boundary (solid lines) against when the droplet is bisecting the boundary (boxes). The system in the left panel uses linear interpolation whilst the system in the right panel uses a cubic spline interpolation. The maximum velocity of the system is 0.01 lattice units and the Capillary number is $\frac{2}{3}$. The simulations were run until a pseudo-steady state in which the droplet shape was no longer changing.

the left panel. Of course, being periodic means the boundary site itself should not influence the flow, hence there should be no difference between the two droplet interface positions. The whole system should have the same shear rate (ignoring the effect of the droplet itself), so the droplet interface should deform uniformly. This is a major concern as it is expected that in concentrated systems there will be droplets near (or on) a boundary almost all the time—particularly when considering the multi-plane implementation where there may be several boundary areas within the system.

5.1.4 Cubic spline interpolation implementation

To remedy this, a third order interpolation was used along the boundary nodes (only in Section 5.1.1), however this was then improved to a cubic spline interpolation. Cubic splines are required for each lattice link and each fluid on each of the Lees-Edwards boundaries. In this implementation the GNU Scientific Library (GSL) [111] was used to generate and interpolate using cubic splines. Third order polynomials are constructed, piecewise, between each lattice point. GSL takes the lattice values,

as mentioned above, and can evaluate the value anywhere along the cubic spline, hence the value at the shifted position is retrieved.

The effect of this higher order interpolation is apparent in the right panel of Fig. 5.3. The droplet interface is no longer effected by bisecting the boundary, hence the boundary is invisible to the flow and the system is fully periodic. Similarly, the loss of mass, as established in Section 3.4.1, is negligible.

5.1.5 Finite-size effects

A consideration before proceeding with emulsion simulations is to ensure the system is large enough to avoid finite-size effects. That is, because the system is fully periodic, the droplets may interact with their periodic images and the behaviour will be skewed. Additionally, the number of droplets within the system must be large enough to obtain a sufficient average. To ensure the independence of the droplet interactions, the self-diffusion coefficient was measured in a set of increasingly large simulations until sufficient convergence was achieved. The effective viscosity of the systems was also measured, but found to be far less susceptible to finite-size issues than the sheared self-diffusion coefficient (except in the smallest of cases). Fig. 5.4

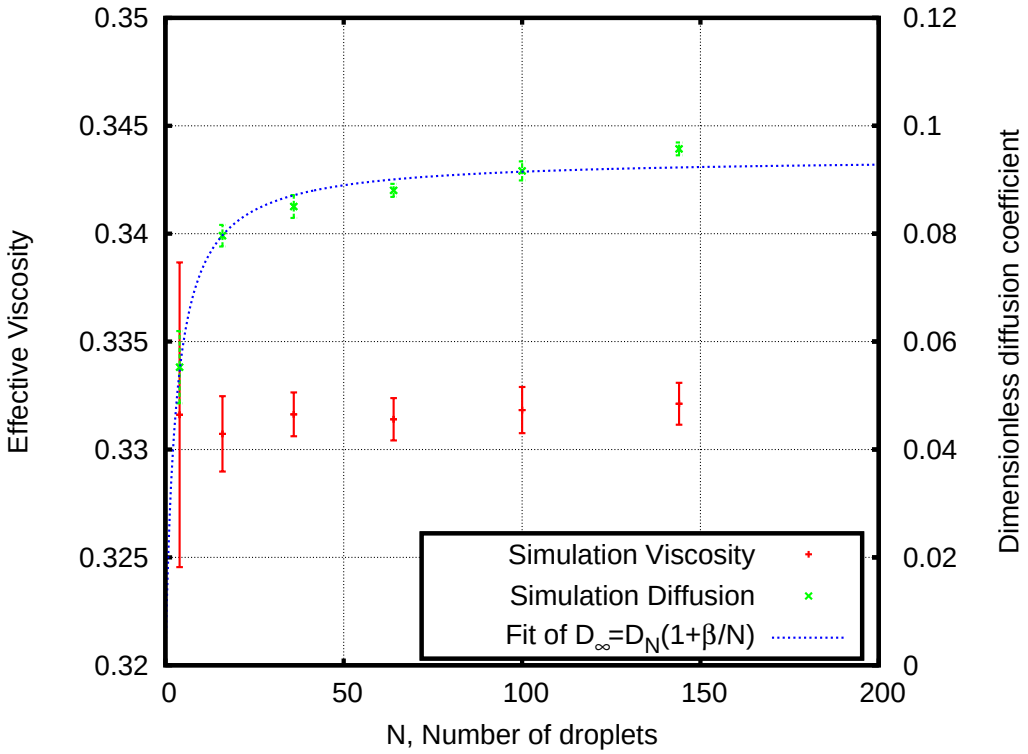

Figure 5.4: The result of a set of simulations to find the optimal system size that lessens the impacts of finite-size effects whilst remaining computationally achievable. The systems were parametrised as: $\sigma_0 = 0.09, \phi = 0.33$, viscosity ratio $\frac{\eta_1}{\eta_0} = K = 1.0$, $\mathrm{Re} = 5.1 \times 10^{-1}$, $\mathrm{Ca} = 7.6 \times 10^{-3}$.

shows the effect of increasing the system size and the number of droplets (whilst

keeping the droplets the same size—this resolved size was determined in Chapter 4) on the effective viscosity and sheared self-diffusion coefficient. All dimensionless parameters were kept constant (Reynolds number, concentration, etc.). As the system is fully periodic, an increase in the system size only requires an adjustment to the LEBC velocity (to impose the same shear rate) and an increase in the number of droplets (to keep a fixed concentration).

The effective viscosity measurements are relatively unaffected by the number of droplets or system size, that is once a sensible minimum is reached (more than 10 droplets). The sheared self-diffusion coefficient is more sensitive and, as seen in previous work on suspensions [51, 112], continues changing above 100 droplets. This continued change is relatively small: 8% from 64 droplets to 144 droplets. Due to available computational resources and time constraints, systems of size 512x512 lattice nodes (that is N=64 in Fig. 5.4) are used in this thesis. In the simulations to follow the value of N will vary in order to simulate systems of varying concentration.

The small, continued rise in the sheared self-diffusion coefficient is attempted to be accounted for by adjusting the obtained values using the equation fit in Fig. 5.4, consistent with the works of Kromkamp et al. [112] and Sierou et al. [51]:

$$D_\infty = D_N \left(1 + \frac{\beta}{N}\right) , \tag{5.4}$$

where D_∞ is the value with infinite droplets, D_N is the value obtained using N droplets, and β is a free parameter. The fitting parameters are $D_\infty = 0.0941$ and $\beta = 2.90$. The reported sheared self-diffusion coefficient values reported here are then D_∞ of (5.4), using the measured D_N and fit β.

5.1.6 Mass

A final check that was already detailed in Section 3.4 is to ensure mass conservation. As mentioned, this check used the LEBC (with cubic spline interpolation) outlined here, which verified that mass is being conserved by the algorithm.

5.2 Results

The model has been shown to reproduce the correct analytical transient flow behaviour, conserve mass, and have minimal finite-size effects. It has also been shown that the droplets can bisect the LEBC planes with no impact on themselves or the flow.

Data can now be gathered, with confidence, for a variety of phase spaces. The system is set up as follows:

- 512 by 512 node lattice.

- Droplets of area 1369 lattice units (lu), radius $R = 20.88$ lu, distributed randomly. Keeping the system monodisperse to limit the phase space.
- Varying numbers of droplets providing a variable **concentration**, ϕ.
- All fluid densities $\rho_0 = 1.0$.
- Viscosity of the background fluid, $\eta_0 = \frac{1}{6}$ lu, $\tau_0 = 1.0$.
- Viscosity of the droplet fluids, $\frac{1}{12} \leq \eta_1 \leq \frac{100}{6}$ lu, is varied to provide a variable **viscosity ratio**, $0.5 \leq K \leq 100$.
- Interface segregation parameter, $\beta = 0.65$.
- Interfacial tension parameter droplet to background, $0.03 \leq \sigma_0 \leq 0.09$ lu, is varied to adjust the **Capillary number**.
- Interfacial tension parameter droplet to droplet, $\sigma_1 = 10 \times \sigma_0$.
- Negligible fluid concentration threshold value, $\frac{\rho^{(k)}}{\rho} \leq 1 \times 10^{-9}$.
- The imposed velocity of the LEBC, $0.001 \leq U_{\text{LE}} \leq 0.48$ lu, is varied to provide a variable **Reynolds number** (via the shear rate). Note this velocity may be split over several LEBC planes to restrict the maximum nodal fluid velocity in the system.

The dimensionless numbers are defined as:

$$\text{Re} = \frac{\text{Inertial forces}}{\text{Viscous forces}} = \frac{\rho_0 \dot{\gamma} R^2}{\eta_0}, \tag{5.5}$$

$$\text{Ca} = \frac{\text{Viscous forces}}{\text{Interfacial forces}} = \frac{\eta_0 \dot{\gamma} R}{\sigma_0}. \tag{5.6}$$

The Capillary number will also vary with the shear rate, $\dot{\gamma}$, but adjusting the interfacial tension will allow for tweaking the Capillary number whilst keeping the Reynolds number constant. Where possible, results will be shown using these dimensionless numbers.

From this model, macroscopic material properties can be measured, free from boundary effects, i.e. effective fluid viscosity and sheared self-diffusion coefficient. Being in a bi-periodic, sheared system, the viscosity is related to the bulk shear stress [43] as:

$$\eta_{\text{eff}} = \frac{\bar{\sigma}_{xy}(\mathbf{x})}{\dot{\gamma}}, \tag{5.7}$$

where $\bar{\sigma}_{xy}(\mathbf{x})$ is the mean of the xy component of bulk stress throughout the system [13]:

$$\bar{\sigma}_{\alpha\beta}(\mathbf{x}) = \frac{1}{X} \sum_{\mathbf{x}} \sigma_{\alpha\beta}(\mathbf{x}), \tag{5.8}$$

where X is the number of nodes summed over. This bulk stress must include contributions of the component interfaces [43], hence it is of the form:

$$\sigma_{\alpha\beta} = -p\delta_{\alpha\beta} + 2\eta_0 D_{\alpha\beta} + \sigma^I_{\alpha\beta}\,, \tag{5.9}$$

where p is the pressure, $D_{\alpha\beta}$ is the rate of deformation tensor, and $\sigma^I_{\alpha\beta}$ is the interfacial stress. In the present model, these terms are expressed as:

$$D_{\alpha\beta} = \frac{1}{2}\left(\partial_\alpha u_\beta + \partial_\beta u_\alpha\right) = \frac{-1}{2\rho_0 c_s^2 \tau \Delta t}\sum_i \left(f_i - f_i^0\right) c_{i\alpha} c_{i\beta}\,, \tag{5.10}$$

$$\sigma^I_{\alpha\beta} = -\Delta t \sum_{m,m\neq n} 2\beta^{mn}\sigma^{mn}\frac{\rho^{(m)}\rho^{(n)}}{\rho^2}\left(\hat{n}^{mn}_\alpha \hat{n}^{mn}_\beta - \delta_{\alpha\beta}\right)\,. \tag{5.11}$$

Hence, the stress can be calculated as:

$$\sigma_{\alpha\beta} \;=\; -\rho c_s^2\delta_{\alpha\beta} - \left(1 - \frac{1}{2\tau_s}\right)\left[\sum_i \left(f_i - f_i^{(\mathrm{eq})}\right) c_{i\alpha}c_{i\beta} + \frac{\tau_s \Delta t}{2\tau_s - 1}\sum_i F_i c_{i\alpha} c_{i\beta}\right]\,, \tag{5.12}$$

including both viscous stresses and interfacial stresses. The relaxation parameter, τ_s, will need to be interpolated through a fluid-fluid interface, as described in Section 3.3.

The relative viscosity, η_r, is the ratio of the effective viscosity to the suspending fluid viscosity: $\eta_\mathrm{r} = \frac{\eta_\mathrm{eff}}{\eta_0}$.

The sheared self-diffusion coefficient can be obtained from the displacement of the droplets in the velocity gradient direction. These displacements are due only to the droplet interactions (i.e. hydrodynamics). Measuring the mean-squared displacement:

$$\zeta \;=\; \frac{\sum_m \left[C_y^{(m)}(t) - C_y^{(m)}(t - \Delta t)\right]^2}{M}\,, \tag{5.13}$$

where $C_y^{(m)}(t)$ is the centre of mass of droplet m at time t in the y axis (the velocity gradient direction), Δt is the timestep interval between measurements (in the range of 50–1000 timesteps in this data), and M is the number of droplets. The sheared self-diffusion coefficient in lattice units is then [112]:

$$D \;=\; \frac{\zeta}{2\Delta t R^2 \dot{\gamma}}\,. \tag{5.14}$$

Then the non-dimensional sheared self-diffusion coefficient is:

$$\hat{D} \;=\; \frac{D}{\Delta t \dot{\gamma}}\,. \tag{5.15}$$

Another property that may be of interest is the average deformation of the droplets in the flow. This can be obtained using the eigenvalues of the inertia

tensor. Firstly, the inertia tensor of fluid m:

$$I_{\alpha\beta}^{(m)} = -\sum_{\mathbf{x}} \frac{\rho^{(m)}}{\rho} \left[\left(x_\alpha - C_\alpha^{(m)} \right) \left(x_\beta - C_\beta^{(m)} \right) - \left(x_\gamma - C_\gamma^{(m)} \right) \left(x_\gamma - C_\gamma^{(m)} \right) \delta_{\alpha\beta} \right] , \tag{5.16}$$

i.e. perform the above calculation over all nodes in the system (or nodes with non-negligible mass of fluid m) with $x_\alpha - C_\alpha^{(m)}$ being the distance in the direction α between the node and the centre of mass (see below) of fluid (droplet) m. The deformation parameter of fluid m, then, is calculated using the eigenvalues, ϵ_1 and ϵ_2, of $I_{\alpha\beta}^{(m)}$:

$$\mathrm{Def}^{(m)} = \frac{\epsilon_1 - \epsilon_2}{\epsilon_1 + \epsilon_2} , \text{where } \epsilon_1 > \epsilon_2 . \tag{5.17}$$

The mean deformation parameter of all droplets then provides an average deformation, Def , in the system. Again, GSL [111] was used to efficiently calculate the eigenvalues.

The calculation of the centre of mass of a droplet within this bi-periodic system is no longer straightforward. Half of a droplet can be present on the bottom of the system with the other half at the top, a simple algorithm for the centre of mass would place it right in the centre of the system rather than on the boundary. To add to the complexity, the regions between Lees-Edwards boundaries have physical locations that are detached from the computational nodes (node $\mathbf{x}$ may not be physically interacting with node $\mathbf{x} + 1$ due to the system displacements).

The latter issue can be resolved by shifting each *slice* of the system by the LE displacement when required for any calculations. Appendix B describes this solution within the context of creating a continuous system snapshot (rather than a snapshot with LE discontinuities). Given that the slices are shifted in such a way, the new coordinates can be used for calculations. The issue of periodicity still remains, but a correct centre of mass can be calculated by transforming the coordinates onto a circle [113]. Firstly then, the angle:

$$\theta_\alpha = \frac{x_\alpha}{W_\alpha} 2\pi ,$$

where α is either direction x or y, and W_α is the system dimension in direction α. Using this angle, the coordinates on a unit circle are:

$$\begin{aligned} a_\alpha &= \cos\theta_\alpha , \\ b_\alpha &= \sin\theta_\alpha . \end{aligned}$$

The centre of mass of droplet k in this new coordinate system is then calculated

from a weighted sum throughout the domain:

$$\begin{aligned} a_\alpha^{(k)} &= \sum_{\mathbf{x}} \frac{\rho^{(k)}}{\rho} a_\alpha \,, \\ b_\alpha^{(k)} &= \sum_{\mathbf{x}} \frac{\rho^{(k)}}{\rho} b_\alpha \,. \end{aligned}$$

These coordinates can then be transformed back into an angle in the original coordinate system:

$$\bar{\theta}_\alpha = \operatorname{atan2}\left(-b_\alpha^{(k)}, -a_\alpha^{(k)}\right) + \pi \,,$$

where atan2 provides the angle between the x-axis and the point $\left(-b_\alpha^{(k)}, -a_\alpha^{(k)}\right)$ within the interval $(-\pi, \pi]$. The angle for the centre of mass then provides the coordinates for the centre of mass:

$$C_\alpha^{(m)} = \frac{W_\alpha \bar{\theta}_\alpha}{2\pi} \,.$$

Hence, the centre of mass calculation is now able to cope with both the periodicity of the system and the shifting slices due to the LE boundaries. These coordinates will point to the centre of mass no matter if a droplet straddles a boundary or even a corner of the periodic system.

A final complication is that a droplet can cross the periodic boundaries, therefore the centre of mass can go from $W_\alpha - 1$ to 1 (for example) within a few timesteps, assuming that the coordinates are adjusted to fit within the system dimensions. This will cause discontinuities in the centre of mass data, which is intended to be used to measure the sheared self-diffusion coefficient. Such data should then be continuous in order to obtain an accurate measurement, else the sheared self-diffusion coefficient will be overestimated. The algorithm should therefore check whether the droplet position has changed by more than $\frac{W_\alpha}{2}$ (assuming that a droplet cannot physically move this far between measurements) and adjust the coordinate by incrementing by W_α.

All of these measurements can change over time, whether that be as the system progresses to a pseudo-steady state or small fluctuations even whilst pseudo-steady. Time averages of these measures are therefore undertaken. The deformation parameter is a time average of an average of many droplet deformations, which makes it quite a stable measurement. The other two parameters, the viscosity and the sheared self-diffusion coefficient, are less stable and may depend on the initial condition of the system. Kromkamp et al. [112] note that hard-sphere suspensions need a strain of $\dot{\gamma}t = 8$ to pass through a transitional period and achieve a stable mean-squared displacement. This transitional strain appears to be the same in these emulsion simulations.

Periodically during the time averaging, the value is stored and the time averaging

begins anew from the current timestep, effectively providing time averages from many initial configurations from a single simulation [51]. The time interval between restarting the time averaging process was set to 1.5×10^6 timesteps, which equates to a range of strains of $3 \leq \dot{\gamma}t \leq 1406$, depending on the shear rate of the system. The lower end of this strain interval is low compared to the transitional period and the strain of 30 that Kromkamp et al. [112] use, however the collection of many of these periods helps stabilise the value. For the low shear rate system it wasn't possible to lengthen the simulations due to the available computational resources and time requirements.

Note: Throughout these results there will be citations linking to animations of the systems. These videos are produced by using simulation snapshots as frames of a video. The snapshots themselves are based on the local droplet fluid concentration, where red (or light grey) represents the suspending fluid and blue (or dark grey) represents the suspended droplet fluid. Animations of systems that exhibit behaviours of particular interest will be cited in the text, but links to many more simulation animations (and more detail of their production) can be found in Appendix B. The Digital Object Identifier (DOI) links should provide a page on figshare.com where the animations can be watched or downloaded.

5.2.1 Concentration Dependence

Starting with a fixed interfacial tension parameter ($\sigma_0 = 0.09$ lu) and viscosity ratio of 1, Fig. 5.5 shows the relative viscosity of the simulations as a function of the droplet concentration. There is a clear increase in relative viscosity as the concentration increases, more pronounced in the lower Reynolds number systems. This is to be expected as there are increased contributions from the interfacial stresses (see (5.12)) as the concentration increases; there is also an increase in interfacial stresses due to the increased frequency of droplets moving past each other.

Comparisons to macroscopic models and experimental results are also visible in Fig. 5.5; although the models and experiments are three dimensional the trends agree very well with the two dimensional simulation data (particularly when looking at the lower Reynolds number results). As discussed in Section 2.1, these macroscopic models assume a creeping flow, i.e. low Reynolds number, hence the agreement with the models decreases as the Reynolds number of the simulation increases. The experimental results of Pal also show the same trend, and again this was a low Reynolds number flow.

These results differ, as expected, with those from Chapter 4, as seen in Fig. 5.6. The pipe flow viscosity measurements are clearly reduced due to the alignment of the droplets. Removing the solid walls has provided viscosity measurements much more in line with the predictions of macroscopic models than the previous experiments. The Reynolds and Capillary numbers are not directly comparable between the two

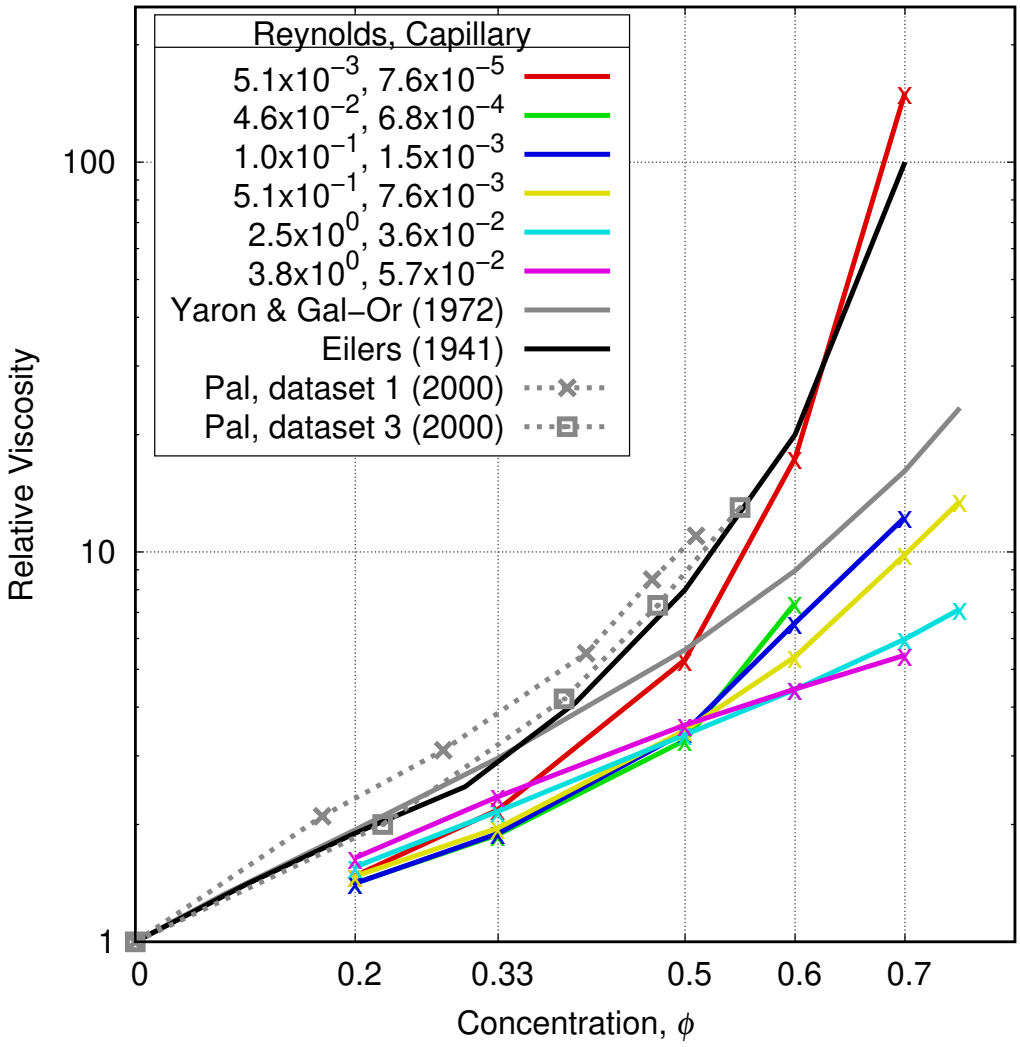

Figure 5.5: A graph of relative viscosity against concentration, each line has a constant Reynolds and Capillary number. Points are results from simulation systems, with connecting lines as a guide to the eye. The solid lines are macroscopic models [7, 23]. Dotted lines are the experimental results of Pal [28]. The simulation results follow the trends of previous models and experiments, especially the lower Reynolds number flows. Lines between experimental results are just as a guide to the eye.

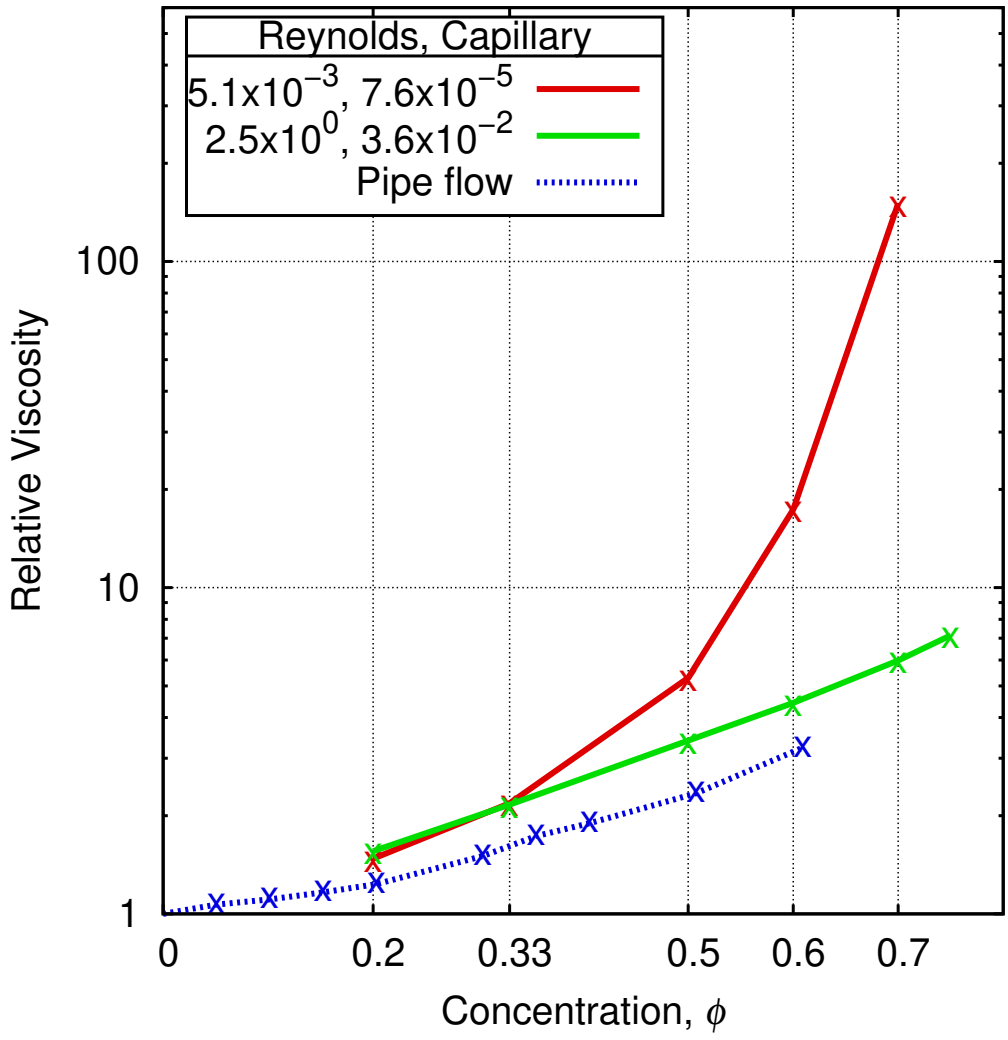

Figure 5.6: A graph of the relative viscosity against concentration, comparing bulk measurements to those taken in the pipe flow from Chapter 4. The bulk measurements show a greatly increased viscosity, indicating that the alignment forced upon the droplets by the solid walls had a large impact on the measurements.

types of systems due to the pipe flow not having a fixed shear rate. However, even if considering the high Reynolds number bulk measurements, the pipe flow results underpredict the viscosity. This throws into question the applicability of measurements obtained this way as they will be highly specific to the geometry [110, 109].

Fig. 5.7 show the sheared self-diffusion coefficient of the same systems as above as a function of the concentration. The trends are similar to the relative viscosity,

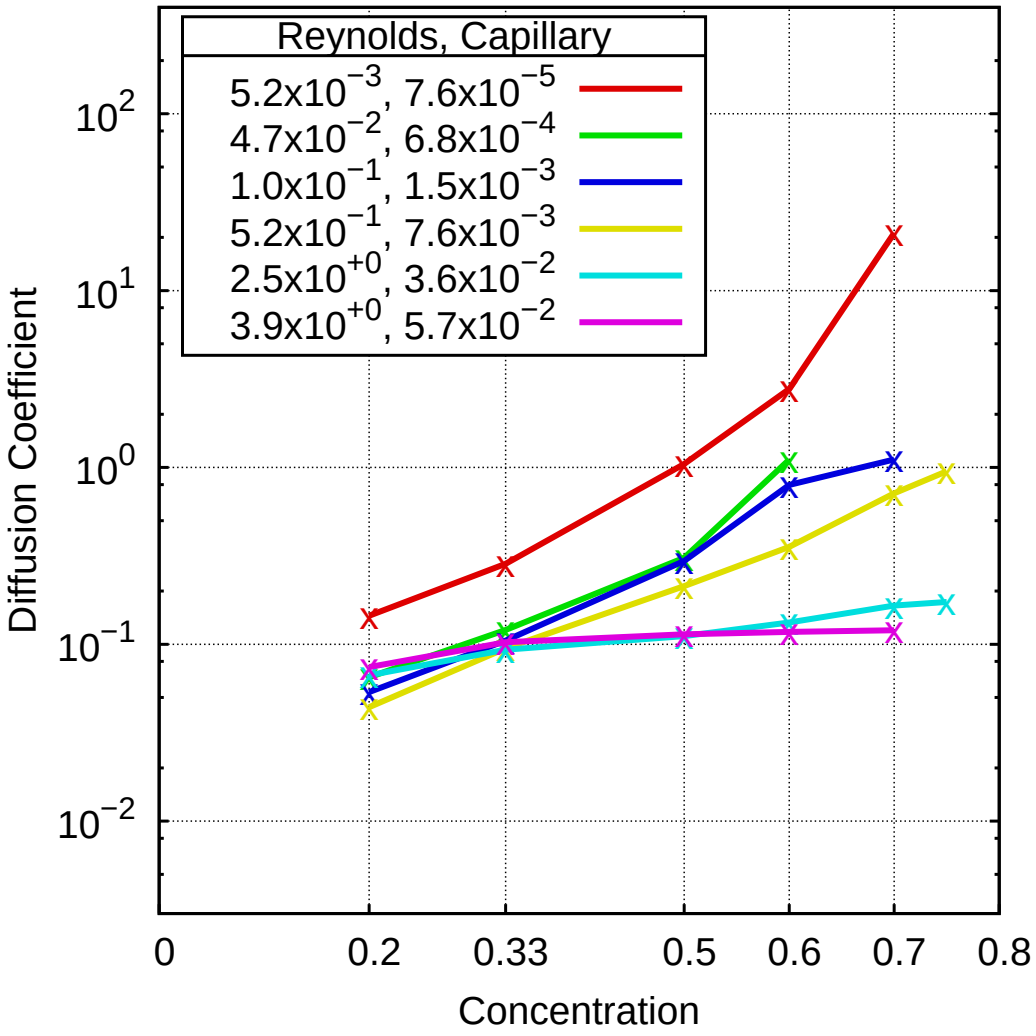

Figure 5.7: A graph of the sheared self-diffusion coefficient against concentration, each line has a constant Reynolds and Capillary number. There is an upwards trend, however a higher shear rate means the effect becomes less prominent. Lines are just as a guide to the eye.

where increasing the concentration increases the sheared self-diffusion coefficient. More droplets in the flow means there are likely to be more interactions between droplets and they will have to move around each other more often.

At the higher Reynolds number end of the simulations, the sheared self-diffusion coefficient becomes almost constant with changing concentration. This is likely to be due to two effects: the high shear makes the droplets align in layers in the

flow, removing the need for them to move around each other, and the shear makes them more deformable, which will reduce the distance they need to move around each other. The former option is less likely here as fully aligned systems have been removed from the displayed data (hence the incomplete data lines). Both the relative viscosity and sheared self-diffusion coefficient of these aligned systems dropped drastically, more so than visible anywhere in Figs. 5.5–5.12. Such systems will be discussed in Section 6.1.1. The second is more likely the cause in these results, and will be discussed when looking at the results' shear dependence soon.

A physical explanation of why the high shear systems overlap the lower shear systems in the low concentration regime is unclear.

The deformation parameter of these systems is shown in Fig. 5.8. Again, in-

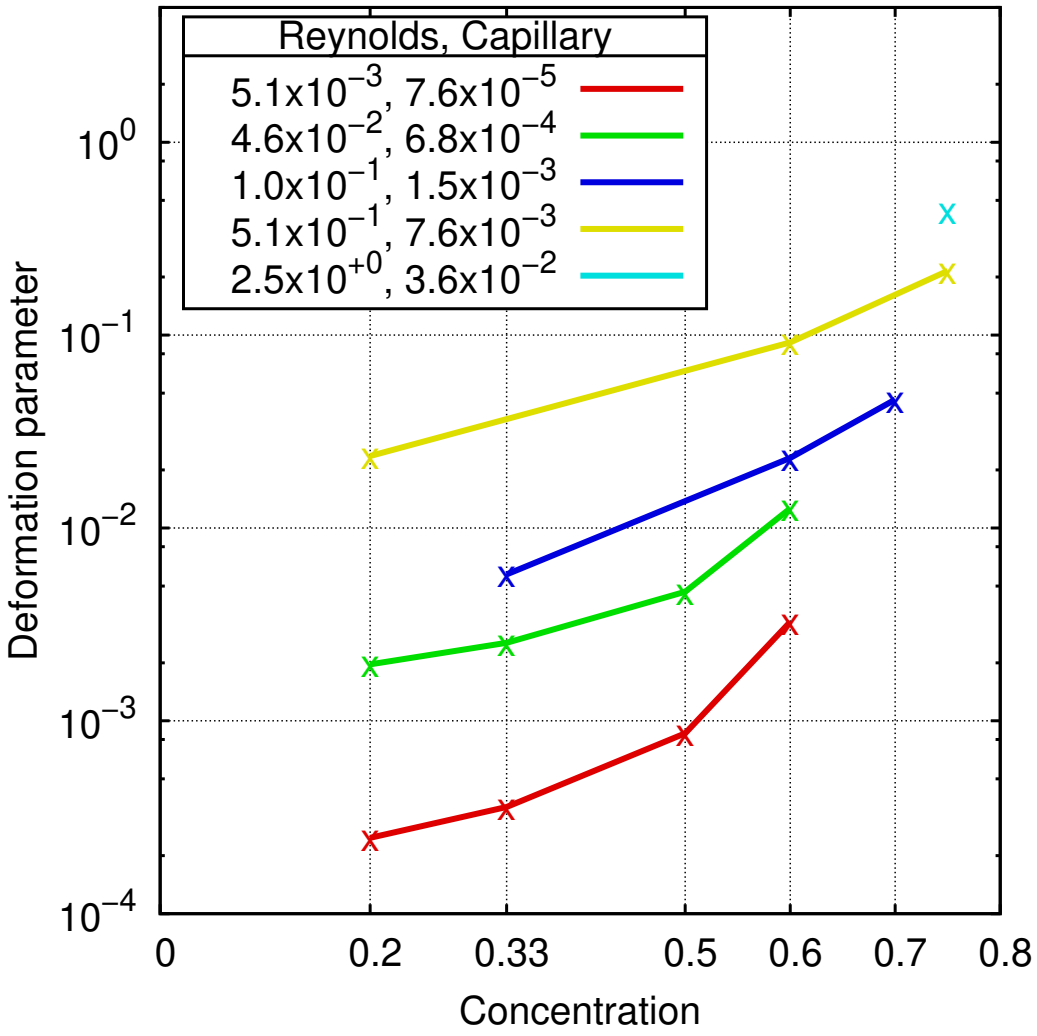

Figure 5.8: A graph of deformation parameter against concentration, each line has a constant Reynolds and Capillary number. There is an upwards trend, higher shear rates even make this change more pronounced. Lines are just as a guide to the eye.

creasing the concentration increases the average deformation in the system. The droplet-droplet interactions deform the droplets, hence more interactions will result in a greater average deformation. It is also clear that increasing the shear rate will

increase the deformation, which will be discussed soon. As with the relative viscosity and sheared self-diffusion coefficient, the increasing shear rate reduces the impact of the concentration. An increased shear rate will raise the number of droplet interactions, which will also increase with a higher concentration; these two effects appear to compound.

Note that data around the deformation parameter of the droplets was not gathered in the earliest versions of the programmed simulations. Hence, there may be more incomplete lines in the figures demonstrating deformation data than figures displaying other data.

5.2.2 Shear Dependence

The shear dependence (via the Reynolds number) of the relative viscosity is displayed in Fig. 5.9. There is clear shear thinning behaviour, whereby an increase in the shear rate (hence Reynolds and Capillary numbers) results in a less viscous fluid. This effect becomes more prominent at higher droplet concentrations. The droplets become more deformable at higher shear rates, hence they flow more easily (i.e. lower viscosity).

As mentioned in Section 2.1.3, shear thinning behaviour is an avid topic for macroscopic modelling. The viscosity can drop by orders of magnitude, so predicting this allows for a clearer understanding of manufacturing requirements (i.e. how powerful does a pump need to be to force the fluid at a specific flow rate?). Section 2.1.3 outlines various models that aim to capture this shear thinning behaviour, i.e. the behaviour visible in Fig. 5.9. It is possible to fit these models against this data to see which, if any, accurately reproduce the trends and may be appropriate to use in further macroscopic studies.

Using the relative viscosity data visible in Fig. 5.9, i.e. $\sigma_0 = 0.09$ and $K = 1$, a least-squares fitting algorithm adjusted the model parameters to find the best fit for the 5 different concentrations over the range of shear rates. The average R^2 values of these 5 fits is provided in Fig. 5.10. The Carreau and Cross models (see (2.16) and (2.15)) are clearly the best fitting models for this data. These models in particular have an infinite-shear plateau, which the data is quite close to reaching. The yield stress of the fluid and the zero-shear limit, on the other hand, are not displayed in the simulation data. These are key concepts of the Herschel-Bulkley and Casson models (see (2.12) and (2.14)), which explains their less accurate fit when the range of data lies outside this region. Without modelling the infinite-shear viscosity limit, the Herschel-Bulkley and Casson models are far less appropriate for data in this range as they cannot reproduce the visible curve in the data. The power-law model does not account for Newtonian behaviour at either limit, hence the fit is unable to reproduce the required curve to fit the data. Interestingly, the Herschel-Bulkley and Casson models are far superior to the power-

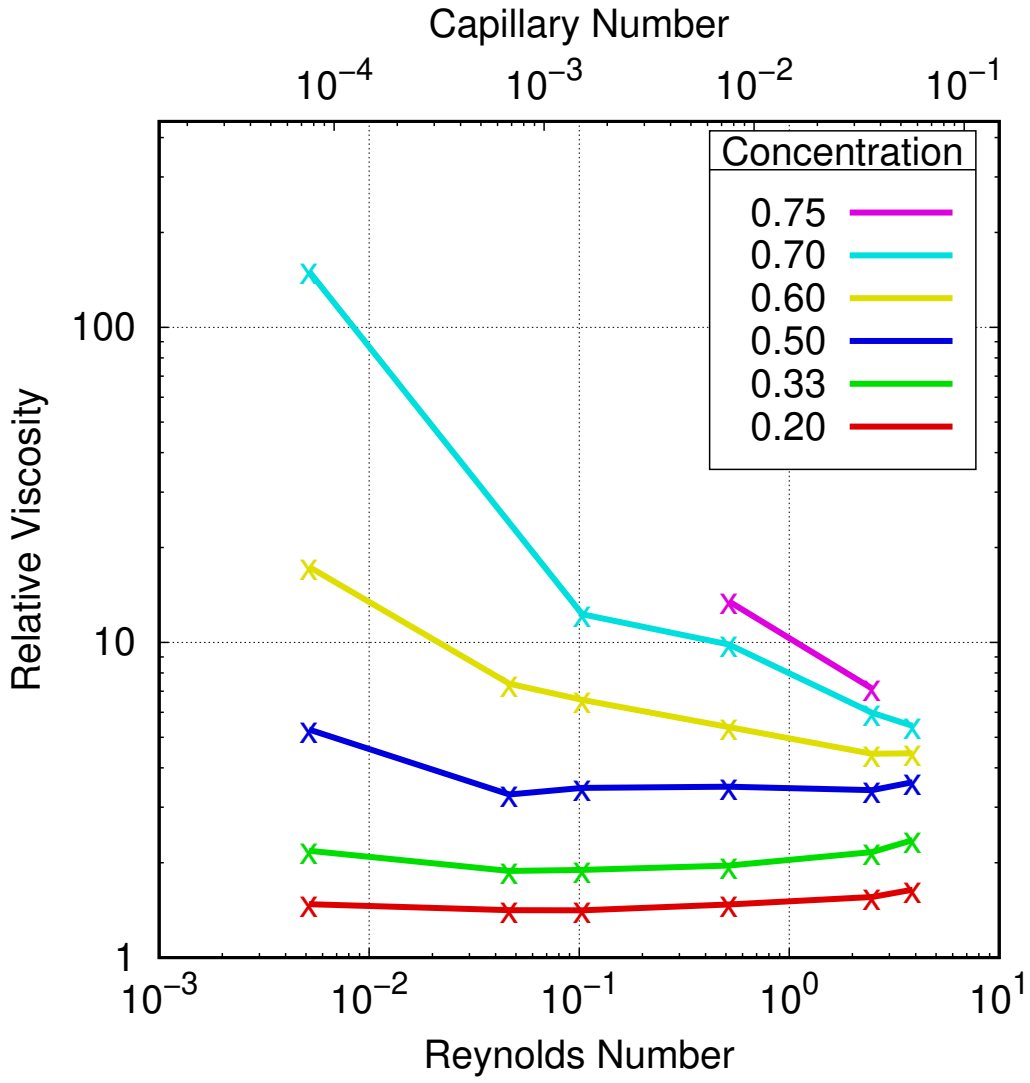

Figure 5.9: A graph of relative viscosity against Reynolds number, each line of constant concentration. Shear thinning behaviour is clear and more prominent in higher concentration systems. Both Capillary number and Reynolds number are linear in shear rate, hence both scales displayed. Lines are just as a guide to the eye.

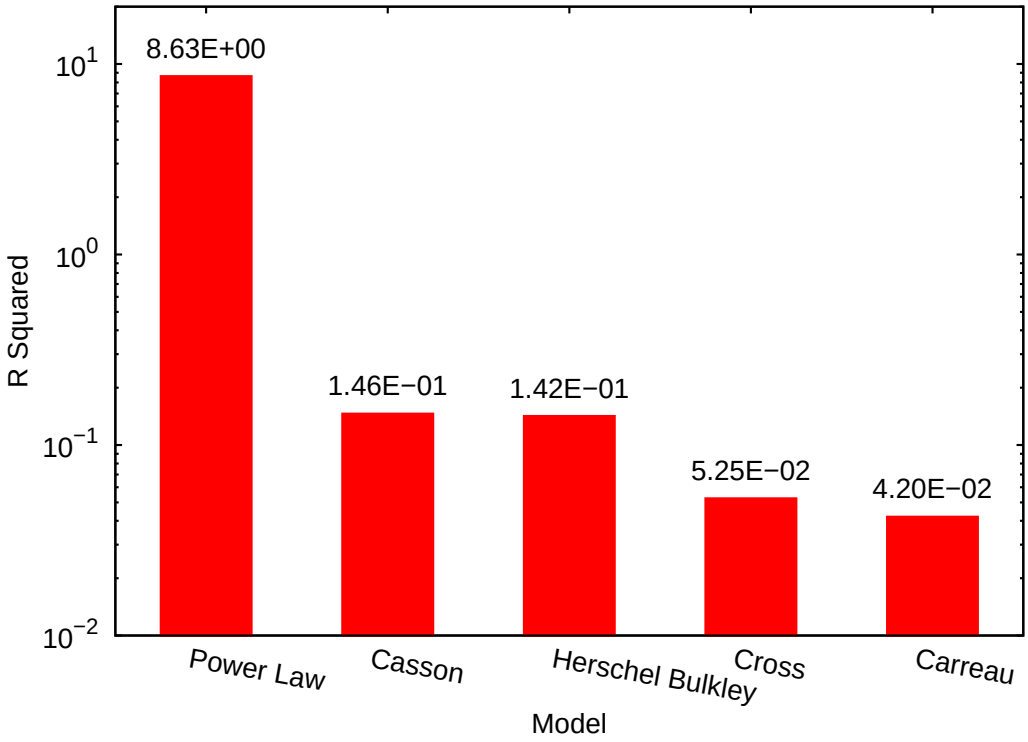

Figure 5.10: The average R^2 value of fits across the simulation data. A least-squares fitting algorithm was carried out on systems with $\sigma_0 = 0.09$ and $K = 1$. The average R^2 value from the fits where $\phi = [0.2, 0.33, 0.5, 0.6, 0.7]$ is plotted for each non-Newtonian model. The Cross model failed to fit the line of $\phi = 0.2$.

law model even when their zero-shear regime isn't present—the lack of the limit in the data does provide them with the freedom to place this limit at any point to get the lowest R^2. The Cross model was unable to fit the data for $\phi = 0.2$, which may be a result of the slight shear thickening that is seen.

Given that the best fitting model for this data is the Carreau model, a plot of each of the fits is displayed in Fig. 5.11 and the fitting parameters in Table 5.1.

The model fits the data well over the range of Reynolds number simulated, with a smooth increase in η_{inf} as the concentration increases. However, improvements could be made by obtaining data at the low-shear limit to be able to pinpoint the η_z plateau—in which case the models would have to be reassessed as this missing feature limited the fit of all the models. With the current data, the plateau is not seen and the fits therefore appear to have two free parameters (η_z, the zero-shear plateau, and λ, related to the point at which the shear thinning begins and the slopes turns downwards). In the lower concentration regime ($\phi \leq 0.5$), there is either zero or one data point to characterise the actual shear thinning, hence the power index, n, also becomes unreliable. At higher concentrations, where the shear thinning is more pronounced and displayed over several data points, the power index provides a good fitting slope.

As with viscosity, the sheared self-diffusion coefficient also shows a downwards

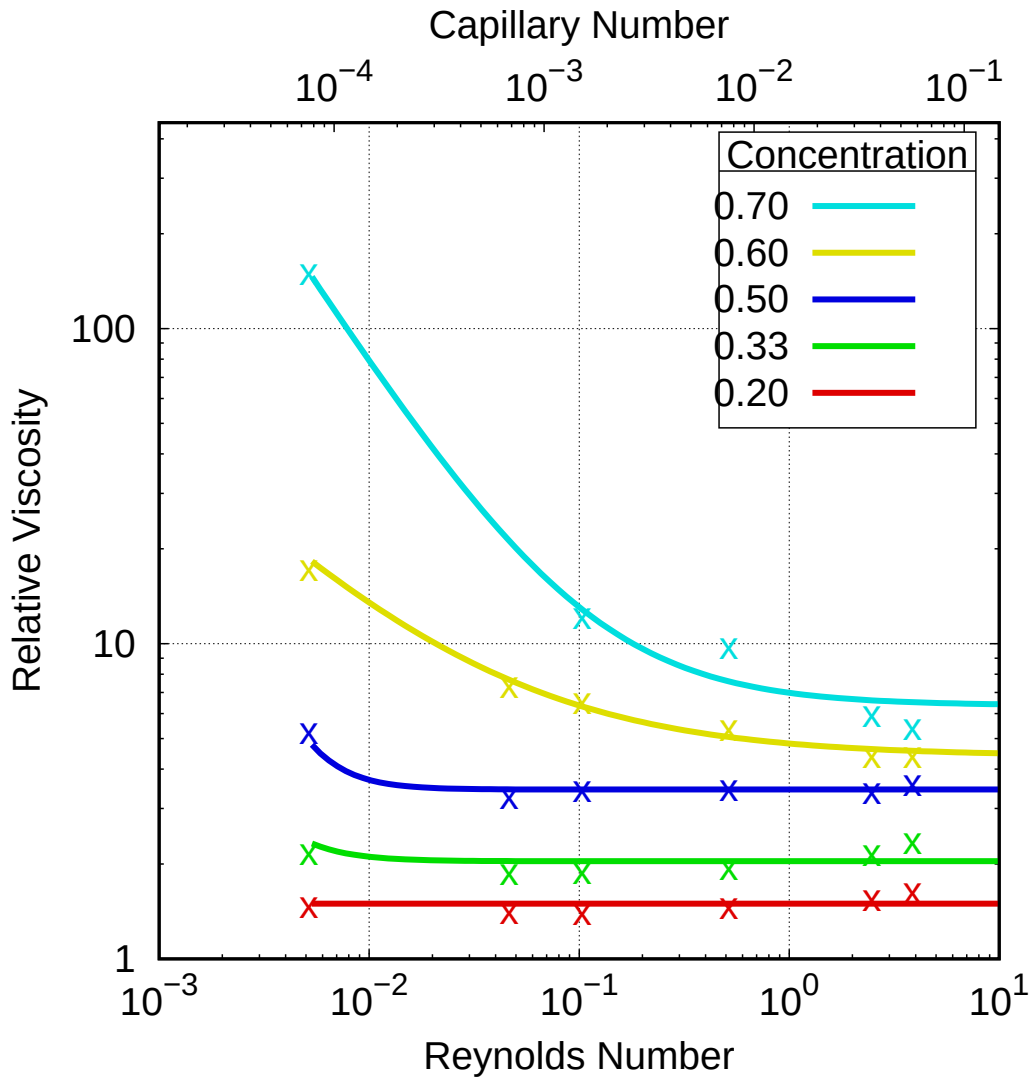

Figure 5.11: A graph of relative viscosity against Reynolds number. Points are simulation data, solid lines are a best fit of the Carreau model, with fitting parameters in Table 5.1. The fit is most appropriate for the high concentration data where the model can get a clear fit to the shear-thinning curve.

Table 5.1: Fitting parameters determined by least-squares fitting of the Carreau [12] model to the simulated data. Carreau model being: $\frac{\eta-\eta_\infty}{\eta_z-\eta_\infty} = \left[1+(\lambda\dot{\gamma})^2\right]^{\frac{n-1}{2}}$. Fit error percentage provided in columns following each fitting parameter, where $\mathrm{Er}(\eta_\infty) = 6\times10^{-2}$ is a fitting error of 6% for the η_∞ parameter.

ϕ	η_∞	$\mathrm{Er}(\eta_\infty)$	η_z	$\mathrm{Er}(\eta_z)$	λ	$\mathrm{Er}(\lambda)$	n	Er(n)	R^2
0.20	0.249	6×10^{-2}	100	4.37×10^{27}	500000000	7.44×10^{26}	-6.65	1.83×10^{26}	1.1×10^{-3}
0.33	0.340	8.89×10^{-2}	1590	2.76×10^{7}	500000000	1.23×10^{7}	-1.26	1.04×10^{3}	5.2×10^{-3}
0.50	0.574	2.76×10^{-2}	46000	9.86×10^{6}	500000000	3.72×10^{6}	-1.65	2.85×10^{2}	1.5×10^{-3}
0.60	0.733	1.15×10^{-1}	50.5	6.96×10^{3}	500000000	1.06×10^{4}	0.334	1.04×10^{1}	8.4×10^{-3}
0.70	1.06	4.62×10^{-1}	21400	3.1×10^{6}	3590000000	2.99×10^{6}	-0.036	6.02×10^{1}	1.9×10^{-1}

trend over the range of Reynolds number simulated, as seen in Fig. 5.12. The re-

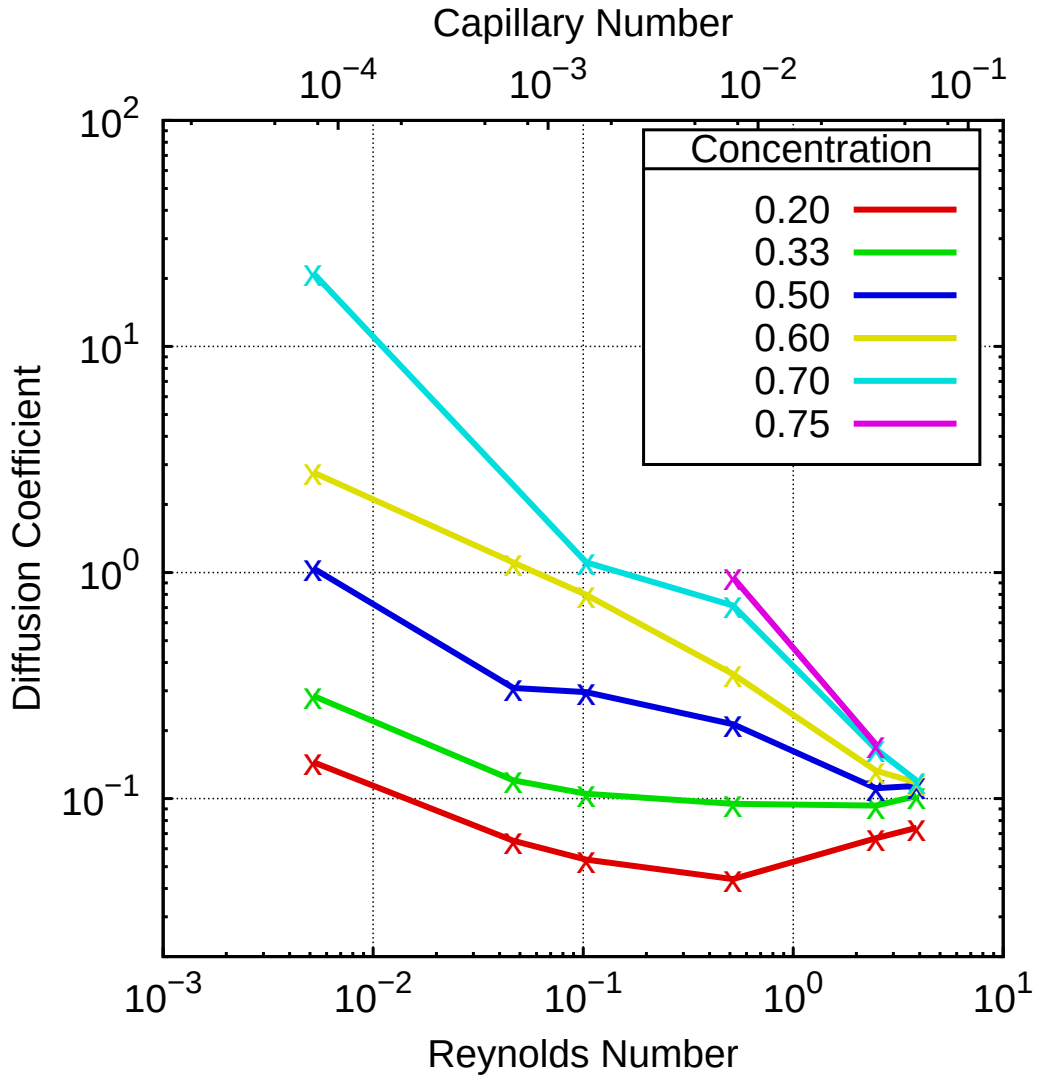

Figure 5.12: A graph of sheared self-diffusion coefficient against Reynolds number, each line of constant concentration. There is a clear downwards trend through most of the data, similar to the shear thinning behaviour. Capillary number is scaled and displayed, since it is also linear in shear rate. Lines are just as a guide to the eye.

duction of the sheared self-diffusion coefficient with increasing shear is due to the increasing deformability of the droplets. As they become more deformable, they need to travel less distance (perpendicular to the flow direction) around other droplets. This is reinforced by Fig. 5.13, where the deformation parameter is displayed. With increasing shear, the average deformation in the system increases significantly. The increased shear rate simultaneously makes the droplets more deformable whilst increasing the number of droplet interactions. Of course, the higher the concentration, the more droplet interactions will also occur, increasing the average deformation even further.

Quantitative comparisons of the deformation parameter with literature and analytic solutions (Taylor relation) would require a three dimensional model, however even in 2D the results are in good agreement. For instance, the Taylor relation [6, 86]

states the deformation parameter is related to the Capillary number as: $D = \frac{35}{32}\mathrm{Ca}$. The relation considers a lone droplet, so the closest comparison to be made here is of the least concentrated system ($\phi = 0.2$): at $\mathrm{Ca} = 7.6 \times 10^{-5}$ the predicted deformation is 8.3×10^{-5} whilst the measured value is 2.5×10^{-4}, approximately three times the predicted value. It is expected that a more concentrated system will have more deformation on average and it is noted that the measurement at $\phi = 0.2, \mathrm{Ca} = 7.6 \times 10^{-3}$ is also approximately three times higher than the prediction of Taylor.

It is interesting in Fig. 5.12 that there is an apparent convergence, with all the different concentrations collapsing onto a single sheared self-diffusion coefficient at the highest shear rates. At such high shear rates the droplets are on the verge of breaking apart—systems with breakup were witnessed, but excluded from data to keep the regime monodisperse—as the deformation of the droplets becomes extreme. With so much deformation it may be that no matter how many droplets are in the flow, they don't have to move far at all to manoeuvre around other droplets. At the highest of concentrations, layered systems are formed leading to marked reductions in the macroscopic transport properties (discussed in Section 6.1.1).

The sheared self-diffusion coefficient results compare well with the simulation data reported by Mountrakis et al. [114] for red blood cells. That data shows a reduction in the sheared self-diffusion coefficient with an increase in the shear rate, as well as the slight increase in the high-shear low-concentration regime. The convergence in the high shear regime of the present data cannot be reconciled with that of Mountrakis et al. as their data does not have a high enough shear rate. On the other hand, the upwards shift in the low concentration data makes it appear as though a similar convergence may have presented itself if such data was gathered.

5.2.3 Viscosity Ratio Dependence

The results up until this point have been for a fixed interfacial tension and viscosity ratio. Allowing the viscosity of the droplet fluid to vary provides a variable viscosity ratio. The effect of this on the relative viscosity of the emulsion is shown in Fig. 5.14. There is a clear upwards trend in the relative viscosity of the emulsion as the viscosity ratio increases. The effect of the viscosity appears to be fairly constant when other parameters change, unlike before where the effects of concentration and shear rate were heavily intertwined.

As mentioned in Section 2.1.2, macroscopic models have attempted to capture the effect of concentration and viscosity ratio. One such model is that of Yaron and Gal-Or [7], which has been plotted alongside the data in Fig. 5.15. Whilst the trend is quite similar between the data and the macroscopic model, the model of Yaron and Gal-Or over-predicts the relative viscosity. The macroscopic model includes assumptions that the capillary number is low (i.e. zero or low shear rate,

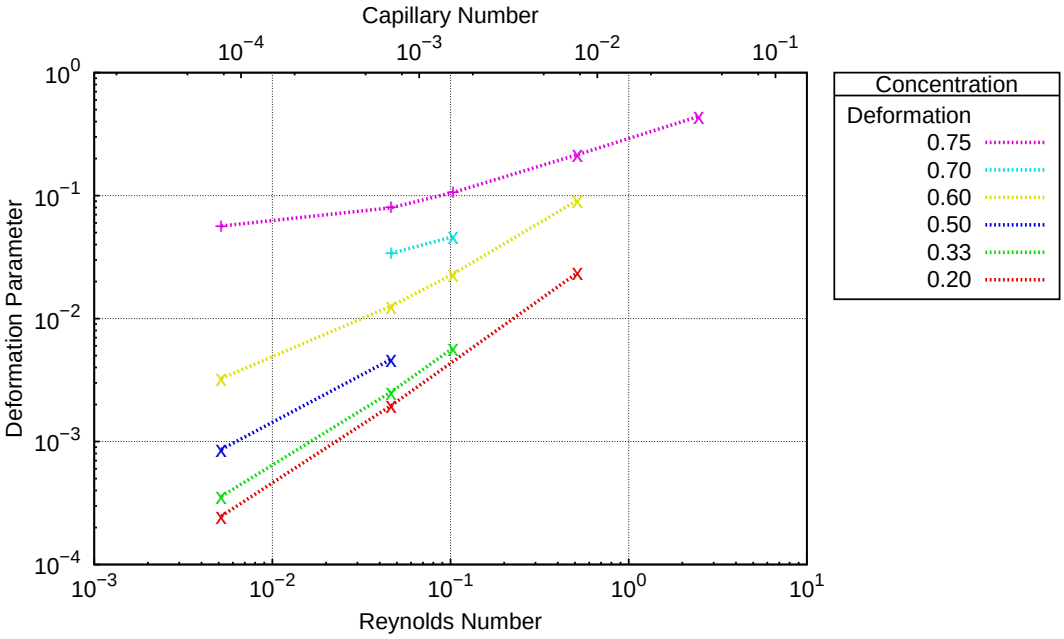

Figure 5.13: A graph of the average deformation parameter against Reynolds number. A higher shear rate increases the deformation in the flow, which may explain the reduction in the sheared self-diffusion coefficient visible in Fig. 5.12. Capillary number is scaled and displayed, since it is also linear in shear rate. Note, there are fewer data points visible here than in previous figures as the deformation data wasn't collected for the entire data set. Lines are just as a guide to the eye.

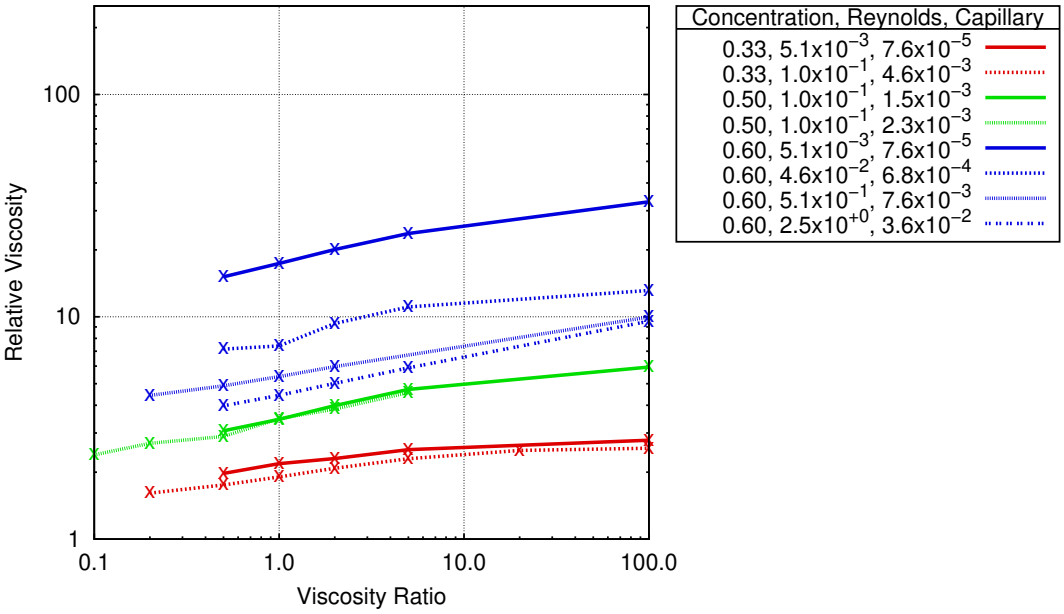

Figure 5.14: A graph of relative viscosity against viscosity ratio, each line has a fixed concentration and shear rate. As the viscosity ratio between the droplet and the suspending fluid increases, the overall fluid becomes more viscous. Lines are just as a guide to the eye.

with interfacial forces dominating the system), so that the droplets do not deform. These assumptions do not carry over to the data well, as low enough shear rates are too computationally expensive to achieve. The droplets are also going to deform in various ways throughout the system (deforming differently over time as well). Hence, the recovery of similar trends is encouraging, reproducing quantitative values is not to be expected.

The sheared self-diffusion coefficient shows a much different trend. Visible in Fig. 5.16 is that there is almost no change in sheared self-diffusion coefficient with a change in viscosity ratio. There is a slight increase with viscosity ratio in the low concentration regime, and the opposite in the higher concentration regime. An increase in the viscosity ratio would tend to make the droplets more "solid", which could result in less (or less responsive) deformation, hence the need for both increased movement and increased sheared self-diffusion coefficient. It is therefore unclear why an increase in the viscosity ratio would reduce the sheared self-diffusion coefficient.

Unfortunately, the hypothesis of lower deformation is not backed up by the data. Fig. 5.17 shows the average deformation parameter in systems of varying viscosity ratios. As the viscosity ratio increases, a small increase in the deformation parameter is witnessed. This is counter-intuitive as the droplets become physically more "solid", taking longer to deform. A thorough explanation of this effect is still unknown, however one hypothesis is that the more viscous droplets deformed due to consistent droplet-droplet interactions and take longer to relax to their preferred less deformed state—as opposed to less viscous droplets which may be able to relax their shape between encountering another droplet.

There is also a major outlier in the low Reynolds number regime, for a viscosity ratio of 0.5 . This system displayed some "clustering" behaviour that is only visible in a couple of other simulations; the droplets occasionally group up and proceed through the flow together. This clustering results in an increased deformation, and it may be noted that looking at the average deformation in the system for time periods where these clusters are absent provides a result 3.2×10^{-4} , in line with the other results. The clustering behaviour will be looked at in more detail in Section 6.2, however a animation/video of this particular system is available at this reference: [115].

5.2.4 Interfacial tension dependence

Finally, the interfacial tension parameter has been constant throughout the previous results, but this is a variable parameter within this model. In Fig. 5.18 a lower interfacial tension regime ($\sigma_0 = 0.03$ lu) is plotted alongside the previous results. The relative viscosity decreases when the interfacial tension is reduced, which is to be expected as the droplets will become more deformable and thus less resistant to flow. The interfacial tension has just as much impact as the other variables displayed

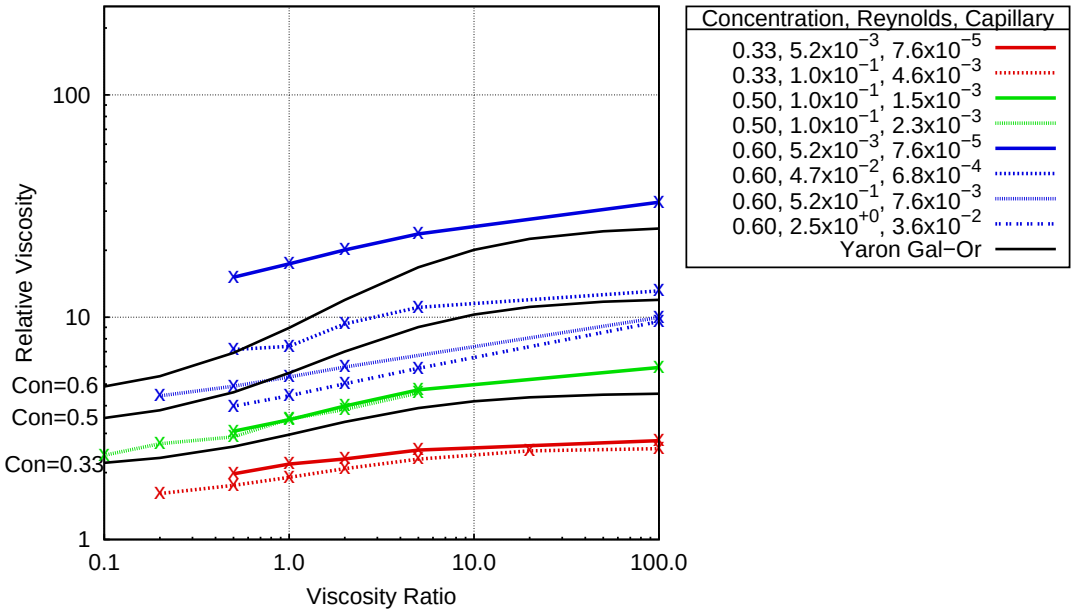

Figure 5.15: A graph of relative viscosity against viscosity ratio, each line has a fixed concentration and shear rate, including the theoretical model of Yaron and Gal-Or [7]. The trend is similar in the data and the macroscopic model, with an increase of viscosity ratio increasing the relative viscosity. The Yaron and Gal-Or model assumes a low capillary number, so the shear rate must be low and the droplets undeformed. Lines between simulation data are just as a guide to the eye.

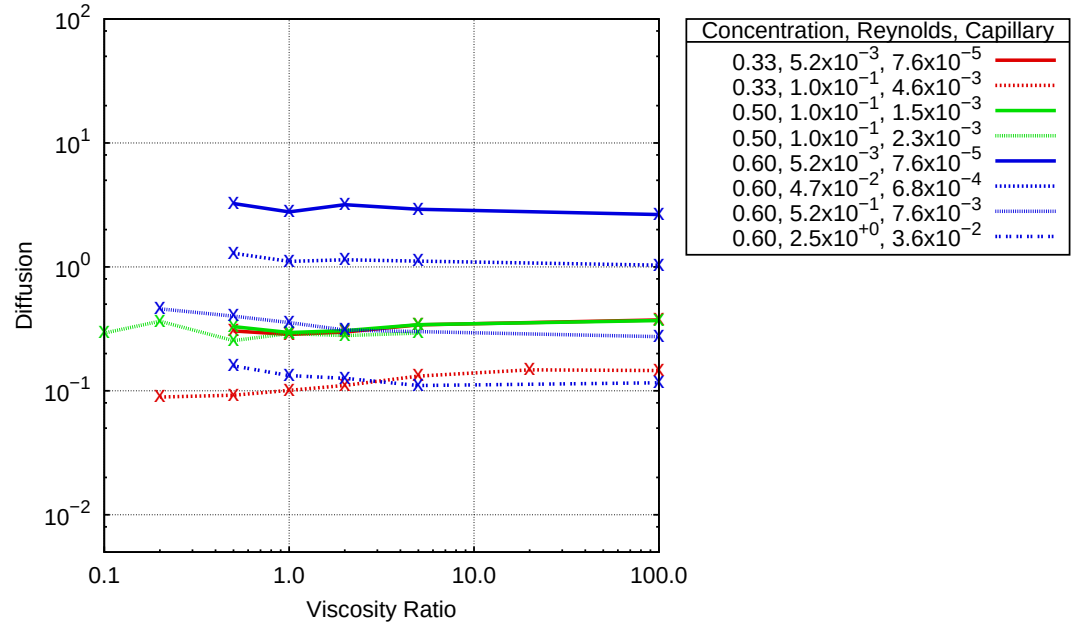

Figure 5.16: A graph of self-diffusion coefficient against viscosity ratio, each line has a fixed concentration and shear rate. There is little to no change in the sheared self-diffusion coefficient in relation to the viscosity ratio. Lines are just as a guide to the eye.

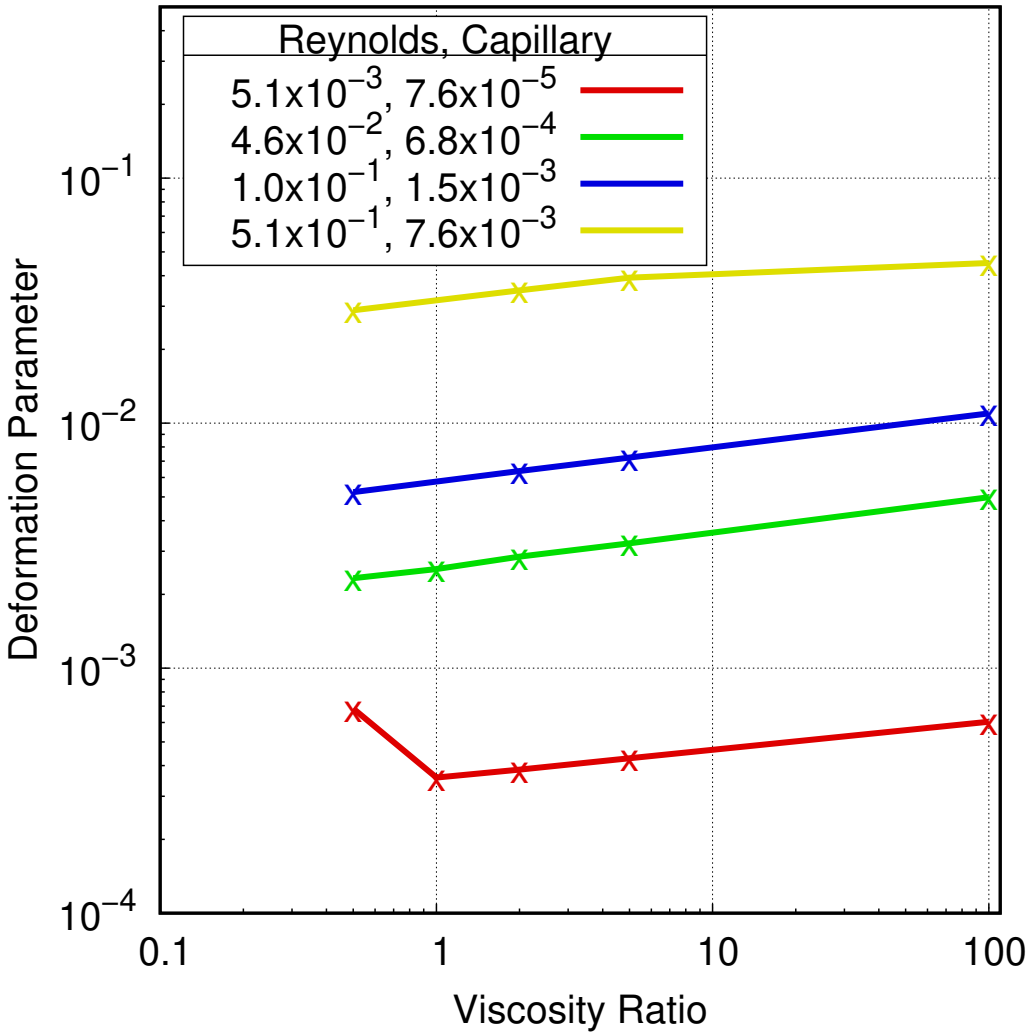

Figure 5.17: A graph of deformation parameter against viscosity ratio, each line has a fixed concentration ($\phi = 0.33$) and shear rate. Small upwards trend, the opposite of what may intuitively be expected. Lines are just as a guide to the eye.

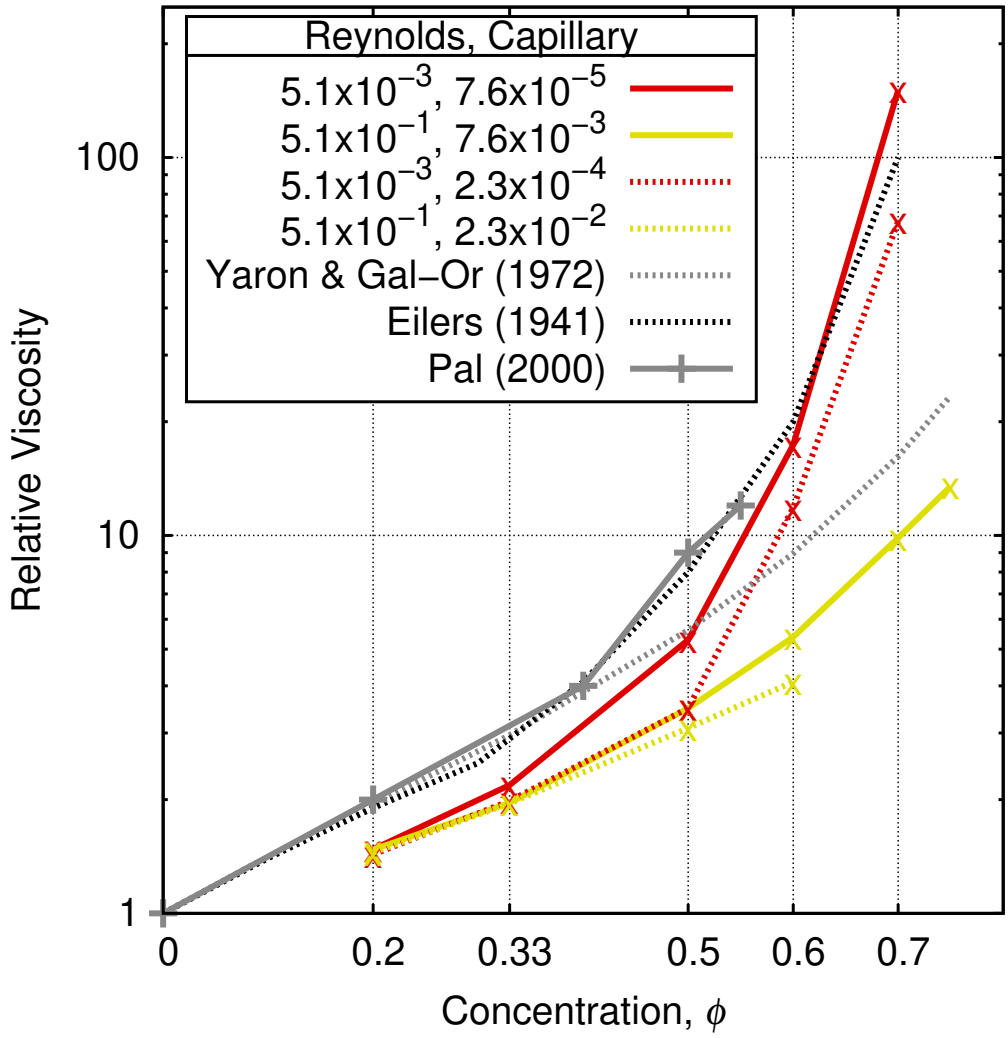

Figure 5.18: A graph of relative viscosity against concentration, each line has a constant Reynolds and Capillary number. Extension of Fig. 5.5 with dashed lines representing systems with reduced interfacial tension parameter $\sigma_0 = 0.03$ lu (with solid lines having $\sigma_0 = 0.09$ lu). The reduction in the interfacial tension also reduces the relative viscosity of the emulsion. Lines between experimental data are just as a guide to the eye.

here; a reduction of 66% decreased the relative viscosity by 55% in some cases.

The same effect is visible in the sheared self-diffusion coefficient, shown in Fig. 5.19. When the interfacial tension is reduced, the sheared self-diffusion coefficient also

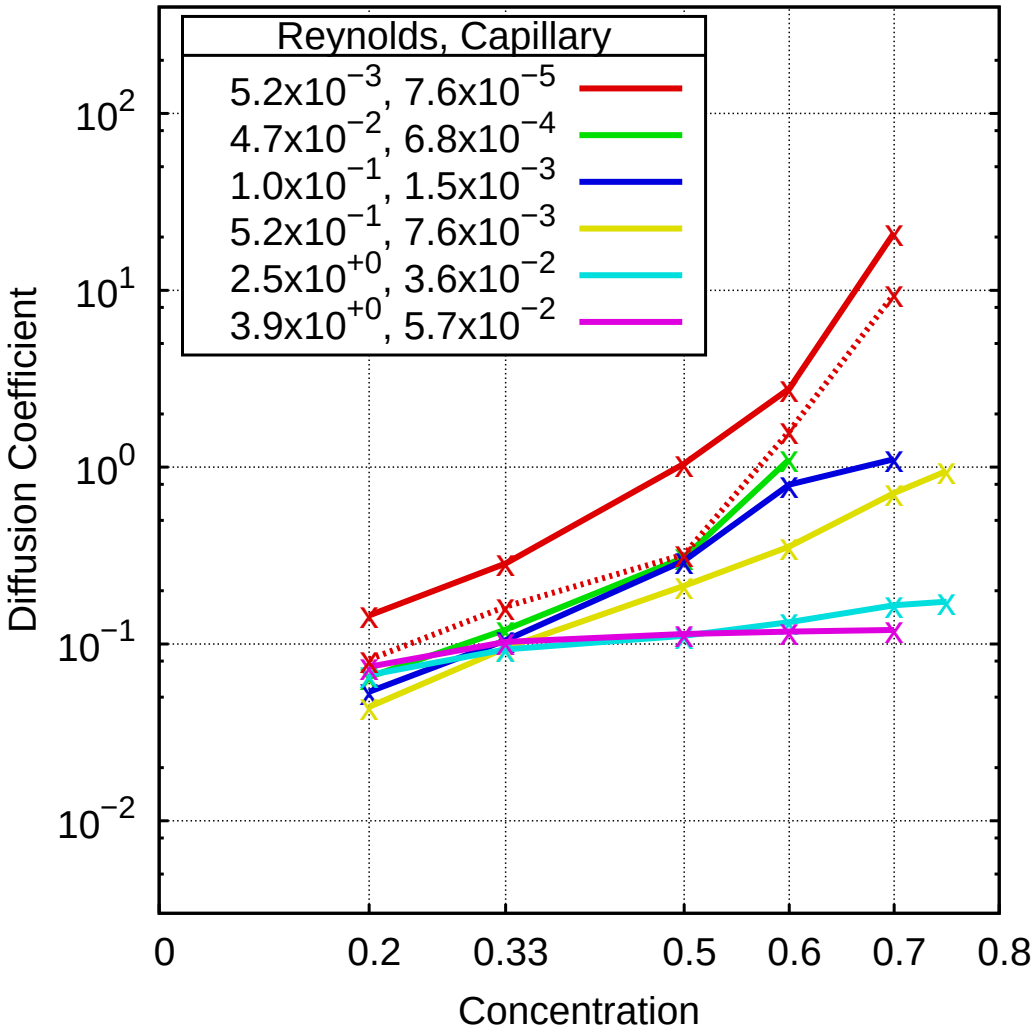

Figure 5.19: A graph of the sheared self-diffusion coefficient against concentration, each line has a constant Reynolds and Capillary number. Extension of Fig. 5.7 with the dashed line representing the system with reduced interfacial tension parameter $\sigma_0 = 0.03$ lu (with solid lines having $\sigma_0 = 0.09$ lu). The reduction in the interfacial tension also reduces the sheared self-diffusion coefficient of the emulsion. Lines are just as a guide to the eye.

reduces, likely due to the droplets deforming more and thus travelling less to manoeuvre around each other. The effect is even more pronounced than in the relative viscosity; here the reduction can be as much as 70% (when the concentration $\phi = 0.5$).

This data highlights a significant space in the literature for macroscopic models in which the interfacial tension is a variable. Such models would certainly be meaningful as physical emulsions may have the interfacial tension tweaked by making adjustments to the surfactants on the fluid-fluid interface (or by using slightly

different fluids).

5.3 Conclusion

The solid boundaries of the pipe flow were removed to prevent wall effects and gain bulk measurements of the fluid properties. A Lees-Edwards boundary condition, specifically applied to a multi-component flow using a cubic-spline interpolation, provided a sheared bi-periodic system. These boundary conditions allow for an arbitrarily high shear rate by increasing the number of boundaries in the system. The fluid viscosity, sheared self-diffusion coefficient (both key parameters in any complete macroscopic model [47]), and deformation were then measured for varying droplet concentrations, shear rates, viscosity ratios, and interfacial tensions. Viscosity models depending on concentration and viscosity ratio were shown to be in good agreement with the simulation results, despite the difference in dimensions. Similarly, non-Newtonian viscosity models were fit to the data and the best-fitting model (that of Carreau [12], see (2.16)) was shown to represent the data well. This relationship between the data and the macroscopic models was complicated by the lack of results at very low shear rates. Some macroscopic models show a Newtonian plateau in this region, hence the fits suffered from being unable to pinpoint this.

Overall, this chapter shows that two dimensional simulations of many interacting emulsion droplets provides rheological measurements comparable to that of experiments and macroscopic models.

Chapter 6

Structure Analysis

This chapter will look at the droplet structure within the previous bulk flow experiments. The mesoscopic nature of the models allows for the detailed study at the droplet level, which previously may have required challenging image analysis of experimental systems.

As shown in Section 5.2, certain systems (of high concentration and/or shear rate) have a tendency to form a layered regime, these are easily pinpointed in the data of Section 6.1 by their pronounced, repeated peaks. This chapter will also consider the formation of temporary clusters within the flow, showing that the formation of them may result in the shear-thickening behaviour seen in the last chapter (see Fig. 5.9).

6.1 Radial Distribution Function Analysis

Using the centre of mass data it was possible to post-process radial distribution functions (RDFs) for the simulations. The radial distribution, $g(r)$, compares the local density at r away from a droplet to the average density of the system. A perfectly homogeneous system would be represented by a flat line at $g(r) = 1$, where values above (below) show that, compared to an ideal gas, it is more (less) likely to find particles at this point than expected.

The distance between every unique pair of droplets in the system is categorised into the bins of a histogram which are small enough to give the appearance of a continuous function. The amount within the *shell* (the "doughnut" of space between the start and end of the histogram bin) is then normalised by the amount expected to be within that area/volume in an ideal gas mixture of the same concentration.

A look at this function for various systems provides insight into the structure of the fluid and the droplet behaviour, as peaks and troughs display the *important* distances in the fluid. The structure is most obvious when looking at the layered system mentioned previously.

6.1.1 Layered systems

As mentioned, some figures in Chapter 5 contain incomplete lines of data, as the layering behaviour makes the system enter an incomparable flow regime. An overview

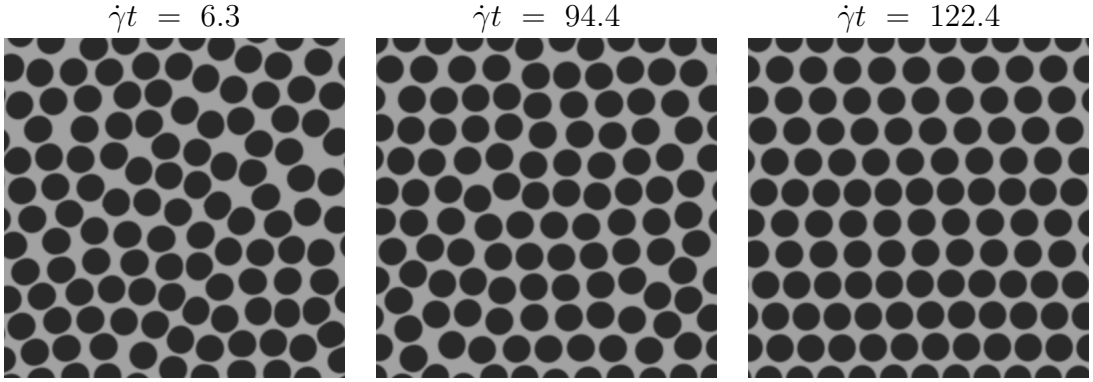

Figure 6.1: Overviews of a system that becomes layered. The system itself has parameters: $\mathrm{Re} = 1.0 \times 10^{-1}$, $\mathrm{Ca} = 4.5 \times 10^{-3}$, $\phi = 0.6$, $\sigma_0 = 0.03$, $K = 1.0$.

of a system entering such a state is shown in Fig. 6.1. The droplets line up behind each other in layers; this appears to be the easiest way for them to flow, which is reflected in a dramatically decreased viscosity measurement. This appears to happen quite randomly, there isn't a fixed point in time at which the systems enter this state. The change is sudden, with relative viscosity and sheared self-diffusion coefficient data quite stable until the moment the droplets line up. Once in such a regime the droplets stay in this formation indefinitely. Out of the 50 layered systems, one of them has ~80% of the droplets in consistent rows of 11 droplets whilst two other rows (containing 12 droplets) don't appear to settle down—not pushing the system out of the layered state but introducing velocity perpendicular to the flow. Another three of these layered systems actually form diagonal layers, which appear to have a yield stress—they prevent flow for a small period of time and then the layers *snap* past each other (again locking and preventing flow).

The layered systems' periodic peaks are usually a pair of repeating peaks: one for the distance between droplets in the same layer and another for the droplets in adjacent layers, as seen in Fig. 6.2. Clearly the number of droplets in the layer determines how close each droplet must get, so these systems show very pronounced peaks every $2R$ (or close to it). The droplets cannot get any closer than that without deformation and once layered they end up in a periodic system. Due to the specific number of droplets, the layers end up being made up of different amounts of droplets, which just means the peaks are more broad or short than otherwise.

6.1.2 Shear rate dependence

When considering the effect of the shear rate on the structure of the fluid, almost all systems show the same trend (except layered systems and one other, discussed

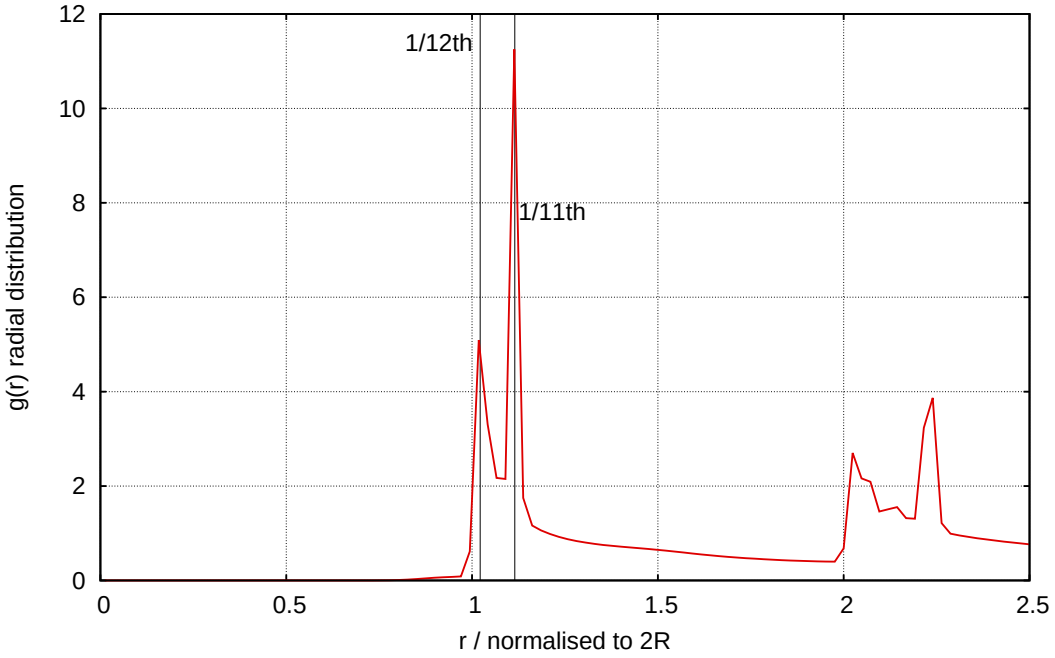

Figure 6.2: A radial distribution function of a layered system. This system is characterised by: $\mathrm{Re} = 5.1 \times 10^{-1}$, $\mathrm{Ca} = 2.3 \times 10^{-2}$, $\phi = 0.7$, $\sigma_0 = 0.03$, $K = 0.5$. This system is made up of 12 layers, 10 with 11 droplets and 2 with 12 droplets. The first peak corresponds to the distance spacing of 12 droplets in the system size whilst the second peak is in line with 11 droplets. The first peak is lower and broader than the second because the layers are moving past each other so the distance between drops in other layers oscillates, whilst the distance between droplets in the same layer stays constant.

later). The first peak moves left (i.e. less distance between droplet centres) with an increasing shear rate, due to being more deformed so the droplets are able to get closer. This first peak starts outside the 2R *exclusion zone*, since the low shear rate doesn't deform the droplets much and doesn't force the droplets into the zone. As the shear increases, the first peak eventually gets closer than 2R (particularly at high concentrations), indicating that the shear has deformed the droplets and altered the zone of exclusion (droplet interface). An example of this behaviour (seen across

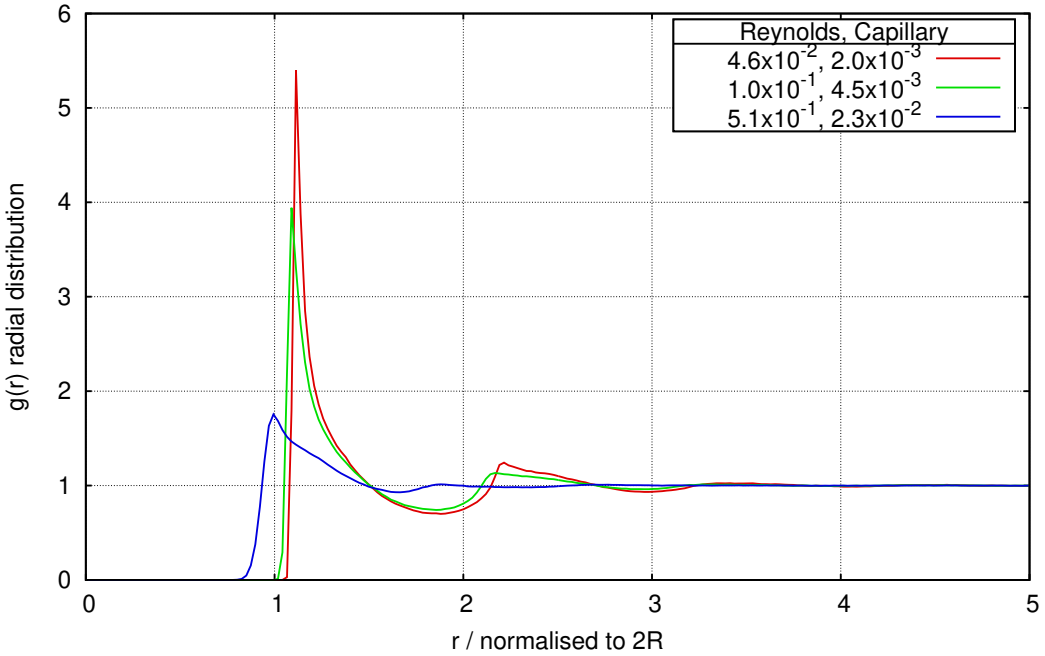

Figure 6.3: Radial distribution functions for systems with differing shear rates. These systems have $\phi = 0.5\,, \sigma_0 = 0.03\,, K = 2\,$. The trend displayed here is visible throughout the data, where increasing the shear rate lowers, broadens, and moves the first peak left. The higher shear makes the droplets more deformable and allows them to get closer.

many of the systems) is shown in Fig. 6.3.

The peaks also get lower and broader with an increasing shear rate, as the less deformable droplets enforce a very specific minimum separation due to the undeformed interfaces. As the droplets become deformable, the distance between them can occasionally decrease but it isn't a consistent effect like the layering behaviour, hence the exact separation becomes more varied (lower and broader).

The outlying behaviour (the exception mentioned earlier) seen in Fig. 6.4, is due to the clustered system that was first visible in Fig. 5.17. This results in the lowest shear rate system having a shorter (and broader) peak than would be expected from the rest of the data.

6.1.3 Viscosity ratio dependence

Considering the effect of the viscosity ratio on the RDFs, there is very little noticeable effect, especially at lower shear rates. A small visible trend is that the first peak moves left and lower with an increasing viscosity ratio, as shown in Fig. 6.5. The peak moving left shows the droplets tending to be closer to each other, an explanation for which is unclear as the droplets would tend to be more *solid*. This does match with the average deformation data (see Fig. 5.17), where the droplets become more deformed as the shear rate increases.

At high shear rates, however, the highest viscosity ratio ($K = 100$) consistently bucks this trend. This effect can be seen in Fig. 6.6.

6.1.4 Concentration dependence

Looking now at the effect of the droplet concentration on the fluid structure, there appears to be a different effect depending on how high the shear rate is. At the higher shear rates the droplets tend to get closer as the concentration increases (over and above the inherent packing effect of increasing concentration). This is visible in Fig. 6.7. The peak gets much broader as the concentration increases, which indicates there are more droplets in this region, but the high shear rate allows them to deform (making a specific peak lower and broader).

At lower shear rates, the first peak in the RDF gets higher as the concentration increases, as seen in Fig. 6.8. This is even true for the layered systems. As the peak gets higher it is also sharper, indicating that as the concentration increases the droplets are located at more specific points, with less free space to flow into.

6.2 Clustering analysis

The same centre of mass data can also be used to look at the *clustering* behaviour of the droplets. Droplet clusters create areas of higher viscosity, effectively creating larger droplets and restricting the flow. Such phenomenon should be avoided for the system to be homogeneous, and for consistency in macroscopic properties.

6.2.1 Method

This clustering data wasn't gathered during the lattice-Boltzmann method (LBM) simulations, but enough other data was output to allow for an analysis to be undertaken. Using the droplet centre of masses and the deformation of each droplet (both output frequently), a simulation snapshot can be recreated. An approximation to ellipses is possible using this data, a comparison of which can be seen in Fig. 6.9. This is representative to the bulk of the simulations, but can break down at high shear rates when the droplets are forced to deform into different, non-elliptical shapes.

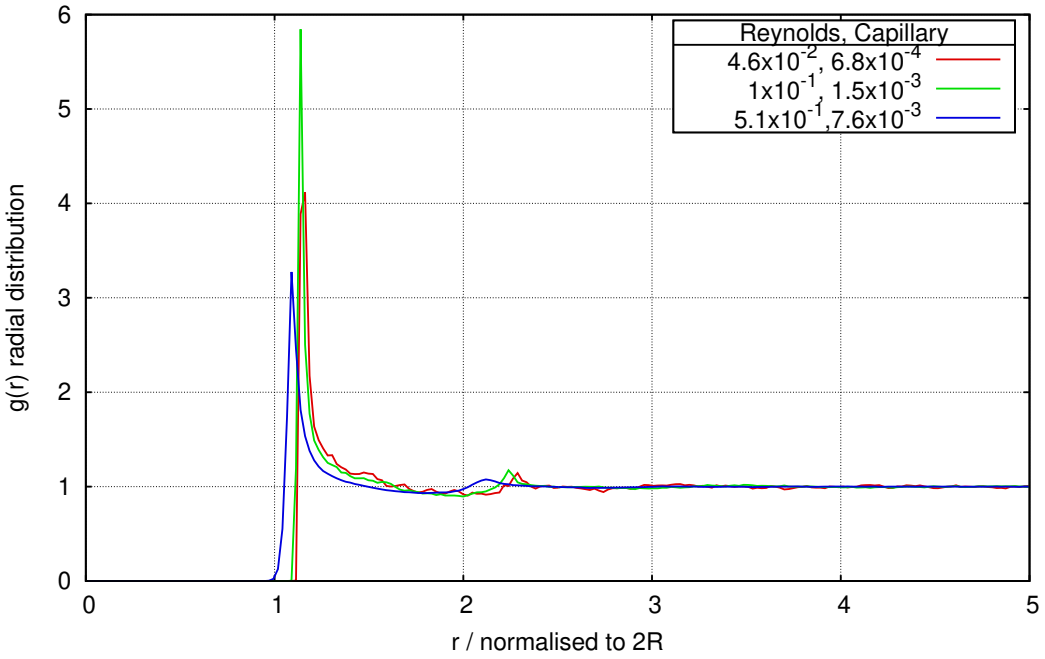

Figure 6.4: Radial distribution functions for systems with differing shear rates. These systems have $\phi = 0.33\,, \sigma_0 = 0.09\,, K = 0.5\,$. The trend in this data differs from the rest as the peaks don't get consistently lower and left with an increasing shear rate.

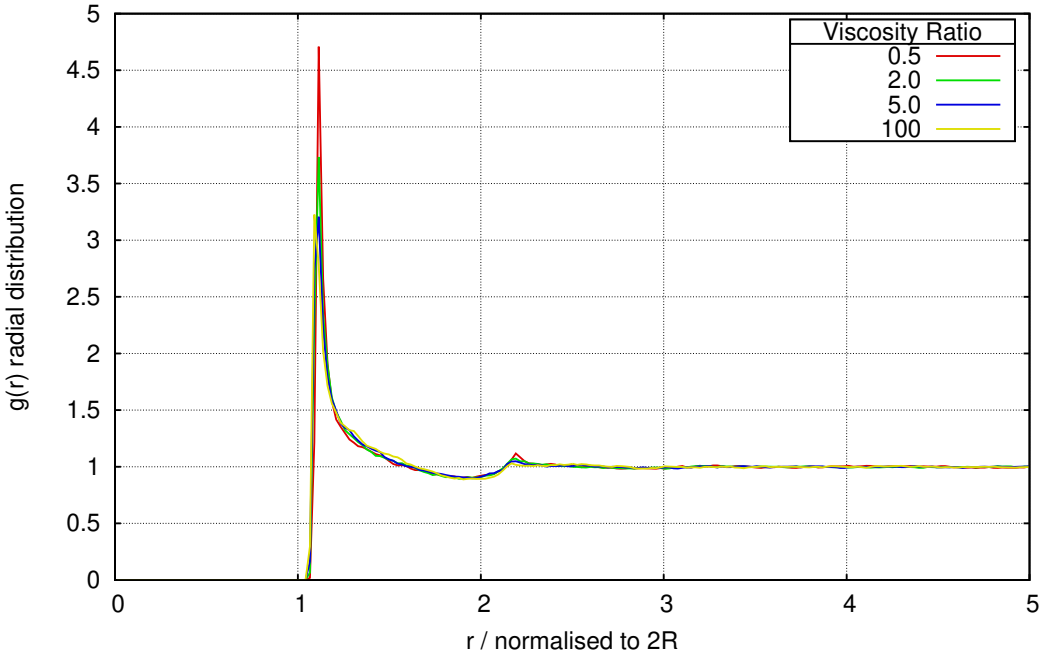

Figure 6.5: Radial distribution functions for systems with differing viscosity ratios. Each of these systems have $\phi = 0.33\,, \sigma_0 = 0.03\,, \mathrm{Re} = 1.0 \times 10^{-1}\,, \mathrm{Ca} = 2.7 \times 10^{-2}\,$. The peak gets lower and broader, whilst moving left, with an increasing viscosity ratio, indicating that the droplets are able get closer to each other.

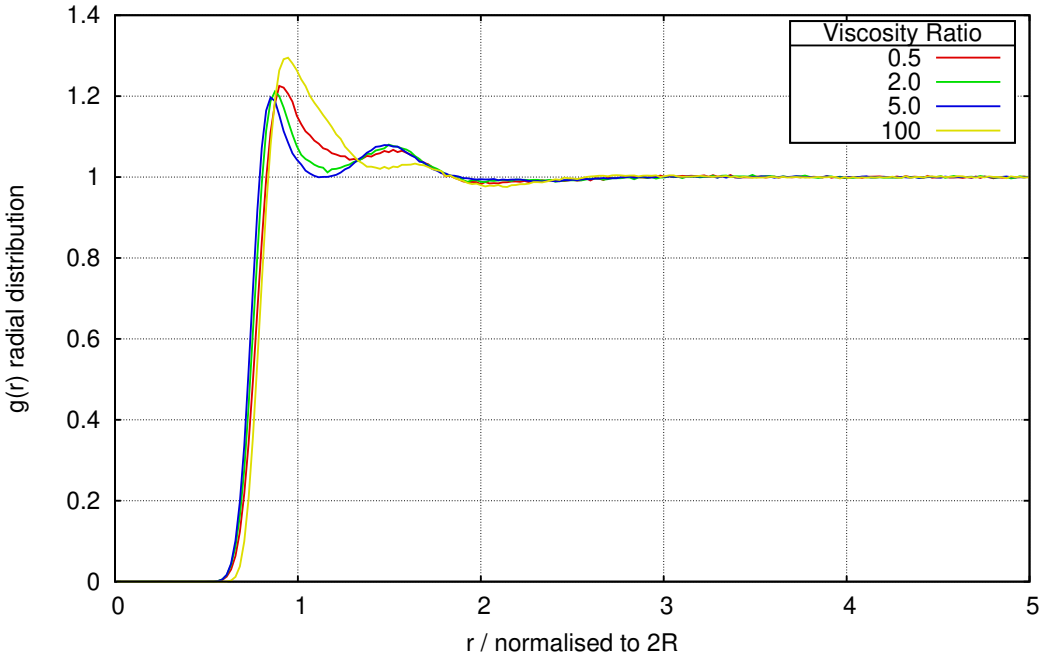

Figure 6.6: Radial distribution functions for systems with differing viscosity ratios. These systems have $\phi = 0.6\,, \sigma_0 = 0.09\,, \mathrm{Re} = 2.5\,, \mathrm{Ca} = 2.2 \times 10^{-1}$. At this high shear rate, the $K = 100$ result reverses the trend.

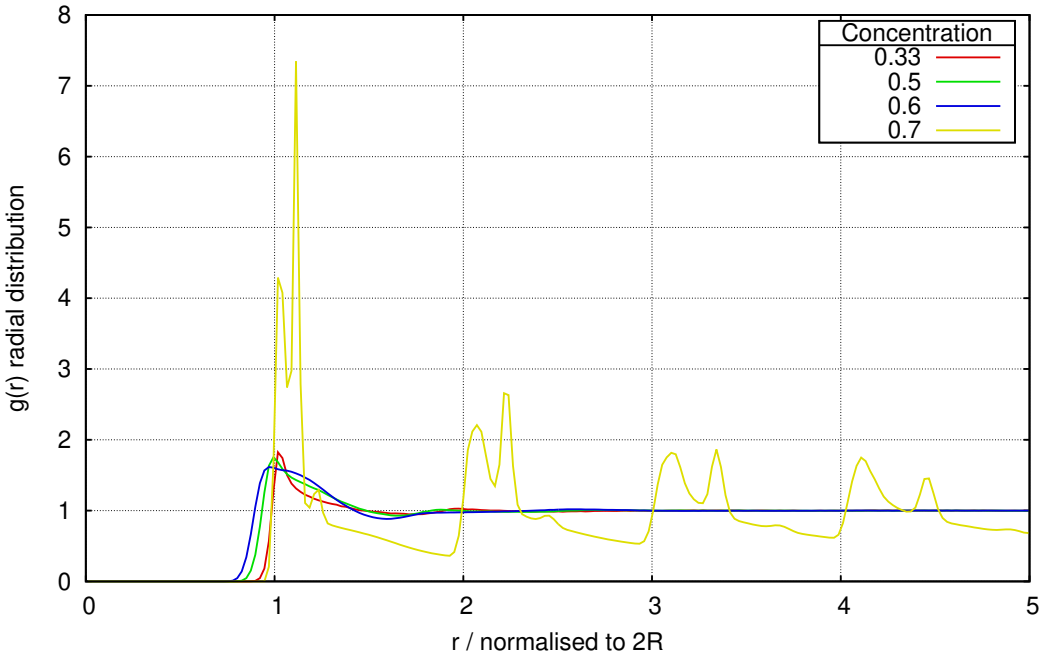

Figure 6.7: Radial distribution functions for systems with differing concentrations. The systems here have $\sigma_0 = 0.03\,, K = 2.0\,, \mathrm{Re} = 5.1 \times 10^{-1}\,, \mathrm{Ca} = 1.4 \times 10^{-1}$. The first peak moves left as concentration increases, as well as getting lower and broader.

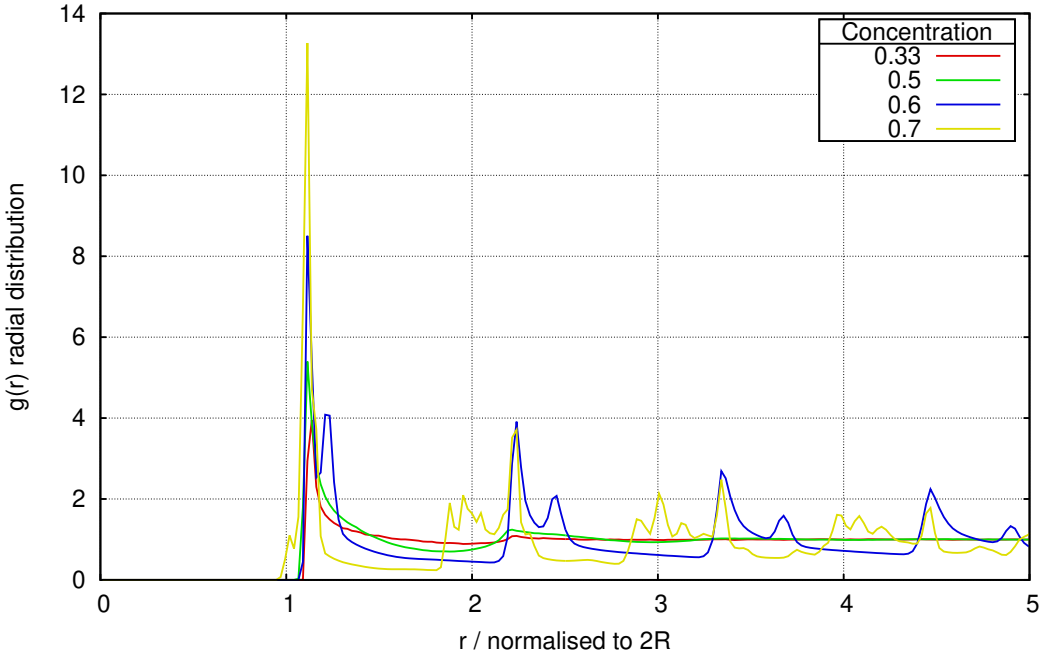

Figure 6.8: Radial distribution functions for systems with differing concentrations. The systems here have $\sigma_0 = 0.03\,, K = 2.0\,, \mathrm{Re} = 4.6 \times 10^{-2}\,, \mathrm{Ca} = 1.2 \times 10^{-2}\,.$ The first peak gets higher as the droplet concentration increases.

The first row of data in Fig. 6.9 shows a system with a shear rate at the higher end of these simulations, which is still quite well represented by the ellipses. The second row is less well represented due to being at the limit of shear rates studied here.

Zheng and Palffy-Muhoray detailed [116, 117] a solution to the closest approach of two arbitrary ellipses. Knowing the closest approach and the centre of masses, the actual distance between the droplets' interfaces can be estimated. Knowing the closeness of each droplet to another, the algorithm of Stoddard [118] was applied to efficiently develop a list of clusters through each time interval (usually every 100 timesteps). A cluster is deemed to be a group of three or more droplets which have interfaces within 2 lattice nodes (10% of the droplets radius).

Most clusters "survive" longer than the interval of the measurements, hence the algorithm must decide which clusters in a specific timestep are the same ones from a previous timestep. These surviving clusters were identified by the following rules (note that droplets themselves were identifiable via a unique ID):

1. the cluster has the exact same droplets as a cluster in the last interval, OR
2. the cluster contains all the droplets that a cluster in the last interval contained (with extras), OR
3. the cluster contains at least one droplet that a cluster in the last interval contained.

The algorithm checks these conditions in order, so if an exact match is found at point 1, then the algorithm stops. Conditions 2 and 3 can be met several times,

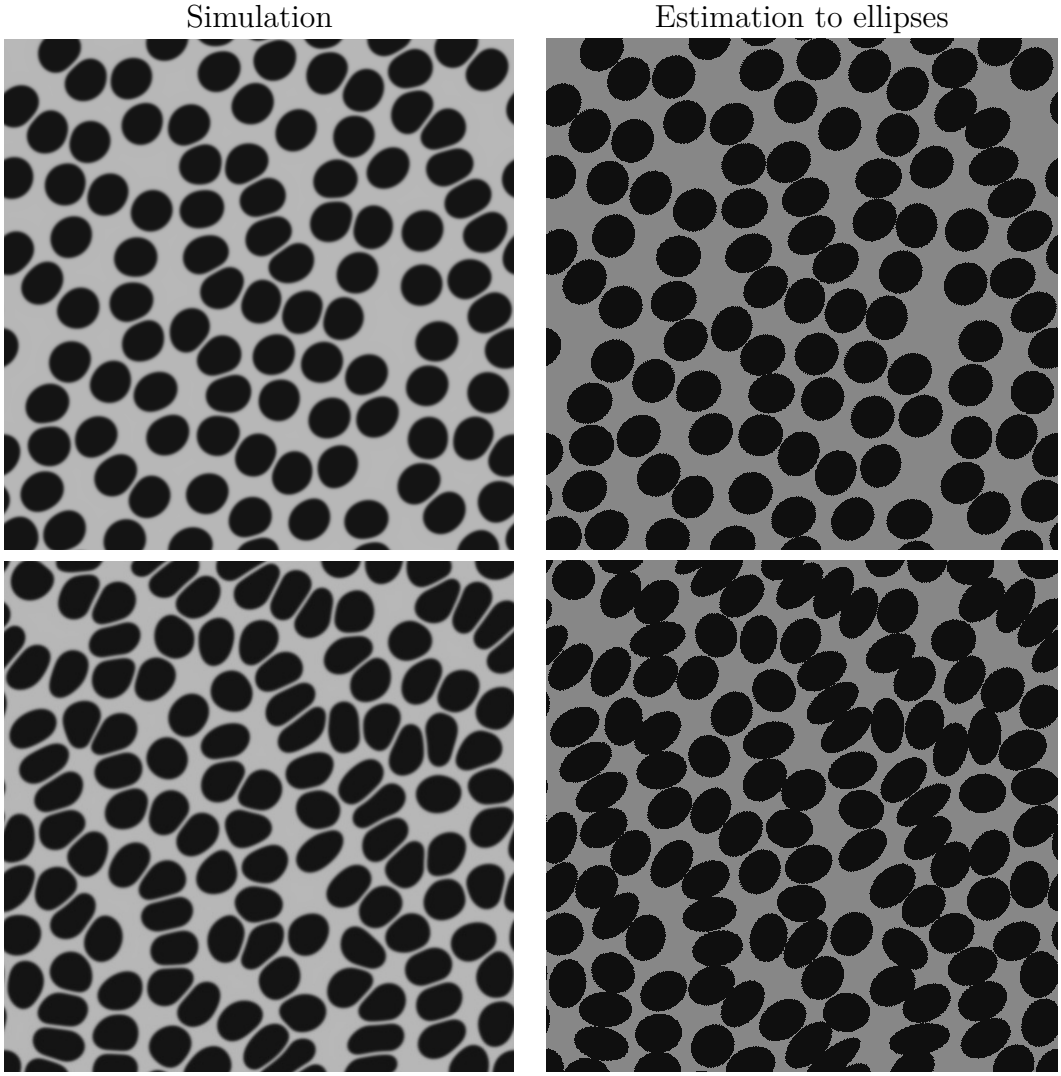

Figure 6.9: Comparison of simulated droplets with estimated ellipses. The first row is a system parametrised as: $\sigma_0 = 0.03\,, \phi = 0.5\,, K = 5\,, \mathrm{Re} = 5.1 \times 10^{-1}\,, \mathrm{Ca} = 1.4 \times 10^{-1}$. The second row is parametrised as: $\sigma_0 = 0.09\,, \phi = 0.6\,, K = 0.5\,, \mathrm{Re} = 2.5\,, \mathrm{Ca} = 2.2 \times 10^{-1}$. The second row shows much more deformation (due to the higher shear rate) and isn't as well represented by ellipses as the first system.

when multiple clusters form a larger cluster, in which case the new cluster inherits the age of the oldest cluster it is found to contain. Note that the algorithm stops if a particular step is successful in its search, i.e. if condition 2 is satisfied then the algorithm doesn't consider condition 3. Following these rules, clusters can be tracked through a flow, gaining and losing droplets, whilst accruing a *lifespan* that may help characterise the flows.

Mountrakis et al. [114] have studied the clustering behaviour of suspensions of elastic particles, similarly using LBM. Whilst direct comparison can't be made between elastic particles (red blood cells (RBCs)) and emulsion droplets, it may be useful to see what trends are reproduced in both datasets. Fig. 6.10 shows some clustering data of emulsion that may be comparable to the data in Fig. 6 of Mountrakis et al. There are different methods and cluster definitions that may have

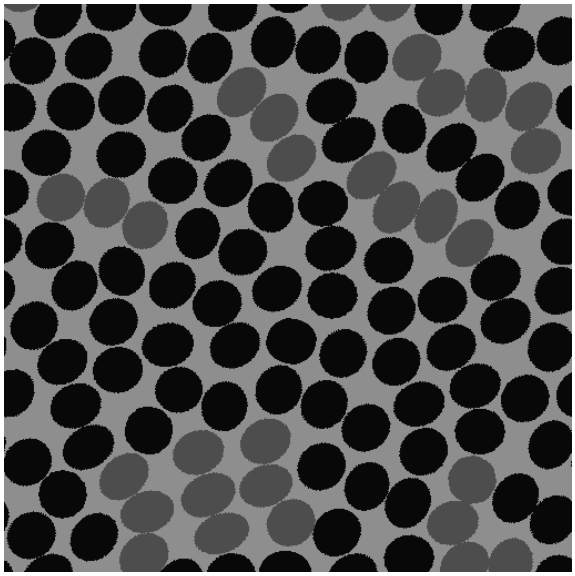

(a) Snapshot of clustering

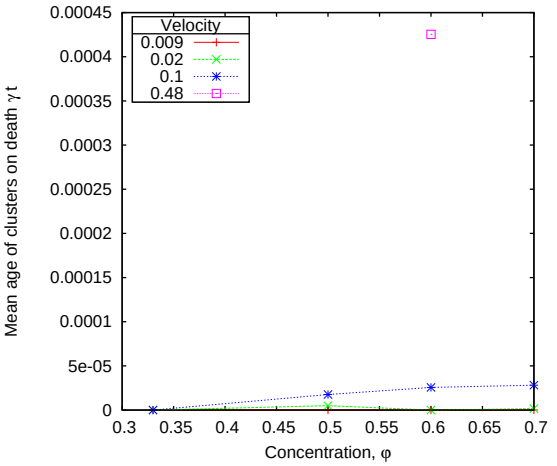

(b) Cluster age (timescale)

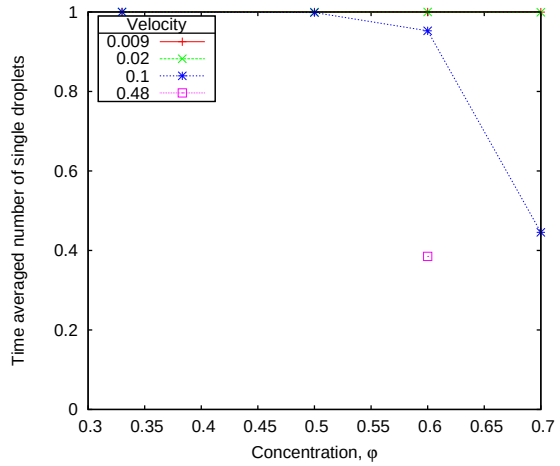

(c) Proportion of single droplets

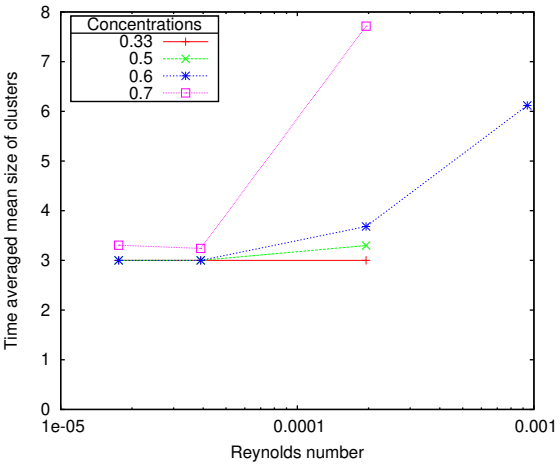

(d) Average cluster size

Figure 6.10: The simulation data here uses $\sigma_0 = 0.09$ and $K = 0.5$, with varying shear rates and concentrations. The snapshot system has a lower σ_0 as these images were only output for a select number of systems.
Subfigure a shows a snapshot of a simulation with parameters: $\sigma_0 = 0.03, \phi = 0.6, K = 0.5, \mathrm{Re} = 5.1 \times 10^{-1}, \mathrm{Ca} = 1.4 \times 10^{-1}$. Droplets that are identified as being in a cluster are lightened.
Subfigure b shows the average lifespan of clusters. Unfortunately, many of the simulations didn't have clusters that fit the definition, leaving only one line to draw conclusions from. This shows that increasing the concentration increases the lifespan of the clusters.
Subfigure c displays the time averaged proportion of single droplets in the system. The decrease of these single droplets indicates that more droplets are becoming part of clusters. Again, only one line of data had any significant amount of clusters detected.
Subfigure d shows the time averaged mean size of clusters. Clusters in this algorithm are a minimum of 3 droplets. A few data points didn't exist (no clusters), so they are plotted at 3 as the minimum possible. The plot shows that as the concentration or shear rate is increased the cluster is likely to contain more droplets.

an effect: the algorithm above defines clusters having a minimum of 3 droplets. This means that the cluster size average starts at 3 and there are likely to be more "single drops" that may be pairs. One set of data is shown here (surface tension $\sigma_0 = 0.09$ and viscosity ratio $K = 0.5$), but these figures look quite similar across the board.

Still, it may be possible to draw comparisons with Fig. 6 of Mountrakis et al. [114] Specifically, Fig. 6.10b and Fig. 6e of Mountrakis et al. display a characteristic timescale of the cluster behaviour. Both show an increasing timescale as the concentration is increased. This indicates that at lower concentrations interactions are more brief, whereas in a more concentrated system the droplets are forced into contact for a longer time. The droplets have less freedom to move and escape a cluster when the flow is more densely packed.

Fig. 6.10c agrees with this as well, showing that the proportion of droplets in a cluster increases as the concentration increases. This compares well with Fig. 6c of Mountrakis et al. and indicates that the denser packed systems force more droplets into longer lasting clusters (when taking both figures into consideration). A big difference between this data and that of Mountrakis et al. is that these emulsion systems don't reach a zero number of single droplets, whereas the algorithm used with the RBCs shows that all of the inclusions are contained in clusters by $\phi \approx 0.5$.

Finally, Fig. 6.10d shows the mean size of clusters in each system, noting that this is defined to start at three droplets. The data shows that increasing either concentration or shear rate can increase the size of clusters. This agrees well the data shown in Fig. 6d of Mountrakis et al. and the data in the previous subfigures. The concentration has already been shown to force more droplets into clusters, but the shear rate is also displayed doing the same here; this is likely related to the increased deformation and the droplets forming structures parallel to their long axis (as highlighted in Fig. 6.11).

Now, looking at simulation data in more detail Figures 6.12 to 6.17 show histograms of cluster sizes and cluster lifespans. It isn't possible to compare *frequencies* between figures since they may have been compiled over different non-dimensional time (t* = simulation time * shear rate), either due to different simulation lengths (low shear means a lower t*) or running analysis on a specific section (layered regimes). Systems within the same figure, however, have been analysed over the same non-dimensional time, so the distribution of the histogram is comparable. Also note that the total frequency of cluster sizes may not be equal to the total frequency of the cluster ages, because they are measured in different ways: the cluster sizes are counted each time interval they are detected, whereas the cluster ages are only counted once a cluster breaks up. Clusters that don't break up before the end of the simulation would therefore not be in the age data, but would be present in the size data. The cluster size data, counted each time interval, incorporates a timescale into the measurement, i.e. the longer a cluster stays at a certain size the

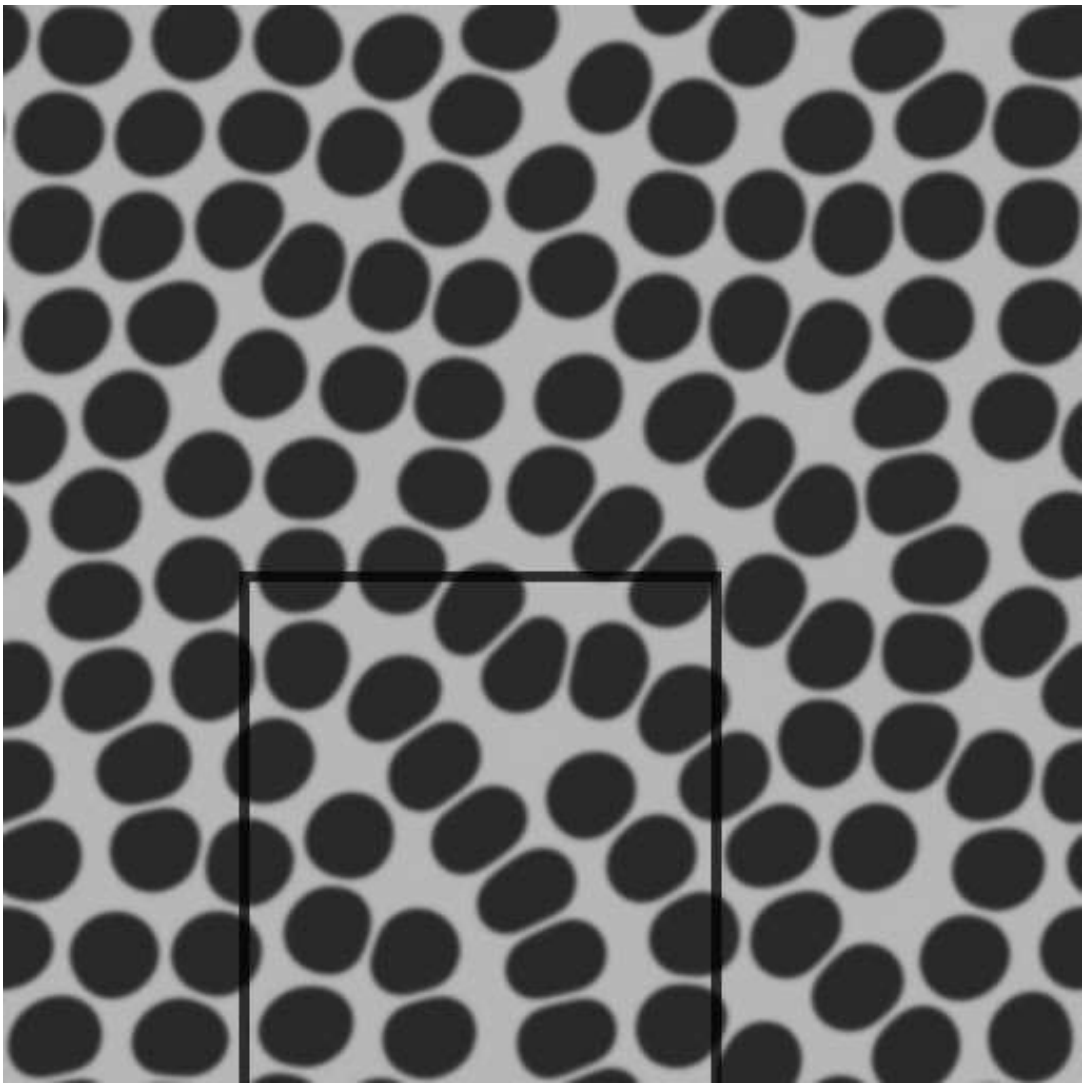

Figure 6.11: A snapshot of a system with temporary droplet structures highlighted. This isn't unique to this system but it was parametrised as $\sigma_0 = 0.03\,, \phi = 0.6\,, K = 2.0\,, \mathrm{Re} = 5.1 \times 10^{-1}\,,$ and $\mathrm{Ca} = 1.3 \times 10^{-1}\,.$

more it is counted in the data. This has the advantage of acting like a probability, showing which size clusters are most likely to be found at any given time. It also has the disadvantage of obscuring any very brief clusters.

6.2.2 When viewed as functions of shear rate

Now, looking at the clustering behaviour across a wider set of simulation data. Firstly, looking at the effect of the shear rate on the clustering behaviour, Fig. 6.12 shows this for a low concentration. These low concentration systems require a high

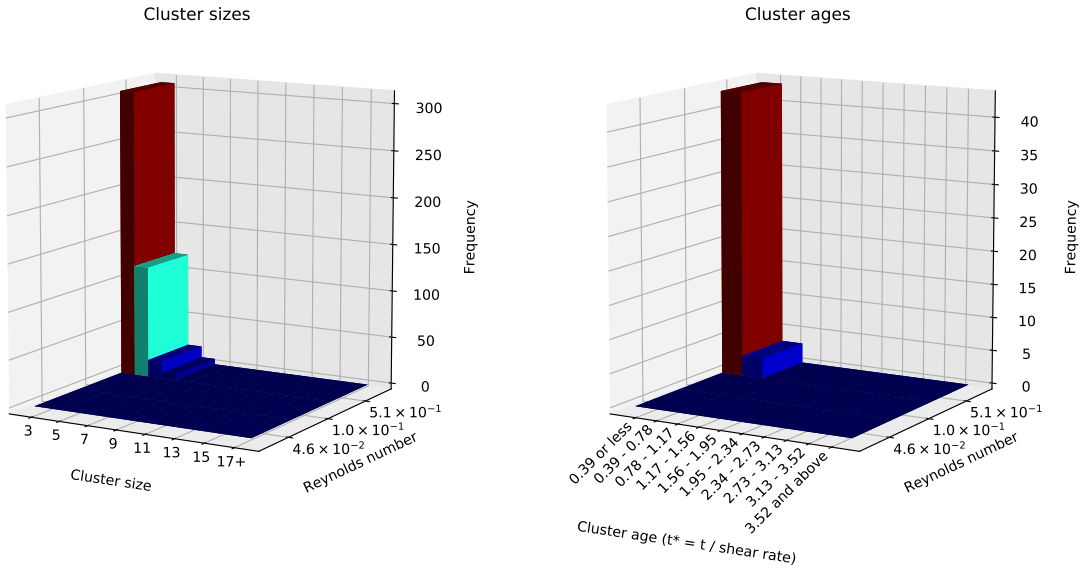

Figure 6.12: Clustering figures for systems of varying shear rates. Left panel: cluster size distribution. Right panel: cluster age distribution. These systems have: $\phi = 0.33\,, \sigma_0 = 0.03\,, K = 0.5\,.$

shear rate to start seeing small, short-lived clusters forming. These clusters appear to be made up of very quick interactions between a few droplets that break down fairly rapidly. The low inertial effects seem unable to overcome the repulsive forces of the droplet interfaces, so they don't get close enough to be classified as a cluster. In more concentrated systems ($\phi = 0.6\,$) clusters also form more frequently at higher shear rates, seen in Fig. 6.13. Here, increasing the shear rate creates larger clusters, with significantly stretched droplets sometimes, as well as longer lasting clusters. As mentioned earlier, this is likely related to the droplet deformability, as well as there being more interactions at a higher shear rate.

6.2.3 When viewed as functions of concentration

When considering the effect of the concentration on the clustering behaviour, this is again inter-dependent on the shear rate. At a low shear rate, there needs to be a very high concentration to start to see clustering behaviour, which can be seen in the previous Figs. 6.12 and 6.13. At higher shear rates, however, the effect of

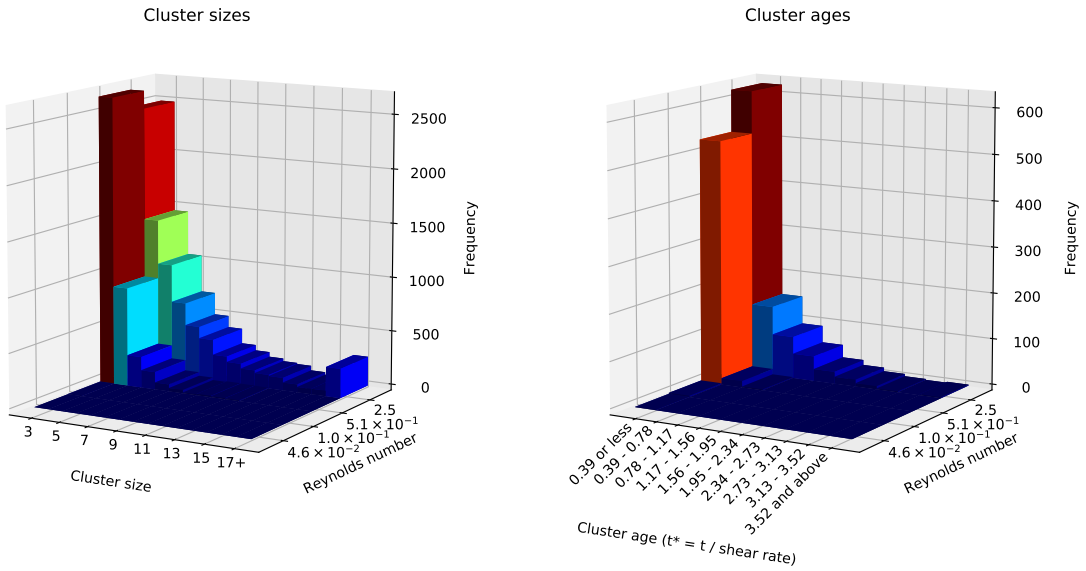

Figure 6.13: Clustering figures for systems of varying shear rates. Left panel: cluster size distribution. Right panel: cluster age distribution. These systems have: $\phi = 0.6\,, \sigma_0 = 0.09\,, K = 0.5\,.$

concentration becomes more gradual, which can be seen in Figs. 6.14 and 6.15. Both the cluster size and cluster lifespan increase with an increase in the concentration. It's clear that as more droplets are added to the flow, the droplets within clusters will have less room to break out due to the surrounding droplets.

Fig 6.15 shows the ellipse estimation breaking down, as it detects many clusters within the layered system. The droplets in this system appear to deform into a square shape, due to the lattice-like layers they are forced into. This square deformation makes the cluster analysis unreliable.

6.2.4 When viewed as functions of viscosity ratio

As with previous data, the viscosity ratio appears to play a much more subtle role on the clustering behaviour. This is visible in Figs. 6.16 and 6.17. The small trends are inconsistent between different datasets. Fig. 6.17 shows very little effect on the number of clusters or the cluster size distribution, whereas the age of the clusters appears to be longer for a higher viscosity ratio. On the other hand, Fig. 6.16 appears to show more clusters forming as viscosity ratio increases (with the size distribution being unaffected), whilst the age of the clusters also gets longer for higher viscosity ratios. Note that the highest viscosity ratio on this figure doesn't keep in line with this trend, which is what was seen in the radial distribution functions.

6.2.5 Comparison to material properties

The formation and flow of these clusters would be expected to affect the properties of the emulsion, i.e. the relative viscosity and sheared self-diffusion coefficient.

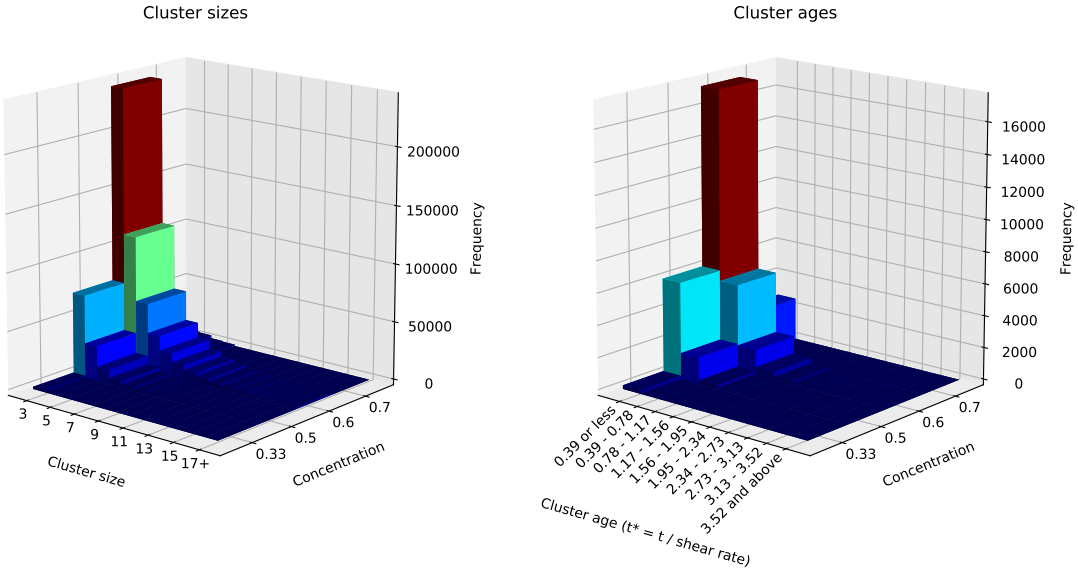

Figure 6.14: Clustering figures for systems of varying concentrations. Left panel: cluster size distribution. Right panel: cluster age distribution. These systems have: $\sigma_0 = 0.03\,, K = 0.5\,, \mathrm{Re} = 5.1 \times 10^{-1}\,, \mathrm{Ca} = 1.4 \times 10^{-1}$. The highest concentration system entered a layered regime and thus minimal clusters are detected.

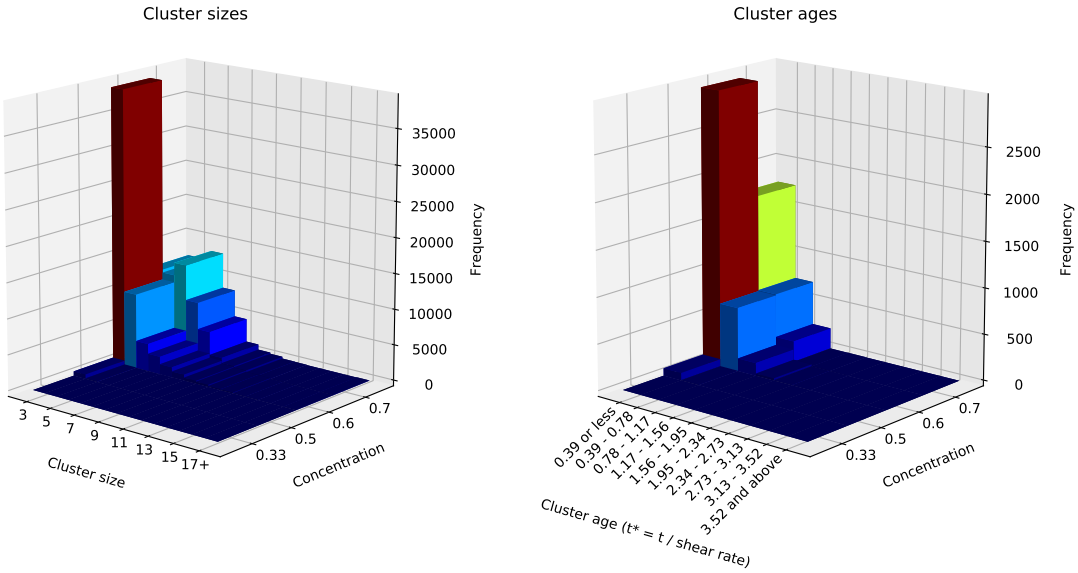

Figure 6.15: Clustering figures for systems of varying concentrations. Left panel: cluster size distribution. Right panel: cluster age distribution. These systems have: $\sigma_0 = 0.09\,, K = 100\,, \mathrm{Re} = 5.1 \times 10^{-1}\,, \mathrm{Ca} = 4.5 \times 10^{-2}$. The highest concentration system entered a layered regime and thus cluster detection is less reliable.

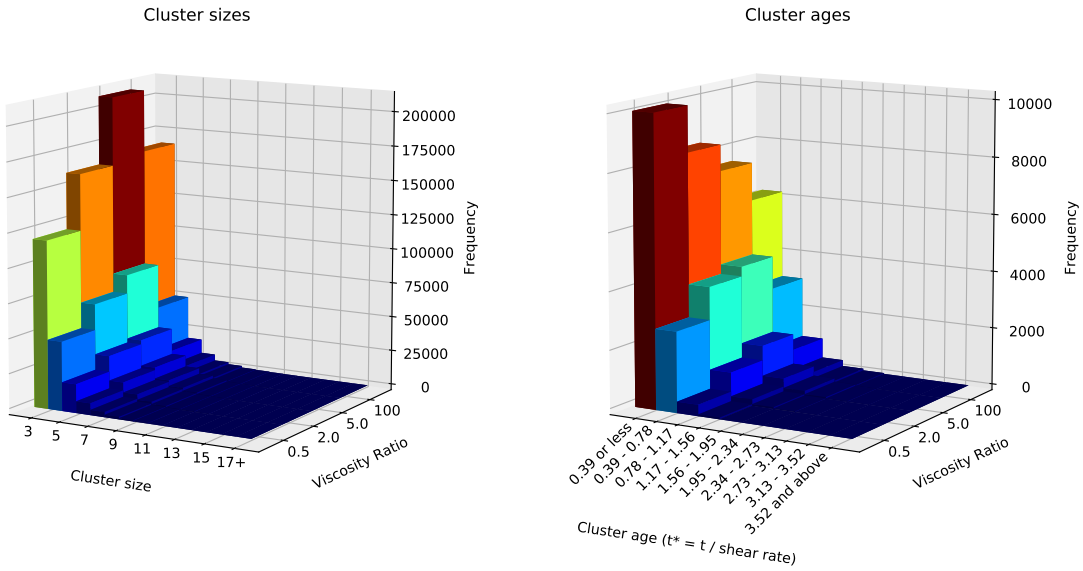

Figure 6.16: Clustering figures for systems of varying viscosity ratios. Left panel: cluster size distribution. Right panel: cluster age distribution. These systems have: $\phi = 0.5\,, \sigma_0 = 0.03\,, \mathrm{Re} = 5.1 \times 10^{-1}\,, \mathrm{Ca} = 1.4 \times 10^{-1}\,.$

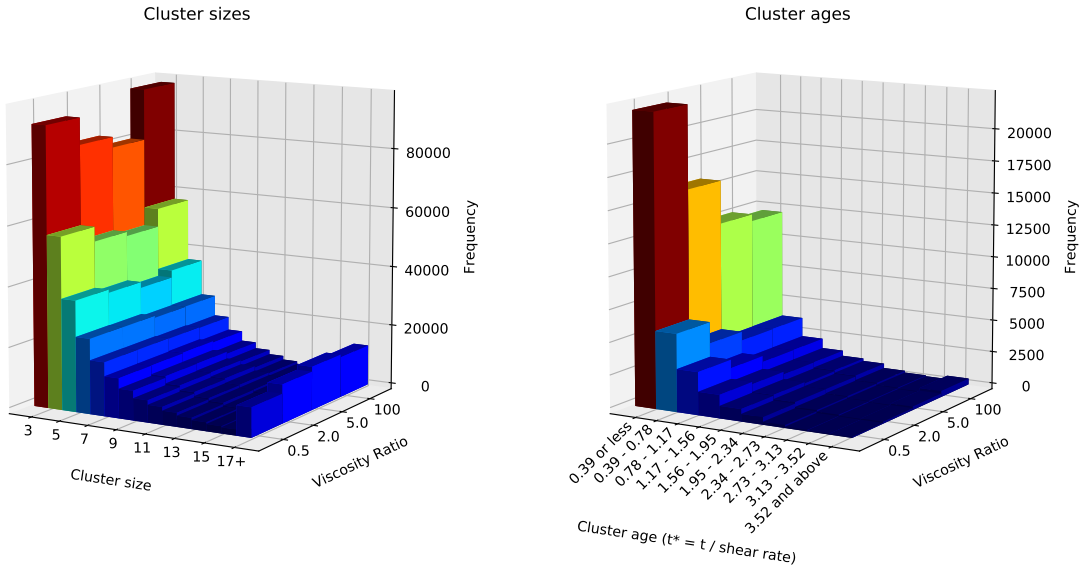

Figure 6.17: Clustering figures for systems of varying viscosity ratios. Left panel: cluster size distribution. Right panel: cluster age distribution. These systems have: $\phi = 0.6\,, \sigma_0 = 0.09\,, \mathrm{Re} = 2.5\,, \mathrm{Ca} = 2.2 \times 10^{-1}\,.$

Comparing the trends in these data sets, the concentration of the emulsion seems to have the same effect on the viscosity, diffusion, and clustering activity, whereby an increase in the concentration increases the given parameter. However, the concentration and increased droplet interactions are likely to be the overwhelming cause of this, rather than the clustering activity. This can be concluded as the opposite effects are witnessed in relation to the shear rate, whereby the increase in shear rate reduces the relative viscosity and sheared self-diffusion coefficient but increases the clustering activity.

A key area where the clusters may impact the macroscopic properties is in the low concentration, high shear rate regime. It can be seen in Fig. 5.9 that there is a slight increase in the relative viscosity in this regime, reversing the overall shear-thinning behaviour. This *shear-thickening* behaviour coincides with the detection of clusters, i.e. clusters don't form in the low concentration regime until the shear rate gets relatively high. As noted by Wagner and Brady [9], this shear-thickening behaviour is known to occur in suspensions due to the formation of clusters. It appears here that the increasing shear rate makes the viscosity decrease, but the formation of clusters impedes the flow at the higher shear rates. The reproduction of such subtle phenomenon shows why experimental data and mesoscopic models are required to inform the development of macroscopic models (particularly when no theoretical solution is known).

6.3 Conclusion

The structure of the fluid and how it changed with various adjustments to fluid properties was shown via the radial distribution function. This insight into the structure reinforced the understanding of the changes in the macroscopic measurements, i.e. the higher shear rates introduce more deformation and allow the droplets to get closer than before, which in turn reduces the sheared self-diffusion coefficient.

Additionally, the clustering behaviour of the droplets was displayed and analysed. An increase in clustering activity coincided with shear thickening in the relative viscosity data, which agrees with literature on suspensions.

Chapter 7

Bidisperse systems

Finally, the previous simulations of monodisperse systems are idealised to enable easier modelling than physical systems that will have some form of droplet size distribution, i.e. they would never be perfectly monodisperse. Clearly many effects of the droplet size distribution will be neglected from these results, in order to study the other phase spaces with more confidence. The model itself requires only the initial conditions to be adjusted in order to change the size distribution, hence the model has now been used to simulate a bidisperse emulsion. Droplets of radius $R = \sqrt{(\frac{889}{\pi})} = 16.8$ were introduced into the flow, in equal numbers to the larger droplets. The size of these droplets is shown in Chapter 4 (Fig. 4.5) to adequately resolve the droplet resting position to within 10% of the highest tested value. Ideally, larger droplets would have been introduced, i.e. droplets of $R = 21$ with $R = 25$, but this would have been too computationally expensive. Also, using slightly more resolved droplets, such as $R = 19$ was felt to not be a large enough difference to the other droplets.

To compare the effect of the bidispersity, the concentration and dimensionless numbers are matched:

- The effective droplet radius is now 18.8 rather than $\sqrt{\frac{1369}{\pi}} = 20.9$,
- The shear rate is adjusted by the ratio (squared) of the new and old droplet radii to ensure matching Reynolds numbers,
- The interfacial tension parameter is adjusted by the same ratio to fix the Capillary number, hence all these simulations use $\sigma_0 = 0.099$,
- The same overall droplet concentration is desired, which means the number of droplets is adjusted as more of the smaller droplets are required.

Now, the effect of introducing a droplet size variation into the flow is firstly visible in Fig. 7.1, showing the relative viscosity. Both sets of data follow very similar trends, but the bidisperse data does increase the relative viscosity in some systems. In particular, the higher concentration data is most affected. Notably,

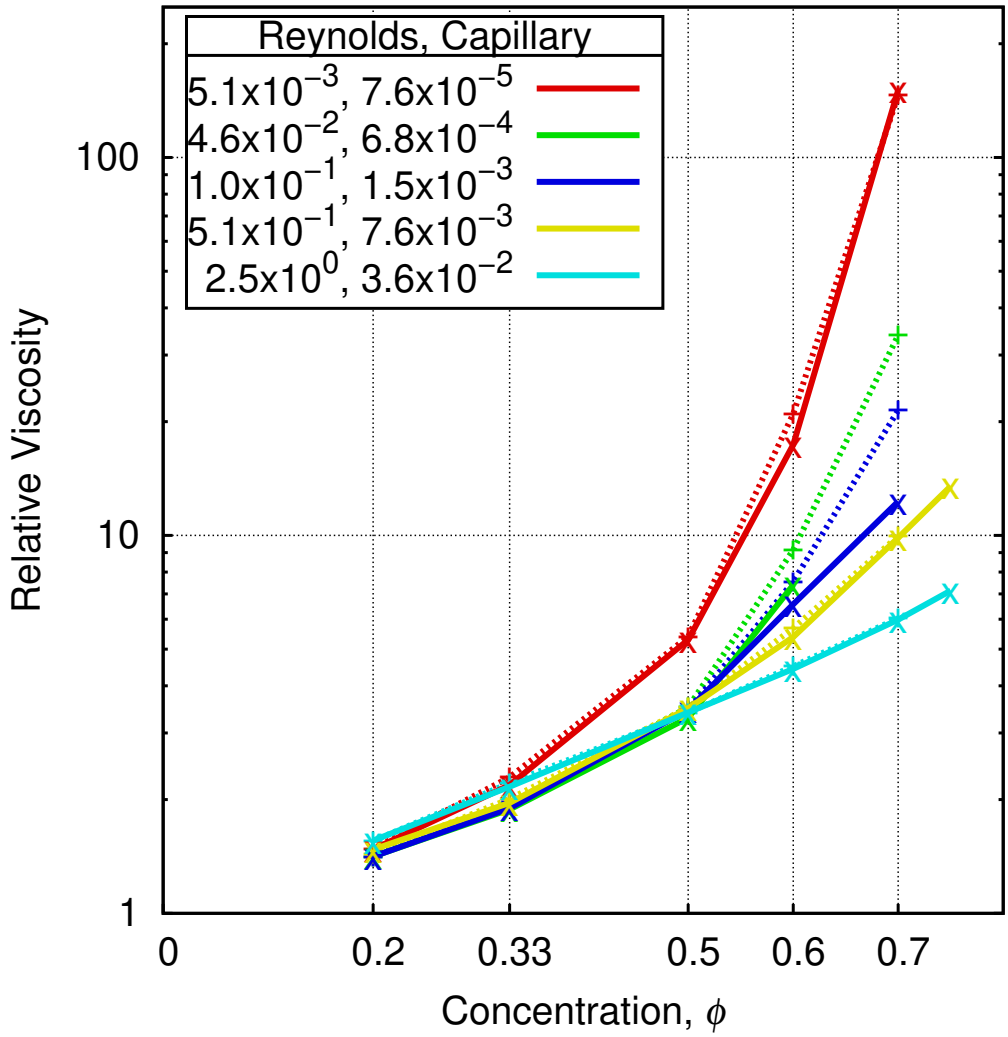

Figure 7.1: A graph of relative viscosity against concentration, each line has a constant Reynolds and Capillary number. Solid lines (crosses) are monodisperse data (visible in previous figures), whilst dotted lines (pluses) are bidisperse data. Both results follow the same trends, but there is a slight increase in viscosity for the bidisperse systems, particularly at high concentrations. Lines are just as a guide to the eye.

the higher concentration regime is where the layered systems form, which appears to be prevented when the droplets are no longer monodisperse. The different sized droplets are likely to prevent the layers forming as layering requires the droplets to flow comfortably behind each other. When other sizes are introduced, the larger droplets are likely to be unstable in the flow behind a smaller droplet and hence the layers don't form. It is conceivable that layers of different sizes could form, however it may be that parallel motion of the droplets interrupts the layering causing them to jump out of their layers; in the monodisperse systems the parallel motion is observed creating waves through the layers and inflicting increased deformation on droplets as they pass each other, hence the effects may be exasperated if two neighbouring layers contain different sized droplets. Of course, it may be that even bidisperse

systems would enter a stable layering regime, given enough simulation time, but this seems unlikely as the bidisperse simulations were run for many times longer than the time it took the monodisperse systems to become layered.

The bidispersity appears to, again, affect the higher concentrations' sheared self-diffusion coefficient results, as shown in Fig. 7.2. The trend is more consistent in

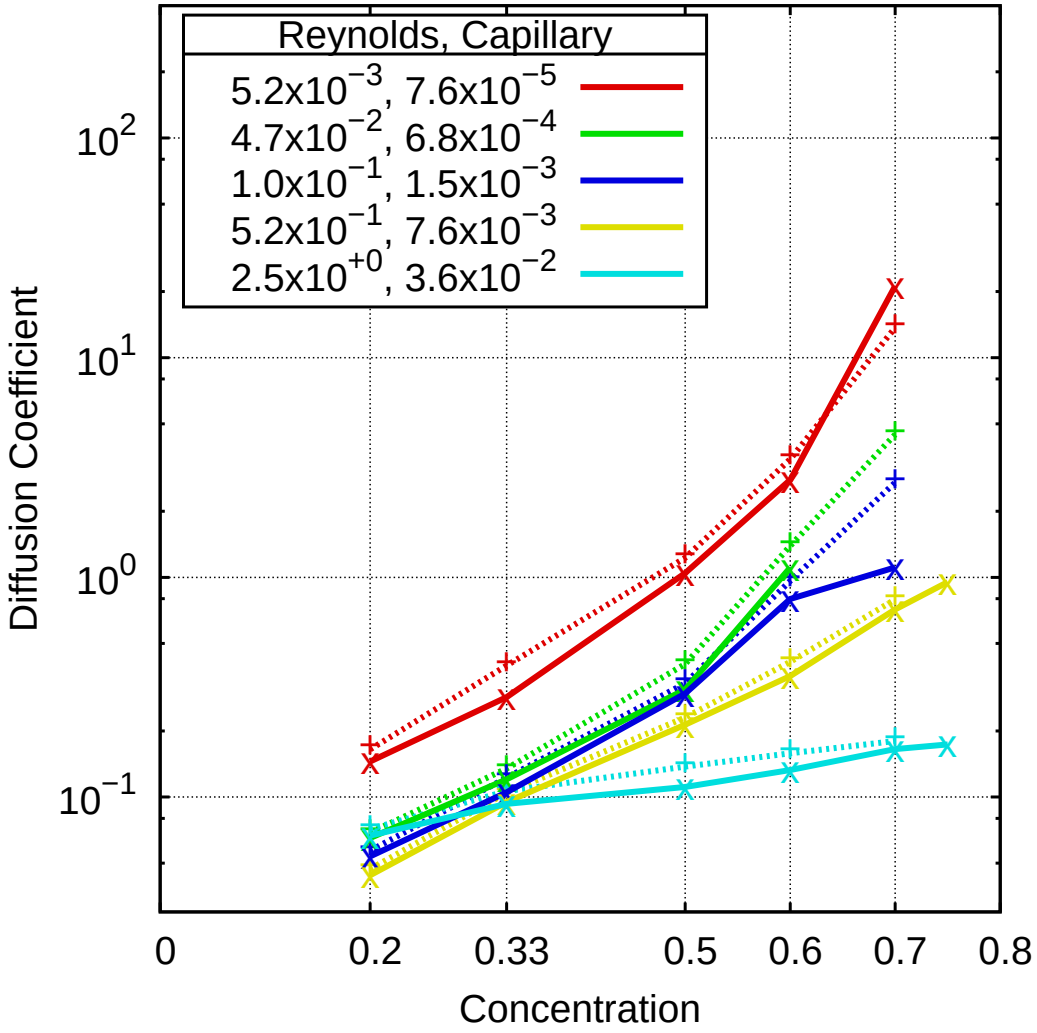

Figure 7.2: A graph of sheared self-diffusion coefficient against concentration, each line has a constant Reynolds and Capillary number. Solid lines (crosses) are monodisperse data, whilst dotted lines (pluses) are bidisperse data. Both results follow the same trends, but the bidispersity prevents the layering behaviour. Lines are just as a guide to the eye.

these measurements, with a clear increase across the data set. Having different sized droplets may provide greater opportunities for droplets to flow into openings that have not been appropriate before, i.e. the smaller droplets may find spaces to flow into (or be forced into) that the original droplets simply couldn't physically fit inside. Again, extra data is visible due to the prevention of the layering behaviour.

When viewed as a function of the shear rate, in Fig. 7.3, there appears to be a more visible and consistent increase in the viscosity when the system is bidisperse.

Again, the modest shear rates and the high concentration systems are most impacted

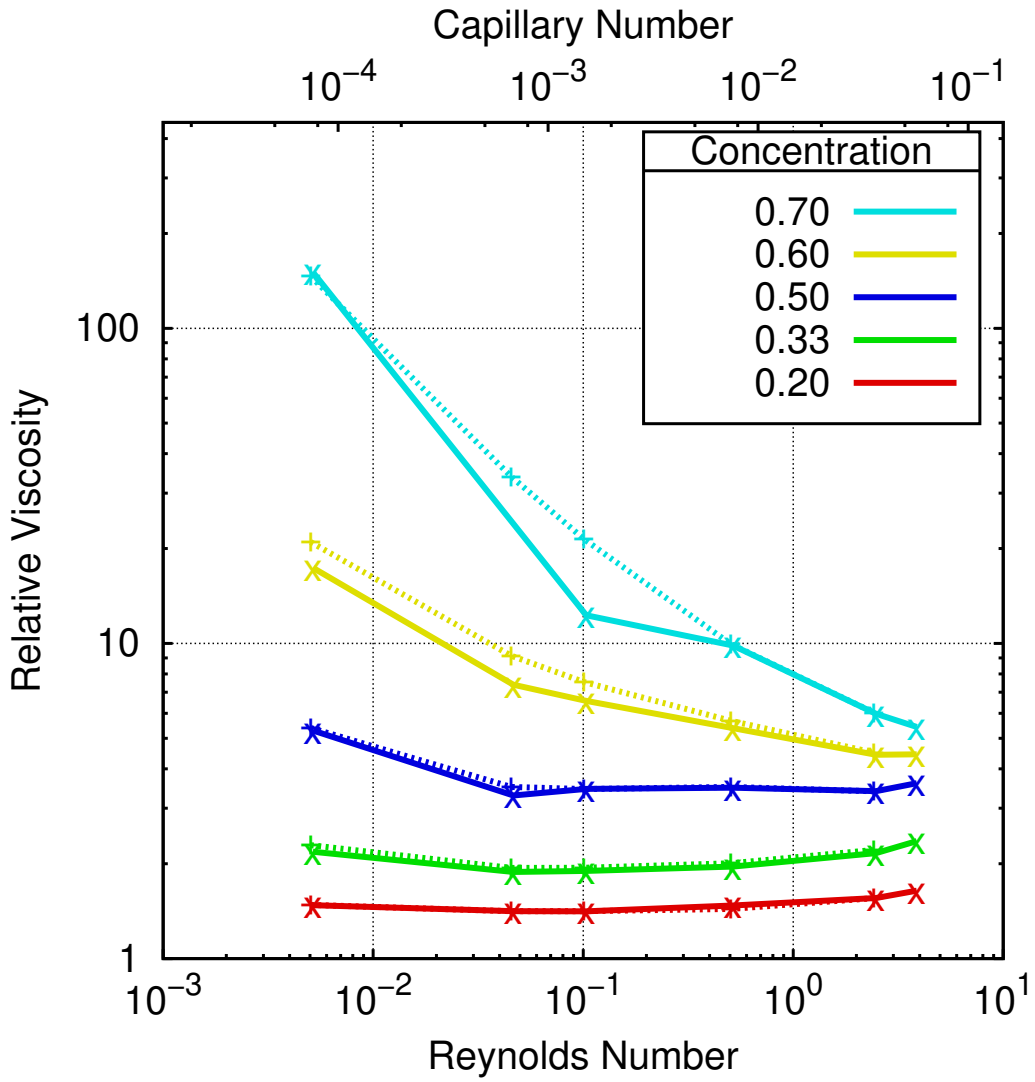

Figure 7.3: A graph of relative viscosity against shear rate, each line has a constant concentration. Solid lines (crosses) are monodisperse data, whilst dotted lines (pluses) are bidisperse data. Both results follow the same trends, but there is a slight increase in viscosity for the bidisperse systems. Lines are just as a guide to the eye.

by the bidispersity. These results corroborate with the study of Javaran et al. [66], whereby the polydispersity of solid particles results in an increase of the relative viscosity. It is worth noting, however, that the witnessed effect depends heavily on the droplet sizes, shear stress, and the proportion of large versus small droplets. Pal [48] shows that as smaller droplets are introduced the relative viscosity can, in fact, decrease to a local minimum and then begin to increase. This effect totally vanishes for larger values of shear stress, whereby the same effect is witnessed as is seen here. The increase in relative viscosity may be less pronounced than that seen by both Pal and Javaran et al. due to the relatively small difference in size between the droplets (24% here and 700% in Pal's work [48]). The work of Javaran et al. [66] also studies a relatively large range of particle sizes, in the range of 4–10

lattice units.

Fig. 7.4 shows the sheared self-diffusion coefficient data as a function of the shear rate. The small increase due to the bidispersity is again visible, with the

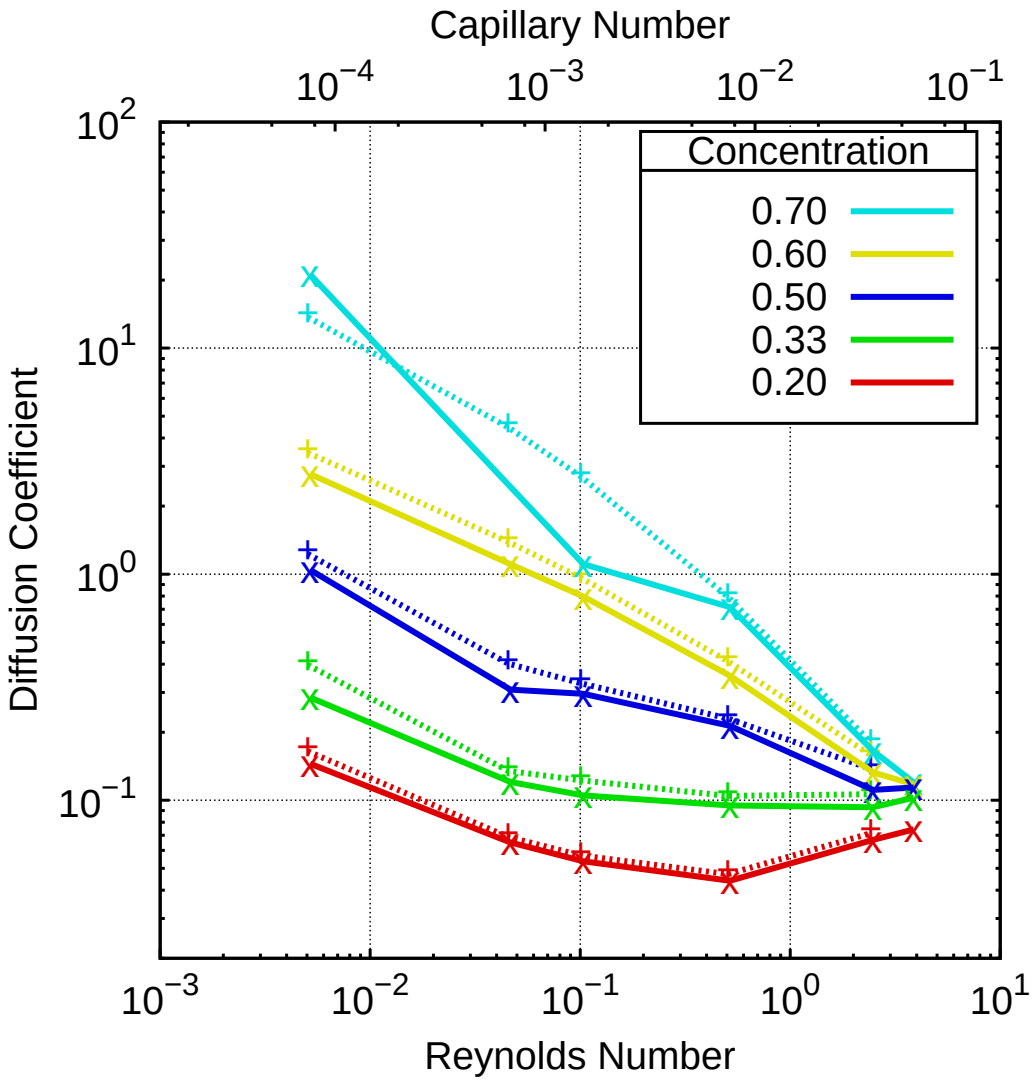

Figure 7.4: A graph of sheared self-diffusion coefficient against shear rate, each line has a constant concentration. Solid lines (crosses) are monodisperse data, whilst dotted lines (pluses) are bidisperse data. Both results follow the same trends, but the highest concentration data is most impacted by the bidispersity. Lines are just as a guide to the eye.

effect becoming more prominent in the higher concentration systems. The increase appears consistent for a varying shear rate. The tendency to converge on a specific sheared self-diffusion coefficient appears unchanged with the addition of smaller droplets.

7.1 Conclusion

To conclude the results chapters of this thesis, and gather exploratory data using the developed method, simulations of bidisperse emulsions were carried out, introducing

smaller droplets into the flow. The bidispersity was seen to increase the relative viscosity and sheared self-diffusion coefficient of the emulsions, which agreed with previous studies of suspensions.

The model is seen to be easily extensible to such systems. Even a bidisperse system is an idealised system, however, initialising with a droplet size distribution would be relatively straightforward.

Chapter 8

Conclusions and Future Work

This chapter concludes the thesis by summarising the outcomes and outlining possible future work. The conclusion also provides an overview of the original contributions that have been put forward, namely:

- the lattice-Boltzmann model of many explicit emulsion droplets, with directly parametrisable interfacial tension parameter and making use of efficient computational techniques, in Chapter 3,
- the periodic pressure boundary condition outlined in Chapter 4,
- the rheological measurements gathered by the developed model and the analysis provided through Chapters 4-6.

8.1 Conclusions

This thesis aimed to model the emergent non-Newtonian behaviour of flowing emulsions. Previous studies in this area either focus on the individual droplet interface or lack a thorough comparison to existing experimental and theoretical work. The computational costs associated with numerical methods at this scale—modelling the fluids and the droplet interface(s)—has usually meant restricting simulations to dilute emulsions, for which non-Newtonian behaviour is less pronounced.

A mesoscopic lattice-Boltzmann method (LBM) was developed and used to model the explicit flow of emulsion droplets. This model was shown to reproduce the rigorous theoretical results of Taylor [6] (see (2.6)) for the viscosity of a dilute emulsion. Similarly, a single-component pipe flow with analytic solution was reproduced; with multi-component simulations beginning to show non-Newtonian behaviour when compared with the power-law viscosity model. A periodic pressure boundary condition was developed that didn't have issues when interacting with multicomponent fluid interfaces with physical pressure steps. Whilst this allowed rheological measurements of emulsions, the solid walls imposed severe boundary effects causing a depletion zone as well as shear banding. The Lees-Edwards boundary

condition was adapted to the emulsion model in order to study the bulk properties of fluids.

This model of the bulk flow then provided a vast amount of data on the macroscopic properties of flowing emulsions and the links to the fluid microstructure. The relative viscosity measurements from the simulations were shown to agree closely with experimental results and macroscopic models. The expected non-Newtonian behaviour did emerge from the simulations, showing shear-thinning behaviour over the majority of the data. Several macroscopic models were compared, with the model of Carreau [12] representing the data most accurately. The majority of the macroscopic non-Newtonian viscosity models incorporate a zero-shear limit whereby the emulsion has Newtonian behaviour, hence the comparisons to macroscopic models would be greatly improved by being able to study even lower shear rates.

The same model is shown to be able to take in to account the viscosity ratio and the interfacial tension forces between the suspending and suspended fluids. The viscosity ratio increases the relative viscosity of the emulsion, as predicted by macroscopic models. Interfacial tension is not present in macroscopic models, yet the impact on the relative viscosity cannot be ignored. It is known that reducing the interfacial energy by introducing more surfactants will reduce the viscosity of an emulsion, however this is complicated as droplets may then become smaller due to the greater surfactant coverage. This model enables the interfacial tension to vary independently and precisely, which allows for the study of this parameter in regards to the macroscopic properties of the fluid.

Whilst the macroscopic properties measured from the simulations agree well with previous studies, the explicitly modelled droplets and the ability to study the microstructure at the same time are the highlight of the work. The explicit model allows the macroscopic behaviour to emerge naturally as a result of the microstructure of the emulsion. For example, the very subtle shear thickening effect in the high-shear low-concentration regime is recovered in the simulations and a cluster analysis shows this coincides with the agglomeration of droplets into clusters. Other studies have highlighted this effect for suspensions (solid particles suspended in a liquid), and it could be expected that the same behaviour would be apparent in emulsions. Yet this behaviour wasn't an assumption in the model, it simply emerged from the droplet hydrodynamics.

Similarly, having access to the precise position and movements of each droplet over time allows computer simulations to easily undertake statistics around this. The sheared self-diffusion coefficient measures the movement of the droplets (or more frequently, particles) perpendicular to the flow, i.e. due to the hydrodynamic interactions of said particles. Outside of simulations, tracer particles that can be tracked must be introduced into the flow, a process that hasn't been extended to emulsions (with deformable droplets). The access to such data allowed for the

measuring of the sheared self-diffusion coefficient for these emulsion simulations, and it is clear that it behaves very similarly to the relative viscosity.

The developed model is also simply extended to bidisperse emulsions, which were also briefly studied here. Introducing a proportion of smaller droplets into the flow was shown to slightly increase both the relative viscosity and sheared self-diffusion coefficient, which is an effect seen in previous studies of suspensions. It has been shown that this increase (in the relative viscosity at least) depends on the shear rate; at low shear rates and with a low proportion of smaller droplets, the relative viscosity can in fact be lower than that of an emulsion of the same concentration with purely the larger droplets.

The range of data collected was limited due to the computational and time costs associated with very low shear systems. If these restrictions were to be lifted, the low-shear limit would then be restricted by the microcurrent activity in the system—these spurious velocities introduced from the multi-component method are of low order, but must be overwhelmed to achieve reliable results. At the high-shear limit, the restriction on the LBM velocity can be overcome by introducing many Lees-Edwards boundary planes. However, there is a physical limit present due to the breakup of the droplets—this already resulted in the exclusion of some data from the current study. The interfacial tension of the droplets could be increased to allow them to withstand greater shear rates, but this introduces larger errors into the multi-component method.

8.2 Future Work

There are several areas where this work could be extended.

Firstly, the introduction of solid particles alongside the emulsion droplets would make the model more applicable to a wide array of complex fluids, such as molten chocolate or ice-creams. Solid particle boundary conditions are well established in the LBM [64, 65], and the combination with an emulsion model is also possible [92].

Similarly, having the model accommodate a density difference between the two fluids would allow for a more accurate representation of various emulsions. The density difference in an oil-water emulsion can vary greatly depending on the oil used, significant in some situations but negligible in others. The developed model would benefit from being able to model this difference.

The fits to macroscopic non-Newtonian models were complicated by the lack of low-shear data, the collection of which is incredibly expensive. Gathering such data would inform the macroscopic model fits, likely increasing the fitting accuracy.

It would be of interest to take the more realistic, and newly predicted, viscosity and sheared self-diffusion data and pass it up the length scales to macroscopic models such as Phillips et al. [47] Such macroscopic models would then be able to reach

larger length scales than achievable by the model here yet still contain the correct mesoscopic physics.

The effect of bidispersity on the relative viscosity is dependant on various factors, most particularly the proportion of small to large droplets. This could be studied in the present model and it would be interesting to see whether the same trend is recovered as in experiments. Additionally, a realistic droplet size distribution could feasibly be simulated, simply by adjusting the initial conditions.

An extension of the work to three dimensions (3D) is a logical next step. It goes without saying that modelling the emulsion droplets in 3D, rather than the infinite cylinders that they are assumed to be in these 2D models, would be more appropriate. Such a system would be very computationally expensive, but as with the validations in Section 3.3 a 3D model could be used on a small scale to validate against the Taylor deformation relation. Moving to 3D would likely improve the models applicability to physical emulsions, but the 2D approximation provides excellent agreement with experimental measurements already.

Word count: 37,600 < 40,000

Appendix A

Chapman-Enskog Analysis

In this appendix a Chapman-Enskog analysis of the lattice-Boltzmann method (LBM) described in Chapter 3 is undertaken. It follows a similar method to the TRT analysis of Servan-Camas and Tsai [119], but applied to the Navier-Stokes equation and multi-component LBM.

The evolution equation of the method is:

$$\begin{aligned} f_i(\mathbf{x}+\mathbf{c}_i\Delta t, t+\Delta t) &= f_i(\mathbf{x},t) - \frac{1}{\tau_s}\left(f_{is}\left(\mathbf{x},t\right) - f_{is}^{(\mathrm{eq})}\left(\mathbf{x},\mathbf{u},\rho,t\right)\right) \\ &\quad - \frac{1}{\tau_a}\left(f_{ia}\left(\mathbf{x},t\right) - f_{ia}^{(\mathrm{eq})}\left(\mathbf{x},\mathbf{u},\rho,t\right)\right) \\ &\quad + \Delta t F_i\,. \end{aligned} \tag{A.1}$$

The symmetric and antisymmetric parts are defined as:

$$\begin{aligned} f_{is} &= \frac{f_i + f_{-i}}{2}, \qquad f_{is}^{(\mathrm{eq})} = \frac{f_i^{(\mathrm{eq})} + f_{-i}^{(\mathrm{eq})}}{2}, \\ f_{ia} &= \frac{f_i - f_{-i}}{2}, \qquad f_{ia}^{(\mathrm{eq})} = \frac{f_i^{(\mathrm{eq})} - f_{-i}^{(\mathrm{eq})}}{2}, \end{aligned} \tag{A.2}$$

where $-i$ refers to the link in the opposite direction to i.

The equilibrium function is:

$$f_i^{(\mathrm{eq})} = t_i\left(\rho + \rho_0\left[\frac{c_{i\alpha}u_\alpha}{c_s^2} + \frac{c_{i\alpha}c_{i\beta}u_\alpha u_\beta}{2c_s^4} - \frac{u_\alpha u_\alpha}{2c_s^2}\right]\right), \tag{A.3}$$

and considering this in the reverse i direction [119]:

$$f_{-i}^{(\mathrm{eq})} = t_i\left(\rho + \rho_0\left[-\frac{c_{i\alpha}u_\alpha}{c_s^2} + \frac{c_{i\alpha}c_{i\beta}u_\alpha u_\beta}{2c_s^4} - \frac{u_\alpha u_\alpha}{2c_s^2}\right]\right). \tag{A.4}$$

Using (A.3) and (A.4) to create the symmetric and antisymmetric parts described

in (A.2):

$$
\begin{aligned}
f_{is}^{(\mathrm{eq})} &= t_i \left(\rho + \rho_0 \left[\frac{c_{i\alpha} c_{i\beta} u_\alpha u_\beta}{2c_s^4} - \frac{u_\alpha u_\alpha}{2c_s^2} \right] \right) , \\
f_{ia}^{(\mathrm{eq})} &= t_i \left[-\rho_0 \frac{c_{i\alpha} u_\alpha}{c_s^2} \right] ,
\end{aligned}
$$

Taking moments of (A.1) gives:

$$
\begin{aligned}
\sum_i f_i &= \sum_i f_i^{(\mathrm{eq})} &&= \rho \\
\sum_i f_i c_{i\alpha} &= \sum_i f_i^{(\mathrm{eq})} c_{i\alpha} &&= \rho_0 u_\alpha \\
\sum_i f_i c_{i\alpha} c_{i\beta} &= \sum_i f_i^{(\mathrm{eq})} c_{i\alpha} c_{i\beta} &&= \Pi_{\alpha\beta}^0 \;=\; c_s^2 \rho \delta_{\alpha\beta} + \rho_0 u_\alpha u_\beta \,,
\end{aligned}
$$

assuming f_i is close to equilibrium. Similarly for the symmetric and antisymmetric parts:

$$
\begin{aligned}
\sum_i f_{is}^{(\mathrm{eq})} &= \rho \,, & \sum_i f_{ia}^{(\mathrm{eq})} &= 0 \,, \\
\sum_i f_{is}^{(\mathrm{eq})} c_{i\alpha} &= 0 \,, & \sum_i f_{ia}^{(\mathrm{eq})} c_{i\alpha} &= \rho_0 u_\alpha \,, \\
\sum_i f_{is}^{(\mathrm{eq})} c_{i\alpha} c_{i\beta} &= \Pi_{\alpha\beta}^0 \,, & \sum_i f_{ia}^{(\mathrm{eq})} c_{i\alpha} c_{i\beta} &= 0 \,.
\end{aligned}
$$

Due to being close to equilibrium, moments of higher f_i become:

$$
\begin{aligned}
\sum_i f_i^{(n)} &= 0, & n \geq 1 \,, \\
\sum_i f_i^{(n)} c_{i\alpha} &= 0, & n \geq 1 \,, \\
\sum_i f_i^{(n)} c_{i\alpha} c_{i\beta} &= \Pi_{\alpha\beta}^{(n)}, & n \geq 1 \,,
\end{aligned}
$$

with the symmetric and antisymmetric parts:

$$
\begin{aligned}
\sum_i f_{is}^{(n)} &= 0, & n \geq 1 \,, \\
\sum_i f_{is}^{(n)} c_{i\alpha} &= 0, & n \geq 0 \,, \\
\sum_i f_{is}^{(n)} c_{i\alpha} c_{i\beta} &= \Pi_{\alpha\beta}^{(n)}, & n \geq 0 \,, \\
\sum_i f_{ia}^{(n)} &= 0, & n \geq 0 \,, \\
\sum_i f_{ia}^{(n)} c_{i\alpha} &= 0, & n \geq 1 \,, \\
\sum_i f_{ia}^{(n)} c_{i\alpha} c_{i\beta} &= 0, & n \geq 0 \,.
\end{aligned}
$$

Now, using the forcing term of Guo et al. [62] to perform a thorough analysis:

$$F_i \;=\; t_i \left[A + \frac{B_\alpha c_{i\alpha}}{c_s^2} + C_{\alpha\beta} \left(\frac{c_{i\alpha}c_{i\beta} - c_s^2 \delta_{\alpha\beta}}{2c_s^4} \right) \right] . \tag{A.5}$$

Note that the specific multi-component force term from Chapter 3 (which in essence adds a coefficient to the last term and sets $A \;=\; B_\alpha \;= 0$) will be considered later to detail the impact of the interfacial tension parameter. The force term has symmetric and antisymmetric parts:

$$\begin{aligned} F_{is} \;&=\; \frac{F_i + F_{-i}}{2} \;=\; t_i \left[A + C_{\alpha\beta} \left(\frac{c_{i\alpha}c_{i\beta} - c_s^2 \delta_{\alpha\beta}}{2c_s^4} \right) \right] , \\ F_{ia} \;&=\; \frac{F_i - F_{-i}}{2} \;=\; t_i \left[\frac{B_\alpha c_{i\alpha}}{c_s^2} \right] . \end{aligned}$$

Taking moments of the force term, (A.5), gives:

$$\begin{aligned} \sum_i F_i \;&=\; A \,, \\ \sum_i F_i c_{i\alpha} \;&=\; B_\alpha \,, \\ \sum_i F_i c_{i\alpha} c_{i\beta} \;&=\; c_s^2 A \delta_{\alpha\beta} + \frac{1}{2} \left[C_{\alpha\beta} + C_{\beta\alpha} \right] , \end{aligned}$$

and for the symmetric and antisymmetric parts:

$$\begin{aligned} \sum_i F_{is} \;&=\; A & \qquad \sum_i F_{ia} \;&=\; 0 \,, \\ \sum_i F_{is} c_{i\alpha} \;&=\; 0 & \qquad \sum_i F_{ia} c_{i\alpha} \;&=\; B_\alpha \,, \\ \sum_i F_{is} c_{i\alpha} c_{i\beta} \;&=\; c_s^2 A \delta_{\alpha\beta} + \frac{1}{2} \left[C_{\alpha\beta} + C_{\beta\alpha} \right] & \qquad \sum_i F_{ia} c_{i\alpha} c_{i\beta} \;&=\; 0 \,, \end{aligned}$$

For the Chapman-Enskog expansion:

$$\partial_t \;=\; \epsilon \partial_{t_1} + \epsilon^2 \partial_{t_2} \tag{A.6}$$

$$\partial_\alpha \;=\; \epsilon \partial_{\alpha_1} \tag{A.7}$$

$$f_i \;=\; f_i^0 + \epsilon f_i^1 + \epsilon^2 f_i^2 \,. \tag{A.8}$$

A Taylor expansion and Chapman-Enskog expansion of (A.1), grouped on orders

of ϵ, gives:

$$
\begin{aligned}
O\left(\epsilon^0\right) \quad & 0 \;=\; -\frac{1}{\tau_s}\left(f_{is}^0 - f_{is}^{(\mathrm{eq})}\right) - \frac{1}{\tau_a}\left(f_{ia}^0 - f_{ia}^{(\mathrm{eq})}\right) \\
O\left(\epsilon^1\right) \quad & \Delta t\left(\partial_{t_1} + c_{i\alpha}\partial_{\alpha_1}\right) f_i^0 \;=\; -\frac{1}{\tau_s} f_{is}^1 - \frac{1}{\tau_a} f_{ia}^1 + \Delta t F_i \qquad \text{(A.9)} \\
O\left(\epsilon^2\right) \quad & \Delta t\partial_{t_1} f_i^1 + \Delta t\partial_{t_2} f_i^0 + \frac{\Delta t}{2}\partial_{t_1}\partial_{t_1} f_i^0 + \Delta t c_{i\alpha}\partial_{\alpha_1} f_i^1 \\
& \Delta t^2 c_{i\alpha}\partial_{t_1}\partial_{\alpha_1} f_i^0 + \frac{\Delta t^2}{2} c_{i\alpha}c_{i\beta}\partial_{\alpha_1}\partial_{\beta_1} f_i^0 \;=\; -\frac{1}{\tau_s} f_{is}^2 - \frac{1}{\tau_a} f_{ia}^2 \\
\Longrightarrow \quad & \Delta t\partial_{t_2} f_i^0 + \Delta t\left(\partial_{t_1} + c_{i\alpha}\partial_{\alpha_1}\right) f_i^1 + \frac{\Delta t^2}{2}\left(\partial_{t_1} + c_{i\alpha}\partial_{\alpha_1}\right)^2 f_i^0 \\
& \;=\; -\frac{1}{\tau_s} f_{is}^2 - \frac{1}{\tau_a} f_{ia}^2 \qquad \text{(A.10)}
\end{aligned}
$$

Taking the symmetric expression of (A.9):

$$
\begin{aligned}
\Delta t\left(\partial_{t_1} f_{is}^0 + c_{i\alpha}\partial_{\alpha_1} f_{ia}^0\right) \;&=\; -\frac{1}{\tau_s} f_{is}^1 + \Delta t F_{is}\,, \\
\Longrightarrow \quad f_{is}^1 \;&=\; -\Delta t\tau_s\left(\partial_{t_1} f_{is}^0 + c_{i\alpha}\partial_{\alpha_1} f_{ia}^0\right) + \tau_s \Delta t F_{is}\,. \qquad \text{(A.11)}
\end{aligned}
$$

Now taking the antisymmetric expression of (A.9):

$$
\begin{aligned}
\Delta t\left(\partial_{t_1} f_{ia}^0 + c_{i\alpha}\partial_{\alpha_1} f_{is}^0\right) \;&=\; -\frac{1}{\tau_a} f_{ia}^1 + \Delta t F_{ia}\,, \\
\Longrightarrow \quad f_{ia}^1 \;&=\; -\Delta t\tau_a\left(\partial_{t_1} f_{ia}^0 + c_{i\alpha}\partial_{\alpha_1} f_{is}^0\right) + \tau_a \Delta t F_{ia}\,. \qquad \text{(A.12)}
\end{aligned}
$$

Combining the symmetric and antisymmetric parts, (A.11) + (A.12), gives:

$$
\begin{aligned}
f_i^1 \;=\; & -\Delta t\tau_s\left(\partial_{t_1} f_{is}^0 + c_{i\alpha}\partial_{\alpha_1} f_{ia}^0\right) - \Delta t\tau_a\left(\partial_{t_1} f_{ia}^0 + c_{i\alpha}\partial_{\alpha_1} f_{is}^0\right) \\
& + \Delta t\left(\tau_s F_{is} + \tau_a F_{ia}\right)\,, \qquad \text{(A.13)}
\end{aligned}
$$

Substituting (A.13) into (A.10) gives:

$$
\begin{aligned}
& \Delta t\partial_{t_2} f_i^0 + \Delta t\left(\partial_{t_1} + c_{i\alpha}\partial_{\alpha_1}\right)\Big[-\Delta t\tau_s\left(\partial_{t_1} f_{is}^0 + c_{i\alpha}\partial_{\alpha_1} f_{ia}^0\right) \\
& -\Delta t\tau_a\left(\partial_{t_1} f_{ia}^0 + c_{i\alpha}\partial_{\alpha_1} f_{is}^0\right) + \Delta t\left(\tau_s F_{is} + \tau_a F_{ia}\right)\Big] \\
& + \frac{\Delta t^2}{2}\left(\partial_{t_1} + c_{i\alpha}\partial_{\alpha_1}\right)^2 f_i^0 \;=\; -\frac{1}{\tau_s} f_{is}^2 - \frac{1}{\tau_a} f_{ia}^2
\end{aligned}
$$

$$
\begin{aligned}
\implies -\frac{1}{\tau_s} f_{is}^2 - \frac{1}{\tau_a} f_{ia}^2 \;=\;& \Delta t \partial_{t_2} f_i^0 \\
&- \Delta t^2 \tau_s \left(\partial_{t_1} + c_{i\alpha}\partial_{\alpha_1}\right)\left(\partial_{t_1} f_{is}^0 + c_{i\alpha}\partial_{\alpha_1} f_{ia}^0\right) \\
&- \Delta t^2 \tau_a \left(\partial_{t_1} + c_{i\alpha}\partial_{\alpha_1}\right)\left(\partial_{t_1} f_{ia}^0 + c_{i\alpha}\partial_{\alpha_1} f_{is}^0\right) \\
&+ \Delta t^2 \quad \left(\partial_{t_1} + c_{i\alpha}\partial_{\alpha_1}\right)\left(\tau_s F_{is} + \tau_a F_{ia}\right) \\
&+ \frac{\Delta t^2}{2}\partial_{t_1}\partial_{t_1} f_i^0 + \frac{\Delta t^2}{2} c_{i\alpha} c_{i\beta}\partial_{\alpha_1}\partial_{\beta_1} f_i^0 \\
&+ \Delta t^2 \partial_{t_1} c_{i\alpha}\partial_{\alpha_1} f_i^0 \,. \qquad \text{(A.14)}
\end{aligned}
$$

Considering this from the opposite i direction:

$$
\begin{aligned}
\implies -\frac{1}{\tau_s} f_{-is}^2 - \frac{1}{\tau_a} f_{-ia}^2 \;=\;& \Delta t \partial_{t_2} f_{-i}^0 \\
&- \Delta t^2 \tau_s \left(\partial_{t_1} - c_{i\alpha}\partial_{\alpha_1}\right)\left(\partial_{t_1} f_{-is}^0 - c_{i\alpha}\partial_{\alpha_1} f_{-ia}^0\right) \\
&- \Delta t^2 \tau_a \left(\partial_{t_1} - c_{i\alpha}\partial_{\alpha_1}\right)\left(\partial_{t_1} f_{-ia}^0 - c_{i\alpha}\partial_{\alpha_1} f_{-is}^0\right) \\
&+ \Delta t^2 \quad \left(\partial_{t_1} - c_{i\alpha}\partial_{\alpha_1}\right)\left(\tau_s F_{-is} + \tau_a F_{-ia}\right) \\
&+ \frac{\Delta t^2}{2}\partial_{t_1}\partial_{t_1} f_{-i}^0 + \frac{\Delta t^2}{2} c_{i\alpha} c_{i\beta}\partial_{\alpha_1}\partial_{\beta_1} f_{-i}^0 \\
&- \Delta t^2 \partial_{t_1} c_{i\alpha}\partial_{\alpha_1} f_{-i}^0 \,. \qquad \text{(A.15)}
\end{aligned}
$$

Using (A.14) and (A.15) to construct the symmetric expression:

$$
\begin{aligned}
-\frac{2}{\tau_s} f_{is}^2 \;=\;& 2\Delta t \partial_{t_2} f_{si}^0 \\
&- 2\Delta t^2 \tau_s \left(\partial_{t_1}\partial_{t_1} f_{is}^0 + \partial_{t_1} c_{i\alpha}\partial_{\alpha_1} f_{ia}^0\right) \\
&- 2\Delta t^2 \tau_a \left(\partial_{t_1} c_{i\alpha}\partial_{\alpha_1} f_{ia}^0 + c_{i\alpha} c_{i\beta}\partial_{\alpha_1}\partial_{\beta_1} f_{is}^0\right) \\
&+ 2\Delta t^2 \left(\tau_s \partial_{t_1} F_{is} + \tau_a c_{i\alpha}\partial_{\alpha_1} F_{ia}\right) \\
&+ \Delta t^2 \partial_{t_1}\partial_{t_1} f_{is}^0 + \Delta t^2 c_{i\alpha} c_{i\beta}\partial_{\alpha_1}\partial_{\beta_1} f_{is}^0 \\
&+ 2\Delta t^2 \partial_{t_1} c_{i\alpha}\partial_{\alpha_1} f_{ia}^0 \,,
\end{aligned}
$$

$$
\begin{aligned}
\implies -f_{is}^2 \;=\;& \Delta t \tau_s \partial_{t_2} f_{si}^0 \\
&- \Delta t^2 {\tau_s}^2 \left(\partial_{t_1}\partial_{t_1} f_{is}^0 + \partial_{t_1} c_{i\alpha}\partial_{\alpha_1} f_{ia}^0\right) \\
&- \Delta t^2 \tau_s \tau_a \left(\partial_{t_1} c_{i\alpha}\partial_{\alpha_1} f_{ia}^0 + c_{i\alpha} c_{i\beta}\partial_{\alpha_1}\partial_{\beta_1} f_{is}^0\right) \\
&+ \Delta t^2 \tau_s \left(\tau_s \partial_{t_1} F_{is} + \tau_a c_{i\alpha}\partial_{\alpha_1} F_{ia}\right) \\
&+ \frac{\Delta t^2}{2}\tau_s \partial_{t_1}\partial_{t_1} f_{is}^0 + \frac{\Delta t^2}{2}\tau_s c_{i\alpha} c_{i\beta}\partial_{\alpha_1}\partial_{\beta_1} f_{is}^0 \\
&+ \Delta t^2 \tau_s \partial_{t_1} c_{i\alpha}\partial_{\alpha_1} f_{ia}^0 \,. \qquad \text{(A.16)}
\end{aligned}
$$

Similarly, the antisymmetric expression:

$$\begin{aligned}
-\frac{2}{\tau_a} f_{ia}^2 \;=\;& 2\Delta t \partial_{t_2} f_{ai}^0 \\
&- 2\Delta t^2 \tau_s \left(\partial_{t_1} c_{i\alpha} \partial_{\alpha_1} f_{is}^0 + c_{i\alpha} c_{i\beta} \partial_{\alpha_1} \partial_{\beta_1} f_{ia}^0 \right) \\
&- 2\Delta t^2 \tau_a \left(\partial_{t_1} \partial_{t_1} f_{ia}^0 + \partial_{t_1} c_{i\alpha} \partial_{\alpha_1} f_{is}^0 \right) \\
&+ 2\Delta t^2 \left(\tau_a \partial_{t_1} F_{ia} + \tau_s c_{i\alpha} \partial_{\alpha_1} F_{is} \right) \\
&+ \Delta t^2 \partial_{t_1} \partial_{t_1} f_{ia}^0 + \Delta t^2 c_{i\alpha} c_{i\beta} \partial_{\alpha_1} \partial_{\beta_1} f_{ia}^0 \\
&+ 2\Delta t^2 \partial_{t_1} c_{i\alpha} \partial_{\alpha_1} f_{is}^0 \,, \\
\\
\implies -f_{ia}^2 \;=\;& \Delta t \tau_a \partial_{t_2} f_{ai}^0 \\
&- \Delta t^2 \tau_s \tau_a \left(\partial_{t_1} c_{i\alpha} \partial_{\alpha_1} f_{is}^0 + c_{i\alpha} c_{i\beta} \partial_{\alpha_1} \partial_{\beta_1} f_{ia}^0 \right) \\
&- \Delta t^2 {\tau_a}^2 \left(\partial_{t_1} \partial_{t_1} f_{ia}^0 + \partial_{t_1} c_{i\alpha} \partial_{\alpha_1} f_{is}^0 \right) \\
&+ \Delta t^2 \tau_a \left(\tau_a \partial_{t_1} F_{ia} + \tau_s c_{i\alpha} \partial_{\alpha_1} F_{is} \right) \\
&+ \frac{\Delta t^2}{2} \tau_a \partial_{t_1} \partial_{t_1} f_{ia}^0 + \frac{\Delta t^2}{2} \tau_a c_{i\alpha} c_{i\beta} \partial_{\alpha_1} \partial_{\beta_1} f_{ia}^0 \\
&+ \Delta t^2 \tau_a \partial_{t_1} c_{i\alpha} \partial_{\alpha_1} f_{is}^0 \,. \qquad \text{(A.17)}
\end{aligned}$$

Combining the symmetric and antisymmetric parts, (A.16) + (A.17), gives:

$$\begin{aligned}
-f_{is}^2 - f_{ia}^2 \;=\;& \Delta t \tau_s \partial_{t_2} f_{si}^0 + \Delta t \tau_a \partial_{t_2} f_{ai}^0 \\
&- \Delta t^2 {\tau_s}^2 \left(\partial_{t_1} \partial_{t_1} f_{is}^0 + \partial_{t_1} c_{i\alpha} \partial_{\alpha_1} f_{ia}^0 \right) \\
&- \Delta t^2 \tau_s \tau_a \left(\partial_{t_1} c_{i\alpha} \partial_{\alpha_1} f_{is}^0 + c_{i\alpha} c_{i\beta} \partial_{\alpha_1} \partial_{\beta_1} f_{ia}^0 \right) \\
&- \Delta t^2 {\tau_a}^2 \left(\partial_{t_1} \partial_{t_1} f_{ia}^0 + \partial_{t_1} c_{i\alpha} \partial_{\alpha_1} f_{is}^0 \right) \\
&- \Delta t^2 \tau_s \tau_a \left(\partial_{t_1} c_{i\alpha} \partial_{\alpha_1} f_{ia}^0 + c_{i\alpha} c_{i\beta} \partial_{\alpha_1} \partial_{\beta_1} f_{is}^0 \right) \\
&+ \Delta t^2 \tau_s \left(\tau_s \partial_{t_1} F_{is} + \tau_a c_{i\alpha} \partial_{\alpha_1} F_{ia} \right) \\
&+ \Delta t^2 \tau_a \left(\tau_a \partial_{t_1} F_{ia} + \tau_s c_{i\alpha} \partial_{\alpha_1} F_{is} \right) \\
&+ \frac{\Delta t^2}{2} \tau_s \partial_{t_1} \partial_{t_1} f_{is}^0 + \frac{\Delta t^2}{2} \tau_a \partial_{t_1} \partial_{t_1} f_{ia}^0 \\
&+ \frac{\Delta t^2}{2} \tau_s c_{i\alpha} c_{i\beta} \partial_{\alpha_1} \partial_{\beta_1} f_{is}^0 + \frac{\Delta t^2}{2} \tau_a c_{i\alpha} c_{i\beta} \partial_{\alpha_1} \partial_{\beta_1} f_{ia}^0 \\
&+ \Delta t^2 \tau_s \partial_{t_1} c_{i\alpha} \partial_{\alpha_1} f_{ia}^0 + \Delta t^2 \tau_a \partial_{t_1} c_{i\alpha} \partial_{\alpha_1} f_{is}^0
\end{aligned}$$

$$\begin{aligned}
\implies -f_i^2 \;=\;& \Delta t\tau_s\partial_{t_2}f_{si}^0 + \Delta t\tau_a\partial_{t_2}f_{ai}^0 + \\
& - \Delta t^2\tau_s\left[\left(\tau_s-\frac{1}{2}\right)\partial_{t_1}\partial_{t_1}f_{is}^0 + (\tau_s+\tau_a-1)\,\partial_{t_1}c_{i\alpha}\partial_{\alpha_1}f_{ia}^0\right. \\
& \qquad \left. + \left(\tau_a-\frac{1}{2}\right)c_{i\alpha}c_{i\beta}\partial_{\alpha_1}\partial_{\beta_1}f_{is}^0 - \tau_s\partial_{t_1}F_{is} - \tau_a c_{i\alpha}\partial_{\alpha_1}F_{ia}\right] + \\
& - \Delta t^2\tau_a\left[\left(\tau_a-\frac{1}{2}\right)\partial_{t_1}\partial_{t_1}f_{ia}^0 + (\tau_s+\tau_a-1)\,\partial_{t_1}c_{i\alpha}\partial_{\alpha_1}f_{is}^0\right. \\
& \qquad \left. + \left(\tau_a-\frac{1}{2}\right)c_{i\alpha}c_{i\beta}\partial_{\alpha_1}\partial_{\beta_1}f_{ia}^0 - \tau_a\partial_{t_1}F_{ia} - \tau_s c_{i\alpha}\partial_{\alpha_1}F_{is}\right]. \qquad \text{(A.18)}
\end{aligned}$$

Taking the zero$^{\text{th}}$ moments of (A.9) and (A.10):

$$\begin{aligned}
\sum_i (\text{A.9}) \qquad & \Delta t\left(\partial_{t_1}\rho + \rho_0\partial_{\alpha_1}u_\alpha\right) \;=\; \Delta t A \\
& \implies \partial_{t_1}\rho + \rho_0\partial_{\alpha_1}u_\alpha \;=\; A\,, \qquad \text{(A.19)}
\end{aligned}$$

$$\begin{aligned}
\sum_i (\text{A.10}) \qquad & \Delta t\partial_{t_2}\rho + \frac{\Delta t^2}{2}\left(\partial_{t_1}\partial_{t_1}\rho + 2\rho_0\partial_{t_1}\partial_{\alpha_1}u_\alpha + \partial_{\alpha_1}\partial_{\beta_1}\Pi_{\alpha\beta}^0\right) + \\
& - \Delta t^2\partial_{\alpha_1}mF_\alpha \;=\; 0 \\
\implies & \partial_{t_2}\rho + \frac{\Delta t}{2}\left(\partial_{t_1}\partial_{t_1}\rho + 2\rho_0\partial_{t_1}\partial_{\alpha_1}u_\alpha + \partial_{\alpha_1}\partial_{\beta_1}\Pi_{\alpha\beta}^0\right) \;=\; \Delta t\partial_{\alpha_1}mF_\alpha\,. \qquad \text{(A.20)}
\end{aligned}$$

Taking the first moment of (A.13):

$$\begin{aligned}
\sum_i c_{i\alpha}(\text{A.13}) \qquad & -mF_\alpha\Delta t \;=\; -\Delta t\tau_a\left(\rho_0\partial_{t_1}u_\alpha + \partial_{\beta_1}\Pi_{\alpha\beta}^0\right) + \Delta t\tau_a B_\alpha \\
\text{Let } B_\alpha \;&=\; nF_\alpha \qquad \text{(A.21)} \\
\implies \rho_0\partial_{t_1}u_\alpha + \partial_{\beta_1}\Pi_{\alpha\beta}^0 \;&=\; \left(\frac{m}{\tau_a}+n\right)F_\alpha\,. \qquad \text{(A.22)}
\end{aligned}$$

Considering (A.19) to (A.22), to obtain the Euler equation let:

$$\frac{m}{\tau_a} + n \;=\; 1 \qquad \text{and} \qquad A = 0\,. \qquad \text{(A.23)}$$

Taking the first moment of (A.18):

$$\begin{aligned}
\sum_i c_{i\gamma}(\text{A.18}) \qquad & -\sum_i c_{i\gamma}f_i^2 \;=\; \Delta t\tau_a\rho_0\partial_{t_2}u_\gamma \\
& - \Delta t^2\tau_a\left[\left(\tau_a-\frac{1}{2}\right)\rho_0\partial_{t_1}\partial_{t_1}u_\alpha + (\tau_a+\tau_s-1)\,\partial_{t_1}\partial_{\alpha_1}\Pi_{\gamma\alpha}^0\right. \\
& \qquad + \left(\tau_s-\frac{1}{2}\right)\rho_0 c_s^2\partial_{\alpha_1}\partial_{\beta_1}\left(u_\alpha\delta_{\beta\gamma} + u_\beta\delta_{\alpha\gamma} + u_\gamma\delta_{\alpha\beta}\right) \\
& \qquad \left. -\tau_a\partial_{\alpha_1}nF_\gamma - \tau_s\partial_{\alpha_1}\left(c_s^2A\delta_{\alpha\gamma} + \frac{1}{2}\left(C_{\alpha\gamma}+C_{\gamma\alpha}\right)\right)\right]
\end{aligned}$$

$$\begin{aligned}\implies \sum_i c_{i\gamma} f_i^2 \;=\; & -\Delta t \tau_a \rho_0 \partial_{t_2} u_\gamma + \Delta t^2 \tau_a \left(\tau_a - \frac{1}{2}\right)\left[\rho_0 \partial_{t_1}\partial_{t_1} u_\gamma + \partial_{t_1}\partial_{\alpha_1}\Pi^0_{\gamma\alpha}\right] \\ & + \Delta t^2 \tau_a \left(\tau_s - \frac{1}{2}\right)\left[\partial_{t_1}\partial_{\alpha_1}\Pi^0_{\gamma\alpha} + c_s^2 \rho_0 \partial_{\alpha_1}\partial_{\beta_1}\left(u_\alpha \delta_{\beta\gamma} + u_\beta \delta_{\alpha\gamma} + u_\gamma \delta_{\alpha\beta}\right)\right] \\ & - \Delta t^2 {\tau_a}^2 \partial_{t_1} n F_\gamma - \Delta t^2 \tau_a \tau_s \partial_{\alpha_1}\left(c_s^2 A \delta_{\alpha\gamma} + \frac{1}{2}\left(C_{\alpha\gamma} + C_{\gamma\alpha}\right)\right). \end{aligned} \tag{A.24}$$

Now, the second moment of (A.13):

$$\begin{aligned}\sum_i c_{i\mu} c_{i\nu} (\text{A.13}) \qquad \sum_i c_{i\mu} c_{i\nu} f_i^1 \;=\; & -\Delta t \tau_s \partial_{t_1} \Pi^0_{\mu\nu} - \Delta t \rho_0 c_s^2 \partial_{\alpha_1}\left(u_\alpha \delta_{\mu\nu} + u_\mu \delta_{\alpha\nu} + u_\nu \delta_{\alpha\mu}\right) \\ & + \Delta t \tau_s \left(c_s^2 A \delta_{\mu\nu} + \frac{1}{2}\left(C_{\mu\nu} + C_{\nu\mu}\right)\right). \end{aligned} \tag{A.25}$$

Using (A.19) and (A.22) in (A.20):

$$\begin{aligned} & \partial_{t_2}\rho - \frac{\Delta t}{2}\partial_{\alpha_1}\left[-\partial_{\beta_1}\Pi^0_{\alpha\beta} + F_\alpha\left(\frac{m}{\tau_a} + n\right)\right] \\ & \quad + \Delta t \partial_{\alpha_1}\left[-\partial_{\beta_1}\Pi^0_{\alpha\beta} + F_\alpha\left(\frac{m}{\tau_a} + n\right)\right] + \frac{\Delta t}{2}\partial_{\alpha_1}\partial_{\beta_1}\Pi^0_{\alpha\beta} \\ & \quad = \; \Delta t \partial_{\alpha_1} m F_\alpha \,. \end{aligned} \tag{A.26}$$

Cancelling $\Pi^0_{\alpha\beta}$ terms and applying (A.23):

$$\begin{aligned} \implies \qquad \partial_{t_2}\rho \;&=\; \Delta t \partial_{\alpha_1} F_\alpha \left(m - \frac{1}{2}\right) \\ \therefore \qquad m \;&=\; \frac{1}{2} \quad \text{hence} \quad n = 1 - \frac{1}{2\tau_a}\,. \end{aligned} \tag{A.27}$$

Using (A.22) in (A.24):

$$\begin{aligned} 0 \;=\; & \rho_0 \partial_{t_2} u_\gamma + \Delta t \left(\tau_a - \frac{1}{2}\right)\left[\rho_0 \partial_{t_1}\partial_{t_1} u_\gamma + \partial_{t_1}\partial_{\alpha_1}\Pi^0_{\gamma\alpha}\right] \\ & + \Delta t \left(\tau_s - \frac{1}{2}\right)\left[\partial_{t_1}\partial_{\alpha_1}\Pi^0_{\gamma\alpha} + c_s^2 \rho_0 \partial_{\alpha_1}\partial_{\beta_1}\left(u_\alpha \delta_{\beta\gamma} + u_\beta \delta_{\alpha\gamma} + u_\gamma \delta_{\alpha\beta}\right)\right] \\ & - \Delta t \tau_a \partial_{t_1} n F_\gamma - \Delta t \tau_s \partial_{\alpha_1}\left[\frac{1}{2}\left(C_{\alpha\gamma} + C_{\gamma\alpha}\right)\right]. \end{aligned}$$

Using (A.22) again and gathering terms:

$$\begin{aligned} \implies \qquad \rho_0 \partial_{t_2} u_\gamma \;=\; & \left(\Delta t \left(\tau_a - \frac{1}{2}\right)\left(\frac{m}{\tau_a} + n\right) - \Delta t \tau_a n\right)\partial_{t_1} F_\gamma \\ & + \Delta t \left(\tau_s - \frac{1}{2}\right)\partial_{t_1}\partial_{\alpha_1}\left(\rho c_s^2 \delta_{\alpha\gamma} + \rho_0 u_\alpha u_\gamma\right) \\ & + \Delta t \left(\tau_s - \frac{1}{2}\right) c_s^2 \rho_0 \partial_{\alpha_1}\left(\partial_{\gamma_1} u_\alpha + \partial_{\alpha_1} u_\gamma\right) \\ & + \Delta t \left(\tau_s - \frac{1}{2}\right) c_s^2 \rho_0 \partial_{\gamma_1}\partial_{\alpha_1} u_\alpha \\ & - \Delta t \tau_s \partial_{\alpha_1}\left[\frac{1}{2}\left(C_{\alpha\gamma} + C_{\gamma\alpha}\right)\right] \end{aligned} \tag{A.28}$$

Considering part of the term on line 2 of (A.28), using (A.19) to simplify:

$$\begin{aligned}
&\partial_{t_1}\rho c_s^2\delta_{\alpha\gamma} + \partial_{t_1}\rho_0 u_\alpha u_\gamma \\
&= \; - c_s^2\rho_0\delta_{\alpha\gamma}\partial_{\beta_1}u_\beta + u_\gamma\left(-\partial_{\beta_1}\Pi^0_{\alpha\beta} + F_\alpha\left(\frac{m}{\tau_a}+n\right)\right) \\
&+ u_\alpha\left(-\partial_{\beta_1}\Pi^0_{\gamma\beta} + F_\gamma\left(\frac{m}{\tau_a}+n\right)\right) .
\end{aligned}$$

Using this to look at the full term on line 2 of (A.28):

$$\begin{aligned}
&\Delta t\left(\tau_s-\frac{1}{2}\right)\partial_{t_1}\partial_{\alpha_1}\left(\rho c_s^2\delta_{\alpha\gamma}+\partial_{t_1}\rho_0 u_\alpha u_\gamma\right) \\
&= \; -\Delta t\left(\tau_s-\frac{1}{2}\right)c_s^2\rho_0\partial_{\gamma_1}\partial_{\beta_1}u_\beta \\
&-\Delta t\left(\tau_s-\frac{1}{2}\right)\partial_{\alpha_1}\left[u_\gamma\partial_{\beta_1}\Pi^0_{\alpha\beta}+u_\alpha\partial_{\beta_1}\Pi^0_{\gamma\beta}\right] \\
&+\Delta t\left(\tau_s-\frac{1}{2}\right)\partial_{\alpha_1}\left[\left(\frac{m}{\tau_a}+n\right)\left(u_\gamma F_\alpha+u_\alpha F_\gamma\right)\right] .
\end{aligned}$$

Substituting the definition of $\Pi^0_{\alpha\beta}$, cancelling terms $\mathrm{O}\left(u^3\right)$, and gathering remaining terms gives:

$$\begin{aligned}
&\Delta t\left(\tau_s-\frac{1}{2}\right)\partial_{t_1}\partial_{\alpha_1}\left(\rho c_s^2\delta_{\alpha\gamma}+\partial_{t_1}\rho_0 u_\alpha u_\gamma\right) \\
&= -\Delta t\left(\tau_s-\frac{1}{2}\right)c_s^2\rho_0\partial_{\gamma_1}\partial_{\beta_1}u_\beta \\
&-\Delta t\left(\tau_s-\frac{1}{2}\right)c_s^2\partial_{\alpha_1}\left[u_\gamma\partial_{\alpha_1}\rho+u_\alpha\partial_{\gamma_1}\rho\right] \\
&+\Delta t\left(\tau_s-\frac{1}{2}\right)\left(\frac{m}{\tau_a}+n\right)\partial_{\alpha_1}\left[u_\gamma F_\alpha+u_\alpha F_\gamma\right] .
\end{aligned} \tag{A.29}$$

Now, substituting (A.29) back into (A.28), after cancelling one of the terms, gives:

$$\begin{aligned}
\rho_0\partial_{t_2}u_\gamma \;=\; &\left(\Delta t\left(\tau_a-\frac{1}{2}\right)\left(\frac{m}{\tau_a}+n\right)-\Delta t\tau_a n\right)\partial_{t_1}F_\gamma \\
&-\Delta t\left(\tau_s-\frac{1}{2}\right)c_s^2\partial_{\alpha_1}\left[u_\gamma\partial_{\alpha_1}\rho+u_\alpha\partial_{\gamma_1}\rho\right] \\
&+\Delta t\left(\tau_s-\frac{1}{2}\right)\left(\frac{m}{\tau_a}+n\right)\partial_{\alpha_1}\left[u_\gamma F_\alpha+u_\alpha F_\gamma\right] \\
&+\Delta t\left(\tau_s-\frac{1}{2}\right)c_s^2\rho_0\partial_{\alpha_1}\left(\partial_{\gamma_1}u_\alpha+\partial_{\alpha_1}u_\gamma\right) \\
&-\Delta t\tau_s\partial_{\alpha_1}\left[\frac{1}{2}\left(C_{\alpha\gamma}+C_{\gamma\alpha}\right)\right]
\end{aligned}$$

Using (A.23) and (A.27) to cancel further, and cancelling the terms of $\mathrm{O}(m^3)$ [58]:

$$\begin{aligned}\rho_0\partial_{t_2}u_\gamma &= \Delta t\left(\tau_s-\frac{1}{2}\right)c_s^2\rho_0\partial_{\alpha_1}\left(\partial_{\gamma_1}u_\alpha+\partial_{\alpha_1}u_\gamma\right)\\ &\quad+\Delta t\left(\tau_s-\frac{1}{2}\right)\partial_{\alpha_1}\left[u_\gamma F_\alpha+u_\alpha F_\gamma\right]\\ &\quad-\Delta t\tau_s\partial_{\alpha_1}\left[\frac{1}{2}\left(C_{\alpha\gamma}+C_{\gamma\alpha}\right)\right]\end{aligned}\tag{A.30}$$

Recombining time scales from (A.22) and (A.30) gives:

$$\begin{aligned}\rho_0\partial_t u_\gamma+\partial_{\alpha_1}\Pi^0_{\alpha\gamma} &= \Delta t\left(\tau_s-\frac{1}{2}\right)c_s^2\rho_0\partial_{\alpha_1}\left(\partial_{\gamma_1}u_\alpha+\partial_{\alpha_1}u_\gamma\right)+F_\gamma\\ &\quad+\Delta t\left(\tau_s-\frac{1}{2}\right)\partial_{\alpha_1}\left[u_\gamma F_\alpha+u_\alpha F_\gamma\right]\\ &\quad-\Delta t\tau_s\partial_{\alpha_1}\left[\frac{1}{2}\left(C_{\alpha\gamma}+C_{\gamma\alpha}\right)\right].\end{aligned}\tag{A.31}$$

We require:

$$\left(\tau_s-\frac{1}{2}\right)\left[u_\gamma F_\alpha+u_\alpha F_\gamma\right] = \frac{\tau_s}{2}\left(C_{\alpha\gamma}+C_{\gamma\alpha}\right).$$

Hence:

$$C_{\alpha\beta} = \left(1-\frac{1}{2\tau_s}\right)\left(u_\alpha F_\beta+u_\beta F_\alpha\right).\tag{A.32}$$

Considering the force term, along with (A.21) and (A.32):

$$\begin{aligned}F_i &= t_i\left[\left(1-\frac{1}{2\tau_a}\right)\frac{c_{i\alpha}F_\alpha}{c_s^2}+\left(1-\frac{1}{2\tau_s}\right)\frac{\left(u_\alpha F_\beta+u_\beta F_\alpha\right)c_{i\alpha}c_{i\beta}}{2c_s^4}\right.\\ &\qquad\left.-\left(1-\frac{1}{2\tau_s}\right)\frac{\left(u_\alpha F_\beta+u_\beta F_\alpha\right)c_s^2\delta_{\alpha\beta}}{2c_s^4}\right]\\ \implies F_i &= t_i\left[\left(1-\frac{1}{2\tau_a}\right)\frac{c_{i\alpha}F_\alpha}{c_s^2}-\left(1-\frac{1}{2\tau_s}\right)\frac{u_\alpha F_\alpha}{c_s^2}+\left(1-\frac{1}{2\tau_s}\right)\frac{c_{i\alpha}c_{i\beta}u_\beta F_\alpha}{c_s^4}\right].\end{aligned}\tag{A.33}$$

Now working towards the stress tensor starting at (A.25):

$$\begin{aligned}\sum_i c_{i\mu}c_{i\nu}f_i^1 &= -\Delta t\tau_s\partial_{t_1}\Pi^0_{\mu\nu}-\Delta t\rho_0c_s^2\partial_{\alpha_1}\left(u_\alpha\delta_{\mu\nu}+u_\mu\delta_{\alpha\nu}+u_\nu\delta_{\alpha\mu}\right)\\ &\quad+\Delta t\tau_s\left(c_s^2A\delta_{\mu\nu}+\frac{1}{2}\left(C_{\mu\nu}+C_{\nu\mu}\right)\right)\\ \implies \Pi^1_{\mu\nu} &= -\Delta t\tau_s\partial_{t_1}\left[c_s^2\rho\delta_{\mu\nu}+\rho_0u_\mu u_\nu\right]\\ &\quad-\Delta t\rho_0c_s^2\partial_{\alpha_1}\left(u_\alpha\delta_{\mu\nu}+u_\mu\delta_{\alpha\nu}+u_\nu\delta_{\alpha\mu}\right)\\ &\quad+\Delta t\tau_s\left(c_s^2A\delta_{\mu\nu}+\frac{1}{2}\left(C_{\mu\nu}+C_{\nu\mu}\right)\right).\end{aligned}$$

Using (A.19) and (A.22), along with the product rule, this reduces to:

$$\begin{aligned}
\Pi^1_{\mu\nu} &= \Delta t\tau_s u_\mu \left[\partial_{\alpha_1} c_s^2 \rho \delta_{\alpha\nu} - F_\nu\right] \\
&\quad + \Delta t\tau_s u_\nu \left[\partial_{\alpha_1} c_s^2 \rho \delta_{\alpha\mu} - F_\mu\right] \\
&\quad - \Delta t\tau_s \rho_0 c_s^2 \partial_{\nu_1} u_\mu - \Delta t\tau_s \rho_0 c_s^2 \partial_{\mu_1} u_\nu \\
\implies \Pi^1_{\mu\nu} &= -\Delta t\tau_s \left[u_\nu F_\mu + u_\mu F_\nu\right] \\
&\quad - \Delta t\tau_s \rho_0 c_s^2 \left[\partial_{\nu_1} u_\mu + \partial_{\mu_1} u_n u\right] \\
&\quad + \Delta t\tau_s \left(1 - \frac{1}{2\tau_s}\right)\left(u_\mu F_\nu + u_\nu F_\mu\right) \\
\implies \Pi^1_{\mu\nu} &= -\Delta t\tau_s \rho_0 c_s^2 \left[\partial_{\nu_1} u_\mu + \partial_{\mu_1} u_n u\right] - \frac{\Delta t}{2}\left(u_\mu F_\nu + u_\nu F_\mu\right) \\
\therefore \sigma_{\alpha\beta} &= -\left(1 - \frac{1}{2\tau_s}\right)\left[\Pi^1_{\alpha\beta} + \frac{\Delta t}{2}\left(u_\alpha F_\beta + u_\beta F_\alpha\right)\right]
\end{aligned} \tag{A.34}$$

We must analyse the implemented multi-component force:

$$F_i = \frac{t_i \beta\sigma}{\tau_s c_s^4} \frac{\rho^{(0)}\rho^{(1)}}{\rho^2} \left(\hat{n}_\alpha \hat{n}_\beta - \delta_{\alpha\beta}\right)\left(c_{i\alpha}c_{i\beta} - c_s^2\delta_{\alpha\beta}\right) \tag{A.35}$$

which is a coefficient of the final term of (A.5). This is specified to a two-component system to allow for the analysis of the pressure step of a droplet. A steady, stationary version of (A.31) with the implemented force term rather than the full force term is considered:

$$\partial_{\alpha_1} c_s^2 \rho = -2\Delta t\beta\sigma\partial_{\beta_1}\left[\frac{\rho^{(0)}\rho^{(1)}}{\rho^2}\left(\hat{n}_\alpha\hat{n}_\beta - \delta_{\alpha\beta}\right)\right]. \tag{A.36}$$

Taking this in two dimensions:

$$\begin{aligned}
-\partial_x c_s^2 \rho &= 2\Delta t\beta\sigma\left[\partial_x\left(\frac{\rho^{(0)}\rho^{(1)}}{\rho^2}\left(n_x^2 - 1\right)\right) + \partial_y\left(\frac{\rho^{(0)}\rho^{(1)}}{\rho^2} n_x n_y\right)\right] \\
-\partial_y c_s^2 \rho &= 2\Delta t\beta\sigma\left[\partial_x\left(\frac{\rho^{(0)}\rho^{(1)}}{\rho^2} n_x n_y\right) + \partial_y\left(\frac{\rho^{(0)}\rho^{(1)}}{\rho^2}\left(n_y^2 - 1\right)\right)\right]
\end{aligned}$$

$$\begin{aligned}
-\partial_x c_s^2 \rho &= 2\Delta t\beta\sigma\left[\partial_x\left(\frac{\rho^{(0)}\rho^{(1)}}{\rho^2} n_x^2\right) - \partial_x\frac{\rho^{(0)}\rho^{(1)}}{\rho^2} + \partial_y\left(\frac{\rho^{(0)}\rho^{(1)}}{\rho^2} n_x n_y\right)\right] \\
-\partial_y c_s^2 \rho &= 2\Delta t\beta\sigma\left[\partial_x\left(\frac{\rho^{(0)}\rho^{(1)}}{\rho^2} n_x n_y\right) + \partial_y\left(\frac{\rho^{(0)}\rho^{(1)}}{\rho^2} n_y^2\right) - \partial_y\frac{\rho^{(0)}\rho^{(1)}}{\rho^2}\right]
\end{aligned}$$

Using the product rule to expand this:

$$\begin{aligned}
-\partial_x c_s^2\rho &= 2\Delta t\beta\sigma\left[\frac{\rho^{(0)}\rho^{(1)}}{\rho^2}\partial_x n_x^2 + n_x^2\partial_x\frac{\rho^{(0)}\rho^{(1)}}{\rho^2} - \partial_x\frac{\rho^{(0)}\rho^{(1)}}{\rho^2}\right.\\
&\quad\left.+\frac{\rho^{(0)}\rho^{(1)}}{\rho^2}\partial_y\left(n_x n_y\right) + n_x n_y\partial_y\frac{\rho^{(0)}\rho^{(1)}}{\rho^2}\right]\\
-\partial_y c_s^2\rho &= 2\Delta t\beta\sigma\left[\frac{\rho^{(0)}\rho^{(1)}}{\rho^2}\partial_x\left(n_x n_y\right) + n_x n_y\partial_x\frac{\rho^{(0)}\rho^{(1)}}{\rho^2} + \frac{\rho^{(0)}\rho^{(1)}}{\rho^2}\partial_y n_y^2\right.\\
&\quad\left.+n_y^2\partial_y\frac{\rho^{(0)}\rho^{(1)}}{\rho^2} - \partial_y\frac{\rho^{(0)}\rho^{(1)}}{\rho^2}\right]
\end{aligned}$$

$$\begin{aligned}
-\partial_x c_s^2\rho &= 2\Delta t\beta\sigma\left[2\frac{\rho^{(0)}\rho^{(1)}}{\rho^2}n_x\partial_x n_x + n_x^2\partial_x\frac{\rho^{(0)}\rho^{(1)}}{\rho^2} - \partial_x\frac{\rho^{(0)}\rho^{(1)}}{\rho^2}\right.\\
&\quad\left.+\frac{\rho^{(0)}\rho^{(1)}}{\rho^2}n_y\partial_y n_x + \frac{\rho^{(0)}\rho^{(1)}}{\rho^2}n_x\partial_y n_y + n_x n_y\partial_y\frac{\rho^{(0)}\rho^{(1)}}{\rho^2}\right]\\
-\partial_y c_s^2\rho &= 2\Delta t\beta\sigma\left[\frac{\rho^{(0)}\rho^{(1)}}{\rho^2}n_x\partial_x n_y + \frac{\rho^{(0)}\rho^{(1)}}{\rho^2}n_y\partial_x n_x + n_x n_y\partial_x\frac{\rho^{(0)}\rho^{(1)}}{\rho^2}\right.\\
&\quad\left.+2\frac{\rho^{(0)}\rho^{(1)}}{\rho^2}n_y\partial_y n_y + n_y^2\partial_y\frac{\rho^{(0)}\rho^{(1)}}{\rho^2} - \partial_y\frac{\rho^{(0)}\rho^{(1)}}{\rho^2}\right] \qquad \text{(A.37)}
\end{aligned}$$

Consider that there is a static droplet of radius R; we pick a directly on the interface ($\rho^N = 0$) on the left side where $\hat{n} = (-1, 0) \implies n_x = -1$ and $n_y = 0$. The curvature of the droplet is $\kappa = \frac{1}{R}$ and $\kappa = -\partial_\alpha n_\alpha = -\partial_x n_x - \partial_y n_y$. Using this to remove terms of n_y and cancelling like terms from (A.37) gives:

$$\begin{aligned}
-\partial_x c_s^2\rho &= 2\Delta t\beta\sigma\left[2\frac{\rho^{(0)}\rho^{(1)}}{\rho^2}n_x\partial_x n_x + n_x^2\partial_x\frac{\rho^{(0)}\rho^{(1)}}{\rho^2}\right.\\
&\quad\left.-\partial_x\frac{\rho^{(0)}\rho^{(1)}}{\rho^2} + \frac{\rho^{(0)}\rho^{(1)}}{\rho^2}n_x\partial_y n_y\right]\\
-\partial_y c_s^2\rho &= 2\Delta t\beta\sigma\left[\frac{\rho^{(0)}\rho^{(1)}}{\rho^2}n_x\partial_x n_y - \partial_y\frac{\rho^{(0)}\rho^{(1)}}{\rho^2}\right]
\end{aligned}$$

Noting that n_y is unchanging in the x direction (at this point), and that $\frac{\rho^{(0)}\rho^{(1)}}{\rho^2}$ is at a local maximum, differentials of these terms are zero:

$$\begin{aligned}
-\partial_x c_s^2\rho &= 2\Delta t\beta\sigma\left[2\frac{\rho^{(0)}\rho^{(1)}}{\rho^2}n_x\partial_x n_x + \frac{\rho^{(0)}\rho^{(1)}}{\rho^2}n_x\partial_y n_y\right]\\
-\partial_y c_s^2\rho &= 2\Delta t\beta\sigma\left[0\right]
\end{aligned}$$

Considering just the x differential now then:

$$\begin{aligned} -\partial_x c_s^2 \rho &= 2\Delta t \beta \sigma \left[\frac{\rho^{(0)}\rho^{(1)}}{\rho^2} n_x \partial_x n_x + \frac{\rho^{(0)}\rho^{(1)}}{\rho^2} n_x \partial_x n_x + \frac{\rho^{(0)}\rho^{(1)}}{\rho^2} n_x \partial_y n_y \right] \\ \implies \quad -\partial_x c_s^2 \rho &= 2\Delta t \beta \sigma \left[\frac{\rho^{(0)}\rho^{(1)}}{\rho^2} n_x \partial_x n_x + \frac{\rho^{(0)}\rho^{(1)}}{\rho^2} n_x \left(\partial_x n_x + \partial_y n_y \right) \right] . \end{aligned}$$

As n_x is unchanging in the x direction (at this point), and using the identity of the curvature from earlier we have:

$$\begin{aligned} -\partial_x c_s^2 \rho &= 2\Delta t \beta \sigma \left[\frac{\rho^{(0)}\rho^{(1)}}{\rho^2} n_x \left(-\kappa \right) \right] \\ \implies \quad \partial_x c_s^2 \rho &= 2\Delta t \beta \sigma \frac{\rho^{(0)}\rho^{(1)}}{\rho^2} n_x \kappa \end{aligned} \tag{A.38}$$

Now, from the segregation algorithm we have:

$$\begin{aligned} \partial_\alpha \rho^N &= 4\beta \frac{\rho^{(0)}\rho^{(1)}}{\rho^2} \hat{n}_\alpha \\ \implies \quad \frac{\rho^{(0)}\rho^{(1)}}{\rho^2} \hat{n}_\alpha &= \frac{\partial_\alpha \rho^N}{4\beta} \\ \implies \quad \frac{\rho^{(0)}\rho^{(1)}}{\rho^2} \hat{n}_x &= \frac{\partial_x \rho^N}{4\beta} \end{aligned} \tag{A.39}$$

Using (A.39) in (A.38):

$$\begin{aligned} \therefore \quad \partial_x c_s^2 \rho &= 2\Delta t \beta \sigma \kappa \frac{\partial_x \rho^N}{4\beta} \\ \implies \quad \partial_x c_s^2 \rho &= \frac{\Delta t \sigma}{2} \kappa \partial_x \rho^N \end{aligned} \tag{A.40}$$

Considering Laplace law behaviour, remembering $p = c_s^2 \rho$, we want:

$$\begin{aligned} \Delta p &= \int_{\text{out}}^{\text{in}} \partial_x c_s^2 \rho \partial_x = \frac{\Delta t \sigma}{2} \kappa \int_{\text{out}}^{\text{in}} \partial_x \rho^N d_x = \left[\frac{\Delta t \sigma}{2} \kappa \rho^N \right]_{\text{out}}^{\text{in}} \\ \implies \quad \Delta p &= \frac{\Delta t \sigma}{2} \kappa \left[\rho^N \right]_{\text{out}}^{\text{in}} = \frac{\Delta t \sigma}{2} \kappa \left(-1 - 1 \right) = -\Delta t \sigma \kappa \end{aligned}$$

Letting $\Delta t = 1 \implies \Delta p = -\sigma\kappa$, which means the pressure step from inside to outside the droplet is directly proportional to the interfacial tension parameter and the radius (curvature) of the droplet.

Appendix B

Video files

Within this Appendix are a selection of animations relating to the bulk emulsion flow of Chapters 5–7. There were approximately 250 unique simulations carried out, but this has been condensed the subset of videos seen in Table B.1.

Firstly, an explanation of what will be seen. As discussed in Chapter 5, these videos are produced by using simulation snapshots as frames of a video. The snapshots themselves are based on the local droplet fluid concentration, where red represents the suspending fluid and blue represents the suspended droplet fluid. The speed of the droplets moving within the video may not be representative of the velocity they travelled within the flow, because their movement within the videos depends on the number of timesteps between each frame of the animation. If the video playback speed was proportional to the droplet velocities, the low shear systems would appear almost paused compared to the high shear systems.

Also of note are the positions of the Lees-Edwards boundaries and the effect they have on the speed of the droplets. Between different systems the number and position of the boundary conditions will change—only one is required if the velocity is small, but to shear over the LBM velocity limit more boundaries can be introduced. The boundaries cause a discontinuity in the systems if the displacement is not accounted for. For the output of the snapshots then, the system "slices" between each boundary are shifted by their displacement. Fig. B.1 shows this process. This process starts at the bottom boundary, shifting by zero, then proceeds upwards shifting the slices as required. This means that the bottom slice will have an effective velocity from $-U_{\mathrm{LE}}$ to U_{LE}, whereas the slices above will have positive velocities from $n \times U_{\mathrm{LE}}$ to $(n+1) \times U_{\mathrm{LE}}$, where n increases as the process moves up a slice (starting at zero for the bottom slice).

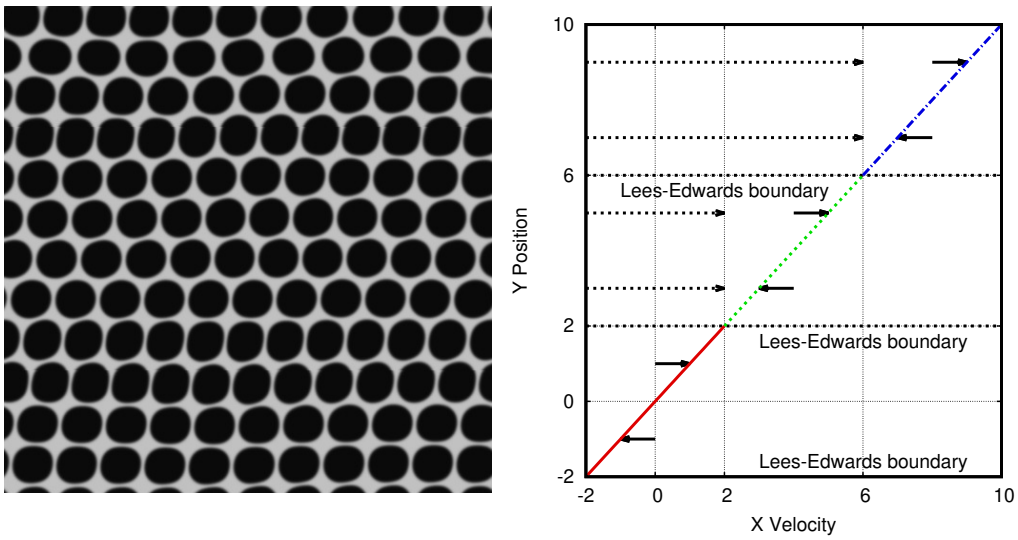

Figure B.1: On the left is an example snapshot of a sheared system. On the right is a schematic of how the *slices* between the Lees-Edwards planes are shifted in order to produce a continuous image. The fluid velocity within each slice stays between $-U_{\mathrm{LE}}$ and U_{LE}, but is shifted into a continuously increasing velocity from bottom to top. This ensures that droplets on the interface line up with their other half on the other side of the boundary.

Table B.1: The list below provides a selection of videos. Firstly, nine monodisperse simulations from a combination of low, medium, and high shear rates and concentrations, which provide a representative sample of the data visible in Chapter 5. Secondly, 7 bidisperse simulations from a combination of low, medium, and high shear rates and concentrations, which provide a representative sample of the data visible in Chapter 7 (note that only one high shear video is available due to the video frames of other simulations being unsuitable—droplets flow too fast to be followed). Finally, a selection of simulations exhibiting unique behaviour. The Digital Object Identifier (DOI) links within the references should provide a page on figshare.com where the animations can be watched or downloaded.

System description	Citation
Free-flowing, unlayered systems, representative of data in Chapter 5:	
$\phi = 0.33, \mathrm{Re} = 5.1 \times 10^{-3}, \mathrm{Ca} = 7.6 \times 10^{-5}, K = 0.5$	[120]
$\phi = 0.33, \mathrm{Re} = 1.0 \times 10^{-1}, \mathrm{Ca} = 4.5 \times 10^{-3}, K = 2.0$	[121]
$\phi = 0.33, \mathrm{Re} = 5.1 \times 10^{-1}, \mathrm{Ca} = 2.3 \times 10^{-2}, K = 2.0$	[122]
$\phi = 0.5, \mathrm{Re} = 5.1 \times 10^{-3}, \mathrm{Ca} = 7.6 \times 10^{-5}, K = 2.0$	[123]
$\phi = 0.5, \mathrm{Re} = 1.0 \times 10^{-1}, \mathrm{Ca} = 4.5 \times 10^{-3}, K = 2.0$	[124]
$\phi = 0.5, \mathrm{Re} = 5.1 \times 10^{-1}, \mathrm{Ca} = 7.6 \times 10^{-3}, K = 2.0$	[125]
$\phi = 0.7, \mathrm{Re} = 5.1 \times 10^{-3}, \mathrm{Ca} = 7.6 \times 10^{-5}, K = 2.0$	[126]
$\phi = 0.7, \mathrm{Re} = 4.6 \times 10^{-2}, \mathrm{Ca} = 2.0 \times 10^{-3}, K = 0.5$	[127]
$\phi = 0.7, \mathrm{Re} = 5.1 \times 10^{-1}, \mathrm{Ca} = 2.3 \times 10^{-2}, K = 0.5$	[128]
Free-flowing, unlayered systems, representative of data in Chapter 7:	
$\phi = 0.33, \mathrm{Re} = 5.1 \times 10^{-3}, \mathrm{Ca} = 7.6 \times 10^{-5}, K = 1.0$	[129]
$\phi = 0.33, \mathrm{Re} = 1.0 \times 10^{-1}, \mathrm{Ca} = 1.5 \times 10^{-3}, K = 1.0$	[130]

$\phi = 0.5, \mathrm{Re} = 5.1 \times 10^{-3}, \mathrm{Ca} = 7.6 \times 10^{-5}, K = 1.0$	[131]
$\phi = 0.5, \mathrm{Re} = 1.0 \times 10^{-1}, \mathrm{Ca} = 1.5 \times 10^{-3}, K = 1.0$	[132]
$\phi = 0.5, \mathrm{Re} = 5.1 \times 10^{-1}, \mathrm{Ca} = 7.6 \times 10^{-3}, K = 1.0$	[133]
$\phi = 0.7, \mathrm{Re} = 5.1 \times 10^{-3}, \mathrm{Ca} = 7.6 \times 10^{-5}, K = 1.0$	[134]
$\phi = 0.7, \mathrm{Re} = 1.0 \times 10^{-1}, \mathrm{Ca} = 1.5 \times 10^{-3}, K = 1.0$	[135]
$\phi = 0.33, \mathrm{Re} = 5.1 \times 10^{-3}, \mathrm{Ca} = 7.6 \times 10^{-5}, K = 0.5$. A cluster forms near the bottom of the video around the 4 minute mark. This clustering appears to be responsible for a significant increase in the droplet deformation.	[115]
$\phi = 0.5, \mathrm{Re} = 5.1 \times 10^{-3}, \mathrm{Ca} = 7.6 \times 10^{-5}, K = 0.5$. The droplets form a single large cluster spanning the entire system. Due to periodicity the cluster joins onto itself and shear banding occurs (the background fluid can more easily flow through the areas lacking droplets). This system was excluded from the main dataset due to the flow regime.	[136]
$\phi = 0.7, \mathrm{Re} = 5.1 \times 10^{-3}, \mathrm{Ca} = 7.6 \times 10^{-5}, K = 5.0$. The droplets never quite break out of the initialisation, but the lattice structure they fall into isn't aligned with the flow direction (unlike in other systems). This diagonal lattice creates a yielding behaviour whereby flow is resisted until the droplet slip past each other into the next jammed state. These systems were excluded from the main dataset due to the flow regime.	[137]
$\phi = 0.6, \mathrm{Re} = 1.0 \times 10^{-1}, \mathrm{Ca} = 1.5 \times 10^{-3}, K = 0.5$. The system is freely-flowing for the majority of the simulation, except an almost imperceptible moment (between 40 and 60 seconds in the video) in which the droplets align to the flow. It's hard to notice in the video, but the result is an order of magnitude drop in the sheared self-diffusion coefficient (for this brief moment, the time averages overcome this). This is the only simulated system with such an event.	[138]
$\phi = 0.7, \mathrm{Re} = 4.6 \times 10^{-2}, \mathrm{Ca} = 2.0 \times 10^{-3}, K = 0.5$. The droplets align almost completely with the flow, but the structure isn't stable. Due to the number of droplets in the system there cannot be an equal number in all the rows; this appears to destabilise the structure, with droplets being forced out and between the rows.	[139]

Bibliography

[1] I. Halliday, S. V. Lishchuk, T. J. Spencer, K. Burgin, and T. Schenkel, "Interfacial micro-currents in continuum-scale multi-component lattice Boltzmann equation hydrodynamics," *Computer Physics Communications*, 2017.

[2] I. Halliday, X. Xu, and K. Burgin, "Shear viscosity of a two-dimensional emulsion of drops using a multiple-relaxation-time-step lattice Boltzmann method," *Physical Review E*, vol. 95, no. 1, p. 023301, 2017.

[3] X. Xu, K. Burgin, M. A. Ellis, and I. Halliday, "Benchmarking of three-dimensional multicomponent lattice Boltzmann equation," *Physical Review E*, vol. 96, no. 5, p. 053308, 2017.

[4] A. Pajouhandeh, A. Kavousi, M. Schaffie, and M. Ranjbar, "Towards a Mechanistic Understanding of Rheological Behaviour of Water-in-Oil Emulsion : Roles of Nanoparticles , Water Volume Fraction and Aging Time," *South African Journal of Chemistry*, vol. 69, pp. 113–123, 2016.

[5] R. Larson, *The structure and rheology of complex fluids*. Topics in Chemical Engineering, OUP USA, 2000.

[6] G. I. Taylor, "The Viscosity of a Fluid Containing Small Drops of Another Fluid," *Proceedings of the Royal Society of London A*, vol. 138, no. 834, pp. 41–48, 1932.

[7] I. Yaron and B. Gal-Or, "On viscous flow and effective viscosity of concentrated suspensions and emulsions," *Rheologica Acta*, pp. 241–252, 1972.

[8] S. J. Choi and W. R. Schowalter, "Rheological properties of nondilute suspensions of deformable particles," *Physics of Fluids*, vol. 18, no. 4, p. 420, 1975.

[9] N. J. Wagner and J. F. Brady, "Shear thickening in colloidal dispersions," *Physics Today*, vol. 62, no. 10, pp. 27–32, 2009.

[10] A. Einstein, "A new determination of molecular dimensions," *Ann. Phys*, vol. 19, no. 2, pp. 289–306, 1906.

[11] M. M. Cross, "Rheology of non-Newtonian fluids: A new flow equation for pseudoplastic systems," *Journal of Colloid Science*, vol. 20, no. 5, pp. 417–437, 1965.

[12] P. J. Carreau, "Rheological Equations from Molecular Network Theories," *Transactions of the Society of Rheology*, vol. 16, no. 1, pp. 99–127, 1972.

[13] L. D. Landau and E. M. Lifshitz, *Fluid Mechanics*. Oxford: Pergamon Press, 2nd ed., 1987.

[14] W. H. W. D. C. Herschel and R. Bulkley, "Measurement of consistency as applied to rubber-benzene solutions," *Colloid & Polymer Science*, vol. 39, no. 4, pp. 291–300, 1926.

[15] N. Casson, "A new flow equation for pigment oile-suspension of the printing ink type," *Rheology of Disperse Systems*, 1959.

[16] I. M. Krieger and T. J. Dougherty, "A Mechanism for Non-Newtonian Flow in Suspensions of Rigid Spheres," *Transactions of the Society of Rheology*, vol. 3, no. 1, pp. 137–152, 1959.

[17] C. Liu, M. Li, R. Han, J. Li, and C. Liu, "Rheology of Water-in-Oil Emulsions with Different Drop Sizes," *Journal of Dispersion Science and Technology*, vol. 37, no. 3, pp. 333–344, 2016.

[18] M. Mooney, "The viscosity of a concentrated suspension of spherical particles," *Journal of Colloid Science*, vol. 6, no. 2, pp. 162–170, 1951.

[19] W. Pabst, "Fundamental considerations on suspension rheology," *Ceramics - Silikaty*, vol. 48, no. 1, pp. 6–13, 2004.

[20] X. Bian, S. Litvinov, M. Ellero, and N. J. Wagner, "Hydrodynamic shear thickening of particulate suspension under confinement," *Journal of Non-Newtonian Fluid Mechanics*, vol. 213, pp. 39–49, 2014.

[21] J. F. Brady, "The rheological behavior of concentrated colloidal dispersions," *The Journal of Chemical Physics*, vol. 99, no. 1, pp. 567–581, 1993.

[22] J. C. van der Werff and C. G. de Kruif, "Hard-sphere Colloidal Dispersions: The Scaling of Rheological Properties with Particle Size, Volume Fraction, and Shear Rate," *Journal of Rheology1*, vol. 33, no. 3, p. 421, 1989.

[23] H. Eilers, "Die Viskosität von Emulsionen hochviskoser Stoffe als Funktion der Konzentration," *Kolloid-Zeitschrift*, vol. 97, no. 3, pp. 313–321, 1941.

[24] J. Bicerano, J. F. Douglas, and D. A. Brune, "Model for the Viscosity of Particle Dispersions," *Journal of Macromolecular Science, Part C: Polymer Reviews*, vol. 39, no. 4, pp. 561–642, 1999.

[25] V. Pryamitsyn and V. Ganesan, "A coarse-grained explicit solvent simulation of rheology of colloidal suspensions," *Journal of Chemical Physics*, vol. 122, no. 10, pp. 1–13, 2005.

[26] W. Pan, B. Caswell, and G. E. Karniadakis, "Rheology, microstructure and migration in brownian colloidal suspensions," *Langmuir*, vol. 26, no. 1, pp. 133–142, 2010.

[27] I. Santamaría-Holek and C. I. Mendoza, "The rheology of concentrated suspensions of arbitrarily-shaped particles," *Journal of Colloid and Interface Science*, vol. 346, no. 1, pp. 118–126, 2010.

[28] R. Pal, "Shear Viscosity Behavior of Emulsions of Two Immiscible Liquids," *Journal of Colloid and Interface Science*, vol. 225, no. 2, pp. 359–366, 2000.

[29] R. Pal, "Evaluation of theoretical viscosity models for concentrated emulsions at low capillary numbers," *Chemical Engineering Journal*, vol. 81, no. 1-3, pp. 15–21, 2001.

[30] W. O. Ostwald, "The velocity function of viscosity of disperse systems," *Kolloid Zeitschrift*, vol. 36, no. 99, p. 157, 1925.

[31] A. de Waele, "Thesis," *Kolloid Zeitschrift*, vol. 36, no. 332, 1925.

[32] T. Guo, K. Zhao, Z. Zhang, X. Gao, and X. Qi, "Rheology Study on Low-Sugar Apple Jam by a New Nonlinear Regression Method of Herschel-Bulkley Model," *Journal of Food Processing and Preservation*, vol. 41, no. 2, 2017.

[33] K. Yasuda, *Investigation of the analogies between viscometricand linear viscoelastic properties of polystyrene fluids*. Phd thesis, Massachusetts Institute of Technology, 1979.

[34] M. A. Rao, "Flow and Functional Models for Rheological Properties of Fluid Foods," in *Rheology of Fluid, Semisolid, and Solid Foods. Food Engineering Series*, ch. 2, pp. 27–36, Boston: Springer, 2014.

[35] E. Álvarez, M. A. Cancela, and R. Maceiras, "Effect of temperature on rheological properties of different jams," *International Journal of Food Properties*, vol. 9, no. 1, pp. 135–146, 2006.

[36] M. Loewenberg and E. J. Hinch, "Numerical simulation of a concentrated emulsion in shear flow," *Journal of Fluid Mechanics*, vol. 321, p. 395, 1996.

[37] P. J. Hoogerbrugge and J. M. Koelman, "Simulating microscopic hydrodynamic phenomena with dissipative particle dynamics," *Europhysics Letters*, vol. 19, no. 3, pp. 155–160, 1992.

[38] P. Meakin and A. Tartakovsky, "Modeling and simulation of pore-scale multiphase fluid flow and reactive transport in fractured and porous media," *Reviews of Geophysics*, vol. 47, no. 3, pp. 1–47, 2009.

[39] S. Chen, N. Phan-Thien, B. C. Khoo, and X. J. Fan, "Flow around spheres by dissipative particle dynamics," *Physics of Fluids*, vol. 18, no. 10, 2006.

[40] M.-b. Liu, J.-z. Chang, and H.-t. Liu, "DPD simulation of multiphase flow at small scales," *2010 The 2nd International Conference on Computer and Automation Engineering (ICCAE)*, vol. 5, pp. 334–337, 2010.

[41] P. Meakin and Z. Xu, "Dissipative Particle Dynamics and other particle methods for multiphase fluid flow in fractured and porous media," *Progress in Computational Fluid Dynamics, An International Journal*, vol. 9, no. 6/7, p. 399, 2009.

[42] A. M. Tartakovsky and P. Meakin, "Pore scale modeling of immiscible and miscible fluid flows using smoothed particle hydrodynamics," *Advances in Water Resources*, vol. 29, no. 10, pp. 1464–1478, 2006.

[43] S. J. Kim and W. R. Hwang, "Direct numerical simulations of droplet emulsions in sliding bi-periodic frames using the level-set method," *Journal of Computational Physics*, vol. 225, no. 1, pp. 615–634, 2007.

[44] S. J. Kim and W. R. Hwang, "Transient stresses of two-dimensional model droplet emulsions subjected to simple shear flow by numerical simulations," *Korea Australia Rheology Journal*, vol. 23, no. 3, pp. 163–171, 2011.

[45] R. Pal, "Novel viscosity equations for emulsions of two immiscible liquids," *Journal of Rheology*, vol. 45, no. 2, pp. 509–520, 2001.

[46] Y. Kagawa, T. Ishigami, K. Hayashi, H. Fuse, Y. Mino, and H. Matsuyama, "Permeation of concentrated oil-in-water emulsions through a membrane pore: numerical simulation using a coupled level set and the volume-of-fluid method," *Soft Matter*, vol. 10, no. 40, pp. 7985–7992, 2014.

[47] R. J. Phillips, R. C. Armstrong, and R. A. Brown, "A constitutive equation for concentrated suspensions that accounts for shear-induced particle migration," *Physics of Fluids*, vol. 4, no. 30, 1992.

[48] R. Pal, "Effect of droplet size on the rheology of emulsions," *AIChE Journal*, vol. 42, pp. 3181–3190, nov 1996.

[49] L. G. Wilson, A. W. Harrison, A. B. Schofield, J. Arlt, and W. C. K. Poon, "Passive and active microrheology of hard-sphere colloids," *Journal of Physical Chemistry B*, vol. 113, no. 12, pp. 3806–3812, 2009.

[50] R. Besseling, E. R. Weeks, A. B. Schofield, and W. C. K. Poon, "Three-dimensional imaging of colloidal glasses under steady shear," *Physical Review Letters*, vol. 99, no. 2, pp. 3–6, 2007.

[51] A. Sierou and J. F. Brady, "Shear-induced self-diffusion in non-colloidal suspensions," *Journal of Fluid Mechanics*, vol. 506, pp. 285–314, 2004.

[52] T. Krüger, H. Kusumaatmaja, A. Kuzmin, O. Shardt, G. Silva, and E. M. Viggen, *The Lattice Boltzmann Method*. Springer, 2017.

[53] S. Succi, *The Lattice Boltzmann Equation for Fluid for Fluid Dynamics and Beyond*. Oxford university press, Oxford, 2001.

[54] Y. H. Qian, D. D'Humières, and P. Lallemand, "Lattice BGK Models for Navier-Stokes Equation," *Europhysics Letters*, vol. 17, no. 6, pp. 479–484, 1992.

[55] S. Chen, H. Chen, D. Martinez, and W. Matthaeus, "Lattice Boltzmann Model for Simulation of Magnetohydrodynamics," *Physical Review Letters*, vol. 67, no. 27, p. 5, 1991.

[56] Y. H. Qian, *Lattice Gas and Lattice Kinetic Theory Applied to the Navier–Stokes Equation*. PhD thesis, Université Pierre-et-Marie-Curie, 1990.

[57] I. Ginzburg, "Equilibrium-type and link-type lattice Boltzmann models for generic advection and anisotropic-dispersion equation," *Advances in Water Resources*, vol. 28, pp. 1171–1195, nov 2005.

[58] X. He and L.-S. Luo, "Lattice Boltzmann Model for the Incompressible Navier–Stokes Equation," *Journal of Statistical Physics*, vol. 88, no. 3/4, pp. 927–944, 1997.

[59] G. Házi and C. Jiménez, "Simulation of two-dimensional decaying turbulence using the "incompressible" extensions of the lattice Boltzmann method," *Computers and Fluids*, vol. 35, no. 3, pp. 280–303, 2006.

[60] J. Zhang and D. Kwok, "Pressure boundary condition of the lattice Boltzmann method for fully developed periodic flows," *Physical Review E*, vol. 73, p. 047702, apr 2006.

[61] S. H. Kim and H. Pitsch, "A generalized periodic boundary condition for lattice Boltzmann method simulation of a pressure driven flow in a periodic geometry," *Physics of Fluids*, vol. 19, pp. 108101–108104, oct 2007.

[62] Z. Guo, C. Zheng, and B. Shi, "Discrete lattice effects on the forcing term in the lattice Boltzmann method," *Physical Review E*, vol. 65, pp. 1–6, apr 2002.

[63] V. W. Azizi Tarksalooyeh, G. Závodszky, B. J. M. van Rooij, and A. G. Hoekstra, "Inflow and outflow boundary conditions for 2D suspension simulations with the immersed boundary lattice Boltzmann method," *Computers and Fluids*, vol. 0, pp. 1–6, 2018.

[64] A. J. C. Ladd, "Numerical simulations of particulate suspensions via a discretized Boltzmann equation. Part 1. Theoretical foundation," *Journal of Fluid Mechanics*, vol. 271, p. 285, 1994.

[65] A. J. C. Ladd, "Numerical simulations of particulate suspensions via a discretized Boltzmann equation. Part 2. Numerical results," *Journal of Fluid Mechanics*, vol. 271, pp. 311–339, 1994.

[66] E. J. Javaran, M. Rahnama, and S. Jafari, "Particulate flow simulation using Lattice Boltzmann Method: A rheological study," *Advanced Powder Technology*, vol. 25, no. 4, pp. 1325–1333, 2014.

[67] A. W. Lees and S. F. Edwards, "The computer study of transport processes under extreme conditions," *Journal of Physics C*, vol. 5, no. 15, pp. 1921–1928, 1972.

[68] A. J. Wagner and I. Pagonabarraga, "Lees-Edwards boundary conditions for lattice Boltzmann," *Journal of Statistical Physics*, vol. 107, pp. 521–537, mar 2002.

[69] E. J. Javaran, M. Rahnama, and S. Jafari, "Combining Lees-Edwards boundary conditions with smoothed profile-lattice Boltzmann methods to introduce shear into particle suspensions," *Advanced Powder Technology*, vol. 24, no. 6, pp. 1109–1118, 2013.

[70] M. R. Swift, W. R. Osborn, and J. M. Yeomans, "Lattice Boltzmann Simulation of Nonideal Fluids," *Physical Review Letters*, vol. 75, pp. 830–833, jul 1995.

[71] X. Shan and H. Chen, "Lattice Boltzmann model for simulating flows with multiple phases and components," *Physical Review E*, vol. 47, no. 3, pp. 1815–1819, 1993.

[72] S. V. Lishchuk, C. M. Care, and I. Halliday, "Lattice Boltzmann algorithm for surface tension with greatly reduced microcurrents.," *Physical Review E*, vol. 67, p. 036701, mar 2003.

[73] I. Halliday, A. P. Hollis, and C. M. Care, "Lattice Boltzmann algorithm for continuum multicomponent flow," *Physical Review E*, vol. 76, p. 26708, aug 2007.

[74] T. J. Spencer, I. Halliday, and C. M. Care, "A local lattice Boltzmann method for multiple immiscible fluids and dense suspensions of drops," *Philosophical Transactions of the Royal Society A*, vol. 369, no. 1944, pp. 2255–2263, 2011.

[75] M. M. Dupin, T. J. Spencer, I. Halliday, and C. M. Care, "A many-component lattice Boltzmann equation simulation for transport of deformable particles," *Philosophical Transactions of the Royal Society A*, vol. 362, no. 1822, pp. 1885–1914, 2004.

[76] M. M. Dupin, I. Halliday, and C. M. Care, "A multi-component lattice Boltzmann scheme: Towards the mesoscale simulation of blood flow," *Medical Engineering and Physics*, vol. 28, no. 1 SPEC. ISS., pp. 13–18, 2006.

[77] D. Grunau, S. Chen, and K. Eggert, "A lattice Boltzmann model for multiphase fluid flows," *Physics of Fluids A: Fluid Dynamics*, vol. 5, no. 10, pp. 2557–2562, 1993.

[78] A. K. Gunstensen, D. H. Rothman, S. Zaleski, and G. Zanetti, "Lattice Boltzmann model of immiscible fluids," *Physical Review A*, vol. 43, pp. 4320–4327, apr 1991.

[79] T. Reis and T. N. Phillips, "Lattice Boltzmann model for simulating immiscible two-phase flows," *Journal of Physics A: Mathematical and Theoretical*, vol. 40, no. 14, pp. 4033–4053, 2007.

[80] S. V. Lishchuk, I. Halliday, and C. M. Care, "Multicomponent lattice Boltzmann method for fluids with a density contrast," *Physical Review E*, vol. 77, no. 3, pp. 1–8, 2008.

[81] H. Liu, A. J. Valocchi, and Q. Kang, "Three-dimensional lattice Boltzmann model for immiscible two-phase flow simulations," *Physical Review E*, vol. 85, no. 4, pp. 1–14, 2012.

[82] Y. Ba, H. Liu, Q. Li, Q. Kang, and J. Sun, "Multiple-relaxation-time color-gradient lattice Boltzmann model for simulating two-phase flows with high density ratio," *Physical Review E*, vol. 94, no. 2, pp. 1–15, 2016.

[83] R. Benzi, S. Chibbaro, and S. Succi, "Mesoscopic lattice Boltzmann modeling of flowing soft systems," *Physical Review Letters*, vol. 102, no. 2, pp. 2–5, 2009.

[84] R. Benzi, M. Sbragaglia, S. Succi, M. Bernaschi, and S. Chibbaro, "Mesoscopic lattice Boltzmann modeling of soft-glassy systems: Theory and simulations," *Journal of Chemical Physics*, vol. 131, no. 10, 2009.

[85] R. Benzi, M. Bernaschi, M. Sbragaglia, and S. Succi, "Rheological properties of soft-glassy flows from hydro-kinetic simulations," *Europhysics Letters*, vol. 104, no. 4, pp. 1–6, 2013.

[86] H. Xi and C. Duncan, "Lattice Boltzmann simulations of three-dimensional single droplet deformation and breakup under simple shear flow," *Physical Review E*, vol. 59, no. 3, pp. 1–15, 1999.

[87] A. Gupta and M. Sbragaglia, "Deformation and breakup of viscoelastic droplets in confined shear flow," *Physical Review E*, vol. 90, p. 023305, aug 2014.

[88] K. M. B. Jansen, W. G. M. Agterof, and J. Mellema, "Droplet breakup in concentrated emulsions," *Journal of Rheology*, vol. 45, no. 1, p. 227, 2001.

[89] A. P. Hollis, T. J. Spencer, I. Halliday, and C. M. Care, "Dynamic wetting boundary condition for continuum hydrodynamics with multi-component lattice Boltzmann equation simulation method," *IMA Journal of Applied Mathematics*, vol. 76, no. 5, pp. 726–742, 2011.

[90] Y. Ba, H. Liu, J. Sun, and R. Zheng, "Color-gradient lattice Boltzmann model for simulating droplet motion with contact-angle hysteresis," *Physical Review E*, vol. 88, no. 4, pp. 1–13, 2013.

[91] H. P. Jansen, K. Sotthewes, J. Van Swigchem, H. J. Zandvliet, and E. S. Kooij, "Lattice Boltzmann modeling of directional wetting: Comparing simulations to experiments," *Physical Review E*, vol. 88, no. 1, pp. 1–10, 2013.

[92] F. Jansen and J. Harting, "From bijels to Pickering emulsions: A lattice Boltzmann study," *Physical Review E*, vol. 83, p. 046707, apr 2011.

[93] H. Farhat, F. Celiker, T. Singh, and J. S. Lee, "A hybrid lattice Boltzmann model for surfactant-covered droplets," *Soft Matter*, vol. 7, no. 5, p. 1968, 2011.

[94] T. Krüger, S. Frijters, F. Günther, B. Kaoui, and J. Harting, "Numerical simulations of complex fluid-fluid interface dynamics," *European Physical Journal: Special Topics*, vol. 222, no. 1, pp. 177–198, 2013.

[95] T. Krüger, "Effect of tube diameter and capillary number on platelet margination and near-wall dynamics," *Rheologica Acta*, vol. 55, no. 6, pp. 511–526, 2016.

[96] I. Halliday, S. V. Lishchuk, T. J. Spencer, G. Pontrelli, and C. M. Care, "Multiple-component lattice Boltzmann equation for fluid-filled vesicles in flow," *Physical Review E*, vol. 87, pp. 1–15, feb 2013.

[97] I. Ginzburg, F. Verhaeghe, and D. D'Humières, "Study of simple hydrodynamic solutions with the two-relaxation-times lattice Boltzmann scheme," *Communications in Computational Physics*, vol. 3, no. 3, pp. 519–581, 2008.

[98] I. Ginzburg, D. D'Humières, and A. Kuzmin, "Optimal stability of advection-diffusion lattice boltzmann models with two relaxation times for positive/negative equilibrium," *Journal of Statistical Physics*, vol. 139, no. 6, pp. 1090–1143, 2010.

[99] H. Ding, P. D. Spelt, and C. Shu, "Diffuse interface model for incompressible two-phase flows with large density ratios," *Journal of Computational Physics*, vol. 226, no. 2, pp. 2078–2095, 2007.

[100] A. Fakhari and M. H. Rahimian, "Phase-field modeling by the method of lattice boltzmann equations," *Physical Review E*, vol. 81, no. 3, pp. 1–16, 2010.

[101] X. He, S. Chen, and R. Zhang, "A Lattice Boltzmann scheme for incompressible multiphase flow and its application in simulation of Rayleigh – Taylor instability," *Journal of Computational Physics*, vol. 663, no. 2, pp. 642–663, 1999.

[102] K. Langaas and J. M. Yeomans, "Lattice Boltzmann simulation of a binary fluid with different phase viscosities and its application to fingering in two dimensions," *European Physical Journal B*, vol. 15, no. 1, pp. 133–141, 2000.

[103] Y. Q. Zu and S. He, "Phase-field-based lattice Boltzmann model for incompressible binary fluid systems with density and viscosity contrasts," *Physical Review E*, vol. 87, no. 4, pp. 1–23, 2013.

[104] H. Liu, A. J. Valocchi, C. Werth, Q. Kang, and M. Oostrom, "Pore-scale simulation of liquid CO2 displacement of water using a two-phase lattice Boltzmann model," *Advances in Water Resources*, vol. 73, pp. 144–158, 2014.

[105] I. Ginzburg, "Lattice Boltzmann modeling with discontinuous collision components: Hydrodynamic and advection-diffusion equations," *Journal of Statistical Physics*, vol. 126, no. 1, pp. 157–206, 2007.

[106] K. Burgin, "Droplet flow simulation, strong pressure fluctuations,", 2018. https://dx.doi.org/10.6084/m9.figshare.7379465.v1.

[107] K. Burgin, "Droplet flow simulation, pressure fluctuations absent,", 2018. https://dx.doi.org/10.6084/m9.figshare.7379468.v1.

[108] T. Inamuro, M. Yoshino, and F. Ogino, "Lattice Boltzmann simulation of flows in a three-dimensional porous structure," *Internatinal Journal for Numerical Methods in Fluids*, vol. 29, no. December 1997, pp. 737–748, 1999.

[109] M. Foglino, A. N. Morozov, O. Henrich, and D. Marenduzzo, "Flow of Deformable Droplets: Discontinuous Shear Thinning and Velocity Oscillations," *Physical Review Letters*, vol. 119, no. 20, pp. 1–6, 2017.

[110] H. Zhou and C. Pozrikidis, "Pressure-driven flow of suspensions of liquid drops," *Physics of Fluids*, vol. 6, no. 1, pp. 80–94, 1994.

[111] M. Galassi, J. Davies, J. Theiler, B. Gough, G. Jugman, P. Alken, M. Booth, and F. Rossi, *GNU Scientific Library Reference Manual*. Network Theory Ltd, third ed., 2009.

[112] J. Kromkamp, D. T. M. van den Ende, D. Kandhai, R. G. M. van der Sman, and R. M. Boom, "Shear-induced self-diffusion and microstructure in non-Brownian suspensions at non-zero Reynolds numbers," *Journal of Fluid Mechanics*, vol. 529, pp. 253–278, 2005.

[113] L. Bai and D. Breen, "Calculating Center of Mass in an Unbounded 2D Environment," *Journal of Graphics Tools*, vol. 13, no. 4, pp. 53–60, 2008.

[114] L. Mountrakis, E. Lorenz, and A. G. Hoekstra, "Scaling of shear-induced diffusion and clustering in a blood-like suspension," *Europhysics Letters*, vol. 114, no. 1, p. 14002, 2016.

[115] K. Burgin, "Emulsion droplets flow simulation, clustering increasing deformation [Video file],", 2018. https://dx.doi.org/10.6084/m9.figshare.6557039.

[116] X. Zheng, W. Iglesias, and P. Palffy-Muhoray, "Distance of closest approach of two arbitrary hard ellipsoids," *Physical Review E*, vol. 79, no. 5, pp. 1–6, 2009.

[117] X. Zheng and P. Palffy-Muhoray, "Subroutine to calculate the distance of closest approach of two ellipses,", 2010.

[118] S. D. Stoddard, "Identifying clusters in computer experiments on systems of particles," *Journal of Computational Physics*, vol. 27, no. 2, pp. 291–293, 1978.

[119] B. Servan-Camas and F. T.-C. Tsai, "Lattice Boltzmann method with two relaxation times for advection-diffusion equation: Third order analysis and stability analysis," *Advances in Water Resources*, vol. 31, no. 8, pp. 1113–1126, 2008.

[120] K. Burgin, "Emulsion droplets flow simulation, low shear and concentration [Video file],", 2018. https://dx.doi.org/10.6084/m9.figshare.6507026.v1.

[121] K. Burgin, "Emulsion droplets flow simulation, modest shear and low concentration [Video file],", 2018. https://dx.doi.org/10.6084/m9.figshare.6544388.v1.

[122] K. Burgin, "Emulsion droplets flow simulation, high shear and low concentration [Video file],", 2018. https://dx.doi.org/10.6084/m9.figshare.6544949.v1.

[123] K. Burgin, "Emulsion droplets flow simulation, low shear and modest concentration [Video file],", 2018. https://dx.doi.org/10.6084/m9.figshare.6544238.v1.

[124] K. Burgin, "Emulsion droplets flow simulation, modest shear and concentration [Video file],", 2018. https://dx.doi.org/10.6084/m9.figshare.6507122.v1.

[125] K. Burgin, "Emulsion droplets flow simulation, high shear and modest concentration [Video file],", 2018. https://dx.doi.org/10.6084/m9.figshare.6544637.v1.

[126] K. Burgin, "Emulsion droplets flow simulation, low shear rate and high concentration [Video file],", 2018. https://dx.doi.org/10.6084/m9.figshare.6543086.v1.

[127] K. Burgin, "Emulsion droplets flow simulation, modest shear and high concentration [Video file],", 2018. https://dx.doi.org/10.6084/m9.figshare.6507194.v1.

[128] K. Burgin, "Emulsion droplets flow simulation, high shear and high concentration [Video file],", 2018. https://dx.doi.org/10.6084/m9.figshare.6544724.v1.

[129] K. Burgin, "Emulsion droplets flow simulation, low shear and low concentration [Video file],", 2018. https://dx.doi.org/10.6084/m9.figshare.6768512.

[130] K. Burgin, "Emulsion droplets flow simulation, modest shear and low concentration [Video file],", 2018. https://dx.doi.org/10.6084/m9.figshare.6561710.v1.

[131] K. Burgin, "Emulsion droplets flow simulation, low shear and modest concentration [Video file],", 2018. https://dx.doi.org/10.6084/m9.figshare.6768536.

[132] K. Burgin, "Emulsion droplets flow simulation, modest shear and concentration [Video file],", 2018. https://dx.doi.org/10.6084/m9.figshare.6561713.v1.

[133] K. Burgin, "Emulsion droplets flow simulation, high shear and modest concentration [Video file],", 2018. https://dx.doi.org/10.6084/m9.figshare.6561692.v1.

[134] K. Burgin, "Emulsion droplets flow simulation, low shear and high concentration [Video file],", 2018. https://dx.doi.org/10.6084/m9.figshare.6768548.

[135] K. Burgin, "Emulsion droplets flow simulation, modest shear and high concentration [Video file],", 2018. https://dx.doi.org/10.6084/m9.figshare.6561716.v1.

[136] K. Burgin, "Emulsion droplets flow simulation, clustering in honeycomb-like structure [Video file],", 2018. https://dx.doi.org/10.6084/m9.figshare.6506834.

[137] K. Burgin, "Emulsion droplets flow simulation, diagonal clustering [Video file],", 2018. https://dx.doi.org/10.6084/m9.figshare.6561626.v2.

[138] K. Burgin, "Emulsion droplets flow simulation, brief layering [Video file],", 2018. https://dx.doi.org/10.6084/m9.figshare.6561650.v1.

[139] K. Burgin, "Emulsion droplets flow simulation, unstable layering [Video file],", 2018. https://dx.doi.org/10.6084/m9.figshare.6561665.v1.